UNIVERSIDADE FEDERAL DO CEARÁ

CENTRO DE CIÊNCIAS

DEPARTAMENTO DE QUÍMICA ANALÍTICA E FÍSICO-QUÍMICA

PROGRAMA DE PÓS-GRADUAÇÃO EM QUÍMICA

TIAGO MELO FREIRE

DEVELOPMENT OF 0D AND 2D MATERIALS FOR WATER REMEDIATION, HYDROGEN EVOLUTION REACTION, AND CANCER TREATMENT

FORTALEZA

2021

TIAGO MELO FREIRE

DEVELOPMENT OF 0D AND 2D MATERIALS FOR WATER REMEDIATION, HYDROGEN EVOLUTION REACTION, AND CANCER TREATMENT

PhD thesis presented at Chemistry Graduated Program in Chemistry from Federal University of Ceará, as partial requisition in obtaining the Chemistry PhD title. Concentration field: Physical Chemistry

Supervisor: Prof. Dr. Pierre Basílio Almeida Fechine

FORTALEZA

2021

Dados Internacionais de Catalogação na Publicação
Universidade Federal do Ceará
Biblioteca Universitária
Gerada automaticamente pelo módulo Catalog, mediante os dados fornecidos pelo(a) autor(a)

F935d Freire, Tiago Melo.

Development of 0d and 2d materials for water remediation, hydrogen evolution reaction, and cancer treatment / Tiago Melo Freire. – 2021.
161 f. : il. color

Tese (doutorado) – Universidade Federal do Ceará, Centro de Ciências, Programa de Pós-Graduação em Química, Fortaleza, 2021.
Orientação: Prof. Dr. Pierre Basílio Almeida Fechine.

1. magnetita/quitosana. 2. nanocristais bimetálicos. 3. eletrocatálise. 4. nitreto de carbono. 5. câncer . I. Título.

CDD 540

TIAGO MELO FREIRE

DEVELOPMENT OF 0D AND 2D MATERIALS FOR WATER REMEDIATION, HYDROGEN EVOLUTION REACTION, AND CANCER TREATMENT

PhD thesis presented at Chemistry Graduated Program in Chemistry from Federal University of Ceará, as partial requisition in obtaining the Chemistry PhD title. Concentration field: Physical Chemistry

Approved in: 15/06/2021.

EXAMINATORS

Prof. Dr. Pierre Basílio Almeida Fechine (Supervisor)

Universidade Federal do Ceará (UFC)

Prof. Dr. Antoninho Valentini

Universidade Federal do Ceará (UFC)

Prof. Dr. Pedro de Lima Neto

Universidade Federal do Ceará (UFC)

Prof. Dr. Juliano Casagrande Denardin

Universidad de Santiago de Chile (USACH)

Prof. Dr. Ralph Santos-Oliveira

Universidade Estadual da Zona Oeste (UEZO)

I dedicate this work to my wife, Jessica Miranda Abreu Freire, my parents, Jonivaldo Freire de Souza e Maria Rosario Melo (*in memoriam*), my brother, Rafael Melo Freire, my sister-in-law Maria do Socorro and my dear friends who have helped me to become the professional I am today.

ACKNOWLEDGMENTS

Firstly, I would like to thank God for all opportunities and challenges I have passed through in my life. All personal and professional teachings I have learned made me a better man and professional. Secondly, I would like to thank the constant support and unconditional love of my family, vital to making me move forward. My father and mother, Jonivaldo Freire de Souza and Maria do Rosario Melo Freire, have always provided the assistance and love I needed. My brother, Rafael Melo Freire, and his wife, Maria do Socorro Gonçalves da Costa, have supported me and provided me their valuable friendship. My dear wife, Jessica Miranda Abreu Freire, has always encouraged me to overcome all kinds of challenges since the very beginning of our graduation at Universidade Federal do Ceará (UFC). My achievements would hardly have been accomplished without them. Thus, I am grateful to God for giving me a beautiful and wonderful family.

From Grupo de Química de Materiais Avançados (GQMat), I have made dear friends and for that I am really grateful. Therefore, my warm thanks to Davino Machado, Denis Valony, Eduardo Viana, Victor Moreira, Anderson Valério, Fernando Lima, Jessica Sales, Clinton Silva, Leticia Xavier, Emanuel Queiroz, Yale Luck, Samuel Veloso, Sheyliane Pontes, Wesley Galvão, Eduardo Mallmann, Paulo Henrique, Antonio Alvernes, Janaína Sobreira, and Lillian Dutra, and my advisor Pierre Basilio Almeida Fechine. Each of you has marked my trajectory, and I am very grateful for all the happy memories shared with you. I would also like to thank all my childhood friends. Undoubtedly, having so many people like you around me was very important to make life lighter and more enjoyable.

I would like to express my sincerest gratitude to my advisor and one of my best friends, Pierre Basílio Almeida Fechine. Your patience to guide me during nine years in different research projects was essential to make me the professional I am today. Being one of Pierre’s students was extremely pleasant. All the meetings were always full of valuable knowledge, which helped me both personally and professionally. Other professors of the Chemistry course were also important to me. In particular, I would like to thank Professors Antoninho Valentini, Elisane Longhinotti, Ronaldo Nascimento, Adriana Correia, Pedro Neto, Gisele Lopes and Ruth Vidal for their support and advice. My colleagues of work as a technician at UFC, Andréa, Dafne, Natalia, Adson, Penha e Cristina. I would like to thank you for the welcome and partnership in these years.

Additionally, I want to thank the UFC itself for the opportunity to study chemistry during my graduation, master and doctorate degrees. Furthermore, it was the place I met my wife and my dear friends, Aline Maia, Monica Aparecida, Nívea Araujo, and Diana Kelly. So, I can say that studying at UFC had a very positive impact on my life because I met incredible people and had beautiful experiences.

I would also to thank the Coordenação de Aperfeiçoamento de Pessoal de Nível Superior (CAPES) and Conselho Nacional de Desenvolvimento Científico e Tecnológico (CNPq) for all financial support provided.

RESUMO

Nanocompósitos de magnetita/quitosana foram capazes de remover corantes a partir de efluentes têxteis. Assim, um estudo comparativo desses materiais frente a adsorção do corante reativo preto 5 e do alaranjado de metila mostraram que os materiais possuem uma capacidade de adsorção dependente do pH, sendo o pH 4 mais apropriado para as amostras reticuladas e o pH 8 para a amostra não reticulada. De fato, foi evidenciado que a capacidade de adsorção é influenciada por forças eletrostáticas e pelo efeito do tamanho molecular para as amostras modificadas e não modificadas, respectivamente. No segundo momento, foram sintetizados nanoligas de FeM (M = Ag, Co, Cu e Ni) via decomposição térmica para aplicação na produção de hidrogênio. Estas apresentaram comportamento de ferrimagnético mole, com diferentes morfologias a depender da composição (esferas, cubos e prismas). Contudo, as amostras contendo Ag e Cu apresentaram uma distribuição de tamanho bimodal, possivelmente devido à grande diferença entre o potencial de redução desses metais e do íon férrico, o que gera diferentes taxas de nucleação. Ensaios eletrocatalíticos mostraram que a liga de FeCu apresentou melhor desempenho devido ao seu menor sobrepotencial (494 mV) em comparação com as demais ligas, e todos os eletrocatalisadores apresentaram estabilidade durante o período de 8 h de operação contínua. Finalmente, produziu-se g-C_3N_4 a partir da polimerização térmica da ureia a 550 °C para uso no tratamento de câncer. A formação de uma estrutura em forma de folhas empilhadas de C_3N_4 foi evidenciada pelas técnicas de DRX, FTIR, Raman, AFM e TEM. Análises de DRX e XPS mostraram defeitos na estrutura do g-C_3N_4 devido à incompleta polimerização da ureia, acarretando na diminuição do espaço interplanar. O material sintetizado apresentou uma *band gap* de 2,87 eV e uma banda de emissão em 448 nm sendo independente do comprimento de onda excitante. Ensaios biológicos revelaram uma excelente biocompatibilidade do g-C_3N_4 com células normais e o efeito inibitório sobre linhagens de células cancerígenas. Testes de biodistribuição em tecidos indicaram que o material se acumula nos pulmões nas duas primeiras horas, sendo posteriormente encontrado principalmente no fígado após 24 h. Nesse sentido, o g-C_3N_4 mostrou grande potencial para o tratamento de vários tipos de câncer.

Palavras-chave: magnetita/quitosana; adsorção; nanocristais bimetálicos; eletrocatálise; nitreto de carbono; câncer.

ABSTRACT

Magnetite/chitosan nanocomposites were able to remove dyes from textile effluents. Thus, a comparative study of these materials toward adsorption of reactive black 5 and methyl orange showed a pH-dependent adsorption capacity, with pH 4 being more indicated for crosslinked samples and pH 8 for non-modified material. Indeed, it demonstrated that the adsorption capacity is influenced by molecular size effect and electrostatic attraction for unmodified and modified nanocomposites, respectively. In the second moment, bimetallic FeM (M = Ag, Co, Cu, and Ni) materials were synthesized by thermal decomposition for hydrogen production application. These samples presented soft ferrimagnetic behaviour and varied morphology depending of the composition (e.g., spheres, cubes, and triangles). However, the samples containing Ag and Cu showed a bimodal size distribution, possibly due to the significant difference between the reduction potential of these metals and ferric ions, which generates different nucleation rates. Electrocatalytic tests showed that the FeCu alloy performed better due to its lower overpotential (494 mV) compared to the other alloys, and all electrocatalysts were stable during the 8 h period of continuous operation. Finally, g-C_3N_4 was produced from the thermal polymerization of urea at 550° C for use in cancer treatment. The formation of a typical structure in the form of stacked C_3N_4 sheets was evidenced by XRD, FTIR, Raman, AFM, and TEM techniques. Analysis of XRD and XPS showed defects in the structure of g-C_3N_4 due to incomplete polymerization of urea, resulting in decreased interplanar space. The synthesized materials presented a band gap of 2.87 eV and an emission band at 448 nm, regardless of the exciting wavelength. Biological tests have shown excellent biocompatibility of g-C_3N_4 with normal cells and the inhibitory effect on cancer cell lines. Biodistribution tests in tissues indicated that the material accumulated in the lungs in the first two hours and was later found mainly in the liver after 24 hours. In this sense, g-C_3N_4 showed great potential for the treatment of various types of cancer.

Keywords: magnetite/chitosan; adsorption; bimetallic nanocrystals; electrocatalysis; carbon nitride; cancer.

LIST OF FIGURES

LIST OF TABLES

CONTENTS

1. CHAPTER 1 – INTRODUCTION AND OBJECTIVES

1.1. Introduction

The concept of nanotechnology came up in 1959 when Richard Feynman predicted the application of this technology in the future. However, only in the 2000s, it was observed its use in commercial products, such as cosmetics, sunscreen, cleaning, food, and household appliances (HOANG *et al.*, 2017). In recent years, the use of nanotechnology in different areas of knowledge, such as chemistry, physics, and biology, has boosted the miniaturization of devices and the emergence of new research fields such as biomedicine and spintronic (TAN *et al.*, 2015; HOANG *et al.*, 2017). In addition, the current trends in this technology involve the use of nanomaterials for water treatment (ZAHEER *et al.*, 2019), hydrogen production (ZHANG, Z. *et al.*, 2020), and biomedicine (ZHOU *et al.*, 2020). However, manipulating the matter on this level is complex since it is necessary a precise control of many parameters to obtain the desired properties. With the development of new techniques of synthesis, the obtention of nanostructures with distinguished dimensionality has become possible, being usually classified as zero-dimension (0D), one-dimension (1D), two-dimension(2D) and three-dimension (3D) (CHEN *et al.*, 2015). This categorization is based on the number of dimensions of the material with a size below 100 nm: 0D, 1D, 2D and 3D have three, two, one and no dimension smaller than 100 nm, respectively. Among these, 0D and 2D nanomaterials have gained significant attention due to their magnetic, electronic, and optical properties, which have helped to improve their performance in several industrial applications, mainly in water treatment and electrochemical hydrogen production fields (JIN, H. *et al.*, 2018; T.C *et al.*, 2018).

1.2. Magnetic nanoparticles

Magnetic nanoparticles (MNPs) are an important class of functional nanoparticles (NPs) that have attracted great attention due to their excellent nanoscale magnetism and potential application (ASHRAF *et al.*, 2020). It has been predicted that ferromagnetic materials below a critical limit would have a single magnetic domain. All the magnetic moments within the particle rotate coherently in this state, resulting in a large magnetization (LOW *et al.*, 2018). In addition, it has been found that reducing the nanoparticle size is observed a change in the magnetic behavior from ferromagnetic to superparamagnetic, showing that MNPs have unique size-dependent magnetic properties (NETO *et al.*, 2017). Figure 1 shows this behavior transition, as well as its effect on the magnetization curve.

Figure 1 – Illustration of the particle size effect on the domain, coercivity, and hysteresis loop in the magnetization curve.

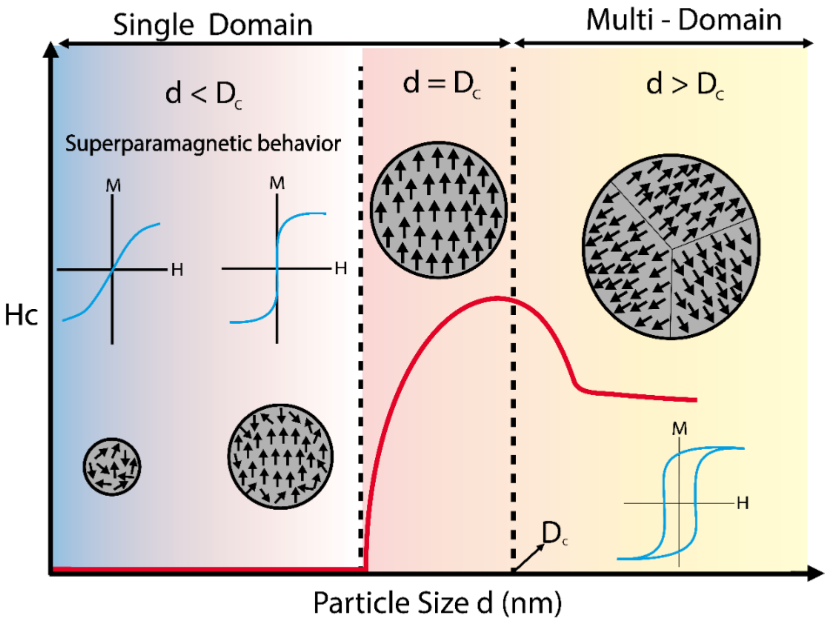

Source: modified from (MOHAPATRA *et al.*, 2019).

The critical diameter (D_c) for spherical MNPs can be estimated using equation (1).

$$D_{c} \approx \frac{36\sqrt{AK}}{\mu_{0}M_{S}^{2}} \qquad (1)$$

where A is the exchange stiffness, K is the magnetocrystalline anisotropy, μ_0 is the permeability of free space ($4\pi \times 10^{7}$ H/m), and M_S is the saturation magnetization. It is important to highlight the alignment of magnetization directions into each domain is controlled by the anisotropy energy and volume of the particle. When d (MNP diameter) for equal to D_C, the single magnetic domain is formed, which leads to a substantial enhancement of the coercivity. For MNPs with diameters below the Dc, only a single magnetic domain is observed due to the decrease of the magnetic anisotropy energy ($Ea = KV$, where V is the particle volume). Also, further reduction in the size leads to a fast reduction in the coercivity occasioned by the decrease of the anisotropy energy value, which becomes comparable to or even lower than the thermal energy K_BT (where K_B is the Boltzmann constant and T is the temperature). Thus, when the MNP is small enough, K_BT will overcome KV and the MNPs become superparamagnetic, leading to a zero net magnetization (or $H_c = 0$) (WU *et al.*, 2016). This concept is exemplified in Figure 1.2.

Figure 2 – Schematic illustration showing the magnetic moment for ferromagnetic bulk and free rotation for superparamagnetic NPs (Top) and the decrease of the barrier energy with the size of the nanoparticles (bottom).

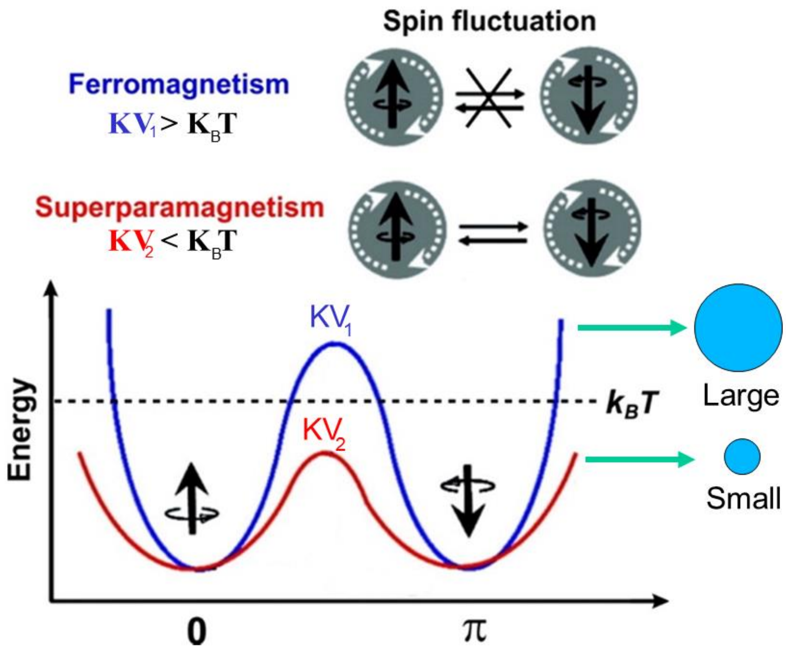

Source: modified from (JUN *et al.*, 2008).

The crystalline arrangement, shape, and composition also strongly influence the magnetic properties of the NPs. The structure effect can be easily observed in FePt NPs. It is known that equiatomic FePt can form two different crystalline arrangements: a chemically ordered face-centered tetragonal (fct) and a chemically disordered face-centered cubic (fcc). These NPs present distinct magnetic properties due to the difference between Fe and Pt interaction originated from the spin-orbital coupling and the hybridization of the orbitals 3d and 5d of Fe and Pt, respectively (WU *et al.*, 2016). Thus, fct-structure, formed by stacking of alternate of Fe and Pt layers along the 001 direction, has more substantial Fe 3d and Pt 5d coupling than fcc-structure, resulting in a significant anisotropy constant in the former. Therefore, when both fct and fcc structures are synthesized in sub-10 nm dimensions, the ordered FePt structure nanoparticles are ferromagnetic, while the disordered FePt structure is superparamagnetic (SUN, 2006). A similar phenomenon was observed by Junrui Li and coauthors, wherein two different types of CoPt nanoparticles were synthesized: one ordered ferromagnetic and other disordered superparamagnetic (LI *et al.*, 2019).

The effect of the shape on the magnetic properties has been widely studied for various nanoparticles such as Co (SRIKALA *et al.*, 2010), Fe (ESSAJAI *et al.*, 2019), and

Fe_3O_4 (QIAO *et al.*, 2017). For example, while in bulk magnetic materials the anisotropy arises from the Fermi surface, in NPs the anisotropy depends on both morphology and Fermi surface (COWBURN, 1999). Shape anisotropy can induce the presence of an easy magnetic axis within the material. This effect can be observed comparing bulk particles and NPs of spherical shape. The spherical bulk has no shape anisotropy due to its isotropic structure, while spherical NPs have a longitudinal magnetic easy axis (WU *et al.*, 2016). In addition, Ahed A. El-Gendy and coauthors have shown that the increase in the anisotropy enhances the magnetic properties of Co_3C NPs mainly due to spin-orbit coupling (EL-GENDY *et al.*, 2016). Other examples of magnetic properties enhanced by shape anisotropy can also be found elsewhere (WALTER *et al.*, 2014; SATHYA *et al.*, 2016). Therefore, the shape control of the MNPs can provide an excellent way to enhance the magnetic properties of these nanomaterials.

Magnetic elements as Fe, Ni, Co, and Mn are well known to produce magnetic ferrites MFe_2O_4 (M = Fe, Ni, Co, or Mn) with spinel structures (HARADA *et al.*, 2020). There are tetrahedral (*T*) and octahedral (*O*) interstices occupied by M^{2+} and Fe^{3+} cations in these crystalline structures. When *O* sites are occupied by Fe^{3+} and *T* sites by M^{2+}, the structure is called normal spinel. On the contrary, when *O* sites are occupied by M^{2+} and *T* sites by Fe^{3+}, the structure is denominated inverse spinel. The magnetic moments in the inverse spinel structure are canceled due to the antiferromagnetic coupling between the Fe^{3+} in *T* and *O* sites. Thus, the total magnetic moment for this structure depends only on the net magnetic moments of M^{2+}. In this sense, the net magnetization can be engineered from Bohr magneton (μ_B) which is found to be $5\mu_B$, $4\mu_B$, $3\mu_B$ and $2\mu_B$ for Mn^{2+}, Fe^{2+}, Co^{2+}, and Ni^{2+}, respectively (WU *et al.*, 2016). Indeed, it was experimentally observed that the saturation magnetization increases in the following order $MnFe_2O_4$, Fe_3O_4, $CoFe_2O_4$, and $NiFe_2O_4$, which is in accordance to the μ_B observed for Mn^{2+}, Fe^{2+}, Co^{2+}, and Ni^{2+}. Moreover, the formation of complex structures involving two types of M^{2+} ($(M_x M_{(1-x)})Fe_2O_4$) have also been proposed (FREIRE *et al.*, 2018). In this sense, Jung-Tak Jang and coauthors showed that incorporating Zn^{2+} dopants in *T* sites of manganese ferrite leads to an increase in the saturation magnetization due to partial cancellation of antiferromagnetic coupling between *T* and *O* sites (JANG *et al.*, 2009).

The modification of the composition can also be used to adjust the H_c in magnetic nanoparticles. For example, when Nd^{3+} in *O* sites substitutes Fe^{3+} in $CoFe_2O_4$, there is an increase of the *Hc* due to strong spin-orbit coupling (ALMESSIERE *et al.*, 2019). However, the *Hc* is a magnetic property that depends on the strain, defects, non-magnetic atoms, and surface effect (YADAV *et al.*, 2016). Since the modification of the composition can affect many of these factors, it is difficult to assign the change in H_c to one cause only. Therefore, the strong spin-orbit coupling that occurs when rare-earth occupies *O* sites in cobalt ferrite is only one reason for *Hc* increasing.

Due to the easily tuned magnetic properties, many efforts have been devoted to studying synthesis methods over the past decade, which has led to the formation of MNPs with controlled shape, composition, size, and structure. In this sense, since iron oxide and bimetallic nanoparticles can be easily synthesized, their magnetic properties can be modulated by modifiying simple parameters. As result, these materials gained prominence, being considered as an essential part of the class of magnetic nanoparticles.

1.2.1. Iron Oxide

The magnetic phenomena in iron oxide NPs and derivates have motivated researchers to investigate their structure and morphology (REDDY & LEE, 2013; USMAN *et al.*, 2018). Due to their properties, these materials have gained attention as a platform for different applications such as theragnostic, electrochemical sensor, catalyst, and water treatment (URBANOVA *et al.*, 2014; NABAVINIA & BELTRAN-HUARAC, 2020). In laboratory scale, it is possible to synthesize various iron oxides such as goethite (α-FeOOH) (TANG *et al.*, 2018), hematite (α-Fe_2O_3) (LIU, Z. *et al.*, 2018), amorphous hydrous iron oxide (HUA *et al.*, 2017), maghemite (γ-Fe_2O_3) (JIANG *et al.*, 2013), magnetite (Fe_3O_4) (VOJOUDI *et al.*, 2018), and mixed iron oxides (FONTECHA-CÁMARA *et al.*, 2016). Among them, hematite, maghemite, and magnetite are the most common in industrial and technological applications (LEONEL *et al.*, 2021).

Hematite is found in nature as a rhombohedral corundum structure (space group $R\bar{3}c$), with Fe^{3+} ions surrounded by a distorted octahedral of oxygen (PICCININ, 2019). At room temperature, Fe species can exhibit two ferromagnetic superlattices anti-ferromagnetically coupled in a superexchange interaction. Therefore, hematite should present an antiferromagnetic behavior. Nevertheless, experimentally, a weak ferromagnetic feature is observed, which is assigned to a slight canting of the spins in the Fe plane (SANSON et al.). In the literature, the saturation magnetization and coercivity of bulk hematite are found to vary from 0.1 to 0.4 emu g^{-1} and from 1000 to 5000 G, respectively (SHOKROLLAHI, 2017). Hematite is the most stable iron oxide under ambient conditions used in various areas such as catalysts, gas sensors, and water splitting. However, their magnetic properties make it less suitable than other iron oxides such as magnetite (LEONEL *et al.*, 2021).

Magnetite is one the most iron-based material studied due to its unique magnetic properties, originated from the presence of Fe^{2+} and Fe^{3+} arranged in a cubic inverse spinel structure (GAWANDE *et al.*, 2013). The unit cell of magnetite has 32 O^{2-} ions regularly packed in a regular cubic closet along the [110] direction, with octahedral sites shared by Fe^{2+} and Fe^{3+} and tetrahedral sites occupied only by Fe^{3+} (Figure 1.3) (ASHRAF *et al.*, 2020). Its structural formula can be written as $Fe^{3+}_{tet}[Fe^{2+}\ Fe^{3+}]_{oct}O_4$ and, since magnetite has an inverse spinel structure, its ferrimagnetic behavior is due to Fe^{2+} in octahedral sites. Compared to other iron oxides, this ferrite has superior magnetic properties such as high saturation magnetization (92 emu g^{-1}), magnetic susceptibility, and high electrical conductivity (USMAN *et al.*, 2018). Also, magnetite nanoparticles with a diameter size around 25 nm display a superparamagnetic behavior and good biocompatibility (NUZHINA *et al.*, 2019), being widely investigated for biomedical and environmental applications.

Figure 3 – Crystal structure of magnetite. Octahedral Fe ions are in orange, tetrahedral Fe ions are green, and oxygen ions are red.

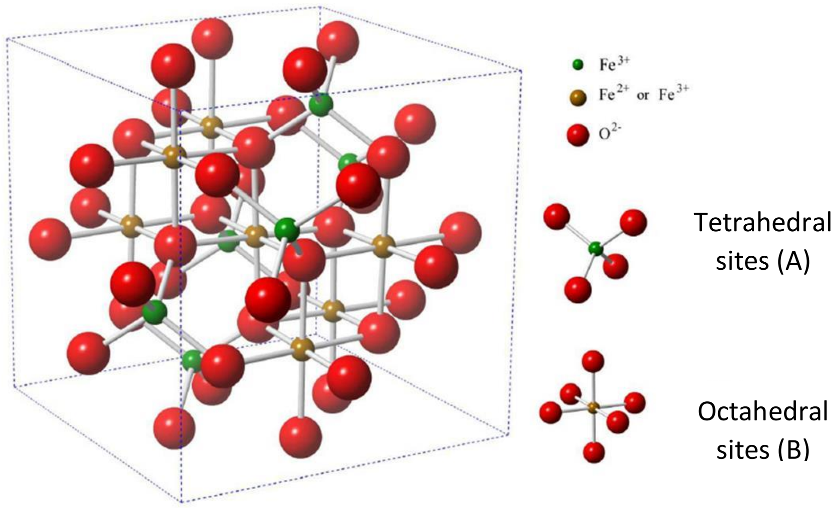

Source: (GALVÃO, WESLEY S. *et al.*, 2016).

Maghemite is the fully oxidized form of magnetite, with similar properties and octahedral vacancies originated from the increased positive charge. The maghemite formula can be described as $Fe^{3+}_{T}\,(Fe_{5/3}\ \boxdot_{1/3})_O O_4$, being considered as a defective spinel, with $\boxdot$ representing the vacancies in cation sites. Interestingly, these octahedral holes provide an easy way for doping maghemite with cations that strongly tend to occupy octahedral sites such as Zn^{2+}, Mo^{6+}, and V^{4+} (ASGARIAN *et al.*, 2017; AHMED & SANAD, 2021). The saturation magnetization and H_c of bulk maghemite can be found in the range of 74 – 80 emu g^{-1} and 50 – 800 G, respectively, at room temperature (SHOKROLLAHI, 2017). Therefore, maghemite can be considered as a material with intermediary magnetic properties compared to other iron oxides. Although maghemite is less magnetic than magnetite, it is more stable under ambient condition and does not require a stabilization shell (ISRAEL *et al.*, 2020).

1.2.2. Bimetallic Nanoparticles

Metals correspond to more than 75% of the periodic table of elements and are the source for the synthesis of countless materials that have fascinated and changed the society in human history. For example, in Bronze Age humans discovered how to mix two different metals to form alloys with more significant mechanical resistance than which one of the involved metals, which allowed… (GILROY *et al.*, 2016). Also, the human being observed that it could shape the metal alloys to produce a tool with more strength. Today, conventional metal alloys can be found in many products, mainly for the automotive industry and civil engineering. Some examples are bronze (copper and tin), stainless steel (iron, chromium, nickel, and carbon), cupronickel (copper and nickel), and brass (copper and zinc). More recently, much research involving metals and their alloys is more focused on nanoscale production for application in photonics, catalysis, energy storage and conversion, electronics, and medicine (STEPHANIE *et al.*, 2021; ZHOU *et al.*, 2021).

Although monometallic NPs have an immense relevance in industrial field, it is well-documented that these NPs do not met all the requirements for practical applications, such as high activity and selectivity, good chemical and physical resistance, and low cost (ZHOU *et al.*, 2021). Thus, to obtain materials with these desired properties, bimetallic nanocrystals have gained attention due to their superior chemical and physical properties (RAJEEV *et al.*, 2021). Incorporating a second metal to monometallic NPs generally alters their spatial arrangement modes and electronic structure, resulting in a novel material that shows new chemical and physical properties. In addition, the bimetallic nanocrystals should inherit characteristics of both metals in their constitution, becoming possible to adjust the properties of these nanomaterials by changing the composition, further improving the performance of a determined system (SCARIA *et al.*, 2020).

The properties of bimetallic nanocrystals are also assigned to their architecture in terms of atomic ordering, crystal structure, internal structure, shape or type of facet, and configuration. Thus, considering the nuclear arrangement of two metals in a spherical morphology, the bimetallic nanocrystals can be classified according to four main types of mixing patterns (Figure 1.4). A typical core-shell structure (Figure 1.4a) consists of a core formed by a metal A fully coated by a shell constituted of a metal B commonly represented by A@B (GHOSH CHAUDHURI & PARIA, 2012). Figure 1.4b shows two metallic parts sharing a mixed interface (right) or a small number of A – B bonds (left), classified as subclusters segregated. In another configuration, the bonds between A and B metals can be distributed in the bimetallic structure orderly or randomly (Figure 1.4c): when A – B bonds are orderly distributed and occupy the lattice with a specific atom stoichiometry, the compound is commonly denominated intermetallic (Figure 1.4c – left); when the A – B bonds are randomly distributed across the lattice, the material can be designated alloy (Figure 1.4 c – right) (ZHOU *et al.*, 2021). In Figure 1.4d, it is represented multishell bimetallic nanocrystals as layered or onion-like alternating A – B – A shell structure. It was demonstrated by dynamic simulation that A – B – A onion-like structure can be favored for systems containing Ag as core and Cu, Ni or Pd as shell (BALETTO *et al.*, 2003).

Figure 4 – Schematic illustration of six possible mixing patterns: a) core-shell; b) subclusters segregated and dumbbell; c) ordered and randomly mixed; and d) multi-shell.

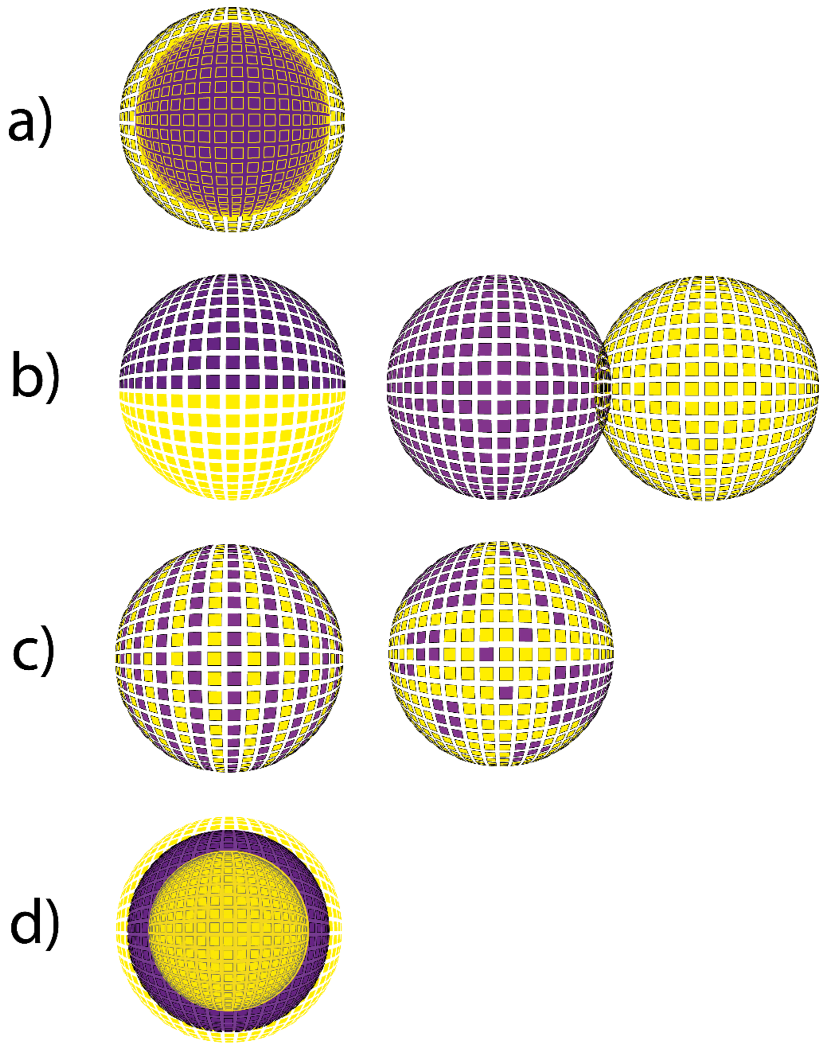

Source: the author.

1.3. Synthesis of magnetic nanoparticles

Since the MNPs are strongly dependent on the structure, composition, and dimensions, many efforts have been made to develop synthetic methods that efficiently control the synthesis parameters. Consequently, there are many different methods to prepare iron oxides and bimetallic nanocrystals, and both can be carried out in hydrophobic or hydrophilic solutions. In this sense, Figure 1.5 summarizes the most used synthetic routes. However, only the most relevant for this thesis will be discussed in the following sections.

Figure 5 – Various synthesis pathways to prepare bimetallic NPs and iron oxide NPs.

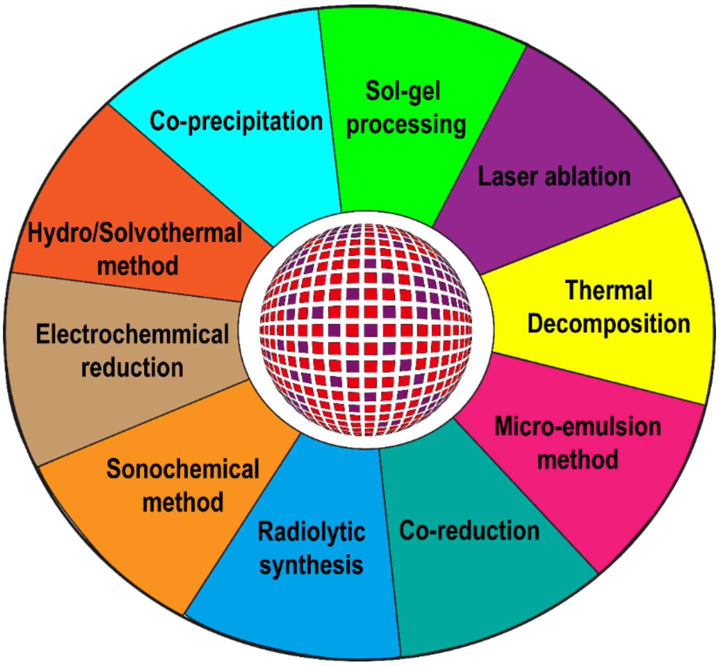

Source: the author

1.3.1. Co-precipitation

The co-precipitation method in aqueous solution is the most used procedure to prepare MNPs (ADEWUNMI *et al.*, 2021), specially ferrites (VINOSHA *et al.*, 2021). In this method, a solution containing the inorganic precursors in the temperature range of 50 to 80 °C is precipitated by addition of a base (MAJIDI *et al.*, 2016). This is the conventional route to synthesize Fe_3O_4 and γ-Fe_2O_4 nanoparticles (SHOKROLLAHI, 2017; ASHRAF *et al.*, 2020). On the other hand, to prepare other ferrites, in general it is required an additional synthesis step such as solvothermal or calcination at controlled temperature (GALVÃO, WESLEY S *et al.*, 2016). Magnetic nanoparticles synthesized by chemical co-precipitation have their size, shape, and composition varying according to the precursor salt (e.g., sulfates, nitrates and chlorides), reaction temperature, Fe^{2+}/Fe^{3+} ratio, pH, and ionic strength of the medium (REDDY *et al.*, 2012). However, when the experimental conditions are well established, the quality of the NPs is fully reproducible (LU *et al.*, 2007).

The synthesis of magnetite using this method consists in the precipitation of Fe(III) and Fe(II) as ferric and ferrous hydroxides, respectively, around the temperature of 70 °C, by the addition of a base (equation 2). Although being easy the obtention of magnetite by this route, it typically provides nanoparticles with spherical morphology and large size distribution. Thus, since magnetic properties are strongly dependent on size, a broad size distribution results in a wide range of blocking temperatures and, consequently, non-ideal magnetic behavior for many applications (REDDY *et al.*, 2012).

$$Fe^{2+}_{(aq)} + 2Fe^{3+}_{(aq)} + 8OH^{-}_{(aq)} \rightarrow \quad Fe_3O_{4(s)} + 4\ H_2O_{(L)} \tag{2}$$

The control of nucleation and growth processes is crucial for synthesizing MNPs with narrow size distribution and homogeneous shape. In the last decade, the use of organic additives in co-precipitation has been shown to promotes monodisperse nanoparticles with narrow size distribution due to the chelation of the metal ions and to the adsorption of additives on the nuclei. While the former limits the nucleation step, resulting in large particles due to a small number of formed nuclei, the last inhibit the growth of the nanoparticles favoring the formation of small units (LU *et al.*, 2007).

Although it is widely established that organic additives are effective to control size and morphology, the experimental conditions may also influence the morphologic and magnetic properties during co-precipitation (CASTRO & DE QUEIROZ, 2011; KIKUCHI *et al.*, 2011; BAUMGARTNER *et al.*, 2013; GALVÃO *et al.*, 2015). In this sense, particle size and morphology of NPs can be controlled by parameters such as the concentration of the precipitant agent, salt concentration, and pH (KIKUCHI *et al.*, 2011). It was demonstrated that base concentration may acts in the nucleation process, causing an increase of the particle size and saturation magnetization (M_s), having a large effect on the purity of the obtained product (BAUMGARTNER *et al.*, 2013). Besides, the type of base have a great influence on the synthesis. It has been observed that non-magnetic species are formed when strong alkalis, such as KOH and NaOH, are used (GALVÃO *et al.*, 2015). By contrast, other authors have demonstrated the use of ammonium hydroxide in the pH range of 8.8 to 10 does not form any non-magnetic species (NETO *et al.*, 2017). Furthermore, the reaction temperature is another parameter commonly used to control the kinetics of NPs formation. For example, Fe_3O_4 obtained at low temperature is preferred for co-precipitation, since high temperatures can lead to magnetite oxidation and a consequent formation of maghemite.

1.3.2. Thermal Decomposition

The thermal decomposition approach has been extensively used to synthesize MNPs in organic solutions (LÓPEZ-ORTEGA *et al.*, 2015). This method is based on the thermal decomposition of organometallics, including but not limited to M(acetylacetonate), M(oleate), M(acetate), or M(carbonyl), where M is a metal element in the presence of surfactants and an organic solvent with high boiling point (GALVÃO *et al.*, 2015; LESZCZYŃSKI *et al.*, 2016). The synthesis of MNPs in organic solvents has some advantages over the traditional hydrolytic way. It provides a chemically inert reaction environment and an extensive range of synthesis temperature (180°C – 350°C), allowing fine control of structure, size, and uniformity mainly due to the control of the nucleation process and crystal growth (Figure 1.6). Since these parameters have a great influence on the magnetic properties of the nanoparticles, thermal decomposition is an excellent alternative for the synthesis of different MNPs such as monometallic, bimetallic, and oxide nanocrystals (GHOSH CHAUDHURI & PARIA, 2011; WU *et al.*, 2016).

Figure 6 – (a) Overall scheme for ultra-large-scale synthesis of monodisperse nanocrystals; (b) and (c) show HRTEM images of FeCo and Fe_3O_4 nanoparticles coated with oleic acid, respectively.

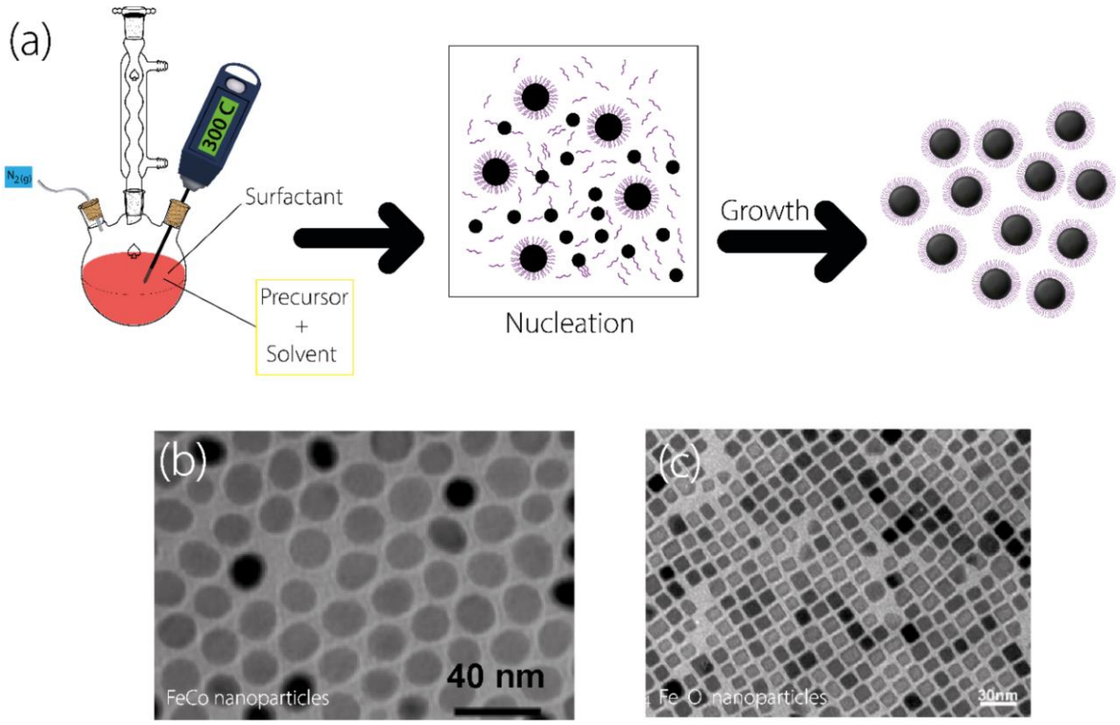

Source: (a) - the author; (b) - (CHAUBEY *et al.*, 2007); (c) - (GAO *et al.*, 2010).

Monodisperse nanoparticles can be synthesized using this method by means of two different thermal steps. One way requires a “hot-injection,” consisting of the rapid injection of the metal precursor at a high temperature in a furnace. The second way uses the “heating-up” approach, in which all the mixture is heated to the desired temperature to initiate the nucleation and NPs growth. This last is the most convenient for large-scale synthesis since it does not require a large volume of reactant solution (PARK *et al.*, 2005).

Thermal decomposition allows the formation of NPs with different architecture and atomic ordering. Generally, core/shell structures with a controlled composition are readily synthesized from this method. Furthermore, metals containing a vacant d-orbital in the valence layer allows the formation of complexes through formation of a secondary bond between the metal and the electron-donating ligands. This methodology consists in a initial stabilization of the metal salts with surfactants solutions. Afterward, the solution is mixed with an organic compound to form the organometallic complex, which is decomposed to the metal itself or to metal oxides depending on the type of surfactant and/or metalorganic precursors (LU *et al.*, 2007; GHOSH CHAUDHURI & PARIA, 2011). Whether the metalorganic precursor is formed by a zerovalent metal, for example the iron-pentacarbonyl, the decomposition initially leads to the formation of monometallic nanoparticles, which can be partially oxidized to provide metal/metal oxide core/shell structure (LU *et al.*, 2007).

The presence of a surfactant in the organic phase during thermal decomposition has great importance since these molecules act in the control of the size and morphology through coordination with the surface of the nanoparticles. Thus, an essential factor for the choice of the surfactant is related to its functional group since this is the main site of interaction between the surfactant and the nanoparticles. It is well accepted that the chemical binding concept based on “hard and soft acids and bases” can be used to guide the surfactant choice (WU *et al.*, 2016). However, there is not a specific rule to follow and, in the literature, are found many surfactants such as oleic acid (OA), oleylamine (OLA), octadecylamine (ODA), trialkilphosphine (TOP), and trialkilphosphine oxide (TOPO) applied for the synthesis of mono and bimetallic nanoparticles by thermal decomposition. OLA has gained attention among these surfactants due to its low cost and specially to its ability to act as an electron donor at high temperatures. In addition, OLA is liquid at room temperature and is easily removed by ethanol in the step of purification of the nanoparticles. Together with its elevated boiling point, these advantages allow OLA to be employed as a solvent, surfactant, and/or mild reducing agent in the method of thermal decomposition. In this sense, OLA has been widely used to synthesize bimetallic nanoparticles containing at least one magnetic element (MOURDIKOUDIS & LIZ-MARZÁN, 2013).

1.3.3. Sonochemical

Ultrasound was discovered in 1880 by Pierre Curie and his brother. However, the light emission originated by acoustic cavitation, a physical phenomenon known as sonoluminescence, was firstly seen in 1934 by Frenzel and Schultes (FRENZEL &

SCHULTES, 1934) and has been systematically investigated since then. Pflieger and coauthors have studies about sonoluminescence and multi bubbles sonochemistry and they reported that ultrasound irradiation in water leads to the generation of highly actives radicals (JI *et al.*, 2018). Consequently, today, ultrasound irradiation technology is used in different areas such as nanoemulsion, catalysis in organic reactions, and treatment of organic pollutants (LI, Z. *et al.*, 2021). However, only in the last two decades, its potential for the direct synthesis of functionalized ceramic materials has begun to be explored (HAN *et al.*, 2007; ASHIRI *et al.*, 2015).

In the sonochemistry process, the frequency range of the energy ultrasound (20 – 100 kHz) is widely used since in this range the bubbles cavitation phenomenon occurs (YUSOF & ASHOKKUMAR, 2015). Besides, the shear force and intense shock waves produced by ultrasound irradiation in liquid systems have been essential for the synthesis of nanoparticles (LI, Z. *et al.*, 2021). Although there is no molecular-level interaction between the ultrasound and the chemical species, the high-intensity irradiation produces the acoustic cavitation effect, which accounts for the chemical effects (KIS-CSITÁRI *et al.*, 2008). During this process, the expansive and compressive phases cycle of the acoustic wave creates bubbles and makes these oscillate, accumulating ultrasonic energy while growing to a specific size. When these bubbles are under the right condition, they can overgrow and subsequently suffer a violent collapse, releasing the concentrated energy stored within a very small time and achieving temperatures around 5000 K with a heating and cooling rate in the range of 10^{10} K s^{-1} and pressures around of 1000 bar (BANG & SUSLICK, 2010). Therefore, these extreme conditions observed during acoustic cavitation provides unique chemical effects, which help produce nanoparticles. Moreover, compared to other synthesis methods, the sonochemical process also has advantages such as rapid reaction rates, controlled reaction conditions, production of nanoparticles with a narrow size distribution, being a easy, green, and non-hazardous synthetic route (LI, Z. *et al.*, 2021).

1.4. Two-dimensional nanomaterials

The development of nanoparticles of different dimensionalities and controlled structures have brought new opportunities in various areas of science due to their unique properties. Compared to 1D and 3D, 2D nanomaterials have showed nanosheet structures with large lateral size but with a single or only few atomic layers of thickness, often resulting in unusual physicochemical properties due to their high aspect ratio, unique surface chemistry, and specific quantum-size effect (KONG *et al.*, 2017). However, only after 2004, when K. S. Nonoselov and coauthors showed the graphene production from graphite using the mechanical cleavage method, 2D nanomaterials gained the interest of the scientific community (NOVOSELOV *et al.*, 2004). Nowadays, there are many 2D materials such as transition metal dichalcogenides (TMD), hexagonal boron nitride (HBN), graphitic carbon nitride (g-C_3N_4), black phosphorous, 2D metal oxides/sulfites, 2D polymers, 2D metalorganic frameworks, 2D perovskites, and transition metal carbides, nitrides and carbonitrides (MXenes) which have been explored by researchers in the various fields of science (see Figure 1.7) (CHEN *et al.*, 2018).

Figure 7 – Some possibilities for application of 2D nanomaterials.

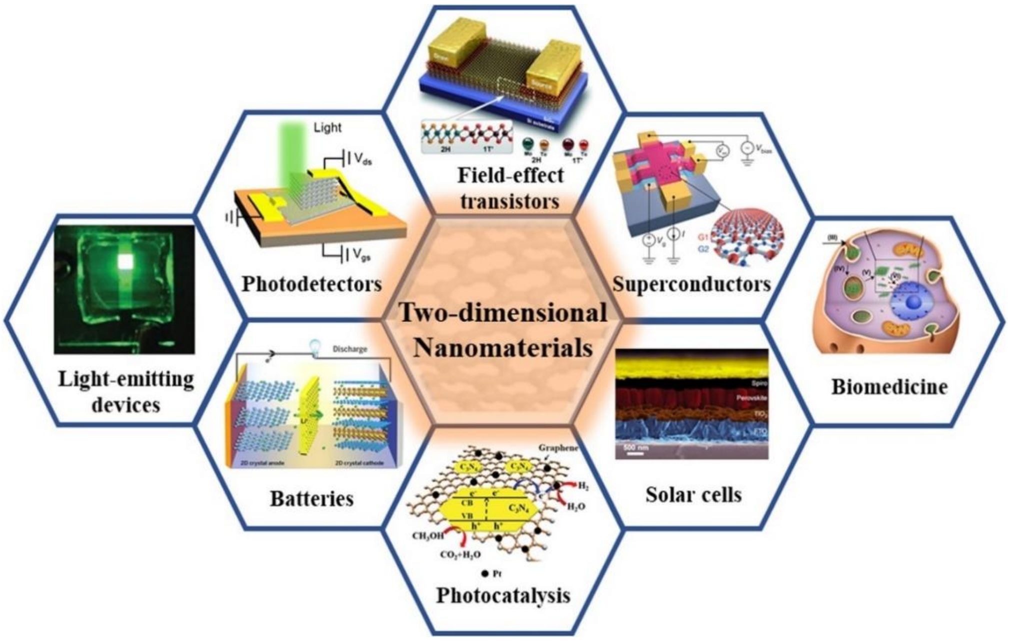

Source: (WANG *et al.*, 2021).

2D nanomaterials with different thicknesses can be synthesized through a top-down process using a crystal bulk as starting material, but the inherent crystalline structure determines the unique layer feature. A crystal can provide a structure formed by polyhedral-thick layers atoms covalently or ionically connected with their neighbors. The Van der Waals force interaction between these sheet layers can be weakened or even broken by a chemical or physical process to form an ultrathin 2D morphology consisting of only one sheet or few nanosheet layers. The formation of ultrathin nanosheets from the crystal leads to the exposition of almost all atoms on the surface, resulting in a high specific surface area with enhanced chemical reactivity and abnormal electronic, magnetic, and catalytic properties (KONG *et al.*, 2017; WANG *et al.*, 2021).

A bottom-up process can also synthesize ultrathin nanosheets using different precursors via chemical reaction at specific experimental conditions. Some typical approaches are chemical or physical vapor deposition (CVD/PVD), wet-chemical synthesis (WCS), and electrochemical deposition (ECD) (CAO *et al.*, 2018). Among these methods, CVD and PVD are largely in the semiconductor industry to fabricate solid thin films. The main advantages of these two techniques are the high-quality nanosheets produced with large lateral sizes and few surface defects. In addition, it is possible to adjust the thickness in a determined film modifying experimental conditions, such as chamber pressure control, substrates/catalyst, temperature and time (YU *et al.*, 2015).

Independent of the synthesis method, the manufacturing materials with ultrathin nanosheets are desired in diverse applications due to their properties. For example, the thickness in atomic scale, large lateral size, and high atom exposition provide an ultrahigh theoretical specific surface area, and consequently, more possibilities for surface modification and elemental doping (VARGHESE *et al.*, 2015; ZHU *et al.*, 2018). Other important characteristics of the thin film is the combination macroscopic properties with quantum confinement microscopic features and strong intraplane chemical bonding, which offers excellent flexibility, optical transparency, mechanical strength, and electrical properties. These features are significant for developing versatile electronic devices, making these nanomaterials very interesting to be applied as wearable biomedical electronic devices (CAO *et al.*, 2018).

Although many ultrathin 2D nanomaterials have been successfully used in many areas, those composed majority by carbon, nitrogen, hydrogen, boron, and phosphorus have attracted significant attention in biomedical applications (Figure 1.8) (LIN *et al.*, 2020). Thus, the employment of these nanomaterials have been reported in a broad spectrum ranging from enhanced drug delivery, even of poorly water-soluble chemotherapy, until tissue-specific targeting of therapeutic, photodynamic (PDT) or photothermal therapy (PTT) (LIU *et al.*, 2019). In addition, due to π-conjugated chemical bonds, these materials have fluorescence and a high loading capacity for chemotherapeutics through π-stacking or hydrophobic interactions between the drug and planar frameworks, making them excellent platforms for theranostic applications (CHEN *et al.*, 2017; LIU *et al.*, 2019). Althoug ultrathin 2D nanosheets have a great potential in the biomedical area, much research it is still demanded to overcome some specific problems about their pharmacokinetics and toxicity. Generally, these problems can cause nanoparticle aggregation in physiological media, presence of impurities and slow metabolism (CHEN *et al.*, 2017).

Figure 8 – Metal-free 2D nanomaterial applied to biomedical research.

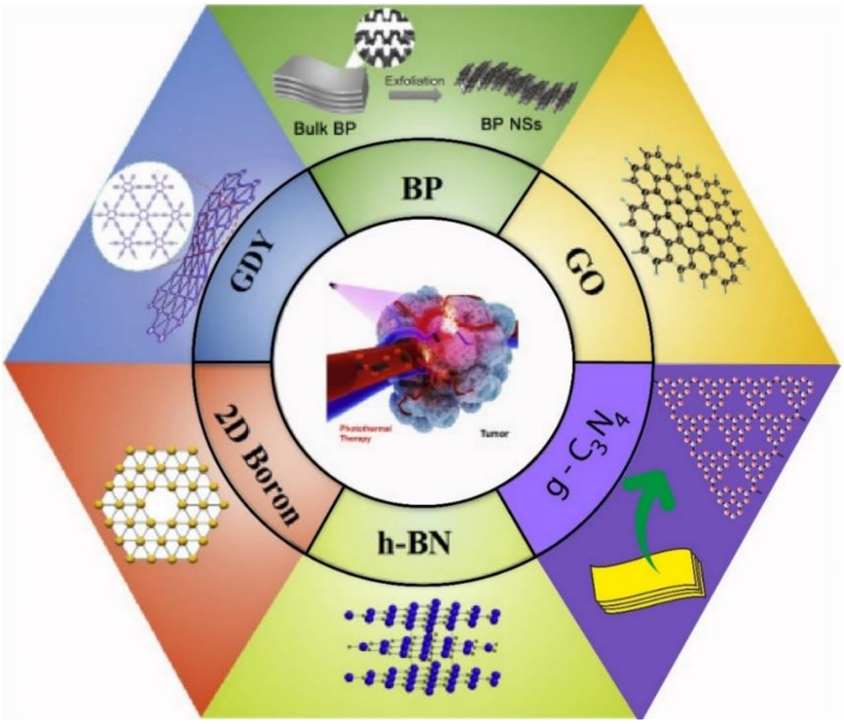

Source: modified from (LIN *et al.*, 2020).

Much research has focused on the application of graphene and their derivates as platforms to combat different cancer cells, but some studies have shown that carbon materials, including graphene oxide, carbon nanotubes, and nanodiamonds, when incubated with HeLa cells, exhibited a dose-dependent toxicity. In addition, it is interesting to mention that in the case of carbon nanotubes and graphene oxide, the generation of reactive oxygen species to induce oxidative stress was found to be a possible mechanism leading to the toxicity of these nanomaterials (YANG *et al.*, 2013). Sasidharan and coauthors have shown that graphene is retained on the macrophage cell surface, and when applied with concentrations larger than 75 µg/mL, it can induce oxidative stress together with abnormal stretched morphology of F-actin filopodial extensions. According to the authors, these toxic effects are associated with strong hydrophobic interactions between graphene and the cell membrane (SASIDHARAN *et al.*, 2012). Thus, many researchers have searched for other graphene-like nanomaterials aiming to overcome this limitation. In this sense, g-C_3N_4, a graphene-like 2D nanomaterial, has emerged as a promising candidate for several biomedical applications due to its excellent biocompatibility and attractive capacity to absorb and convert light radiation to heat or produce cytotoxic activity for killing tumor cells (LIU *et al.*, 2019).

1.4.1. Graphitic carbon nitride (g-C_3N_4)

As a type of metal-free material, carbon nitride has attracted significant attention since 1989, when A. Y. Lui and M. L. Cohen predictions that it could be synthesized as ultrahard materials (LIU & COHEN, 1989). In 1996, D. M. Teter and R. J. Hemley showed by calculation methods that carbon nitride has five structures: α- C_3N_4, β- C_3N_4, cubic-C_3N_4, pseudocubic-C_3N_4, and g-C_3N_4 (TETER & HEMLEY, 1996). All these, except those with graphene-like configurations (g-C_3N_4), have a hardness comparable to diamond. However, g-C_3N_4 unique electronic structure and excellent chemical and thermal stability make it highly valuable (DONG *et al.*, 2014). It is well documented that the basic structural units to build allotropes of g-C_3N_4 are the triazine ring (C_3N_4) and the tri-s-triazine/heptazine ring (C_6N_7), shown in Figure 1.9. These two structures have different stabilities due to the different sizes of the nitride pores and electronic environments of the N atoms (HAN *et al.*, 2017). Density functional theory (DFT) calculations and experimental studies have shown that tri-s-triazine based g-C_3N_4 are the most stable and energetically favored, therefore being the tri-s-triazine units broadly recognized as the base unit for the formation of the 2D sheets of g-C_3N_4 (MAEDA *et al.*, 2009; XU & GAO, 2012).

Figure 9 – (a) Triazine and (b) tri-s-triazine/heptazine structures of g-C_3N_4.

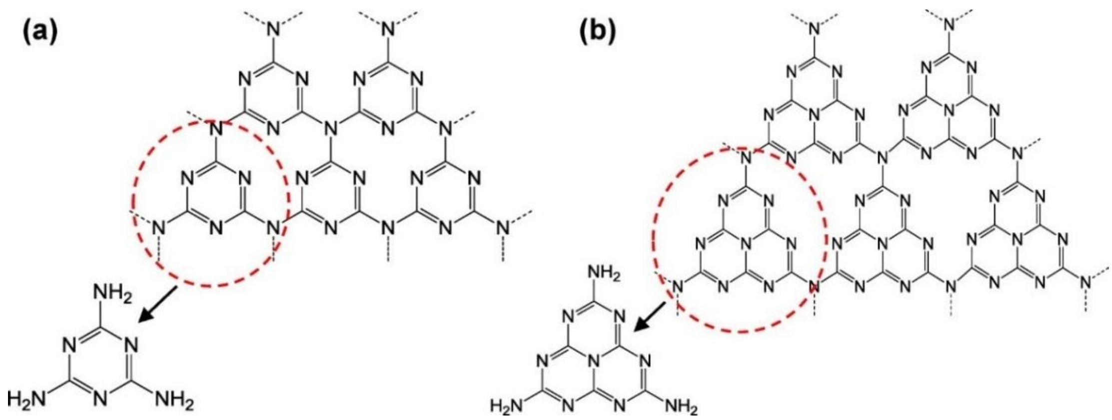

Source: (ONG *et al.*, 2016)

g-C_3N_4 can be synthesized from nitrogen-rich precursors such as cyanamide, dicyanamide, melamine, urea, and thiourea via a typical thermal condensation route. However, ideal g-C_3N_4 (theoretical value of C/N = 0.75) is challenging to obtain from the viewpoint of the materials, since a small number of hydrogen impurities atoms are found from uncondensed amino functions on the edges of g-C_3N_4, which is assigned to incomplete thermal polycondensation. Although the presence of these hydrogens indicates a kinetic problem in the synthetic route, the resulting functional groups (primary/secondary amine groups) provide sites that allow for surface modification of g-C_3N_4 and a way to understand its surface charge

(KUMRU & ANTONIETTI, 2020). Thus, the choice of nitrogen-rich precursors should affect g-C_3N_4 structure due to distinct kinetic parameters leading to sheets with different degrees of defects. In addition, it is interesting to note that for several applications such as catalysis and photocatalysis, these defects are important active sites for reactions, which may improve catalytic performance of these materials when comapred to a defect-free and ideal g-C_3N_4 sheet (KUMRU & ANTONIETTI, 2020; MAJDOUB *et al.*, 2020). Besides thermal condensation, other synthetic routes such as PVD, CVD solid-state reaction, and solvothermal yield a morphology-tailored g-C_3N_4., but specific and expensive conditions are required. Thus, the method of thermal condensation the most commonly employed for the preparation of graphitic-like carbon nitride (DONG *et al.*, 2014).

The polymeric system of g-C_3N_4 with graphitic planes formed by π-π conjugation of tri-s-triazine units provides light response, demonstrating that this material has attractive photoelectric properties. Indeed, it is showed that g-C_3N_4 has a suitable bandgap of 2.7 eV, which allows it to absorb the energy of near-ultraviolet light and emit visible light in the range of 400 to 475 nm (CHAN *et al.*, 2019). In this sense, due to its interesting characteristics, g-C_3N_4 has been used to diverse areas such as photocatalysts, electrochemical sensors, photodynamic therapy, bioimage, biosensing, and theranostic (LIN *et al.*, 2014; LIU *et al.*, 2019; LIN *et al.*, 2020; ROHAIZAD *et al.*, 2021).

Particularly, for biomedical applications, this nanomaterial has become a research hotspot in terms of 2D nanomaterials due to its optical advantages (stable photoluminescence, no light scintillation, and adjustable emission wavelength), low toxicity, and good biocompatibility (LIU, C. *et al.*, 2018; CHAN *et al.*, 2019). Moreover, the conjugated tri-s-triazine structures may provide interesting sites for chemotherapy interaction, showing that g-C_3N_4 has excellent potential for drug delivery. However, the poor colloidal stability has limited its use (LIU *et al.*, 2019). To overcome this, ultrathin g-C_3N_4 with superior properties has been developed, making it a promising candidate for various biomedical applications (ZHANG *et al.*, 2014). Figure 1.10 summarize some of the possible biomedical applications of graphitic-like carbon nitride. Despite the great versatility of ultrathin g-C_3N_4, its potential has been weakly exploited in the oncologic area, since only few works have investigated the effect of isolated ultrathin g-C_3N_4 in biological systems.

Figure 10 – g-C_3N_4 structure and its applications in biomedical areas, including biosensors, bioimaging, and cancer therapy.

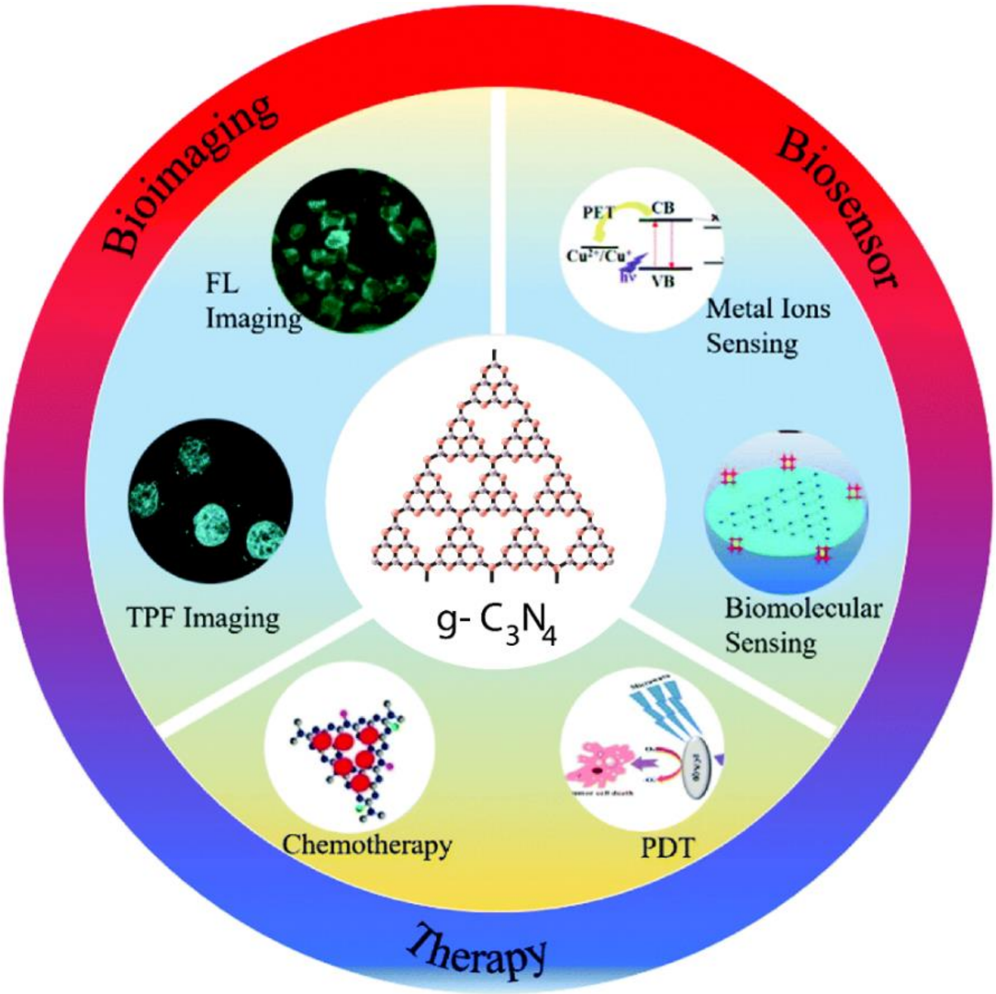

Source: modified from (LIU *et al.*, 2019)

1.5. Objectives and scope of the thesis

In this Ph.D. thesis, we aimed to explore the properties of zero and two-dimensional nanomaterials for water remediation, electrochemical hydrogen production, and cancer treatment. More specifically, we initially synthesized iron oxide (magnetite, Fe_3O_4) coated with chitosan by a simple approach using the co-precipitation method under ultrasonic irradiation and modified this sample with glutaraldehyde and epichlorohydrin. The effect of these modifications was investigated by a detailed structural, morphological, and magnetic characterization to understand their impact on the adsorption of azo dyes. In a second moment, this thesis has focused on electrochemical hydrogen production using low-cost electrocatalysts. Thereby, four iron-based bimetallic nanocrystals (FeAg, FeCo, FeCu, and FeNi) were synthesized via oleylamine reduction of metal salts method. These electrocatalysts were characterized by XRD, FTIR, TEM, VSM, and Mössbauer spectroscopy, and their electrocatalyst performance was evaluated in hydrogen evolution reaction from electrochemical splitting water.

It is well known that synthesized 0D magnetic nanoparticles have biological activities against cell cancer, but their small size may limit their application due to a fast elimination by the body. Therefore, initially were proposed the formation of nanocomposites of 0D magnetic nanoparticles with graphitic-like carbon nitride ($g\text{-}C_3N_4$) for cancer treatment. However, during the bibliography revision, it was observed that pure $g\text{-}C_3N_4$ had not been well investigated as an alternative for the treatment of tumour cells. Thus, in the last work, we aimed to explore the properties of $g\text{-}C_3N_4$ as a nanodrug for the treatment of different lines of tumour cells. The synthesized material was characterized by XRD, FTIR, Raman, TEM, DLS, AFM, DRS, and PL and studies regarding its cytotoxicity, proliferation in cancer cells lines, reactive oxygen species production, and biodistribution were performed.

2. CHAPTER 2 – MAGNETIC POROUS CONTROLLED Fe_3O_4@CHITOSAN NANOSTRUCTURES: AN ECO-FRIENDLY ADSORBENT FOR EFFICIENT REMOVAL OF AZO DYES

2.1. Introduction

In recent years, the social demand for industrialized products has boosted the growth of the industrial sector. However, this growth has been occasioned environmental problems, mainly related to water pollution due to the wastewater discharged from textile dyeing processes (AL-MAMUN *et al.*, 2019). Dyes are widely used in textile, paper, and plastic industries, and due to their high water solubility, after the production process, around 10 – 20 % of these dyes remaining in the wastewater (JIANG & HU, 2019). Consequently, inappropriate wastewater disposal generates several pollution problems since these effluents can negatively affect the aquatic ecosystem (SEMIÃO *et al.*, 2020). Furthermore, most dyes are potentially harmful when in contact with humans since they may cause allergies and dermatitis and are classified as carcinogenic substances (SENTHILKUMAAR *et al.*, 2006).

Herein, considering dyes overuse by industries, numerous efforts have taken to overcome unlikely effluents disposal. For instance, dye-removal methods have been developed, such as adsorption (CERVELLINO *et al.*, 2014), heterogeneous-Fenton process (HUSSAIN *et al.*, 2020), photocatalytic degradation (A. OSAWA *et al.*, 2020), coagulation-flocculation (ZAHRIM *et al.*, 2017), and ultra-filtration through fine membranes (DU *et al.*, 2017). Currently, the adsorption method has been widely applied to remove different types of pollutants from effluents due to their low cost and simplicity of design (TANG *et al.*, 2019; WANG, Z. *et al.*, 2019). However, activated carbon has been used by most industries as an adsorbent, once can remove heavy metals and dyes with high adsorption capacity, which its use is limited concerning economic view due to high cost (SHARMA *et al.*, 2011; NASRULLAH *et al.*, 2018).

Recently, the scientific community has directed some advanced research in developing alternative adsorbents, especially those based on polymers (CHEN *et al.*, 2016; MIN *et al.*, 2016). Chitosan (β-(1,4)-2-amino-2-deoxy-D-glucose), a linear polysaccharide obtained from deacetylation of chitin, has been used as an efficient adsorbent of azo dyes (DEMARCHI *et al.*, 2013). Actually, chitosan and derivates have shown as an outstanding material for adsorption of heavy metal ions (CHEN *et al.*, 2020) and organic dyes (WANG, X. *et al.*, 2019), principally due to high content of amino (- NH_2) and hydroxyl (- OH) groups on the chitosan skeleton. Additionally, this compound is considered environmental friendly, non-toxic and biodegradable (WAN NGAH *et al.*, 2011; KYZAS *et al.*, 2013; RUSMIN *et al.*, 2015). However, chitosan solubility is limited to acidic medium, thus, some studies have reported crosslinking reactions using both amine and hydroxyl-based crosslinking agents, such as epichlorohydrin (WU *et al.*, 2009), glutaraldehyde (XU *et al.*, 2010) and tripolyphosphate (TANG *et al.*, 2019), in order to improve chitosan chemical stability.

In this sense, magnetic chitosan-based nanoparticles have been used as adsorbent of organic dyes due to their adsorption properties, such as high separation efficiency, good relationship of cost-effectiveness and simple operation process (CAO *et al.*, 2014). In the literature, several methods have been applied to prepare magnetic chitosan nanoparticles (MCh NPs), such as co-precipitation (PYLYPCHUK *et al.*, 2016), reduction – precipitation (CAO *et al.*, 2014) and dispersion in a polymer matrix (SURESHKUMAR *et al.*, 2016). However, these methods usually require a long synthesis time and Fe_3O_4 is not well-dispersed in the polymer matrix. Recently, our research group developed an easy and fast method to synthesize MCh NPs *in situ* under US irradiation (FREIRE *et al.*, 2016). The proposed synthetic route takes only 2 min and provides well-dispersed magnetite NPs into the chitosan matrix.

Herein, this work aimed to synthesize Fe_3O_4-chitosan nanocomposite NPs under US irradiation, to investigate their behavior and properties regarding adsorption capacity and anionic azo dyes removal from an aqueous dispersion. After whole structural and magnetic characterizations, reactive black 5 (RB5) and methyl orange (MO) were used as model dyes to evaluate the adsorption profile of ChMs. Indeed, operation and environmental factors, including pH, contact time and dye concentration were also investigated. Furthermore, kinetic and isotherm models were applied to experimental data of RB5 and MO adsorption on Fe_3O_4-chitosan nanocomposite NPs.

2.2. Materials and Methods

2.2.1. Materials

Ferric chloride hexahydrate ($Fe_3Cl{\cdot}6H_2O$, 97%) and glacial acetic acid (CH_3COOH, 99.7%) were purchased from Vetec Ltda, Brazil. Chitosan was provided by DNP – Delta Produtos Naturais Ltda (Molecular weight (M_w) = 31kDa and deacetylation degree (DD) = 92%), Brazil. Ferrous sulfate heptahydrate ($FeSO_4{\cdot}7H_2O$, 99%) and ammonium hydroxide (NH_4OH, 30%) were purchased from Dinâmica Ltda, Brazil, and glutaraldehyde solution 25% and epichlorohydrin (99%) were purchased from Sigma-Aldrich. The dyes, reactive black 5

(RB5, M_w = 991.82 g.mol^{-1}) and methyl orange (MO, M_w = 327.34 g.mol^{-1}) (Figure 1) were purchased from Sigma-Aldrich. All reagents are analytical grade and used as received.

Figure 11 – Chemical structure of the dyes RB5 and MO.

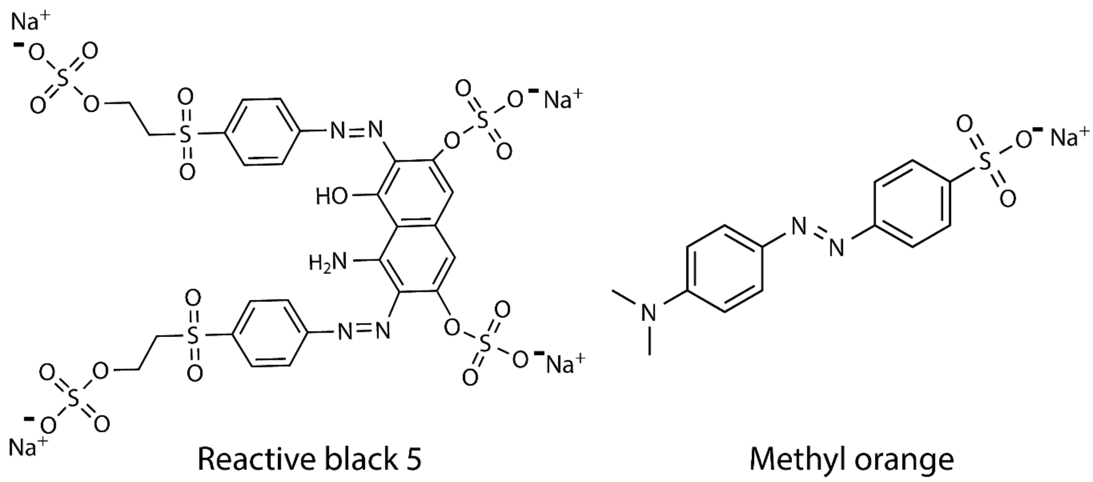

Source: the author

2.2.2. Synthesis of chitosan/Fe_3O_4 NPs

Chitosan/Fe_3O_4 nanoparticles were synthesized following the previously published US method by Freire et al. (2016). Briefly, 0.05g of chitosan were dissolved in 15 mL of acetic acid 1% (v/v) under stirring for 10 min. Then, 10 mL of Fe 0.33 mol.L^{-1} ($FeCl_3{\cdot}6H_2O$:$FeSO_4{\cdot}7H_2O$, 2:1 molar ratio) solution was added and the resultant mixture was homogenized using an ultrasound probe for 4 min (20 kHz, 585 W). Under US irradiation, 2 mL of NH_4OH was slowly added and the system was kept under sonication for more 4 min. Finally, the obtained powder was magnetically separated and washed several times with distilled water, and further dried under vacuum for 24h. The synthesized material was so-called ChM.

2.2.3. *Preparation of surface post-modified chitosan/Fe_3O_4 NPs*

Initially, ChM was synthesized and purified as previously described and further was dispersed into crosslinking agent solutions, GL (Chitosan:GL, 2: 1 molar ratio) and ECH (Chitosan:ECH, 2: 1 molar ratio, pH = 10). The dispersion was maintained under mechanical stirring at 50°C for 2h. The ChM NPs were washed several times with distilled water and dried under vacuum for 48h. Finally, the post-modified NPs were so-called ChM GL and ChM ECH.

2.2.4. Characterization methods

X-ray Powder Diffraction (XRD) analysis was performed to confirm the crystalline structures of magnetite present in chitosan/Fe_3O_4 nanocomposite. All samples were analyzed by X-ray powder diffractometer Xpert Pro MPD (Panalytical) using Bragg–Brentano geometry in the range of 15° – 70° with a rate of $1°.min^{-1}$. However, the samples Fe_3O_4, ChM GL and ChM ECH were analyzed using CuKα radiation (k = 1.54059 Å) and the tube operated at 40 kV and 30 mA. The sample ChM was analyzed using CoKα radiation (k = 1.78896 Å) and the tube operated at 40 kV and 30 mA.

Fourier Transform Infrared Spectroscopy (FTIR) analysis was carried out in a Perkin-Elmer 2000 spectrophotometer used to record spectra in the range between 4000 – $400cm^{-1}$. Previously, the samples were dried and grounded to powder and pressed (~10mg of the sample to 100mg of KBr) in a disk format.

The micrographs were obtained using a HITACHI HT7700 Transmission Electron Microscopy (TEM) operating at an accelerating voltage of 120 kV. Previously, the samples were dispersed in water and one droplet was placed on 300 mesh carbon-coated copper grid and dried overnight under ambient conditions.

Thermogravimetric analysis (TGA) was carried out under a nitrogen atmosphere using a Thermogravimetric Analyzer Q50 V20. The weight loss (%) was monitored by heating the samples from 25 to 850 C with a rate of 10 $C.min^{-1}$. The zero time for the thermal degradation study was taken after temperature stabilization. Differential thermogravimetric (DTG) was obtained by the first derivative of respective TGA curves.

K-Alpha X-ray Photoelectron Spectrometer (XPS) (Thermo Fisher Scientific, United Kingdom), equipped with a hemispherical electron analyzer and an aluminum anode (Kα = 1486.6 eV), was used to determine the chemical surface composition of the nanocomposites. All measurements were carried out using charge compensation during analyses, and the pressure of the chamber was kept below 2×10^{-8} mbar. Survey (i.e. full-range) and high-resolution spectra were recorded using pass energies of 1 and 0.1 eV, respectively. The spectrum fitting was performed by the Shirley method, assuming a mixed Gaussian/Lorentzian peak shape with the ratio of Gaussian to Lorentzian fixed in 0.4. In this work, X-ray photoelectron spectra are a result of the average of three spectra collected at three different regions.

Magnetic properties were investigated by a Vibrating Sample Magnetometer (VSM) Mini 5 Tesla from Cryogenic Ltd. Previously, the VSM was calibrated using a YIG sphere. After measuring the mass of each sample, the magnetization was given in $emu.g^{-1}$.

N_2 adsorption/desorption experiments at 77K were carried out using volumetric adsorption equipment (Autosorb 1c, Quantachome, USA and Micromeritics, ASAP 2000). The specific surface area (S_{BET}) of nanocomposites was estimated according to the Brunauer−Emmett−Teller method. The pore size distribution, average pore diameter, and total pore volume were calculated using the Density Functional Theory (DFT) method. All samples were previously degassed at 100°C.

2.2.5. Adsorption assay

Adsorption experiments were performed in triplicate in an orbital rotary shaker system at 18 rpm and 25 °C (± 1 °C). For all samples, the amount of adsorbent and volume of dye solution, RB5 and MO, were maintained constant, 10 mg and 3 mL, respectively.

2.2.5.1. pH Effect

For all performed experiments, the concentration of RB5 and MO was 100 mg.L^{-1} analyzed at four different pH values (4, 6, 8, and 10) to investigate the effect of the pH level in the adsorption capacity of the nanocomposite samples. Firstly, a stock solution of each dye was prepared using distilled water. Then, 50 mL of the prepared stock solutions were added in a glass flask and further HCl and/or NaOH solution were added to adjust pH level of the medium. The samples were kept for 2 h under shaking in a rotary shaker. The residual concentration of the dyes was determined using an UV spectrophotometer at 597 and 505 nm for RB5 and MO, respectively. For dye amount determination (q_e in mg.g^{-1}) was applied the following equation:

$$q_e = \frac{V_{Sol}(C_0 - C_{eq})}{m_{ads}} \tag{1}$$

where C_0 (mg.L^{-1}) represents the initial dye concentration, C_{eq} (mg.L^{-1}) is the equilibrium concentration of the dye remaining in solution, V_{Sol} (L) is the volume of the aqueous solution, and m_{ads} (g) is the mass of used adsorbent.

2.2.5.2. Adsorption Kinetics

Kinetics experiments were performed by mixing 10 mg of the adsorbent and 3 mL of dye solution (pH 4, C_0 =100 mg.L^{-1}). The adsorbent aliquots were collected at different fixed times, 1, 5, 10, 20, 40, 60, 90, 120, 150 and 180 min, and then removed by magnetic decantation. The pseudo-first-order (PFO) and pseudo-second-order (PSO) models were selected to fit the experimental kinetic data (LAGRERGEN, 1898; HO, 1995). These models assume that the adsorption is a pseudo-chemical reaction, and in addition, the adsorption rate can be determined using the following equations:

Pseudo-first order $$q_t = q_e(1 - \exp(k_1 t)) \quad (2)$$

Pseudo-second order $$q_t = \frac{t}{\left(\frac{1}{k_2 q_e^2}\right) + \left(\frac{1}{q_e}\right)} \quad (3)$$

where k_1 and k_2 are kinetic coefficients of the pseudo-first and second-order (min^{-1} and $g.mg^{-1}.min^{-1}$), respectively, and q_e is theoretical values for the adsorption capacity ($mg.g^{-1}$).
The intraparticle diffusion model was used once PFO and PSO can not determine the diffusion mechanism. The initial rate of the intraparticle diffusional model is obtained by the equation (4):

$$Q_t = K_d.t^{0.5} + C \quad (4)$$

where K_d is the intraparticle rate ($g.mg^{-1}.min^{-5}$) and C is a constant. In general, the intraparticle plots should show three regions assigned to: *(i)* instantaneous adsorption, which is influenced by external mass transfer of the adsorbent; *(ii)* internal diffusion and *(iii)* equilibrium condition (WANG, Z. *et al.*, 2019).

2.2.5.3. Adsorption isotherms

Adsorption equilibrium isotherms are very important to describe the interactive behavior between adsorbate and adsorbent, which is fundamental in the design of an adsorption method. Therefore, isotherm assays were performed adding 10 mg of adsorbent into different systems, varying dye concentration from 25 to 300 mg L^{-1} and keeping the acid medium at pH 4. Various isotherm models such as Langmuir (LANGMUIR, 1918), Freundlich (FREUNDLICH, 1926), Redlich – Peterson (REDLICH & PETERSON, 1959) and Temkin (TEMPKIN & PYZHEV, 1940; ZAHEER *et al.*, 2019) were used to analyze the experimental data. In general, these models are used to describe the adsorption process of dyes on chitosan-based materials (WONG *et al.*, 2003). The Langmuir isotherm considers that adsorption takes place at specific homogeneous sites onto adsorbent, and after adsorption in a specific site, no further adsorption can take place on the same site. In addition, the rate of adsorption capacity should be proportional to concentration of the adsorbate and specific surface area of the adsorbent. The equation of Langmuir isotherm is written below.

$$q_e = \frac{q_m K_a C_e}{1+ K_a C_e} \quad (5)$$

where K_a (L.mg^{-1}) is a constant related to the affinity of binding sites and q_m represents the maximum adsorption capacity of the material (mg.g^{-1}), assuming a monolayer of adsorbate taken up by the adsorbent; C_e (mg.L^{-1}) is the adsorbate concentration at equilibrium condition of adsorption and q_e is the amount of dye per unit of mass of composite (mg.g^{-1}). The essential characteristic of the Langmuir isotherm can be expressed in terms of both equilibrium and dimensionless constant separation factor R_L, which can be rewritten by the following equation (MOU *et al.*, 2017; JIANG & HU, 2019):

$$R_L = \frac{1}{1+ K_a C_0} \quad (6)$$

where C_0 (mg.L^{-1}) is the initial concentration of the dyes. According to the value of R_L, the type of isotherm can be interpreted as unfavorable ($R_L > 1$), Linear ($R_L = 1$), favorable ($0 < R_L < 1$) and irreversible ($R_L < 0$). As shown in Figure 42 (Appendix A), the values of R_L calculated in this work are between 0 and 1, indicating that the adsorption of both dyes are favorable, considering concentration range.

The Freundlich isotherm model is an empirical equation, which assumes another adsorption process-type, heterogeneous surface, where multilayers of the adsorbate is formed onto adsorbent. The model can be described according to Equation 7.

$$q_e = k_F C_e^{1/n} \quad (7)$$

where k_F (L.g^{-1}) is the Freundlich constant that can be defined as adsorption of the distribution coefficient and represents the quantity of dye adsorbed onto adsorbent for an equilibrium concentration. The parameter n is the Freundlich exponent (dimensionless) that is related to surface heterogeneity. In addition, for a favorable adsorption process, the value of $1/n$ should be between 0 and 1 (CESTARI *et al.*, 2012).

The Redlich – Peterson isotherm incorporates the features of Langmuir and Freundlich isotherms. Thus, the isotherm model can be applied in both homogeneous and heterogeneous systems and can be also used to represent adsorption equilibrium over a wide concentration range. In addition, this model assumes that monolayer and multi-sites adsorptions occurring concomitantly. The Redlich – Peterson isotherm is given by Equation 8 (XU *et al.*, 2015).

$$q_e = \frac{K_{RP}C_e}{1+A_{RP}C_e^{\beta}} \quad (8)$$

where C_e is dye concentration in equilibrium, K_{RP} and A_{RP} are the Redlich – Peterson constants ($L.mg^{-1}$) and ($L.mg^{-1})^{\beta}$, respectively. β is the exponent ranging between 1 and 0, and when $\beta \rightarrow 1$ this model tends to Langmuir model, i.e. isotherms at low concentration. Instead, when $\beta \rightarrow 0$, isotherm tends to Freundlich model at high concentration (RAJAR *et al.*, 2016).

The Temkin isotherm model considers adsorbent-adsorbate interactions, assuming that the heat of adsorption in the layer decreases linearly with coverage, in which it occurs with a uniform binding energy distribution up to some maximum binding energy (NIKIFOROV *et al.*, 2017), as described by Equations 9 and 10.

$$q_e = Bln(K_T C_e) \quad (9)$$

$$B = \frac{RT}{b} \quad (10)$$

where C_e is the equilibrium concentration of the dye, T is the temperature, R (8.314 $J.mol.K^{-1}$) is the universal gas constant, K_T ($L.mg^{-1}$) is the equilibrium binding constant, corresponding to the maximum binding energy, and B ($J.mol^{-1}$) is the constant related to the heat of adsorption.

2.3. Results and Discussion

2.3.1. Structure and morphology analyses

2.3.1.1 X-ray Powder Diffraction

XRD was used to confirm the magnetic crystalline structure present in chitosan matrix, and also to verify if the post-modification step could change crystalline structure of the final nanocomposite. The profile diffraction peaks of the cubic spinel phase of magnetite (Fe_3O_4) can be observed in all synthesized samples, as shown in Figure 2, where the pattern diffraction peaks are associated to (220), (311), (400), (422), (511), (440) and (533) crystal planes of the Fe_3O_4 (ICSD, file n° 01-086-1340 and ICSD, file n°01-086-1340). In general, it was possible to notice that the adopted post-modification methodology does not change the crystalline structure of ChM NPs. Indeed, as exepcted, the synthesis strategy based on co-precipitation reaction of the iron-chitosan complex under ultrasound irradiation provides chitosan-coating magnetite NPs, promoting resistance against oxidation. Actually, it is also important to mention that the US irradiation plays a significant rule in the synthesis, obtaining a quick healing and a homogeneous dispersion material. Differently, Jing–Jing Cui and co-workers (CUI *et al.*, 2017) synthesized post-modified magnetite@chitosan nanoparticles with thiosemicarbazide, and observed changes in the magnetite crystalline structure, suggesting a non-efficient chitosan coating.

Figure 12 – XRD patterns of standard Fe3O4 (ICSD, file n° 01-086-1340, standard Fe3O4 (ICSD, file n° 01-086-1340), Fe3O4, ChM ChM GL and ChM ECH. Green lines is the difference between the observed (black dots –IObs) and the calculated (red line –ICalc) intensities.

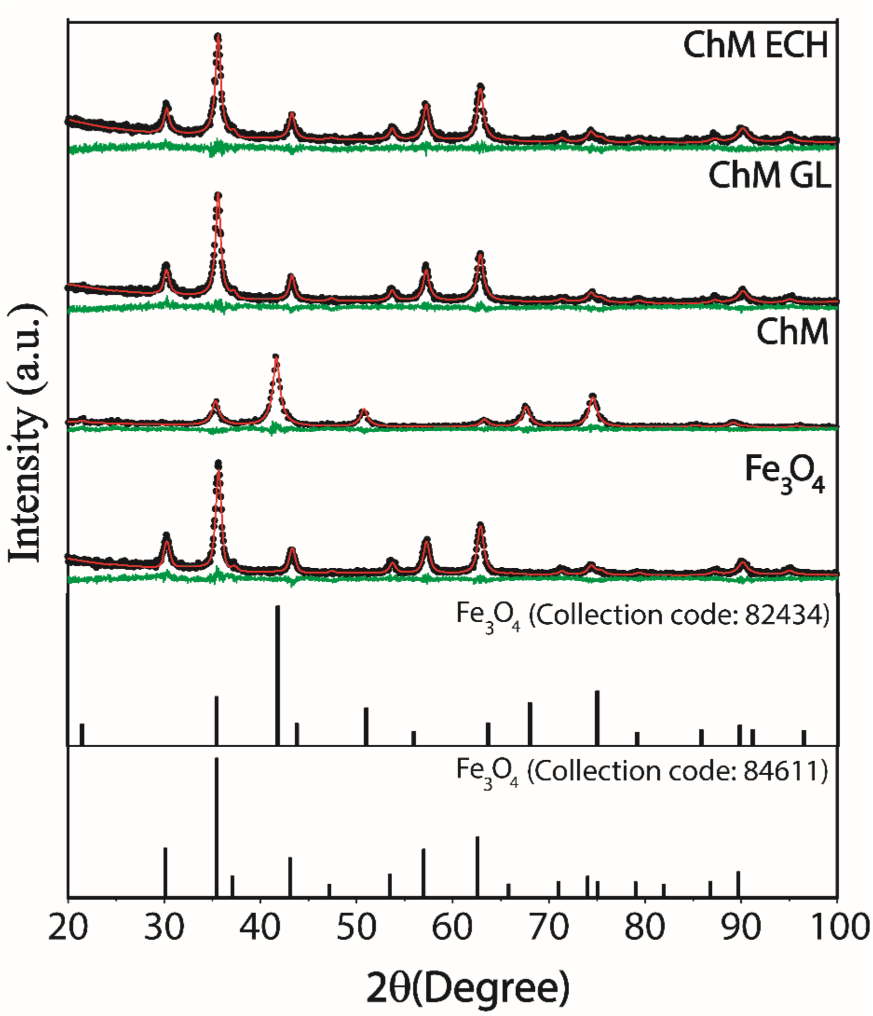

Source: the author

The diffractograms were refined by Rietveld method and the obtained parameters such as weighted profile R-factor (R_{wp}), goodness of fit index (χ^2), lattice parameters (a, b and c) and diameter crystallite size (D) with its respective standard deviation values, were summarized in Table 1. The R_{wp} and χ^2 are parameters used to verify the agreement between calculated and experimental data. For our samples, low values of R_{wp} and χ^2 were observed, suggesting goodness of the Rietveld refinement. Furthermore, after refinement, Equation 10 (Debye-Scherrer equation) was used to estimate the crystallite size of MNPs.

$$D = \frac{k\lambda}{\beta Cos(\theta)} \quad (10)$$

where k is the shape coefficient, λ is the X-ray wavelength, β is the full width at half of the maximum intensity and θ is the Bragg's angle. In Table 1, it was no further observed a significant change in the crystallite size and lattice parametes related to functionalization with chitosan. However, after crosslinking reaction, a small contraction of the unit cell of magnetite was observed, indicating a possible surface passivation effect (CERVELLINO *et al.*, 2014).

Table 1 – Crystallographic data obtained from Rietveld refinement.

Samples	R_{wp} (%)	χ^2	a, b and c (Å)	D (nm)
Fe_3O_4	11.73	1.04	8.3625	11.60 $\pm$0.11
ChM	14.75	0.94	8.3655	13.33 $\pm$ 0.47
ChM GL	12.39	1.14	8.3533	11.92 $\pm$ 0.16
ChM ECH	11.80	1.02	8.3548	11.74$\pm$ 1.73

Source: the author

2.3.1.2. Fourier Transform Infrared Spectroscopy (FTIR)

FTIR was performed to provide the nanocomposite's structural profile. Figure 3(a) shows FTIR spectra of the samples Fe_3O_4, chitosan, ChM , ChM ECH and ChM GL, and for all analyzed samples, excepted chitosan, the bands around 586 and 634 cm^{-1} were assigned to lattice vibrations of Fe – O in tetrahedral and octahedral positions, confirming the presence of Fe_3O_4 into nanocomposite structure (SOARES *et al.*, 2016). For chitosan spectrum, the bands at 1027, 1083 and 1155 cm^{-1} can be related to stretching vibration C – O of ether, stretching vibration of primary alcohol and special adsorption of β (1 →4) glucoside bonds, respectively (TIAN *et al.*, 2003).These bands were also observed in nanocomposite spectra, however, showing a slightly displacement. The bands at 1326, 1382 and 1423 cm^{-1} can be referred to axial deformation C – N of amino groups, and bending vibration of methylene and methyl groups, respectively (MONIER *et al.*, 2012; GUTHA *et al.*, 2017). Interestingly, in nanocomposite spectra, these bands show a different format, as well as the band at 1326 cm^{-1} is displaced to 1316, 1311 and 1315 cm^{-1} for samples ChM , ChM GL and ChM ECH, respectively.

For chitosan spectrum, two bands at 1595 and 1654 cm^{-1} were assigned to N – H bending vibration and C = O stretching vibration, respectively. In ChM sample, these bands arise at lower wavelengths at 1530 and 1621 cm^{-1}, respectively. This displacement might be assigned to the chelation effect of chitosan molecules with iron ions during formation of the nanocomposite, suggesting that Fe atoms on magnetite surface is coordinated to amino groups from chitosan (BHATIA & RAVI, 2000; WANG *et al.*, 2009). For ChM ECH sample, no further evidence was found regarding crosslinking reaction between chitosan and EDH, since any different band was observed in comparison to chitosan and magnetite spectra. However, in ChM GL spectrum, the post-modification with GL is evidenced at 1631 cm^{-1}, which can be assigned to stretching vibration of C = N from imine groups, i.e. Schiff Base-type crosslinking reaction. Additionally, no band was observed in the range of 1725 cm^{-1}, suggesting that aldehyde groups also reacted with chitosan molecules on nanocomposite surface (OLADOJA *et al.*, 2014).

Figure 13 – (a) FTIR spectra, (b) TGA and (c) DTG of samples Fe3O4, chitosan, ChM, ChM ECH and ChM GL.

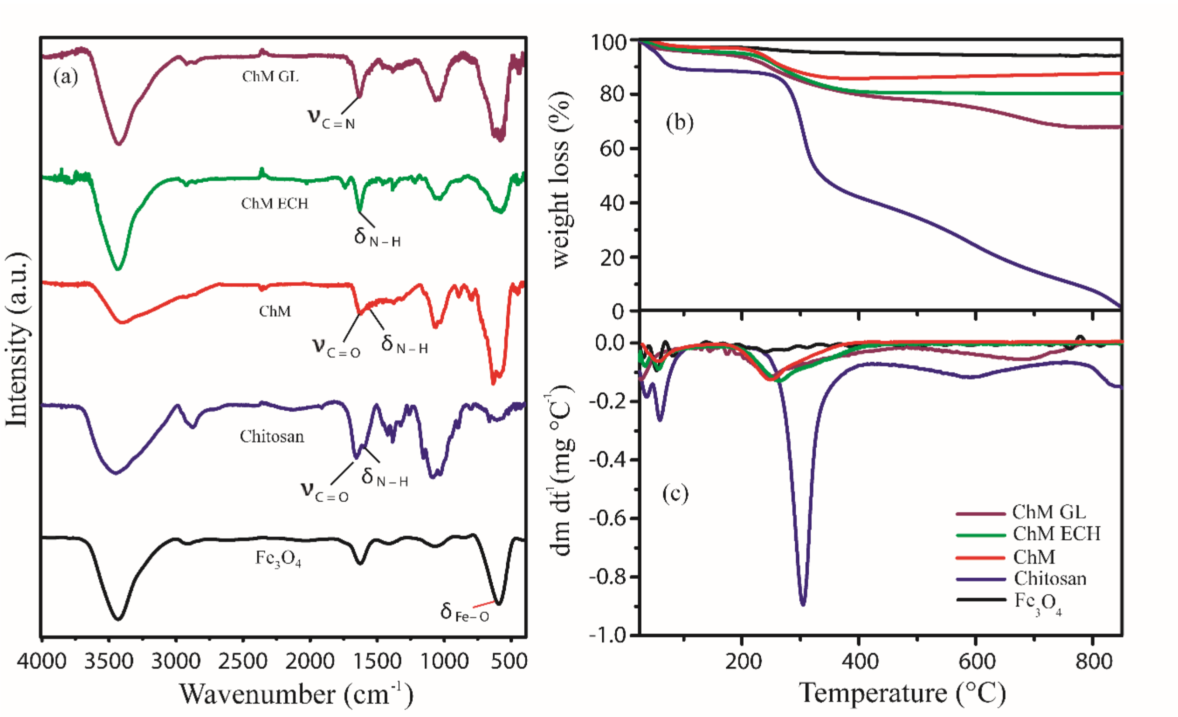

Source: the author

2.3.1.3. TGA– DTG

Thermogravimetric analysis (TGA) was used to evaluate thermal stability of nanocomposites. Figure 3 (b) and (c) show TGA and DTG curves for Fe_3O_4, chitosan and ChM samples, respectively. For all samples, a first event occurs at a temperature ranging from 30 to 130°C, which can be assigned to residual water loss. The hydration of polysaccharides depends on their primary and supramolecular structure, thus, the first event may provide information about the physical and molecular changes caused by the interactions of magnetite and crosslinking reactions (NETO *et al.*, 2005). Therefore, for pure chitosan, it was also verified a first stage of residual water loss of 12%, whereas for ChM was approximately 3%. For pure chitosan, DTG curve shows two events at 36 and 60 °C that can be assigned to the breakdown interaction of water molecules with amine and hydroxyl groups (RUEDA *et al.*, 1999; MARQUES *et al.*, 2016). For all ChM samples, considering initial events, both amine and hydroxyl groups must interact with magnetite surface, becoming less available to interact with water molecules. This profile was also supported by ChM DTG curves, showing just one event at 56 °C related to water loss (NETO *et al.*, 2005). For ChM GL and ECH, the first stage of residual water loss was around 5 and 6%, respectively, and from DTG curves, it was also possible to noticed a similar profile of chitosan and ChM ECH, which initial events can be also assigned residual to water loss. However, for ChM ECH, these events appear displaced to lower temperature due to the crosslinking agent ECH, since the post-modification step can occur in both amine and hydroxyl groups, converting hydroxyl in ether groups and forming a dense crosslinked network (KUMARI *et al.*, 2015). Instead, for ChM GL, the crosslinking reaction converts primary amine to imine groups. Then, water molecules may interact with hydroxyl groups and, consequently, the dehydration process can be considered more difficult (MARQUES *et al.*, 2016).

The second event occurs in the range of 228 – 430 °C for chitosan and 155 – 480 °C for all nanocomposites, corresponding to polymer degradation (ZIEGLER-BOROWSKA *et al.*, 2015), suggesting that covalent binding with GL and ECH on nanocomposite surface decreases chitosan thermal stability. Indeed, this may correspond to the cooperative loss of the hydrogen bond between chitosan chains, due to interactions between amine and hydroxyl groups with magnetite surface from crosslinking agent molecules (POON *et al.*, 2014). In DTG curves, considering second thermal event, it was also noticed a lower rate of weight loss for modified nanocomposites, 47.8, 11.0, 16.8 and 15.0 % for chitosan, ChM, ChM GL and ChM ECH, respectively. For chitosan and ChM GL samples, the thermal degradation continues until 870°C, and may be related to the breakdown of chitosan chains on magnetite surface.

2.3.1.4. X-ray photoelectron spectroscopy (XPS)

XPS spectra could provide interaction information between adsorption sites from chitosan and magnetite. Additionally, XPS was used to determine the valence state of iron and the sites into magnetite structure. Furthermore, since DRX results showed no further change in the magnetite crystalline structure after post-modification step, ChM was chosen as a representative sample for XPS analysis. Herein, Figure 4 only shows spectra regarding ChM sample.

The best fit for C 1s, O 1s and N 1s spectra was obtained with three components, whereas for Fe 2p spectrum was nine components. Table 2 summarizes the results obtained from deconvolution of the peaks observed in all spectra for ChM sample.

Figure 14 – High resolution X-ray photoelectron spectroscopy spectra of (a) C 1s, (b) N 1s, (c) O 1s and (d) Fe 2p of the sample ChM.

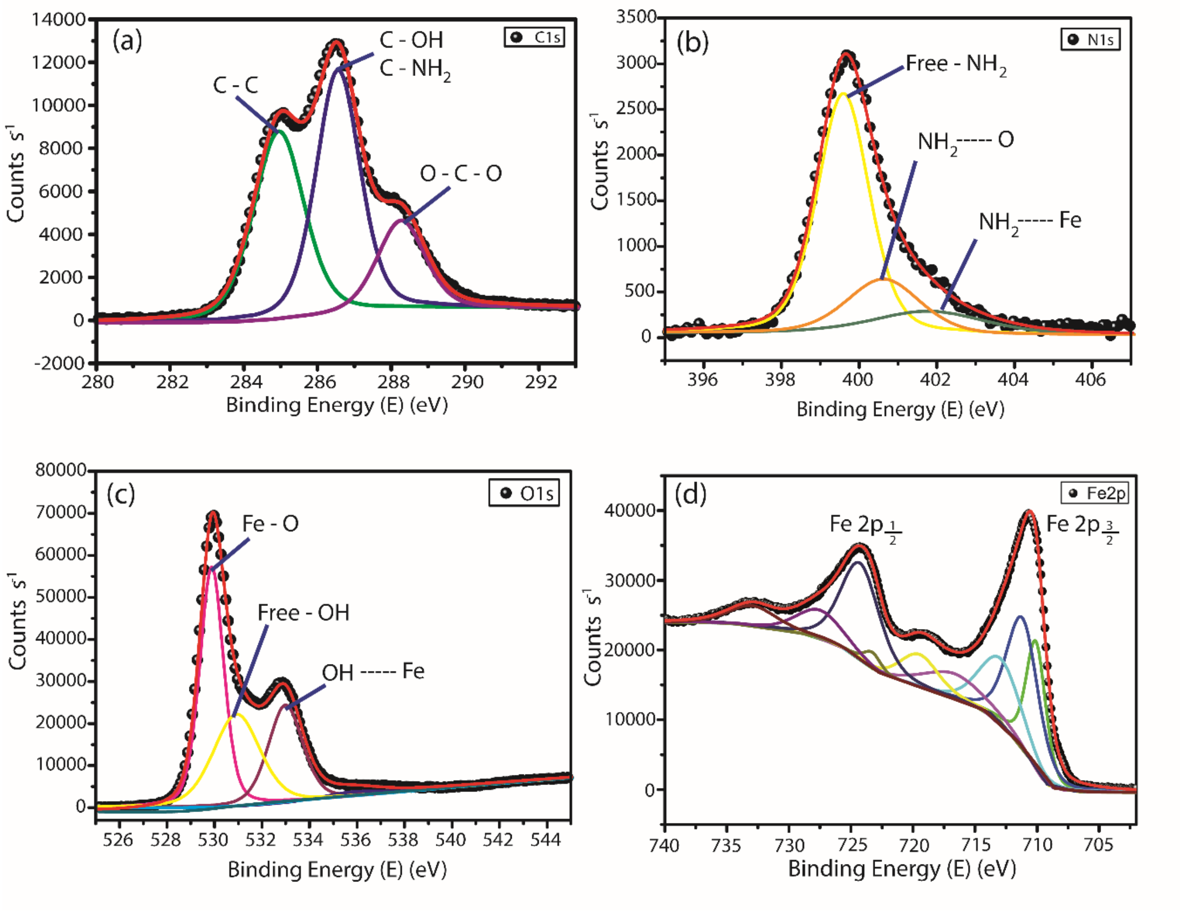

Source: the author

None of the peaks observed in the C 1s spectrum are related to the interactions with iron ions. For N 1s, two peaks arise from the contribution of three components at 399.6, 400.6 and 402.0 eV, which can be attributed to free amino groups (NH_2), where some amino groups are also involved in hydrogen bonds (NH_2---O), and chelated with iron ions (NH_2---Fe). Similar profile was observed for O 1s spectrum, where the components at 529.8 and 530.9 eV may be attributed to the oxygen linkage with iron ions and free hydroxyl groups, respectively. However, the component at 533.0 eV can be assigned to hydroxyl groups in hydrogen bonds (– OH---O and – OH---N) and also chelated with iron ions (– OH---Fe). It is interesting to notice that the binding energy attributed to hydroxyl groups and iron ions may be due to both water adsorption on magnetite surface and chitosan hydroxyl groups.

In Fe 2p spectrum, as seen in Figure 4d, it was observed a doublet Fe 2p3/2 at 710.6 eV and Fe 2p1/2 at 724.2 eV regarding to Fe^{2+} octahedrally and Fe^{3+} octahedrally and tetrahedrally coordinated, which is characteristic of magnetite inverse spinel structure. Thus, these results suggest that both nitrogen and oxygen atoms were involved in the complex formation of iron-chitosan during ChM NPs synthesis. Wang and co-workers, which presented a more detailed XPS study about chitosan, chitosan – iron (II) and iron (III) complex and chitosan-Fe_3O_4, observed that the atomic fraction associated to hydroxyl groups, involved in hydrogen bonds, increases in the sample containing iron. Taken this into consideration, the authors suggested that this profile might be due to interaction of hydroxyl groups and iron ions (OH --- Fe) (QU *et al.*, 2013). Thus, in this work, it is possible to propose that both nitrogen and oxygen participate in the complex formation of iron ions-chitosan.

Table 2 – Assignment of spectral peaks (Fe, C, O and N) based on binding energies and atomic fraction.

Element	Binding Energy (eV)	Atomic Fraction (%)	Assignments
	284.9		C – C
C 1s	286.5	34.36	C – OH ; C – NH_2
	288.2		O – C – O
	399.6		NH_2
N 1s	400.6	3.88	NH_2 --- O
	402.0		NH_2 --- Fe
	529.8		Fe – O
O 1s	530.9	51.7	– OH
	533.0		– OH --- Fe
	710.1		Fe^{2+} Oct
Fe $2p_{3/2}$	711.3		Fe^{3+} Thd
	713.3		Fe^{3+} Oct
	723.4	10.6	Fe^{2+} Oct
Fe $2p_{1/2}$	724.4		Fe^{3+} Oct
	727.7		Fe^{3+} Thd

Source: the author

The results of XPS, FTIR, TGA and XRD are important to understand the type of crystalline structure is being formed after synthesis, as well as, the type of interaction between chitosan and magnetite surface. Additionally, it was also possible to verify that GL and ECH crosslinking agents could affect the intermolecular interactions in chitosan structure. Therefore, in Figure 5 is shown a schematic proposal of nanocomposites surface synthesized in this work. As can be seen, besides all nanocomposites show similar chitosan-iron complex formation on magnetite surface, for ChM GL and ECH, is also shown the crosslinking network between chitosan molecules on ChM NPs after post-modification step.

Figure 15 – Proposal of surface structure of nanocomposites.

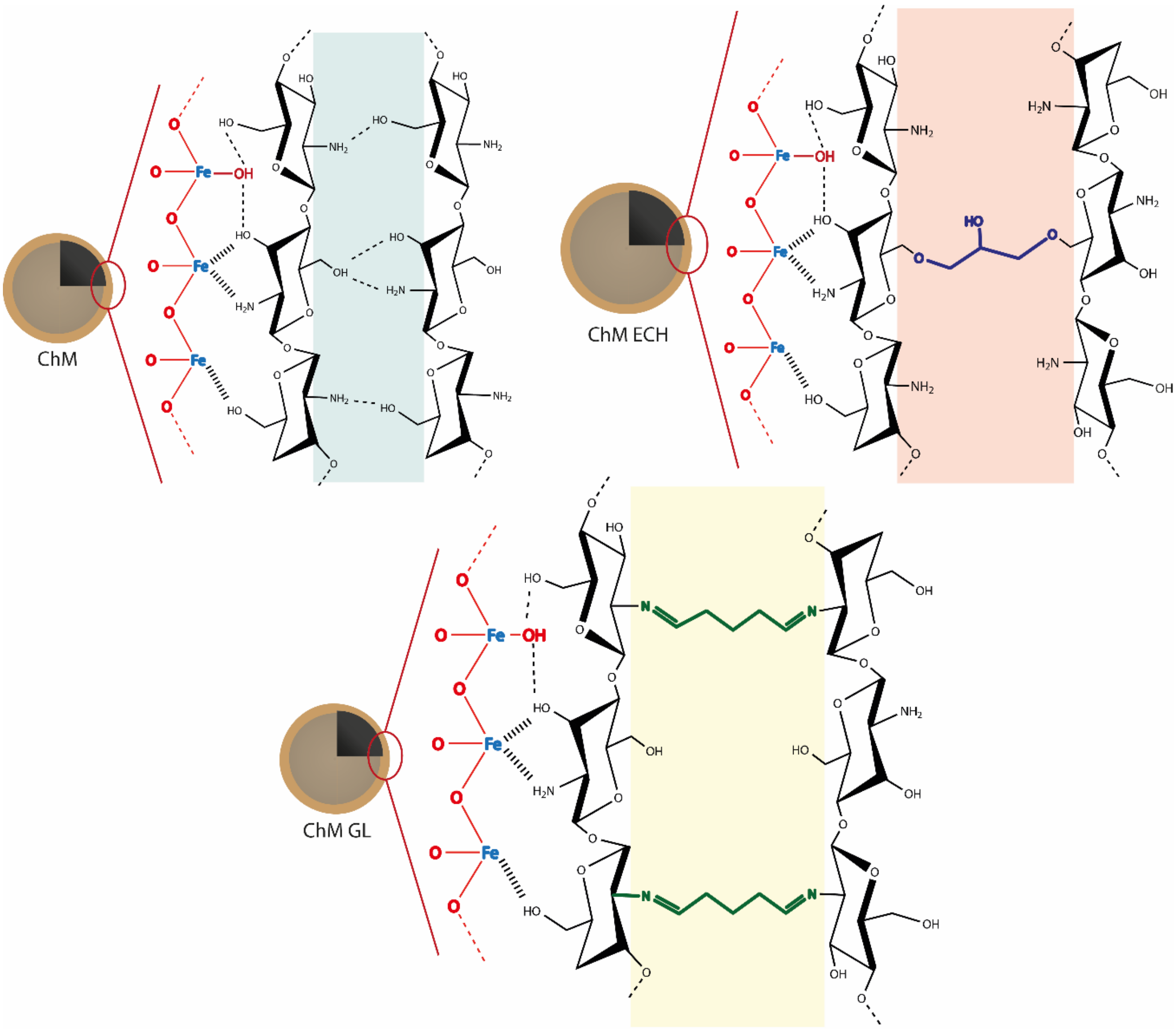

Source: the author

2.3.1.5. Transmission electron microscopy (TEM)

TEM micrographs were used to investigate the morphology of the samples ChM, ChM GL and ChM ECH. As shown in Figure 6, the nanoparticles were successfully obtained in a nanoscale range, however, all samples had two distinct morphologies, rods and spheres, in which the rod particles show heterogeneous length and diameter values. For spherical NPs, the histograms show an average diameter of 9.6 ± 3.4, 9.9 ± 3.1 and 8.7 ± 2.2 for ChM, ChM GL, and ChM ECH, respectively (Figure 6g, h, and i). It is interesting to notice that the nanorods morphology is not presenting in our previous published work (FREIRE *et al.*, 2016). Indeed, in last years, various synthetic routes have been developed to synthesize 1D magnetite nanorods due to specific properties, such as unique electronic transport (YANG *et al.*, 2011; RAJAR *et al.*, 2016), and according to our knowledge, no paper has been reported "one-pot" synthesis of magnetite@polymer nanorod using ultrasound irradiation.

For instance, Li and co-workers (LI *et al.*, 2005) reported that the increase in time reaction under US irradiation may cause a shape change of Se nanoparticles from spherical α-Se to t-Se nanotubes, and further to t-Se nanowires. Neto and co-workers (NETO *et al.*, 2017) have synthesized magnetite@polymers by ultrasound method using a higher time reaction in comparison to our method, instead the final nanoparticles did not present nanorods-type morphology. Besides, it is well-known that the capping agent can play a essential role in the preferential growth of a crystal, due to changes of the free energy of different facets (SINGH *et al.*, 2017). Herein, we believe that the formation of chitosan/magnetite composite nanorods is dependent of both the ultrasound irradiation time increasement and the capping agent chitosan. However, the appearance of nanorods shape will be deeper investigated in further work.

Figure 16 – TEM images of the samples ChM (a and d), ChM GL (b and e) and ChM ECH (c and f) at different amplifications. Histograms for spherical nanoparticles of the sample ChM (g), ChM GL (h) and ChM ECH (i), which were obtained from the count of 159, 201 and 93.

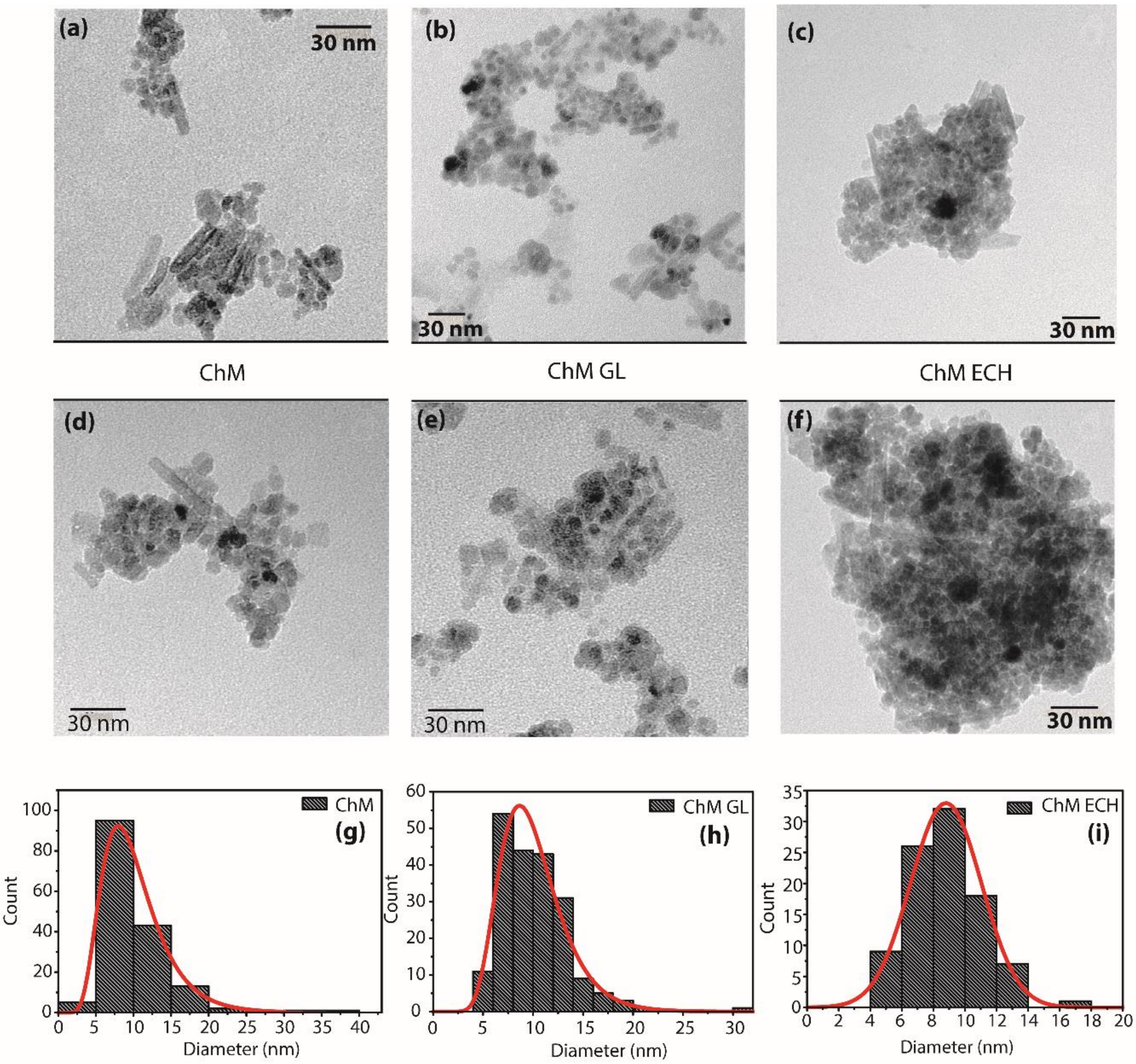

Source: the author

2.3.2. Magnetic property

In order to analyze magnetic behavior of synthesized GL and ECH-modified nanocomposites, the magnetization of the samples ChM GL and ChM ECH were measured as a function of the external magnetic field, and compared to magnetization curve of pure Fe_3O_4, using the same synthesis method. The results are shown in Figure7. In addition, in the inset in Figure 7, a photo of the sample ChM GL disperse in water is shown which presents the macroscopic magnetic behaviour under an external magnetic field.

For all samples, an initial steep slope in magnetization curves is observed, suggesting that nanoparticles are small enough to be considered as single-domain particles (SINGH *et al.*, 2017). The single-domain characteristic provides an data profile with almost no hysteresis loop, indicating that the samples have superparamagnetic behavior. For samples Fe_3O_4, ChM GL and ChM ECH, the saturation magnetization (M_s) are found to be 56.78, 49.54 and 44.01 emu.g^{-1}, respectively. Once the magnetization curve is a function of the material magnetization, MNPs functionalized with diamagnetic polymers trend to show smaller saturation magnetization values than uncovered ones. However, in this work, the obtained nanocomposites have great magnetic properties, even after post-modification of ChM with glutaraldehyde and epichlorohydrin.

Figure 17 – Magnetization curves normalized per gram of sample (emu.g^{-1}).

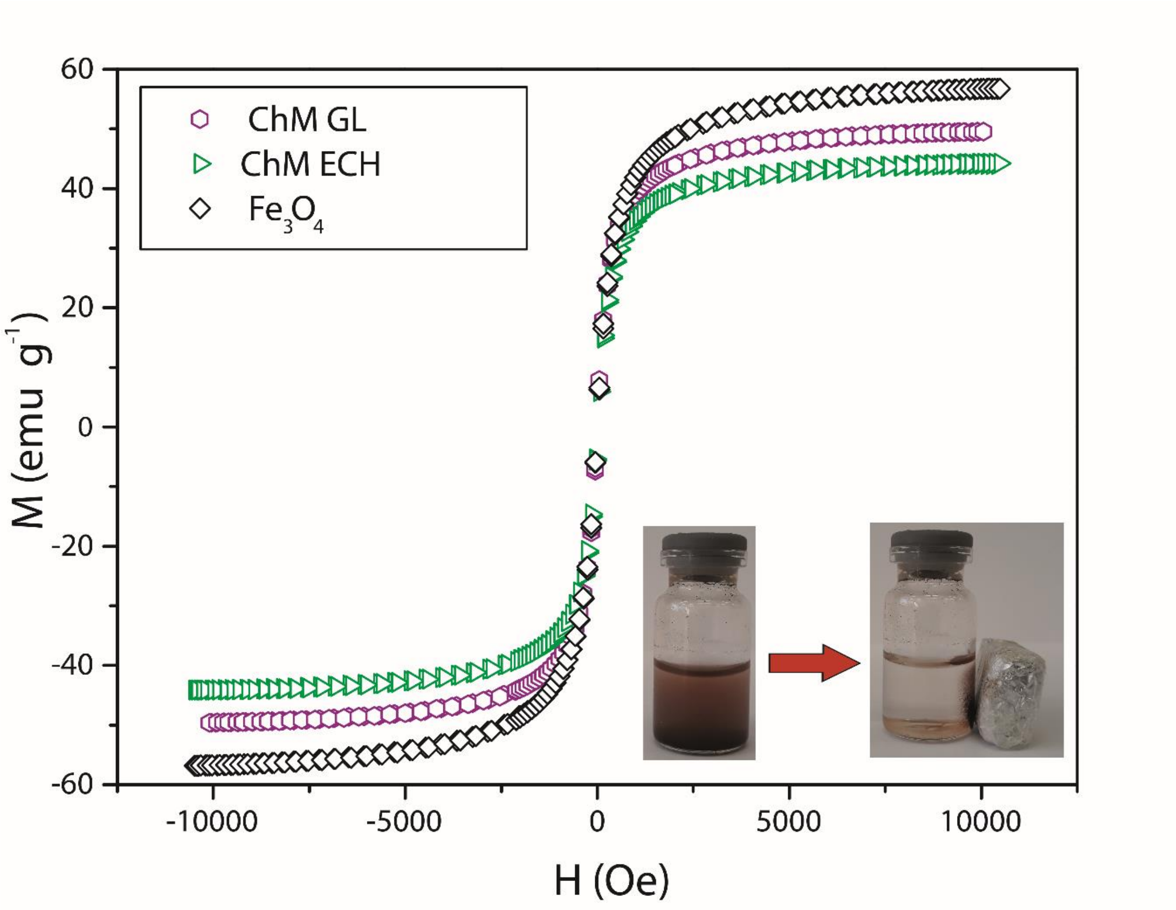

Source: the author

2.3.3. N_2 adsorption-desorption

N_2 adsorption-desorption isotherms of nanocomposites and DFT method for pore size distribution (inset) are presented in Figure 8. The isotherms can be classified as type IV(a), according to IUPAC, which is related to pore size distribution in the range of mesopores (2nm < d < 50 nm) (THOMMES *et al.*, 2015). Besides, for all samples, the isotherm hysteresis loop shows an H2(b)-type, which can be associated to materials with heterogeneous pore size, and generally with an ink-bottle shape pore. From the inset, it is also seen a change in the pore size distribution may promoted by post-modification of chitosan with GL and ECH. For instance, Louis Poon reported that crosslinking reactions may decrease the porosity of final material, mainly due to the decrease in intraparticle diffusion occasioned by highest reaction rate on the surface of the polymer (POON *et al.*, 2014). Thus, in this work, the formation of the ink-bottle shape pore can be due to the higher amount of crosslinking agent on the surface of nanocomposite. Figure 8(d) shows the Brunnauer – Emmett – Teller (BET) surface area and pore volume for ChM, ChM GL and ChM ECH samples. The highest BET surface area was observed for sample ChM GL, 68.0 m^2g^{-1}, followed by ChM ECH and ChM with 66.0 and 59.8 m^2g^{-1}, respectively. It is also important to notice that the pore volume increases for GL and ECH modified-nanocomposites. This behaviour can be related to the decrease in intermolecular interactions between chitosan molecules, mainly occosianed by crosslinking reaction, in which was also evidenced by TGA/DTG curves.

Figure 18 – Nitrogen adsorption-desorption isotherms and pore size distribution of (a) ChM; (b) ChM GL and (c) ChM ECH; and (d) surface area and pore volume of nanocomposite samples.

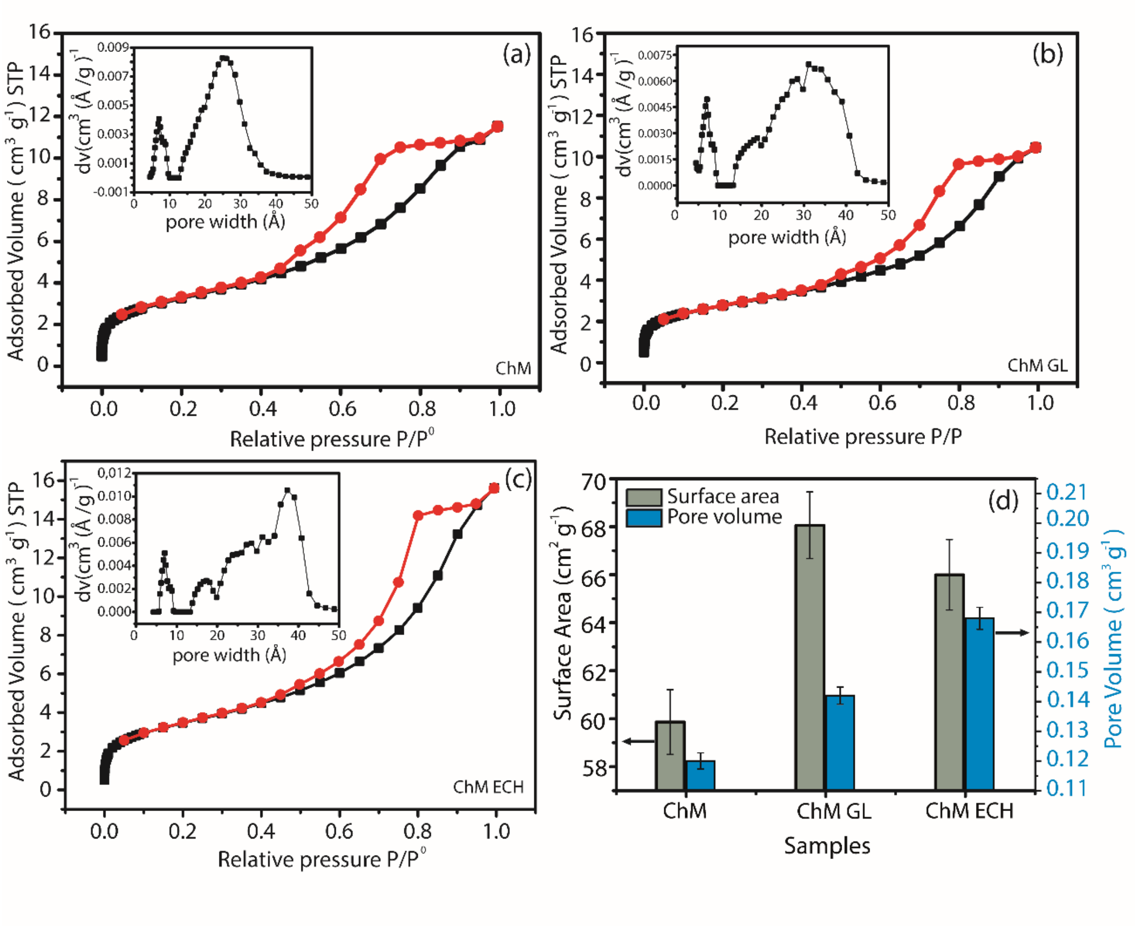

Source: the author

2.3.4. Adsorption evaluation

The adsorption capacity of the nanocomposites was evaluated using RB 5 and MO as model anionic pollutants of textiles industry. Indeed, the chosen dyes have shown some chemical characteristics as model molecules, since both azo (– N = N –) and sulfonic (SO_3^-) groups are found in various textile dyes (NASSAR & ABDALLAH, 2016).

2.3.4.1. pH effect

The pH level of dye solution plays an essential role in the adsorption process since can change the degree of interaction between adsorbent and adsorbate, directly affecting the adsorption capacity. Therefore, the effect of pH in RB5 and MO adsorption was investigated and the results are shown in Fig 9 (a), (b) and (c). For unmodified ChM sample, the adsorption profile was different for both MO and RB5 dyes, the increase of pH from 4 to 10 decreases the adsorbed amount of MO (Figure 9(a)). Interestingly, when the pH increases from 4 to 8, it is notice a slightly increasing in the amount of RB5 adsorbed, and further decreases when pH reaches 10. Generally, the change of the pH to acid medium increases the reactivity of dyes adsorption capacity of chitosan, which is related to protonation of primary amino groups, since protonated groups can interact through electrostatic attraction with anionic groups ($-SO_3^-$) in dye molecules (ZHOU *et al.*, 2014; ZAHEER *et al.*, 2019). Besides this behavior was observed for MO adsorption, the opposite has been noticed for RB5 adsorption, suggesting that the electrostatic interaction does not act as a dominant adsorption mechanism. Additionally, the RB5 adsorption capacity decreases when pH value changes from 8 to 10, which may be related to surface charge change from positive to negative on ChM NPs, since the pH zpc level was 8.91 (Figure 43, Appendix A). Moreover, this decreasing in the adsorption capacity could be due to competition between hydroxyl groups (OH^-) and dye molecules in the reaction medium by adsorption active sites (WAN NGAH *et al.*, 2011).

For ChM GL (Figure 9(b)) and ECH (Figure 9(c)) samples, it can be seen a similar behavior in the adsorption capacity for both dyes, i.e. increasing the pH from 4 to 10 the adsorption capacity decreases. Tomasz and co-workers also observed the same adsorption profile using different reactive dyes for surface-modified chitosan samples (JÓŹWIAK *et al.*, 2017), suggesting electrostatic interactions as the main dominant adsorption mechanism for both GL and ECH-modified nanocomposites.

In this work, it is also seen that both dyes showed a higher adsorption capacity for ChM sample. For MO dye, all samples presented their maximum adsorbed capacity at pH 4. However, the profile was not observed for RB5 dye. For instance, ChM GL and ECH showed their maximum adsorbed amount ($q_{e(max)}$), 27.06 and 31.96 mg g^{-1}, respectively, at pH 4, whereas for ChM the $q_{e(max)}$, 43.50 mg g^{-1}, was obtained at pH 8. Besides the difference between $q_{e(max)}$ values at pH 4 and 8 were quite small, pH 4 seems to be ideal for both dyes, considering all adsorption capacity values.

Figure 19 – Adsorption capacity of RB5 and MO at different pH levels: (a) ChM, (b) ChM GL and (c) ChM ECH.

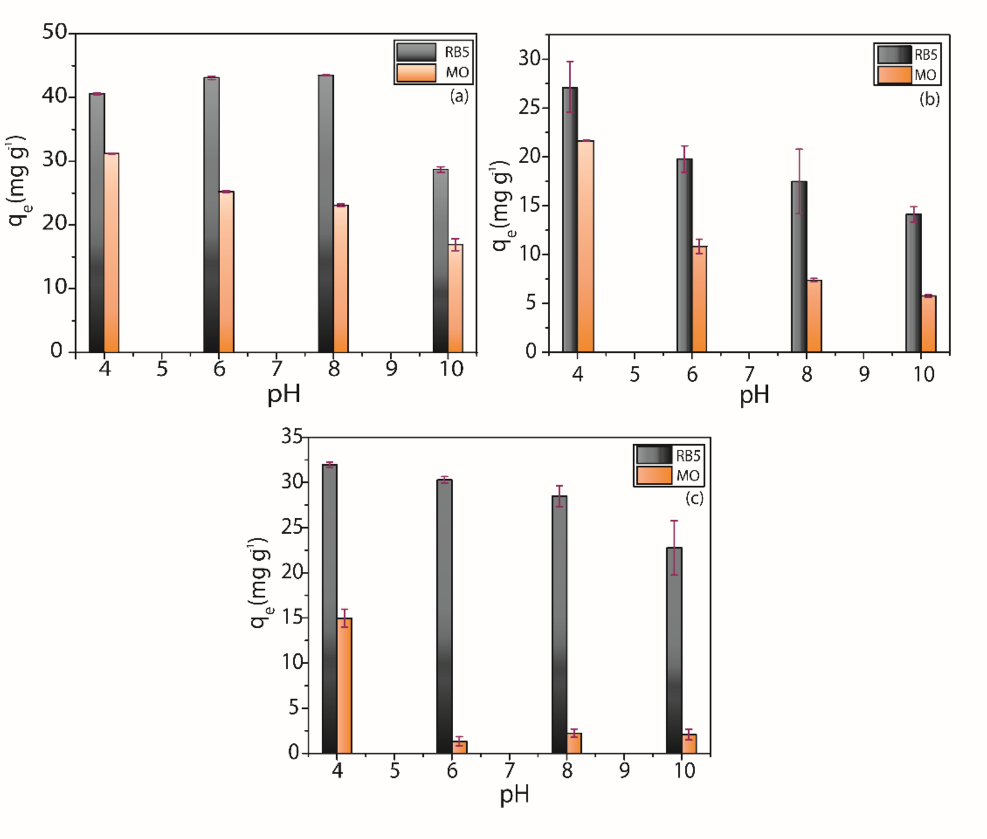

Source: the author

2.3.4.2. Effect of contact time

Figure 10 (a) and (b) show the change in the uptake of RB5 and MO dyes, respectively, by nanocomposites as a time function at dye initial concentration of 100 ppm and pH 4. For RB5, the sample ChM reaches the equilibrium condition at 40 min, whereas modified samples reach the equilibrium after 120 min. Indeed, after 40 min, ChM removed around 99.9% of the dye from acid solution, and ChM ECH and GL, even at equilibrium condition, have only been removed 92.5 and 89.3% of the dye, respectively. For MO, the opposite behavior was observed, i.e. modified samples reach an equilibrium condition at 20 min, whereas ChM just after 40 min.

Munagapati and co-workers synthesized goethite-chitosan composite and verified that the adsorption equilibrium time for MO is reached after 180 min, showing a slower adsorption profile in comparison to our samples (MUNAGAPATI *et al.*, 2017). Additionally, for ChM ECH and ChM samples at equilibrium condition, there was just a slightly difference of the amount of removed dye, 94.3 and 93.2%, respectively. Indeed, adsorption kinetic may be explained mainly by two steps: (I) the initial section of the curve corresponds to a great availability of reactive groups and a large concentration gradient between solution and both surface and internal sorption sites; (II) the second step is controlled by a decrease of the concentration gradient and by resistance to intraparticle diffusion (ELWAKEEL *et al.*, 2016). Aguiar (AGUIAR *et al.*, 2016) has demonstrated that the adsorption of molecules with diameters lower than adsorbent pore diameter is independent of geometry factor of interconnecting pores, as well as surface chemical structure. Herein, once the molecular size of MO is 1.2 nm and RB5 is 2.9 nm, the adsorption kinetic profiles suggest greater access to adsorption pore sites for MO dye, making the second step faster in comparison to RB5.

Figure 20 – Adsorption kinetics of (a) RB5 and (b) MO of ChM, ChM GL and ChM ECH at pH 4.

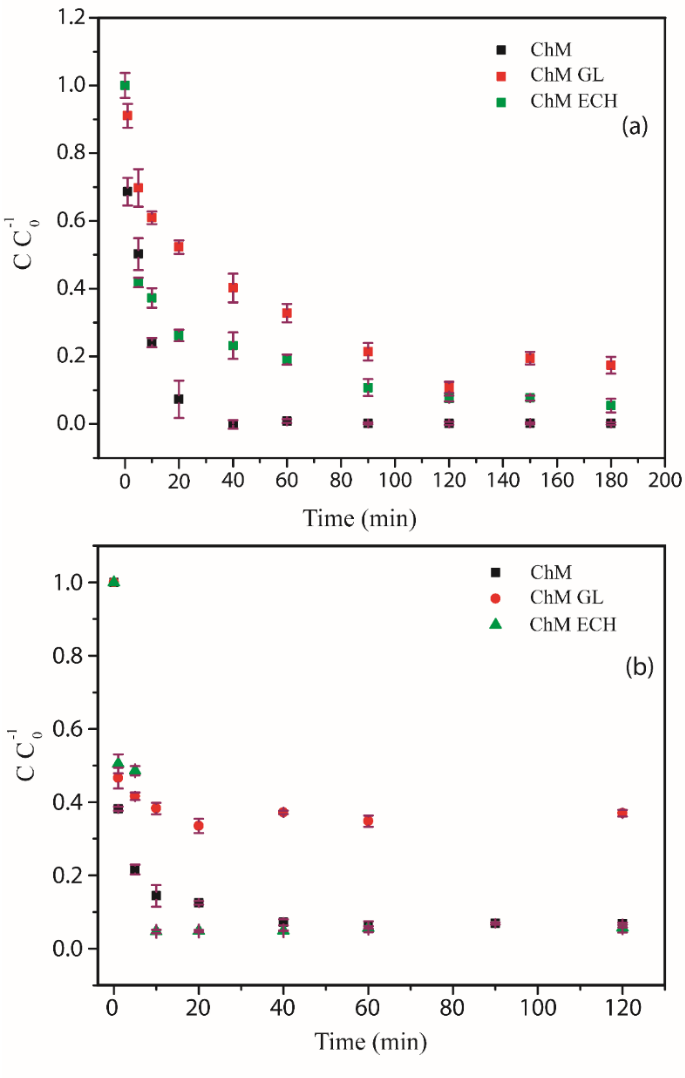

Source: the author

In order to better understand the involved adsorption mechanism for RB5 and MO dyes, the experimental data was analyzed using pseudo-first-order (PFO) and pseudo-second-order (PSO) models. The analyzed kinetic parameters are shown in Table 3.

Table 3 – Kinetic parameters for RB5 and MO dyes adsorptions.

Model	**pseudo-first-order**			**pseudo-second-order**			**Intraparticles diffusion**		
	R^2	q_e (mg g^{-1})	k_1 (min^{-1})	R^2	q_e (mg g^{-1})	k_2 (g mg^{-1} min^{-1})	K_p (g mg^{-1} $t^{-0.5}$)	C	R^2
Reactive black 5									
ChM	0.9770	33.420	0.14675	**0.9998**	**33.200**	**0.01180**	7.7541	1.4071	0.9682
ChM GL	0.9714	23.816	0.4779	**0.9954**	**24.485**	**0.00270**	1.7490	4.759	0.9976
ChM ECH	0.9532	12.062	0.00673	**0.9870**	**35.211**	**0.00206**	0.6260	19.949	0.9856
Methyl orange									
ChM	0.9828	8.682	0.1045	**0.9999**	**27.762**	**0.03858**	3.2495	15.2461	0.9890
ChM GL	-	-	-	**0.9994**	**18.175**	**-0.05491**	2.0206	13.5764	0.9786
ChM ECH	0.9798	15.807	0.8833	**0.9990**	**26.055**	**0.02207**	4.2461	8.5636	0.8749

Source: the author

The adjustment of the applied kinetic models was followed by the correlation coefficient (R^2) in association to linear fit of the models. Comparing both PFO and PSO models, PSO seems to be more adequate to describe experimental results, since R^2 values denote a good fit. Figure 44 (Appendix A) shows the plots for PSO model applied for all samples. According to PSO model, the adsorption mechanism process must be directed by chemical adsorption (WANG *et al.*, 2014). Cao et al. also found that azo reactive dye adsorption process, using Fe_3O_4/chitosan nanoparticles as adsorbent, follows a PSO kinetic model (CAO *et al.*, 2014).

However, this model does not take into account contributions from diffusion mechanism in kinetic control. Thus, the intraparticle model was applied to provide a better undertand of the diffusion and adsorption mechanisms. Figure 45 (Appendix A) showed the plot of Q_t versus $t^{0.5}$ for all adsorption systems. Interestingly, it was observed that RB5 adsorption kinetics by the samples ChM GL and ECH did not exihibit a plateau, suggesting that during all contact time of adorption the process is stongly influencied by intraparticle difussion even at low adsorbate concentrations (SENTHILKUMAAR *et al.*, 2006). The linear portion of the plots should be assigned to a boundary layer sorption and the intercept value (inset in Figure I.4) to a larger boundary layer effect (WU *et al.*, 2009). In addition, the plots do not pass through the origin, indicating that intraparticle diffusion is not only the rate-limiting step in the adsorption process but other kinetic processes also occurred simultaneously, contributing to the sorption mechanism (XU *et al.*, 2010).

2.3.4.3. Adsorption Isotherms

Figure11 (a) and (b) show the influence of RB5 and MO initial concentration in the adsorption capacity of synthesized ChM NPs. For both dyes, the sample ChM did not reach an equilibrium plateau at studied concentration range. Actually, it was observed that the adsorption profile is very similar for both dyes since showed a fast increase of the adsorption capacity by the increasing of initial concentration. This might be assigned to an increase in the adsorption sites occasioned by MNP clusters breakdown under acid medium, related to a better partial solubility of chitosan. As expected, ChM GL and ECH do not follow similar behavior, since crosslinking reactions can decrease chitosan solubility under acid medium. In addition, it was noticed that ChM sample showed a greater adsorption capacity for MO in comparison to RB5, 70.85 and 53.02 mg g^{-1}, respectively, whereas adsorption capacity values found to ChM GL and ECH were 21.93 and 16.44 mg g^{-1} for MO, and 35.77 and 37.39 mg g^{-1} for RB5, respectively.

Wong and co-workers (WONG *et al.*, 2003) reported the improvement of the adsorption capacity being provided by decreasing of molecular size and increasing of dye concentration on chitosan surface, generating a greater penetration of dye molecules into internal structure of chitosan pores. Another relevant point was investigated by Zhou and co-workers (ZHOU *et al.*, 2011), which evaluated the adsorption capacity regarding dye molecular size and different amounts of sulfonic groups. They observed that the dye with highest number of sulfonic groups was mostly adsorbed on the adsorbent surface, suggesting an adsorption mechanism controlled by electrostatic interaction.

Thus, according to the literature for ChM sample, our results suggest that the molecular size seems to be a dominant effect, since a lower adsorption capacity was observed for RB5, even with three more sulfonic groups than MO dye. Interestingly, for modified samples, N_2 adsorption isotherms showed a higher amount of pores with size around < 3 nm, which may provide better access to RB5 molecules in their internal pores in comparison to ChM NPs. Therefore, this increase in pore size together with similar adsorption capacity for both dyes in ChM GL and ECH samples, suggests a strong influence of the molecular size effect in the adsorption process. However, it is important to notice that electrostatic interactions must gorvern dyes adsorption mechanisms, suggesting a smaller adsorption capacity for modified samples. In general, post-modified chitosan-based materials decrease their adsorption capacity due to the decreasing of accessibility to internal sites or blockade of adsorption sites (KIM *et al.*, 2012). The maximum adsorption capacity of chitosan-based adsorbents for RB5 and MO under similar experimental conditions is shown in Table 9 (Appendix A). The synthesized nanocomposites in this work do not have a high adsorption capacity in comparison to other materials. However, this profile can be due to small percentage of chitosan present in the nanocomposite, as already discussed by TGA analyses.

Figure 21 – Effect of initial concentration in the adsorption capacity of (a) RB5 and (b)MO for ChM, ChM GL and ChM ECH samples.

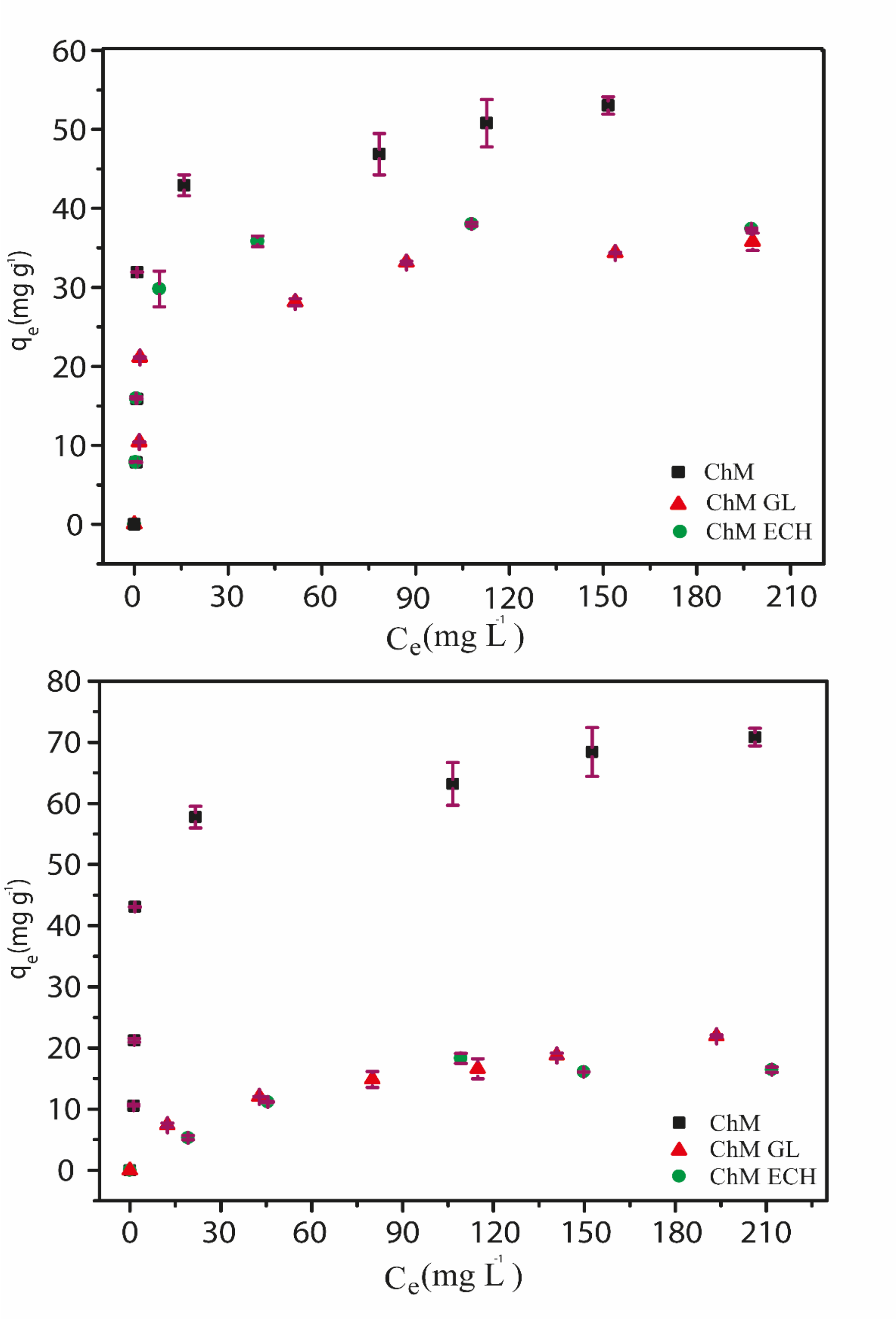

Source: the author

The correlation of isotherms data to each theoretical or empirical equation is essential for a practical and operational planning of the adsorption system. Several mathematical models have been used to describe different adsorption processes, and the establishment of most appropriate correlation for equilibrium curves must be done. Herein, in this work, mathematical models such as Langmuir, Freundlich, Redlich-Peterson and Temkin were applied to better discuss obtained adsorption results. Table 4 summarizes all parameters obtained from the fit applied to unmodified and modified samples with both RB5 and MO dyes. Moreover, Figure 46 and 47 (Appendix A) show all fits applied to experimental data.

Table 4 – Parameters obtained from the fits of Langmuir, Freundlich, Redlich-Peterson and Temkin isotherms for both RB5 and MO dyes.

Dye	**Reactive black 5**				**Methyl orange**			
Langmuir	Adj. R^2	q_m (mg g^{-1})	K_a (L mg^{-1})		Adj. R^2	q_m (mg g^{-1})	K_a (L mg^{-1})	
ChM	**0.913**	**50.004**	**0.820**		**0.903**	**68.004**	**0.402**	
ChM ECH	0.978	36.944	0.932		**0.989**	**20.386**	**0.0229**	
ChM GL	0.923	33.630	0.523		0.964	24.647	0.0231	
Freundlich	Adj. R^2	K_f (L g^{-1})	n		Adj. R^2	K_f (L g^{-1})	n	
ChM	0.873	21.438	5.390		0.861	25.652	5.071	
ChM ECH	0.907	17.346	6.053		0.957	2.248	2.617	
ChM GL	0.938	14.531	5.774		**0.996**	**2.633**	**2.515**	
Redlich-Peterson	Adj. R^2	K_{rp} (L mg^{-1})	A_{rp} (L $mg^{-1})^{\beta}$	β	Adj. R^2	K_{rp} (L mg^{-1})	A_{rp} (L $mg^{-1})^{\beta}$	β
ChM	0.900	47.918	1.167	0.955	0.886	30.964	0.545	0.962

ChM ECH	**0.984**	**40.674**	**1.302**	**0.960**	0.973	0.876	0.154	0.776
ChM GL	0.926	48.866	2.699	0.871	0.986	1.053	0.154	0.768
Temkin	Adj. R^2	K_T (L mg^{-1})	B (J mol^{-1})		Adj. R^2	K_T (L mg^{-1})	B (J mol^{-1})	
ChM	0.899	25.003	6.4895		0.887	10.636	9.3778	
ChM ECH	0.953	35.964	4.6139		0.983	0.194	4.6397	
ChM GL	**0.950**	**25.201**	**4.1678**		0.978	0.299	4.9853	

Source: the author

In general, all applied models showed a value of Adj. R^2 lower than 0.99, except for the sample ChM GL in the MO adsorption. ChM GL obtained a satisfactory Adj. R^2 when adjusted to the Freundlich model, suggesting that the adsorption mechanism of MO should be through multilayers. However, once ChM GL applied as adsorbent of RB5, the Temkin model better described the adsorption mechanism. For ChM ECH, according to all results observed in Table 4, the Langmuir model greatest described the MO adsorption process, whereas for RB5 is the Redlich-Peterson model. Besides, β values suggest that this process is approaching to Langmuir model at low concentration.

Interestingly, for ChM, both MO and RB5 adsorption process obtained low values of Adj. R^2, and comparing applied models, Langmuir greatest described the adsorption processes. Kyzas (KYZAS *et al.*, 2010) investigated the adsorption of dyes on chitosan surface and observed that, at low concentrations of adsorbate, the adsorption process occurred by stronger electrostatic interaction and equilibrium condition is quickly reached. Herein, the fast adsorption may be due to low dye concentration used in the assays, suggesting a monolayer formation, which is in accordance to adjustments of Langmuir model. It is also important to notice that, for both ChM GL and ECH samples, different isotherms were needed to evaluate the adsorption process, whereas for ChM was just applied the Langmuir model for both dyes. This should be assigned to the chemical modification of chitosan molecules occasioned by crosslinking reaction, which also modifies pore volume and surface area of the samples.

Therefore, based on overall results obtained in the adsorption process for both RB5 and MO dyes, both electrostatic and hydrogen bonding interactions can be considered. Herein, in Figure 12 is shown a proposal of the interaction possibilities between dye molecules and ChM sample. For this proposal, we assuming the pH 4 for adsorption systems, which is lower than the pKa of the chitosan (6.5). Indeed, ChM nanocomposites should have a surface rich in protonated amino and hydroxyl groups. Besides, since RB5 and MO have sulfonic groups, under pH 4 a strong ionic interaction must be observed due to chitosan on MNPs surface. Thus, considering that RB5 has low penetration in chitosan network, Figure 12 suggests that the adsorption process occurred by a dye monolayer formation on ChM surface. In addition, for this sample, the Langmuir model was the one that better described the isotherms results.

Figure 22 – Schematic illustration of adsorption possibilities for ChM sample: (a) RB5 and (b) MO.

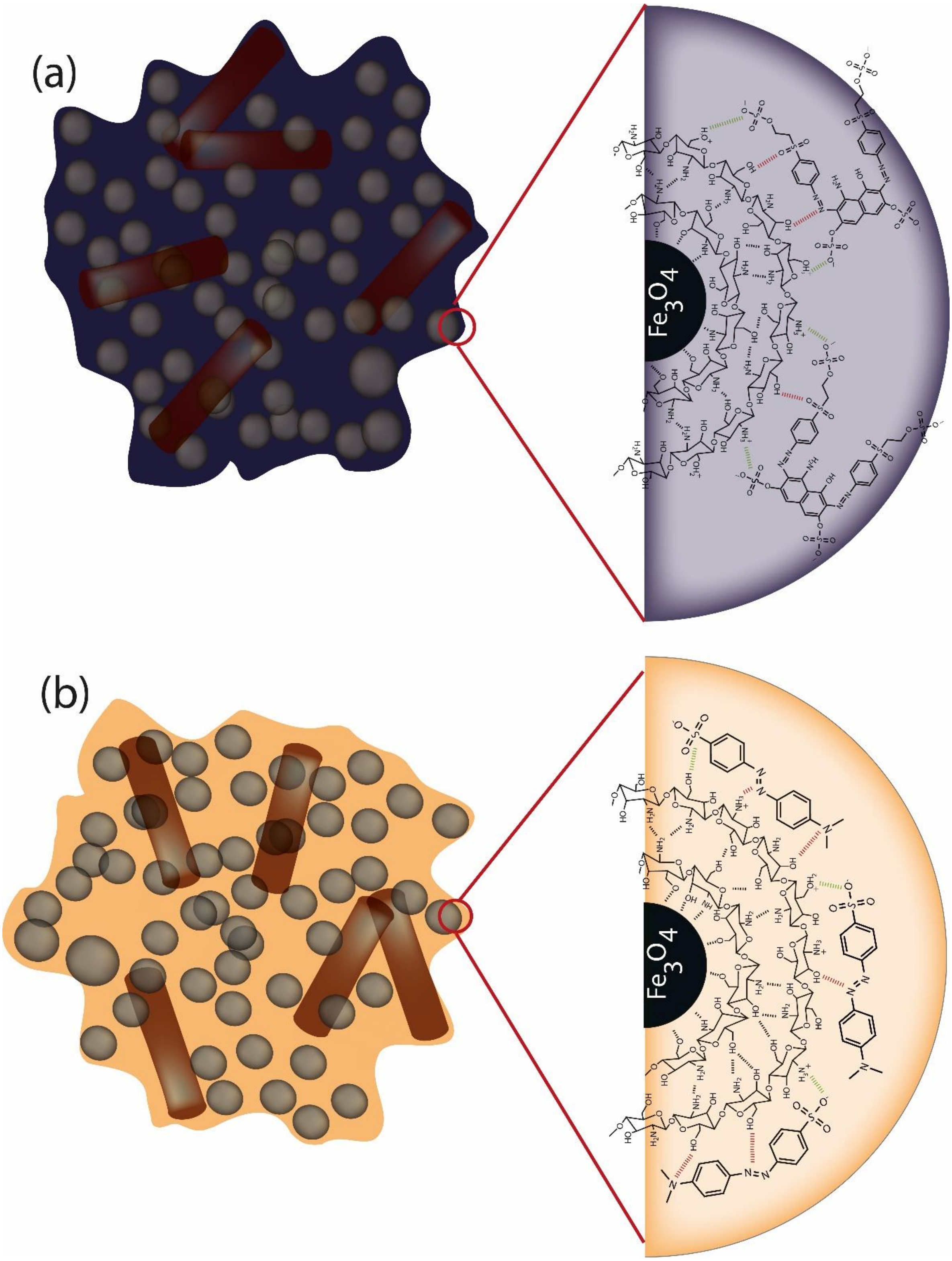

Source: the author

2.4. Conclusions

In summary, magnetic chitosan nanocomposite was successfully synthesized through a well-established ultrafast strategy under US irradiation. All modified and unmodified ChM nanocomposites presented good crystallinity, high M_s ranging from 44 to 57 emu.g^{-1} and high surface area. Besides, the adopted methodology provided MNPs with nanorod and spherical type-morphologies. Regarding adsorption assays, the chosen anionic RB5 and MO dyes were analyzed at different experimental conditions on nanocomposites surface. As expected, the adsorption capacity of both dyes was significantly affected by pH medium, suggesting that electrostatic interactions have great influence in adsorption mechanism. Indeed, kinetic study showed a relevant dependence between molecular size of adsorbates and adsorption process. For instance, adsorption capacity values for unmodified ChM sample were approximately 50 and 70 mg.g^{-1} for RB5 and MO, respectively, i.e. the adsorption process is mainly driven through dye molecular size itself. Considering equilibrium conditions, ChM ECH sample reached the equilibrium faster in comparison to ChM and ChM GL. Herein, according to isotherm models, different profiles of adsorption mechanisms were found. All synthesized nanocomposites seem to be influenced by electrostatic interactions. In this sense, amino-based superparamagnetic materials might present a susceptibility to natural organic matter (NOM), mainly humic acid that can compete by the adsorption sites, decreasing the efficiency of the adsorbents in the removal of azo dyes. However, since textile effluents may show low level of NOM concentration, these nanocomposites show great potential to be applied as adsorption system in textile wastewater.

3. CHAPTER 3 – MAGNETIC FEM (M = Ag, Co, Cu, AND Ni) NANOCRYSTALS AS ELECTROCATALYSTS FOR HYDROGEN EVOLUTION REACTION

3.1. Introduction

Over the past decade, the high demand for nonrenewable fossil fuels in diverse branches of society has occasioned an excessive CO_2 emission in the atmosphere, which provides an environmental imbalance that becomes a cause for global warming (WILLIAMS *et al.*, 2017; BIRHANU *et al.*, 2020; CHEN *et al.*, 2021). However, in 2020, the restriction imposed by governing in many countries due to COVID-19 pandemic had a strong influence on the global energy system, decreasing CO_2 emission and improving air quality in diverse cities (BERMAN & EBISU, 2020; SINGH & CHAUHAN, 2020). According to Christoph Bertram and coauthors, the current situation offers a unique opportunity for the implementation of public politics to the continuous decline of CO_2 emission through investments in new technologies of low-carbon power generation (BERTRAM *et al.*, 2021). In this sense, many resources for clean energy production can be considered such as hydrogen (H_2) (MURTHY *et al.*, 2018), sunlight (YAN *et al.*, 2020), and wind (SADORSKY, 2021). Among these, hydrogen gas (H_2) is one of the most promising due to high energy density production and zero carbon-emission (ZAHRA *et al.*, 2020). Meantime, H_2 commercial production occurs via partial oxidation, pyrolysis, coal gasification and steam reforming, which are not free of fossil fuel influence (ZAHRA *et al.*, 2020; ZHANG, S. *et al.*, 2020). On the other hand, hydrogen fuel can be produced from electrochemical water splitting via hydrogen evolution reaction (HER) (JANA *et al.*, 2020). This method use water as a source for H_2 production and under standard conditions requires an energetic cost of 237.1 kJ mol^{-1}, which corresponding to a theoretical potential of 1.23 eV (HU *et al.*, 2020). To minimize energetic expenditure, electrocatalysts for water splitting are widely studied. In general, outstanding catalytic performance and durability are obtained from the use of noble metal (YOU & SUN, 2018). However, these metals (e.g. Pt and Ru) are scarce on earth and their cost is very elevated, becoming the application on large scale expensive (OLIVEIRA *et al.*, 2021). Thus, the use of catalyst alternative with reduced cost is necessary to overcome this limitation.

Fe, Co, Ni, Cu, and Ag based electrocatalysts have gained great importance due to their low cost and high activity (FREIRE *et al.*, 2016; ZHAO *et al.*, 2018; RODRÍGUEZ-PADRÓN *et al.*, 2020; ZHANG, Z. *et al.*, 2020). However, among these metals, Fe earns the spotlight due to its abundance on earth. Besides, recent reports showed that Fe and its compounds have outstanding efficient HER electrocatalysts under alkaline and acid medium (MA *et al.*, 2016; MOHAMMED-IBRAHIM & SUN, 2019; NIVETHA *et al.*, 2020). Nevertheless, iron-based electrocatalysts are still not competitive against noble-metal electrocatalysts (ZHANG, Z. *et al.*, 2020). This issue can be overcome by the input of the second metal in the monometallic structure to form bimetallic materials. For example, Tang and coauthors showed that Fe substitution of Co in CoFeP becomes the efficiency for HER similar to that seen in Pt-like electrocatalysts (TANG *et al.*, 2016). Indeed, the formation of the system composed of two metals such as bimetallic nanoparticles should enhance the performance of monometallic electrocatalysts in HER.

Bimetallic nanocrystals have unique characteristics that arise from the coupling of physicochemical properties of two different metals (GILROY *et al.*, 2016). These nanomaterials are superior to monometallic nanoparticles since their electronic, physical, and chemical properties are easily modified due to the formation of the different surfaces upon the insertion of a second metal in the structure of the catalyst (RAJEEV *et al.*, 2021). In this regard, since zero-valent iron nanoparticles (nZVI) present excellent electrocatalytic properties for HER, but poor stability (CHEN *et al.*, 2011; OLIVEIRA *et al.*, 2021). Thus, the formation of iron-based bimetallic nanocrystals ($IBBN_C$) should enhance their performance as electrocatalytic. Oliveira and coauthors showed that the formation of FeCo bimetallic alloy has superior mechanical stability and durability than iron monoatomic structure (OLIVEIRA *et al.*, 2021).

$IBBN_C$ can be synthesized by several approaches, such as electrochemical deposition (SUN & ZANGARI, 2020), chemical reduction (AHMAD *et al.*, 2016), polyol (BARBOSA *et al.*, 2019), sputtering process (CABRAL *et al.*, 2019), and mechanical alloying (MOUMENI *et al.*, 2005). However, these techniques often result in wide size distribution, low colloidal stability, and aggregation (GILROY *et al.*, 2016). On the other hand, the oleylamine (OAm) reduction method has been conducted to synthesize monodisperse bimetallic nanocrystals with narrow size distribution (FREIRE *et al.*, 2020). This method provides nanoparticles coated with OAm, which should become the nanoparticles more resistant again oxidation. In addition, the hydrophobic characteristic acquired by nanoparticles can enhance the desorption of hydrogen molecules lead to an efficient water-splitting activity (ASLAM *et al.*, 2020).

Here, the OAm reduction method was chosen to synthesize electrocatalysts of FeM (M = Ag, Co, Cu and Ni) coated with OAm for alkaline HER. The stoichiometric mixture of metals was utilized to produce small and homogeneous bimetallic nanocrystals. However, the use of OAm as a solvent, surfactant and reducing agent has proved to be inefficient to control the shape of the nanoparticles. Furthermore, a detailed study of both structure and magnetic properties was carried out, confirming the formation of $IBBN_C$, which were applied to electrochemical $H_{2(g)}$ production by splitting water. All samples presented different activity for alkaline HER due to distinct electronic interaction and synergistic effect between the Fe and M (M= Ag, Co, Cu, or Ni) metals in the bimetallic nanocrystals. Indeed, the small overpotentials at a current density of 10 mA cm^{-2} and good stability showed that these $IBBN_C$ have excellent electrocatalytic activity.

3.2. Experimental procedure

3.2.1. Reagents

Iron (III) acetylacetonate ($Fe(C_5H_7O_2)_3$, 97%) cobalt (II) acetylacetonate ($Co(C_5H_7O_2)_2$, 97%), Nickel (II) acetylacetonate ($Ni(C_5H_7O_2)_2$, 95%), Oleylamine ($C_{18}H_{37}N_2$, 70%), Copper (II) acetate ($Cu(CO_2CH_3)_2$, 98%), Silver nitrate ($AgNO_3$, ≥ 99.0%) and Nafion perfluorinated resin solution (10% wt) were purchased from Sigma-Aldrich. Ethanol (C_2H_6O, 99.9%) and hexane (C_6H_{12}, 98.7%) were obtained from J. T. Baker Chemical Company. All reagents are analytical grade and were used as received.

3.2.2. Synthesis of FeM bimetallic nanoparticles

Nanocrystals were synthesized by the OAm reduction method (YU *et al.*, 2014), where 0.25 mmol of iron (III) acetylacetonate, cobalt (II) acetylacetonate, and 10 mL of OAm were mixed at room temperature and under N_2 flow. After the formation of a homogeneous solution, the system was heated at 100 °C for 15 min. Then, the solution was heated up to 300 °C and kept like that for 1h. Finally, the dispersion was cooled down and the product was isolated by magnetic separation using a NdFeB magnet and washed many times with a mixture of hexane/ethanol solvents and dispersed in hexane. The synthesis of the other $IBBN_C$ was performed in the same way. However, for FeNi, FeCu, and FeAg samples the precursors were Nickel (II) acetylacetonate, Copper (II) acetate, and silver nitrate, respectively.

3.2.3. Material Characterization

The crystalline structure of the $IBBN_C$ was investigated using an X-ray powder diffraction (XRD) in a Bruker D2 mode X-ray diffractometer with cobalt $K_{\alpha 1}$ radiation (λ = 1.78890100 Å), operating in the range of 10° to 100°, with a rate of 0.02° min^{-1}. The Shimadzu IRTracer-100 infrared spectrometer (China) in transmittance mode in the range 4000 – 400 cm^{-}

^{1} range was used to carry out the FTIR analysis. For this purpose, the samples were dried, grounded, and pressed in a KBr pellet. High-resolution transmission electron microscopy (HRTEM) was performed on a HITACHI HT7700, operating at an accelerating voltage of 120 kV. Previously, the samples were dispersed in hexane and one drop was placed on a 300-mesh carbon-coated copper grid and dried under room conditions. Mössbauer spectroscopy was recorded at room temperature with a FAST (ConTec) Mössbauer system spectrometer using transmission geometry and a ^{57}Co radiative source. Magnetic properties were investigated using a Vibrating Sample Magnetometer (VSM) Mini 5 Tesla, from Cryogenic Ltd.

3.2.4. Electrochemical measurements

The electrochemical studies were carried out in a potentiostat/galvanostat (AUTOLAB PGSTAT30, Metrohm-Eco Chemie controlled by the NOVA software version 2.11) with a conventional cell of three electrodes, in which a platinum plate (1 cm^2) was utilized as a counter electrode, and a reference electrode was a Hg|HgO filling with 1.0 mol L^{-1} KOH solution. The glassy carbon electrode (3 mm in diameter) was cleaned and polished to remove all impurities, and it served as support to prepare the working electrode. The working electrode consisted of glassy carbon surface modified by the catalyst films which were prepared as follow: 5 mg catalyst, 50 μL Nafion of 10 wt % solution, 950 μL ethanol and 1 mg graphite powder were mixed and sonicated for 30 min, in order to form a good dispersion. Onto the surface of glassy carbon, 5 μL of catalyst ink was drip, and it was left to air dry, thereby suggesting 0.353 mg cm^{-2} loading. All electrochemical measurements were carried out in 1 mol L^{-1} KOH at 298.15 K. Linear scanning voltammetry (LSV) was recorded at a scan rate of 1mV s^{-1} to determine the kinetic parameters of the electrocatalysts. Furthermore, all potentials measured in this work were normalized to a reversible hydrogen electrode (RHE) using the equation $E_{vs.RHE} = E_{vs.\ Hg|HgO} + 0.095 + 0.059pH$. Finally, the electrochemical stability of all electrocatalysts for HER was evaluated in a long-term experiment applying a current density of 10 mA cm^{-2} for 8h.

3.3. Results and Discussion

3.3.1. Synthesis of IBBN$_c$

Figure 3.1 shows an easy syntheses protocol and structure for FeM bimetallic nanocrystals. It is important to note that in this method oleylamine acts as a solvent, surfactant, and reduction agent and have been shown that this route can be rapidly adapted to reach gram-scale quantities (ZHANG *et al.*, 2005; SATO *et al.*, 2011). In the literature, the formation of bimetallic nanocrystals by thermal decomposition should occur by different mechanisms depending on the temperature used to decompose the metal-organic precursors. In general, when the precursors have similar decomposition temperatures, the growth and nucleation of bimetallic nanocrystals should occur simultaneously to the formation of zero-valent metal atoms. In contrast, when they have different decomposition temperatures the formation should occur by heterogeneous nucleation (GILROY *et al.*, 2016). Although the metal-organic precursors used in this work have similar decomposition temperatures, except $AgNO_3$, the formation process of bimetallic nanocrystals should not occur due to simultaneous thermal decomposition of $Fe(Acac)_3$ and the second metal precursors. Ling Zhang and coauthor have shown that alone OAm does not produce iron zero-valent nanoparticles by $Fe(Acac)_3$ thermal decomposition (ZHANG *et al.*, 2006). However, Co, Ni, and Ag nanoparticles have been produced by this method (MOURDIKOUDIS & LIZ-MARZÁN, 2013). Thus, we believe that initially Co, Ni, or Ag monometallic nanoparticles are produced in the reactional medium and should act as catalysts in the iron reduction provide active sites for heterogeneous nucleation. In general, this process of synthesis provides a core-shell structure, however high reaction temperature should favor the interdiffusion process, resulting in the alloys or intermetallic nanoparticles (SON *et al.*, 2004; GILROY *et al.*, 2016).

Figure 23 – Scheme of the FeM nanocrystals synthesis by the OAm reduction method.

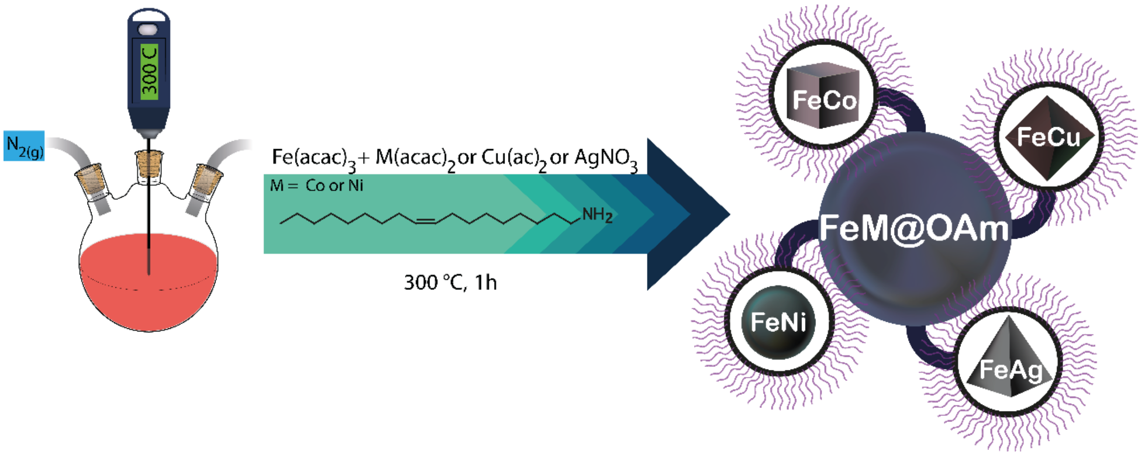

Source: the author

3.3.2. Structure and morphology characterization

In order to confirm the crystalline structure of the synthesized FeM nanocrystals, XRD patterns were obtained and can be seen in Figure 3.2. For FeAg, diffraction peaks can be assigned to the fcc phase (JCPDS 65-8448). The Bragg reflections were found to shift to lower 2θ angles, which suggests the formation of AgFe alloy structures, rich in Ag (JIN, C. *et al.*, 2018; SARHAN *et al.*, 2019). For the samples FeNi, FeCo, and FeCu, the peaks confirm the targeted nanostructures, since these diffraction patterns match with those in the standard card of fcc FeNi (JCPDS 12-0736), bcc FeCo (JCPDS 65-4131), and fcc $FeCu_4$ (JCPDS 65-7002). The additional peaks for FeCu samples were attributed to copper ferrite (JCPDS 77-0010). Its presence suggests that both the iron and copper metals have been oxidized, forming the spinel phase. Once the copper ferrite is not obtained in low-temperature conditions (MASUNGA *et al.*, 2019), it is plausible to infer the influence of substances from the degradation OAm process.

Figure 24 – XRD analysis of the samples AgFe, FeNi, FeCo, and FeCu.

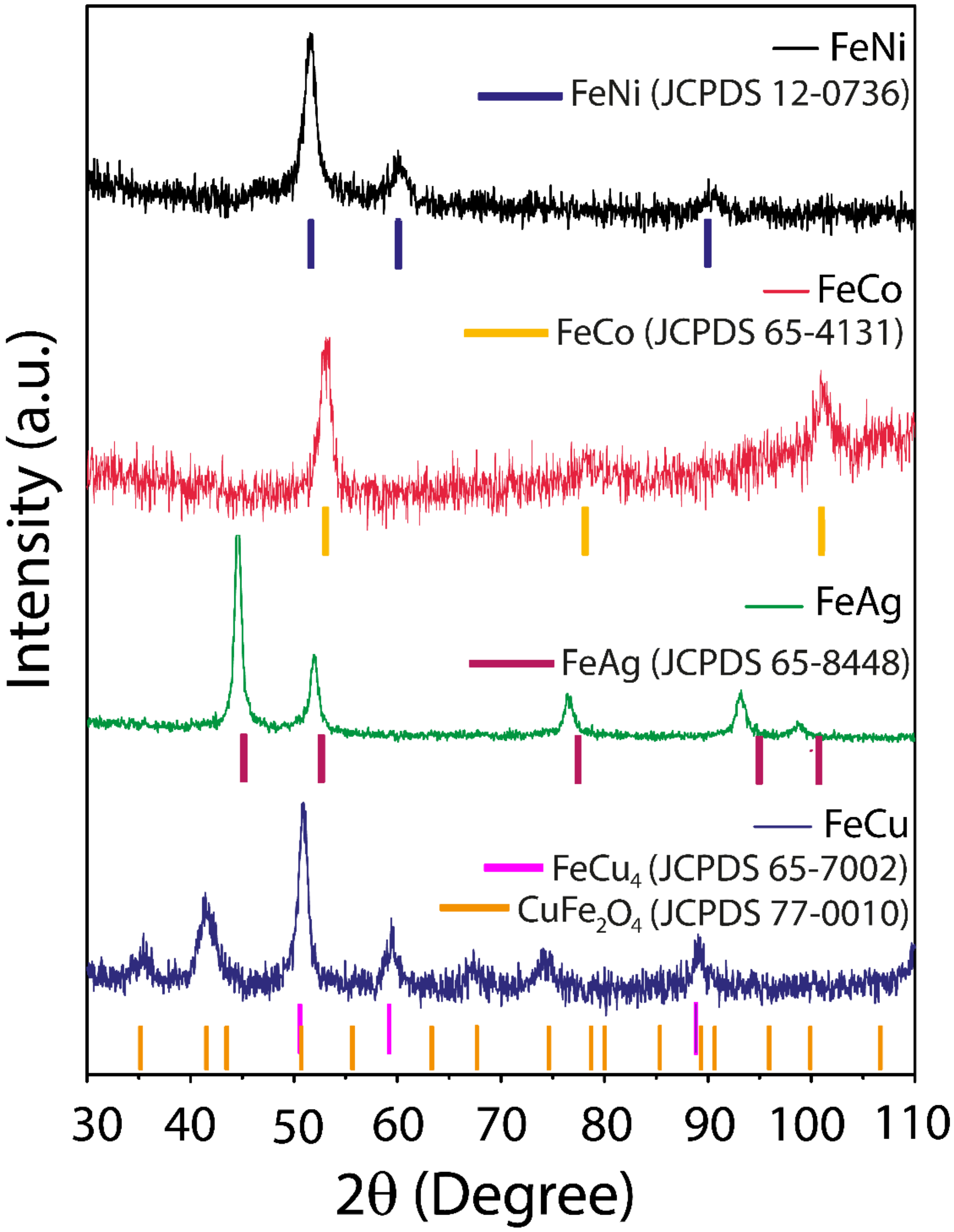

Source: the author

To confirm the presence of OAm on the $IBBN_C$ surface, FT-IR spectra were acquired, and the results are shown in Figure 3.3. For all the samples, it was observed characteristic vibrational modes of alkyl chains from OAm (2920 and 2848 cm^{-1}) . They are assigned to the methylene asymmetric and symmetric C – H stretching, while the band at 1627 cm^{-1} can be assigned to C = C stretch mode, and the band at 1456 cm^{-1} corresponds to C – H bending mode (MOURDIKOUDIS & LIZ-MARZÁN, 2013). Moreover, it was also found signals related to the amine group: broadband at 3440 cm^{-1} due to N – H stretching of the primary amine, a mode at 1554 cm^{-1} due to $–NH_2$ scissoring, and the mode around 1382 cm^{-1} attributed to C – N stretching (CHEN *et al.*, 2007; ZHANG *et al.*, 2012). Further, it was observed broadband around 580 cm^{-1}, corresponding to Fe – O stretching and suggesting surface passivation through the formation of iron oxide (NETO *et al.*, 2017; NETO *et al.*, 2021). Indeed, it is reasonable to consider that $IBBN_C$ were capped by OAm (FeM@OAm), but it is important to mention that all samples have poor colloidal stability in an organic medium.

Figure 25 – FTIR analysis of the samples AgFe, FeNi, FeCo, and FeCu.

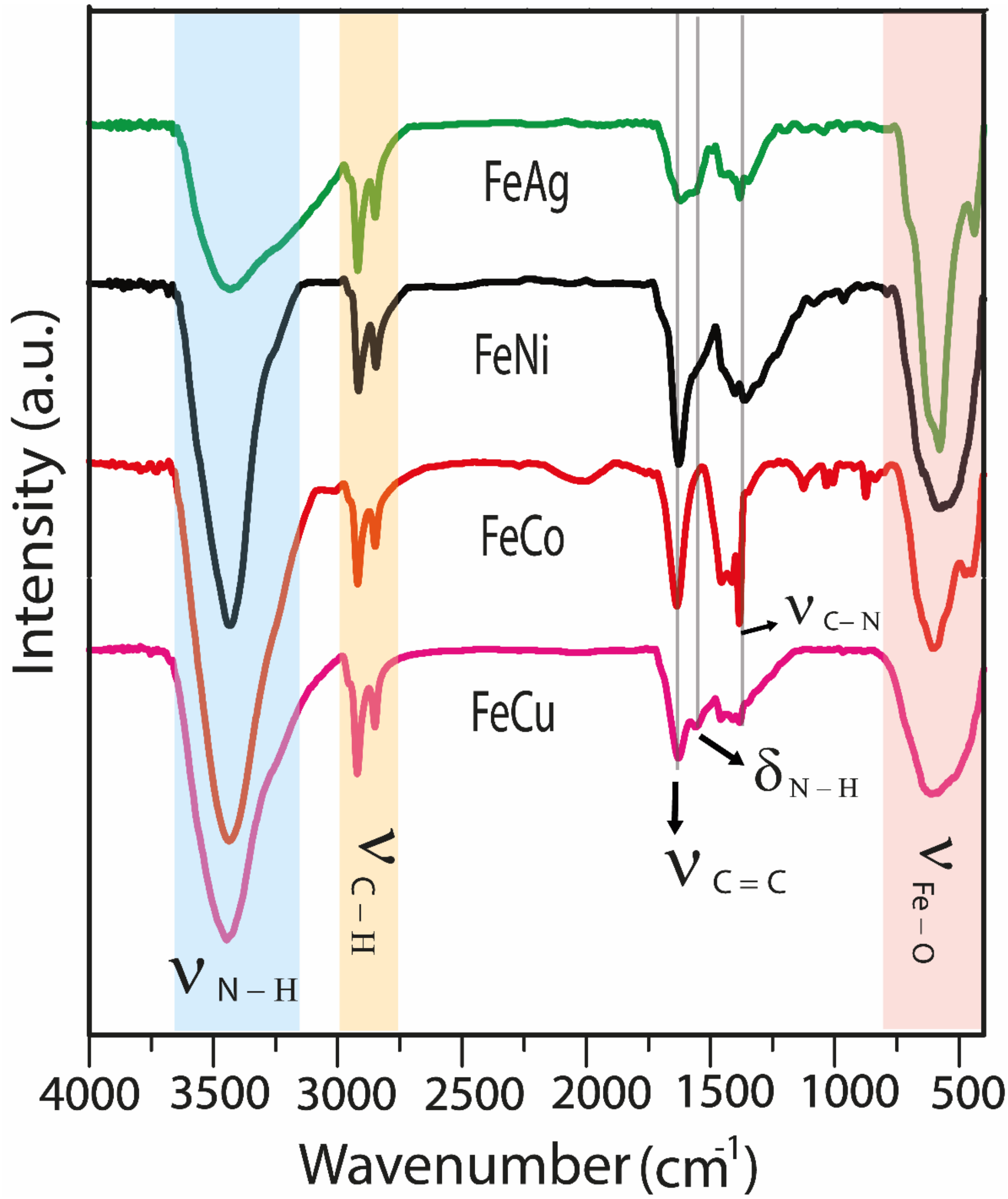

Source: the author

TEM image was carried out to analyze the morphology and size distribution of the synthesized bimetallic nanocrystals (Fig. 3.4). For FeNi (Fig. 3.4 a and b) and FeCo (Fig. 3.4 d and e), the micrographs revealed these samples have more than one morphology. Nanoparticles with spherical or irregular-shaped morphologies were observed for FeNi, while FeCo exhibited nanoparticles with cubic, rod, and spherical shapes. Further, the inset in Figure 3.4 d shows a cubic nanoparticle of FeCo with a shell thickness of 1.8 nm, which can be assigned to the formation of iron oxide on the surface of the nanoparticles. The histograms are shown in Figure 3.4 c and 3.4 f reveal that both samples have a narrow size distribution with an average size of 21.7 $\pm$ 5.1 and 15.1$\pm$ 2.3 nm, for FeNi and FeCo, respectively. For the FeAg sample (Fig. 3.4

g and h), TEM images showed a diversified morphology with the formation of triangular plates, spherical and octahedral type structures. Additionally, this nanocrystal has a bimodal size distribution with average sizes of 6.5 ± 1.2 and 18.8 ± 2.5 nm (Figure 3.4 i). The inset of Fig. 3.4 h shows the lattice fringes of 2.06 Å, corresponding to the (*200*) planes of the AgFe phase observed in XRD. Indeed, this result suggests the presence of AgFe nanocrystals with composition, rate of nucleation, and growth difference, which can occur due to the low miscibility between Fe and Ag (FERRANDO *et al.*, 2008; SANTHI *et al.*, 2014). FeCu sample shows a bimodal size distribution, wherein the average sizes are 6.4 ± 1.0 and 20.8 ± 4.1 nm (Figure 3.4 l). Besides, the larger nanocrystals have a shell thickness of 2.1 nm (Figure 3.4 k). The bimodal size distribution for FeAg and FeCu systems can be assigned to the difference between the reduction potential of these metals, which has a higher rate of reduction and nucleation for Ag and Cu compared to Fe (GILROY *et al.*, 2016).

Figure 26 – TEM image of FeNi (a and b), FeCo (d and e) FeAg (g and h), and FeCu (j and k). Figures c, f, i, and l are the histograms for FeNi, FeCo, FeAg, and FeCu, respectively.

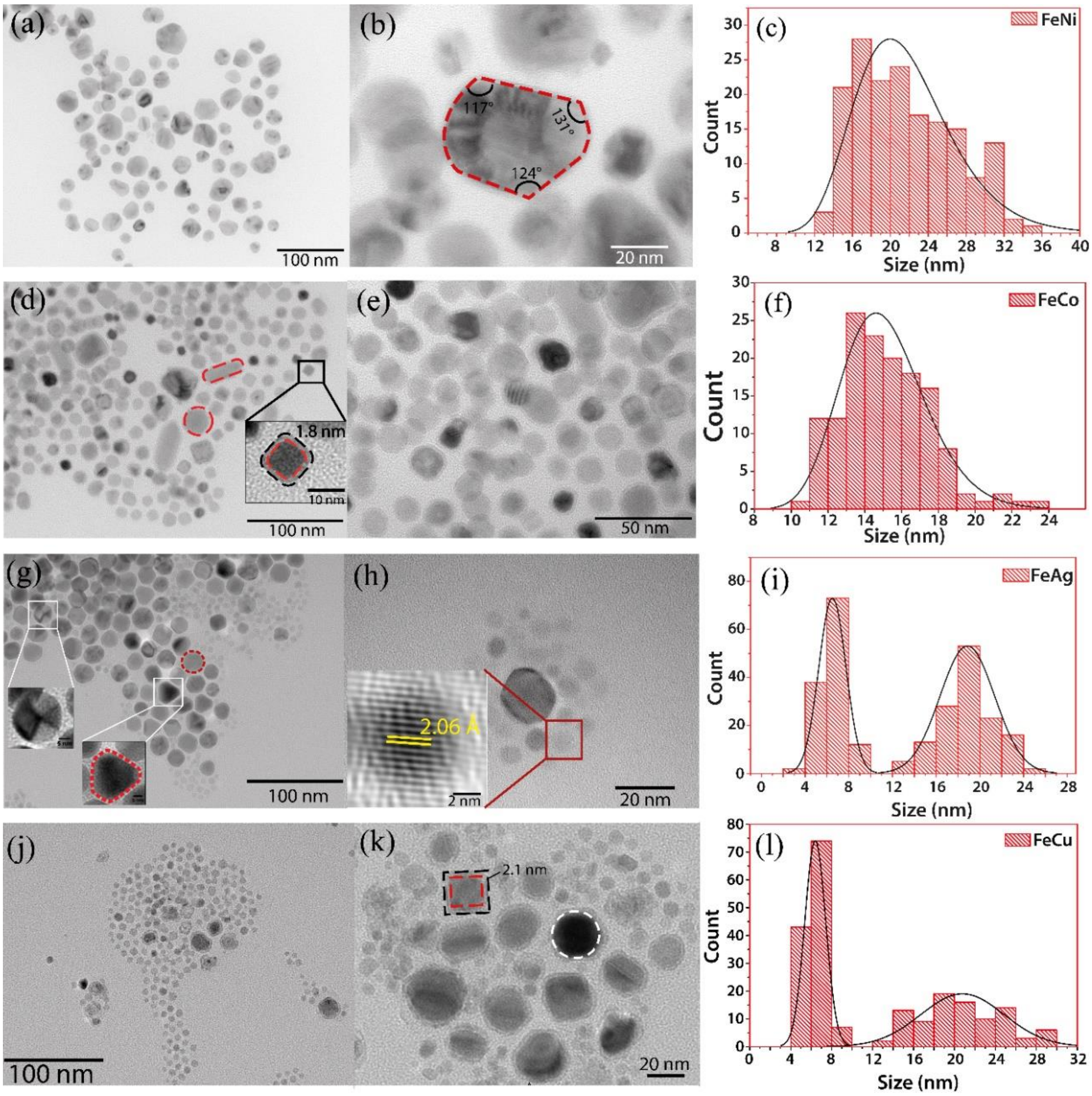

Source: the author

3.3.3. *Magnetic measurements*

Figures 3.5 a and 3.5 b show the magnetization versus applied magnetic field curves at room temperature (300 K) and 5 K for the synthesized nanocrystals. The saturation magnetization (Ms) at room temperature for FeCo, FeNi, FeCu, and FeAg samples were found to be equal to 80.66, 65.09, 17.86, and 6.96 emu g^{-1}, respectively. Furthermore, the nanocrystals exhibit ferrimagnetic behavior with a hysteresis loop not reversible and a coercive field (Hc) of 98, 168, 36.1, and 65.1 Oe for FeCo, FeNi, FeCu, and FeAg, respectively. These results suggest that all samples have soft magnetic characteristics since the curves are narrow, with low values of the coercivity and high values of the Ms. On the other hand, the n $IBBN_C$ exhibit a large hysteresis at low temperature (5 K), with Hc values (1325.6, 429.2, 517.1, and 446.8 Oe for FeCo, FeNi, FeCu, and FeAg, respectively) higher than those found at 300 K, deducing that there is an increase of nanoparticle blocking in this temperature (SHARIFI DEHSARI & ASADI, 2018). In addition, it is important to note that Hc for FeCo at 5 K is larger than room temperature by about 1227 Oe, suggesting the presence of a high anisotropy phase, such as $CoFe_2O_4$ (MOURDIKOUDIS *et al.*, 2007; RAJESH *et al.*, 2019). On the other hand, the increase in FeCu is not significant and can be attributed to the presence of $CuFe_2O_4$ (MONDAL *et al.*, 2019).

Figure 27 – (a) and (b) Magnetization versus applied magnetic field curves at room temperature (300 K) and 5 K for the synthesized $IBBN_C$, respectively.

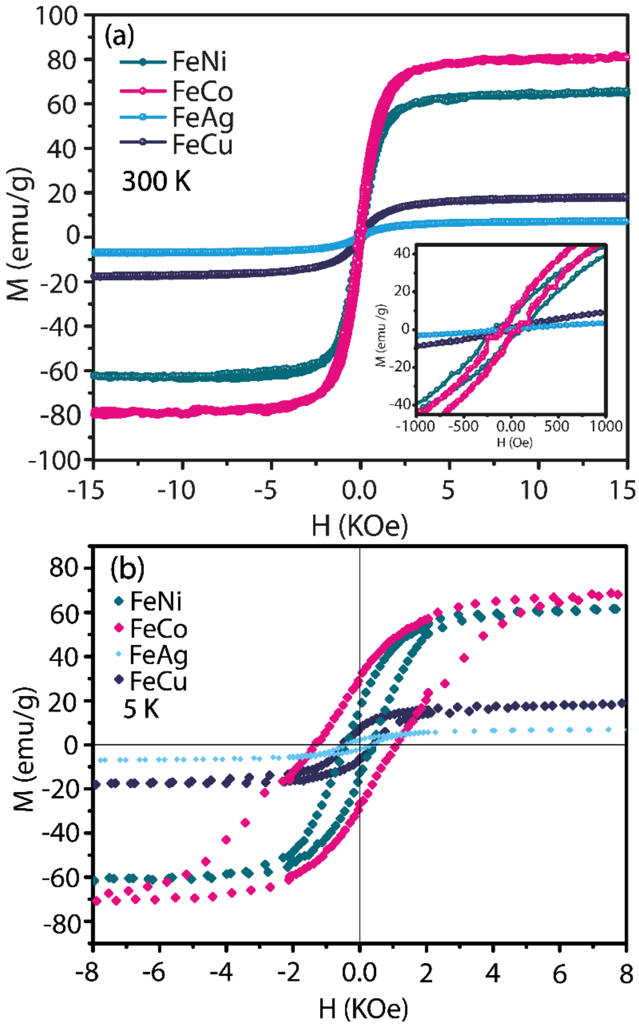

Source: the author

Figure 3.6 a and 3.6 b present the Mössbauer spectra for FeCo, FeNi, FeCu, and FeAg samples and the fit by hyperfine fields (B_{hf}) distributions, respectively. For FeCo, a sextet distribution was identified with a maximum at approximately 34.6 T, which suggests the presence of Co atoms in the bcc Fe structure (JOHNSON *et al.*, 1963; CASULA *et al.*, 2005). Furthermore, the obtained values of the isomer shift (δ) = 0.03 mm s^{-1} and quadrupole splitting (Δ) = 0.01 mm s^{-1} (see Table 3.1) indicate the formation of the FeCo phase with bcc structure, which is consistent with the analysis of XRD. However, it is also observed the presence of a doublet with δ of 0.30 mm s^{-1} and Δ of 0.91 mm s^{-1}, which can be assigned to ferric ions from the Fe-oxide surface shell of FeCo nanoparticles (BABIĆ-STOJIĆ *et al.*, 2013; RAJESH *et al.*, 2019). Finally, the third contribution of the spectrum is a singlet (violet line) with a high-line width value that can be associated with a superparamagnetic incomplete contribution (BABIĆ-STOJIĆ *et al.*, 2013). The reduced size observed in TEM images and the large coercivity at 5 K obtained from VSM measurements agree with this result. The Mössbauer spectrum for FeNi exhibits two contributions. The first is a B_{hf} distribution centered on 29.7 T that corresponds to the formation of fcc γ-(Fe, Ni) phase atomically disordered (RODRÍGUEZ *et al.*, 2019), which according to Johnson et al., starts to form at Ni concentrations above 28% (JOHNSON *et al.*, 1963). Besides, it was observed a doublet with δ of 0.37 mm s^{-1}, which can be attributed to the superparamagnetic behavior due to the small size of the particles as well as the presence of Fe^{3+} from the Fe-oxide layer (MANCIER *et al.*, 2004). Also, it is interesting to note the dominance of the field distribution in samples FeCo and FeNi with 56.3, and 90.5 % relative spectral area (*A*). Indicating that Fe atoms are found mainly in ferrimagnetic sites. Therefore, the Mössbauer results for the FeCo and FeNi samples are following the results from the magnetization measurements (Fig. 3.5 a and b), wherein both samples showed low magnetic hysteresis at room temperature that can be related to the identified superparamagnetic behavior.

Figure 28 – (a) and (b) are room temperature Mössbauer spectroscopy and magnetic hyperfine field distribution, for samples FeAg, FeCo, FeCu, and FeNi, respectively.

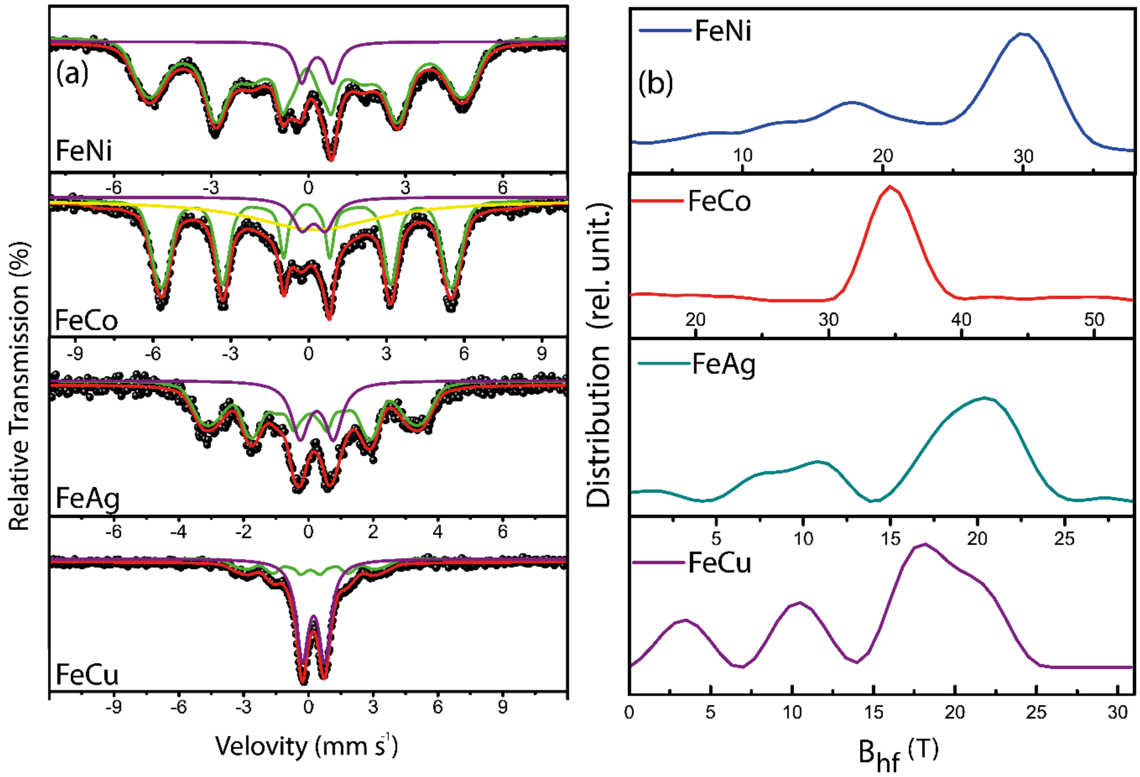

Source: the author

The effect of diamagnetic atoms, such as Cu and Ag on the FeM nanocrystals, was also investigated by Mössbauer spectroscopy. Figure 3.6 a shows the spectrum for FeCu samples, revealing two contributions: a doublet that can be assigned to the fcc $FeCu_{rich}$ phase; and the superparamagnetic phase of $CuFe_2O_4$, with Fe^{3+} ions in tetrahedral sites (CRESPO *et al.*, 1998; CHOI *et al.*, 2008). The sextet fitting by distribution between 0 and 25 T suggests that Fe atoms are fully incorporated into the Cu lattice, formatting a second fcc FeCu nanocrystal richer in Fe (CRESPO *et al.*, 1998). Indeed, the Mössbauer spectrum for FeCu are in accordance with XRD and VSM analysis. Regarding FeAg, the distribution of B_{hf} centered on 20 T is characteristic of the Fe-rich bcc structure, in which the presence of Ag in the structure of α-Fe decreases the B_{hf} due to the diamagnetic characteristic of the silver (RIXECKER, 2002). However, the doublet with high Δ values indicates the presence of an electric field gradient (EFG), which can be due to the presence of Ag atoms with greater electron density around Fe atoms (RIXECKER, 2002). Thus, the doublet suggests the formation of a solid FeAg fcc structure rich in Ag (SPIZZO *et al.*, 2004). The low miscibility between Ag and Fe suggests that the fcc structure arises from Fe diffusion in Ag nanoparticles, while the bcc structure can be derived from Ag diffusion in Fe nanoparticles (FERRANDO *et al.*, 2008; SANTHI *et al.*, 2014; GILROY *et al.*, 2016). To the best of our knowledge, this is the first report wherein a FeAg solid solution is produced by co-reduction method. Therefore, since all characterization showed the obtention of $IBBN_C$, these samples were applied in the electrochemical production of $H_{2(g)}$ by water splitting.

Table 5 – Mössbauer parameters of the FeM nanocrystals.

		Mössbauer parameters			
Sample	**Fiting**	***B_{hf} / T***	***δ / mm/s***	***Δ / mm/s***	***A / %***
FeCu	Distribution (Green)	17.4	0.02	0.05	29.5
	Dublet (Blue)	__	0.33	0.82	70.5
FeCo	Distribution (Green)	34.6	0.03	0.01	56.3
	Doublet (Blue)		0.30	0.91	9.7
	Singlet (Orange)		0.37		34.0
FeNi	Distribution (Green)	29.7	0.05	0.03	90.5
	Doublet (Blue)		0.37	-0.95	9.5
FeAg	Distribution (Green)	20.0	0.12	0.06	73.8
	Doublet (Blue)		0.36	1.02	26.1

Source: the author

3.3.4. Electrochemical measurements

The obtained linear scanning voltammetric curves obtained in the potential range of the HER are displayed in Figure 3.7 a. It can be noted that the FeCu electrocatalyst has the best HER activity since achieved a current density of 10 mA cm^{-2} at a low overpotential of 494 mV. In contrast, the FeAg, FeCo, and FeNi electrocatalysts show a lower HER activity with an overpotential of 533, 584, and 601 mV, respectively, to reach the current density of 10 mA cm^{-2}. From the overpotential, it was possible to see that the presence of the noble metal increases the electrocatalysts performance, which can be assigned to the increase of the electric conductivity. Sebastian Kunze and coauthors also available the electrochemical activity of FeAg and FeCu samples toward CO_2 electroreduction and showed that FeCu samples with a Fe-rich surface have high selectivity to $H_{2(g)}$ due to favor hydrogen evolution reaction (KUNZE *et al.*, 2020). Thus, the best electrocatalytic performance presented by the FeCu electrocatalyst also should be assigned to formation of FeCu nanocrystals with a more Fe-rich surface, which can enhance the free energy of hydrogen adsorption leading to an increase in the electrochemical activity toward to HER (TANG *et al.*, 2016).

Figure 29 – Electrochemical test results. (a) HER polarization curves of all prepared electrocatalyst, (b) the Tafel plots, (c) Stability test in continuous operation for 8 h at 10 mA cm^{-2}.

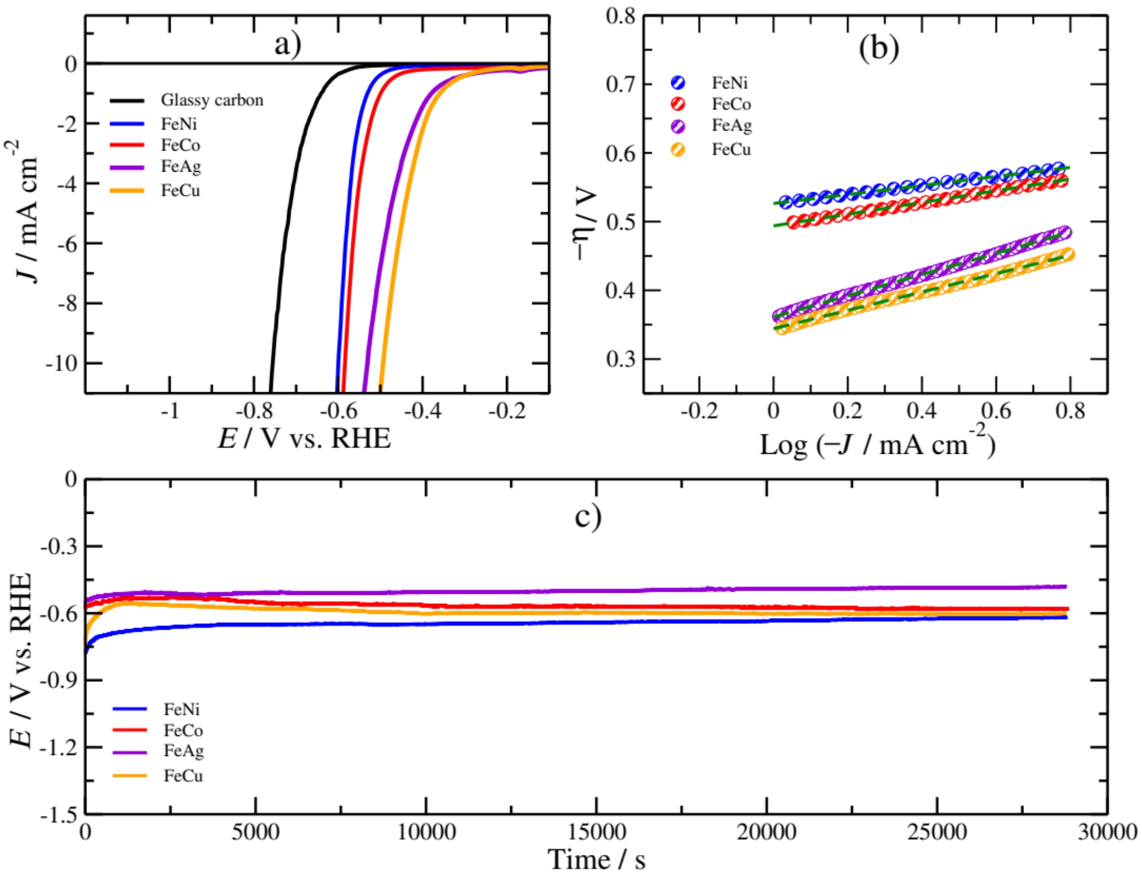

Source: the author

Compared to other non-noble electrocatalysts supported by Nafion (Table 3.2), the larger observed overpotential may be attributed to the presence of OAm on $IBBN_C$ surface. Generally, surface ligands can inhibit catalysis by competitive coordination or inhibiting access to active surface sites. Mingyang G. and coauthors showed that oleylamine capped gold nanoparticles increase the overpotential for HER due to the ligand to coordinate with actives sites on Au nanoparticles surfaces, in the selective electrocatalytic reduction of CO_2 to CO (GAO *et al.*, 2020). Indeed, the presence of OAm may inhibit HER, but it improves the selectivity to CO production, showing that through decrease HER activity, it may be an additive to improve the selectivity of the electrochemical reaction. David Ung and Brandi M. Cossairt showed that the presence of small amounts of OAm on CoP surface does not cause any significant effect of inhibiting the substrate to the electrocatalytic sites (UNG & COSSAIRT, 2019). Thus, since the $IBBN_C$ synthesized in this work have poor colloidal stability, suggesting the low OAm loading, we can speculate that the main ligand effect is related to the poisoning of the electrocatalysts by coordination of the active sites.

The electrocatalytic process for $H_{2(g)}$ production from the water is a two-electron transfer reaction, which mechanism is dependent on the pH (ZHANG, W. *et al.*, 2020). In an alkaline medium, the multi-step elementary reaction can follow by two ways, the Volmer–Heyrovsky or the Volmer–Tafel mechanism, which can be described using the following expressions (SUN *et al.*, 2021):

Volmer step: $\mathbf{H_2O + e^- + \blacksquare \rightarrow H_{ads} + OH^-}$ (1)

Heyrovsky step: $\mathbf{H_2O + H_{ads} + e^- \rightarrow H_{2(g)} + OH^- + \blacksquare}$ (2)

Tafel step: $\mathbf{H_{ads} + H_{ads} \rightarrow H_{2(g)} + 2\ \blacksquare}$ (3)

where, ■ represent an empty active site, and H_{ads} denotes a hydrogen atom adsorbed on the active site. Each one of these steps has a strong significance for HER and the Tafel plots can be used to indicate which reactions have the most control over the kinetics of the reaction.

The Tafel curves were obtained from the linear fits of the polarization curves using the equation $\eta = a + b\text{Log}(J)$ as shown in Fig 3.7 b. From the Tafel slopes, it was possible to evaluate the hydrogen reduction kinetics. For alkaline solutions, the HER kinetics is described by three steps: Tafel, Heyrovsky, and Volmer, the corresponding slope values are 30, 40, and 120 mV dec^{-1} (WANG *et al.*, 2017), respectively. For FeNi and FeCo electrocatalysts, the corresponding slopes are 65.6 and 85.1 mV dec^{-1}, suggesting that HER is mainly controlled by the Volmer-Heyrovsky mechanism with the determining step being the Heyrovsky reaction. However, the slopes for FeCu and FeAg are 133.5 and 145.2 mV dec^{-1}, which suggests that reaction Volmer is the determining step. The results obtained from the stability tests are shown in Fig. 3.7 c. During continuous operation for 8 h at 10 mA cm^{-2}, all electrocatalysts showed stability with a low potential variation. Therefore, those results demonstrated that FeM (M = Cu, Ag, Co, and Ni) electrocatalysts have promising electrocatalytic performance toward HER in alkaline media due to their excellent physical stability and abundance of active sites for HER.

Table 6 – Electrochemical parameters for the HER in 1 mol L−1 KOH at 298.15 K on FeAg, FeCo, FeCu, and FeNi obtained, and comparison with several catalysts in alkaline solution.

Electrocatalysts	b / mV dec^{-1}	η in 10 mA cm^{-2}	Mass loading mg cm^{-2}	Reference
FeCu	133.5	494	0.353	This work
FeAg	154.2	533	0.353	This work
FeCo	85.1	584	0.353	This work
FeNi	65.5	601	0.353	This work
Ag@Zn/NCF-600	125	417	0.253	(DENG *et al.*, 2021)
Ag@ZnCo/NCF-800	153	303	0.253	(DENG *et al.*, 2021)
CoP	93	410	0.255	(YANG *et al.*, 2019)
Cu-foam	77	425	1	(SHANG *et al.*, 2020)
Fe/NC	585	531	0.212	(YU *et al.*, 2019)
Fe-600C@BMC	222	550	0.566	(AHSAN *et al.*, 2020)
Ni3Fe@BC-600	140	500	0.353	(ADEGBEMIGA *et al.*, 2020)

Source: the author

3.4. Conclusion

In summary, we have successfully synthesized the FeM (M = Ag, Co, Cu, and Ni) nanocrystals by oleylamine reduction metal salt. Bimetallic nanocrystals formation was confirmed by XRD, TEM, and Mössbauer analyses, with all nanoparticles coated by OAm (FeM@OAm) as revealed by FTIR measurements. Moreover, the materials exhibited a ferrimagnetic behavior with high saturation magnetization and low coercive field. In view of, the importance of $H_{2(g)}$ production by green method, the investigation kinetic for HER showed that the electrocatalysts contained noble metal has the mechanism controlled mainly by Volmer step, while the electrocatalysts formed by FeNi and FeCo have as determined step the Heyrovsky reaction. Although the Tafel plots suggest different mechanism, all samples showed high electrocatalysts activity and good stability toward HER under alkaline conditions. Indeed, considering all aspects presented in this work, such as the variated morphology, formation of solid solution, high stability and low overpotential observed in the synthesized $IBBN_C$, using the simplified method, are sustainable for electrocatalysts HER.

4. CHAPTER 4 – BIOMEDICAL APPLICATION OF GRAPHITIC CARBON NITRIDES: TISSUE DEPOSITION IN VIVO, INDUCTION OF REACTIVE OXYGEN SPECIES (ROS) AND CELL VIABILITY IN TUMOR CELLS

4.1. Introduction

At present, cancer is an of the primary cause of human death in the world. According to estimates from the GLOBOCAN 2020 produced by the International Agency for Research on Cancer, almost 19.9 million cancer deaths occurred in 2020. In addition, according to the World Health Organization (WHO), in 2019, cancer ranged from first to fourth place as the leading cause of death before the age of 70 years in 135 of 183 countries (SUNG *et al.*, 2021). In order to minimize its impact, conventional therapies such as chemotherapy, immunotherapy, radiotherapy, and surgery have been accepted as principal clinical strategies for cancer treatment. Among these therapies, chemotherapy has demonstrated outstanding potential for metastatic-cancers treatment. However, it has limitations like nonspecific delivery, cytotoxicity to normal cells, poor water solubility, and reappearance rate of cancer tumor-cells (DONG *et al.*, 2018; SHAMIM *et al.*, 2021). Therefore, new chemotherapies and new treatment strategies that provide adequate reduction of undesired side effects and more specific cancer treatment are still needed.

In this sense, nanomaterials can be excellent candidates for providing more specific cancer treatments with reduced side effects due to their particular interactions with biological systems and advantages such as easy penetration into the membrane, more solubility in water, and long circulation periods (RABINOW, 2004). Besides, owing to their particular properties, nanoparticles provide a great opportunity to develop clinical strategies aimed at diagnostic and treatment in one step (XU *et al.*, 2019). In this scenario, two-dimensional (2D) materials have attracted great interest since they present several unique characteristics compared to their counterparts with other dimensionalities, including maximum mechanical flexibility, specific electronic, optical, and magnetic properties, and high specific surface area (CAO *et al.*, 2018). These characteristic makes they promising candidates for the development of electronic biomedical devices, efficient bioimage probes or a favourable tool for drug delivery (WANG & YANG, 2019). Nevertheless, the biomedical application of bulk 2D materials is limited main owing to their poor dispersibility, being this problem overcome, in general, by the production of ultrathin 2D (ZHAO *et al.*, 2016).

The scientific and technological development of ultrathin 2D nanomaterials with controlled structure and adjusted optical, electronic, chemical, and biological properties, has allowed the diagnosis and therapy of many diseases, mainly in the oncologic field (LU *et al.*, 2020; RAJA *et al.*, 2020). In this sense, a variety of 2D nanomaterials such as graphene (JAGIEŁŁO *et al.*, 2020), MnO_2 nanosheets (GRAY *et al.*, 2020), transition metal dichalcogenides (MX_2, M = Mo, W, etc. and X = S, Se and Te) (ZHOU *et al.*, 2020), metalorganic framework (GILIOPOULOS *et al.*, 2020) and graphitic carbon nitride (g-C_3N_4) (CHAN *et al.*, 2019) have attracted significant attention due to promising results in tumor therapy such as radiation therapy, gene, and drug delivery, photothermal therapy and photodynamic therapy (FENG *et al.*, 2016; WANG & YANG, 2019; LIMA-SOUSA *et al.*, 2020; XU *et al.*, 2020). In addition, in the last years, these nanomaterials were also used as imagining agents, improving the imaging quality in several modalities, like magnetic resonance imaging, computed tomography, fluorescent imaging, positron emission tomography, and photoacoustic imaging (RAJA *et al.*, 2020), corroborating the use of these 2D nanomaterials as potential platforms for theranostic application.

g-C_3N_4 is a new metal-free conjugated polymer with semiconductor properties widely used in photocatalytic applications (PATNAIK *et al.*, 2021). This material has a graphitic-like structure formed by periodically linked tris-s-triazine units, with van der Waals force between C – N layers and an interlayer distance of 0.326 nm (JIANG *et al.*, 2014). This structure, mainly formed by carbon and nitrogen atoms, has a tremendous advantage for application in the biomedical field due to the highly non-toxic effect (CHAN *et al.*, 2019). Indeed, g-C_3N_4 has shown excellent biocompatibility, high stability under physiological conditions, low production cost, high intrinsic photoabsorption, and photoresponsiveness (ZHU *et al.*, 2020).

Recently, Zheng and coauthors showed that g-C_3N_4 has a great potential in photodynamic therapy (PDT) due to its efficient water splitting effect, generating O_2, corroborating the application, especially in oncology as a PDT agent (ZHENG *et al.*, 2016). Although the well-known applicability as a PDT agent, just a few works have explored the potential use of g-C_3N_4 for cancer treatment as a pure nanodrug. In this direction, we have fully synthesized as characterized the 2D g-C_3N_4. This nanodrug has also been evaluated *in vitro* to identify the cytotoxic effect. Finally, we have performed the biodistribution as the pharmacokinetics assays to understand the biological behavior better.

4.2. Experimental Section/Methods

4.2.1. Synthesis of g-C_3N_4

The bulk g-C_3N_4 was prepared by direct heating of 6g of urea in a crucible (50 mL in volume) with a cover at 550°C for 3h with a heating rate of 5 °C min^{-1} in air. After the reaction, the crucible was cooled to room temperature. The resultant g-C_3N_4 sponge-like was collected, ground into powder, and stored in a desiccator.

4.2.2. Characterization

The crystalline structure of g-C_3N_4 was analyzed by X-ray powder diffractometer Xpert Pro MPD (Panalytical) using Bragg–Brentano geometry and cobalt $K_{\alpha 1}$ radiation (λ = 1.7889 Å) with angle scanning from 10° to 80° (2θ) at a step of 0.013° using 70 s. Fourier Transform Infrared Spectroscopy (FTIR) analysis was carried out in a Shimadzu IRTracer-100 infrared spectrometer (China) in transmittance mode in the range between 4000 – 400cm^{-1}. Previously measurement, the sample was pressed (~10mg of sample to 100mg of KBr) in disk format. Raman analysis was established with a WITec α300R confocal Raman imaging system. The samples, either in powder form or aqueous dispersion (1 mg/mL), were excited with a 785 nm laser at 30 mW, and the Raman spectra were collected with an integration time of 5 s. The morphology of the g-C3N4 was observed by transmission electron microscopy (TEM) at an accelerating voltage of 100 kV (JEOL Co., Tokyo, Japan). The size distribution and mean size were determined by dynamic light scattering (DLS) using the equipment Zetasizer Nano ZS (Malvern Instruments, UK). Measurements were performed in triplicate at 25 ºC and the laser incidence angle in relation to the sample was 173º using a 12 mm^2 quartz cuvette. The mean ± standard deviation (SD) was assessed. The dilution used for the DLS analysis was 1:40.000. The samples of g-C_3N_4 were also characterized by Atomic Force Microscopy (AFM) in a Multimode 8 microscope (Bruker) using SuperSharpSilicon SSS-NCLR-10 probes (Nanosensors) in scan mode PeakForce Quantitative Nanomechanics, with 256 x 256 samples per lines resolution and 0.5 Hz scan rate. Samples were diluted in Milli-q water and sonicated for 15 minutes and then deposited on a previously cleaved mica surface for AFM analysis. The UV-vis diffuse reflection spectroscopy (DRS) was obtained on a Shimadzu UV-2600 with integrating sphere ISR-2600 plus, using $BaSO_4$ as a reference sample. The photoluminescence analysis was performed in the Shimadzu RF-6000 spectrofluorophotometer. Before the analyses, the sample was dispersed in deionized water (0.25 mg/mL) and sonicated for 30 min.

4.2.3. In vitro Assay

4.2.3.1. Cell Culture

Human gingival fibroblast (FGH) cell lines were obtained from Cell Bank of Rio de Janeiro, Brazil (0190). The cells were maintained in DMEM/F12 medium, supplemented with 10% FBS, $NaHCO_3$ (3.7 g/L), HEPES (5.2 g/L), penicillin (0.5 U/mL) and streptomycin (0.5 mg/mL). Cells were incubated at 37 °C in a humidified atmosphere of 5% CO_2. Cells were grown to confluence in 75 cm² culture flasks and were detached by brief treatment with trypsin (0.1%)/EDTA (0.01%). MV3 human melanoma cells previously selected by others from a highly metastatic human melanoma fragment were donated by Cezary Marcinkievicz, Temple University, Center for Neurovirology and Cancer Biology (PA, USA). Human breast cancer cell line (MDA-MB-231) and Human prostate cancer cell lineage (PC-3) were obtained from Cell Bank of Rio de Janeiro (Rio de Janeiro, Brazil). The MV3, MDA-MB-231, PC-3 cells were routinely maintained in DMEM supplemented with 10% FBS, NaHCO3 (3.7 g/L), HEPES (5.2 g/L), penicillin (0.5 U/mL) and streptomycin (0.5 mg/mL). Cells were incubated at 37°C in a humidified atmosphere of 5% CO2. Cells were grown to confluence culture flasks. Cells were detached by brief treatment with trypsin (0.1%)/EDTA (0.01%)[11].

4.2.3.2. Proliferation Assay MTT

4.2.3.2.1. Normal Cells Line

FGH cells (5×10^3 cells/well) were seeded and allowed to attach for 24 h. These cells were cultured in medium with 10%FBS (untreated) or in medium containing graphitic carbon nitride (g-C_3N_4) in different concentrations (10 µg/mL, 20 µg/mL, 50 µg/mL and 100 µg/mL). After 24 h, the cells were washed and the number of attached cells was determined by using the MTT assay [11]

4.2.3.2.2. Tumor Cells Line

Tumor cells (MDA-MB-231, PC3, and MV3) were cultured in a concentration of $5x\ 10^3$ cells per well and seeded in a 96-well plate. Then the cells were treated in the presence or absence of different concentrations of g-C_3N_4 (1.56, 3.125, 6.25, 12.5, 25. 50, and 100 µg/mL) for 24, 48, and 72 h. After that period, the number of attached cells was determined using the MTT assay.

4.2.3.3. Proliferative assay by High Content Analysis (HCA)

For cell proliferation analysis, human foreskin fibroblasts (HFF-1) and human prostate carcinoma cell line (DU-145) were plated in black, flat-bottom 96-wells plates (Corning Incorpo rated Costar, Corning, NY, USA) at a density of 10^4 cells/well (HFF-1) or 10^3 cells/well (DU-145) in 300 μL/well with DMEM-High (HFF-1) or RPMI (DU-145) supplemented with 10% FBS containing 0.5 μg/mL Hoechst 33258 dye (Sigma-Aldrich, St. Louis, MO, USA) at 37°C. After, 24h plating, the cells were incubated in the presence of 1,56 – 100 μg/mL of g-C_3N_4 or 24, 48 and 72 h at 37 °C (5% CO_2). An untreated control was performed in the absence of g-C_3N_4. Fluorescence images were obtained using an GE IN Cell Analyzer 2000 system and the digital images were acquired in 6 random fields within each well using the DAPI filter (spectral region between 410-480 nm) with a 10 × objective. After segmentation, the objects (cell nuclei) were automatically quantified to estimate cell proliferation. The number of stained nuclei was counted using IN Cell Investigation software. Cell proliferation after 24, 48 and 72 h of treatment was calculated relative to the percentage of the number of cell nuclei counted in the control condition (untreated cells). Inhibitory potency was also determined by the half maximal inhibitory concentration (IC_{50}).

4.2.3.4. ROS production assays

Tumor cell lineages DU-145, MV3, MDA-MB, and PC3 were suspended in HBSS without phenol red and placed in a white-bottom 96 well plate (3 x 10^5 cells/well, final volume 200 μL). Then, cells were loaded with luminol (50 μM) and pretreated with or without g-C_3N_4 at 50 and 100μg. H_2O_2 was used as a positive control. Cells that remained unstimulated were considered the control group. The plate was placed in an Envision® Plate Reader (PerkinElmer, Waltham, MA, USA), and each chemiluminescence was read for 1 second performing time kinetics of 5 to 120 min in luminol assay. Results are expressed as mean ± SD.

4.2.3.5. Radiolabeling with 99mTc

The labelling process was done using 150 µg of graphitic carbon nitride. The g-C_3N_4 was incubated with stannous chloride ($SnCl_2$) solutions (80 µL/mL) (Sigma-Aldrich) for 20 minutes at room temperature. Then, was added 100 µCi (approximately 300 µL) of technetium-99m and rested for another 10 minutes in order to label their structures [13].

4.2.3.6. Quality Control of the Labeling Process with Tc-99m

To confirm the efficacy of the radiolabeling process, Radio Thin Layer Chromatography (RTLC) was done using Whatman paper nº 1. In this regard, 2 μl of ^{99m}Tc- g-

C_3N_4 and acetone (Sigma-Aldrich) as mobile phase at times of 2 and 4 and 24 hours was evaluated. The radioactivity of the strips was verified in a γ-counter (Perkin Elmer Wizard® 2470, Shelton, CT City, State). The RTLC was performed in triplicate for each time.

4.2.3.7. Tissue Deposition - Biodistribution

A total of 6 male naïve mice (C57BL/6J) (3 animals per group) were anesthetized with 4.5-5.0 % sevoflurane in the air for the retroorbital injection of 100µL of 99mTc- g-C_3N_4. Animals were sacrificed in 2h and 24h post-injection, and their organs were removed weighted and the radiation analyzed by γ-counter (Perkin Elmer Wizard® 2470, Shelton, CT City, State).

4.3 Results and Discussion

4.3.1 Synthesis of 2D g-C_3N_4

The 2D g-C_3N_4 sheet was synthesized by a fast and straightforward thermal process, which occurred both formation and exfoliation of g-C_3N_4 (XU *et al.*, 2014). According to previous reports (ZHU *et al.*, 2015; XU & ZHANG, 2018), a possible copolymerization process is proposed in Figure 4.1.

Figure 30 – Schematic diagram of the fabrication of g-C_3N_4.

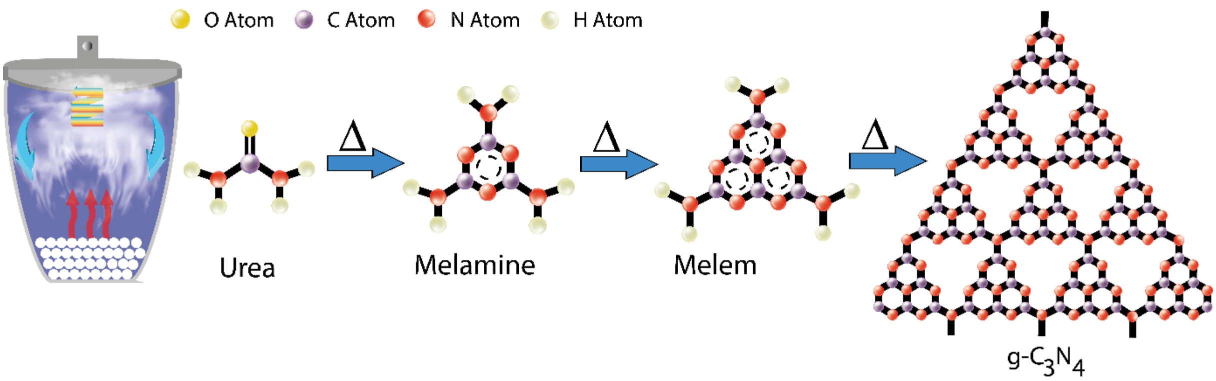

Source: the author

4.3.2. Characterization

The X-ray powder diffraction (XRD) pattern of the sample is shown in Figure 4.2. The formation of graphite-like stacking of C_3N_4 was confirmed by two characteristic diffraction peaks at 32.4° and 15.1°, which are indexed to the crystalline structure of g-C_3N_4 (HUANG *et al.*, 2016). The intense peak at 32.4° is assigned to the interlayer piling of an aromatic system with an interlayer distance of 0.319 nm and could be indexed to (002) plane seen for graphite materials (WANG *et al.*, 2018). It is important to note that the (002) peak is up-shift, suggesting the obtention of a well-compacted structure of g-C_3N_4. Fan. and coauthors published similar results and indicated that this compaction has resulted from the increased strengths in the $\pi - \pi$ staking interaction from interlayers occasioned by planarization of these layers (FAN *et al.*, 2015). Another peak at 15.1°, can be indexed as (100) plane, representing the in-plane structural packing motif of tris–s–triazine units (YAN *et al.*, 2019). Also, this peak corresponds to a hole-to-hole distance of 0.618 nm of the nitride porous in the crystal (MARTHA *et al.*, 2013). This value is found to be less than those observed in the literature for g-C_3N_4 (ABDEL MONEIM *et al.*, 2016; TAMEU DJOKO *et al.*, 2020), suggesting a distortion in the structure of nitride porous.

Figure 31 – XRD pattern obtained for synthesized g-C_3N_4.

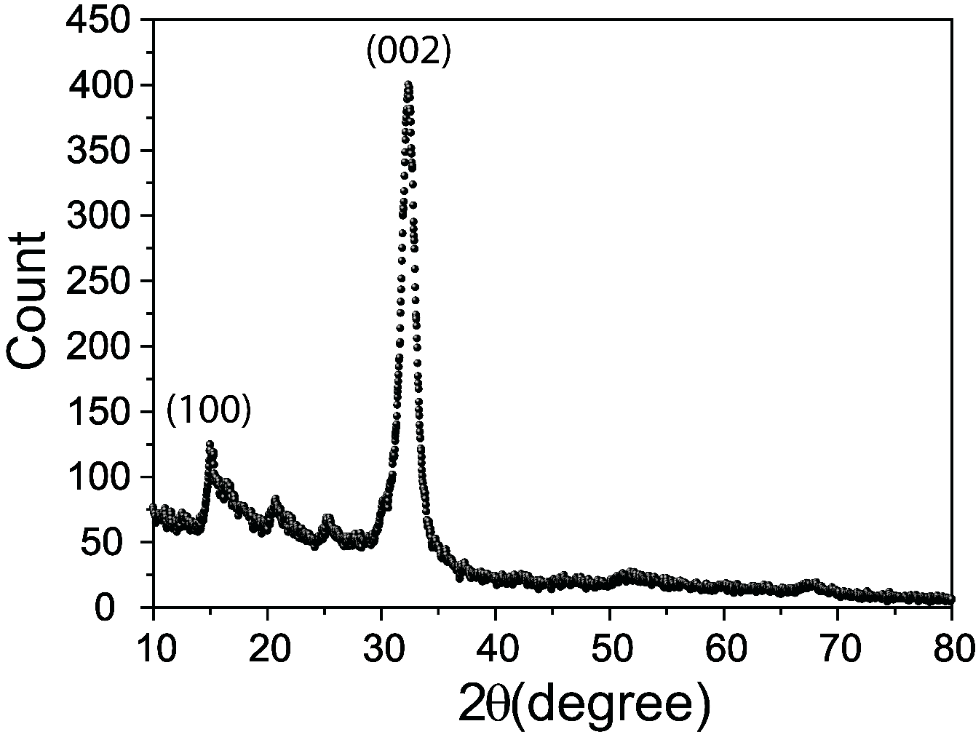

Source: the author

Figure 4.3 a shows the FTIR spectrum from g-C3N4. The narrow absorption bands at 807 and 891 cm-1 can be attributed to the breathing mode of tris-s-triazine rings and the cross-linked heptazine deformation mode, respectively (YAN *et al.*, 2019). The several bands from 1237 to 1639 cm-1 are corresponding to the characteristic stretching modes from C – N heterocycles, with attention to bands at 1461 and 1640 cm-1, corresponding to C – N, C = N, and melem (tris-s-triazine units) respectively (KUMAR *et al.*, 2017; IBRAHIM *et al.*, 2020). The formation of dimelem by the connection of two melem molecules can be seen from the bands at 1237, 1335, and 1406 cm-1 since these modes are assigned to stretching vibrational of connected trigonal units of C – N(-C) – C or C – NH – C bonds (SONG *et al.*, 2015). The broad bands at 3077, 3161, and 3267 cm-1 correspond to the vibrational stretching mode of uncondensed amine groups (CHIDHAMBARAM & RAVICHANDRAN, 2017). Finally, the band at 2141 cm^{-1} may be assigned to – C ≡ N – bond, which may arise due CN heterocycles deformation occasioned by imperfect polymerization (ZOU *et al.*, 2015; GUO *et al.*, 2016). However, in relation to this last band, the literature also has shown that it may be assigned to the stretching of C – O – C bonds, which will be possible owing to the start materials used for the synthesis of g-C_3N_4 in this work (WEI *et al.*, 2018). Thus, further analyses are needs to improve the understanding of the g-C_3N_4 structure.

The analysis of Raman for g-C_3N_4 is shown in Figure 4.3 b. The band seen at 1241 cm^{-1} is assigned to vibration modes of CN heterocycles (JIANG *et al.*, 2014). Similar to graphite, the band at 1387 cm^{-1}, which also is known as D band, is assigned to structural defects and partially distorted structures of the C-sp^2 (WANG, H. *et al.*, 2015). The graphitic-like structure of g-C_3N_4 is confirmed by the presence of a band at 1589 cm^{-1}, which is defined as G band and can be attributed to C = N stretching vibration (LI *et al.*, 2017).

Figure 32 –The Figure (a), and (b) showed the FTIR, and Raman for graphitic carbon nitride, respectively.

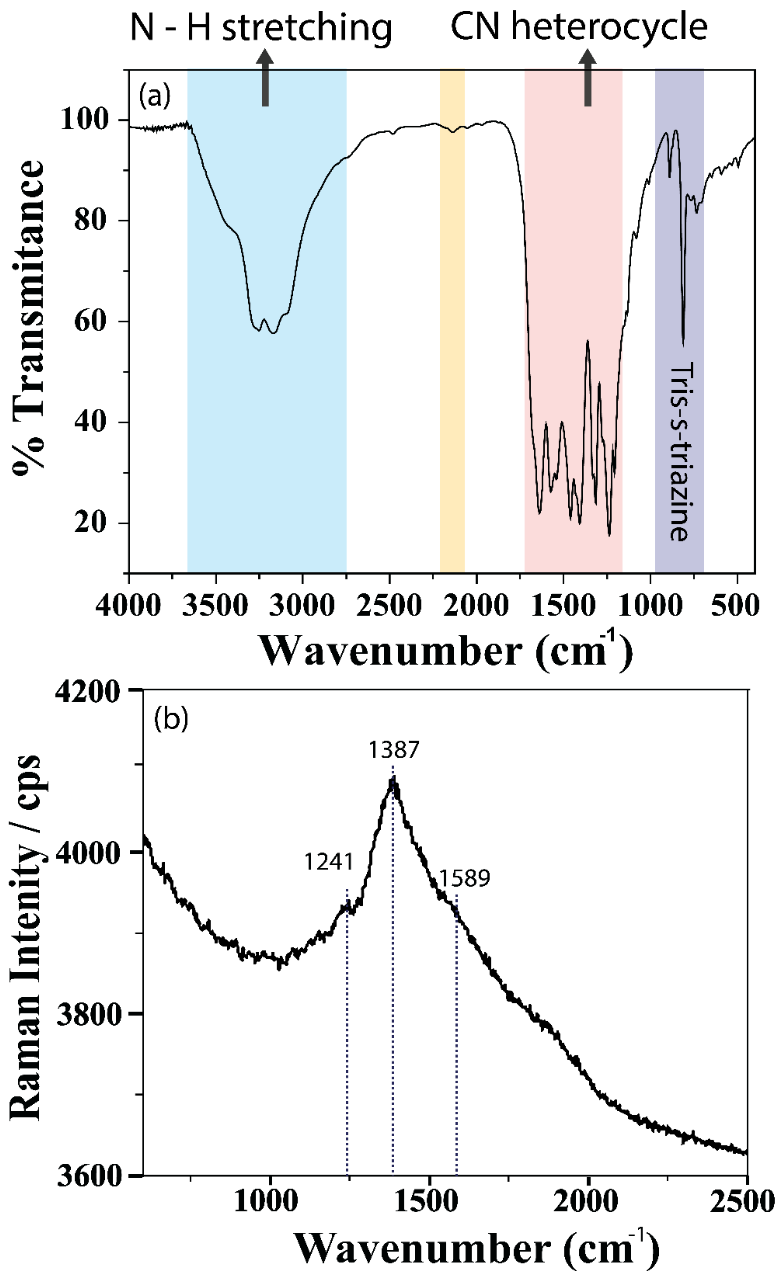

Source: the author

The morphology observed by TEM is represented in Figure 4.4 (a and b). Figure 4.4 a is shown the aggregation of the sample. However, Figure 4.4 b reveals that these aggregates are formed by highly folded carbon nitride sheets, like 2D nanosheets with wrinkles and rolling edges. Besides, it is also observed the formation of porous with irregular shapes in the aggregates. Similar results have been found to g-C_3N_4 synthesized from urea (WANG, Z. *et* *al.*, 2015; THURSTON *et al.*, 2017). The hydrodynamic radius (Figure 4.4 c) reveals that the sample forms large aggregates with an average size of 1000 ± 500 nm. This value is following the results observed in TEM images.

Figure 33 – (a) and (b) are TEM images of g-C_3N_4 to different magnetization. (c) The hydrodynamic radius measurement of g-C_3N_4 in an aqueous medium.

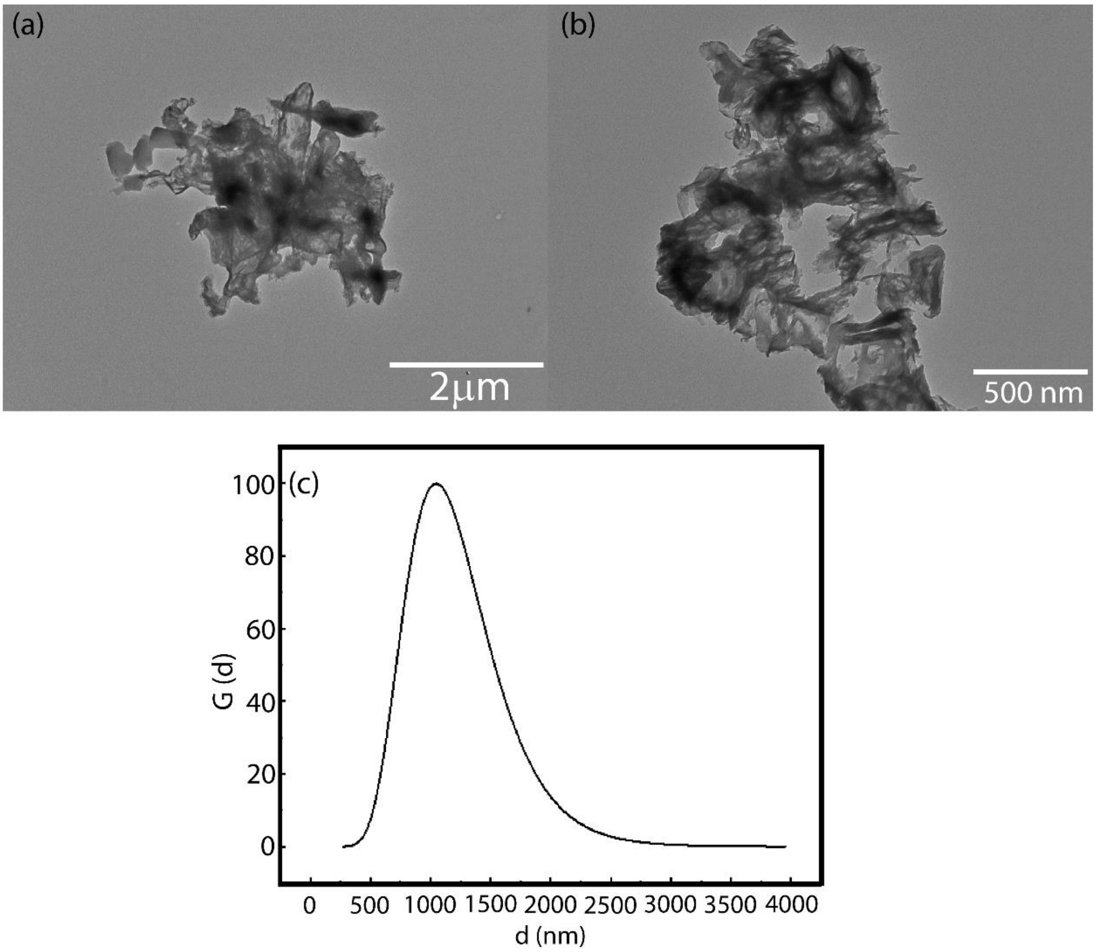

Source: the author

The g-C_3N_4 samples also had their structure analyzed by AFM. As in TEM, many regions presented clusters. These clusters were selected to be better analyzed, as shown in Figure 4.5 (a-d). It is possible to observe the g-C_3N_4 sheets with a two-dimensional structure and a cross-section of approximately 1.8 ± 0.2 nm. The theoretical thickness of the monolayer of g-C_3N_4 observed in XRD analyses is 0.319 nm. Therefore, this result suggests that the material synthesized should be composed of five or six C-N layers.

Figure 34 – AFM height images of g-C_3N_4: (a) topographic image showing flakes of g-C_3N_4, the green square indicates the region presented in figure (b) and its respective three-dimensional image (c). The cross-section shown in (d) corresponds to the area pointed in the image (b).

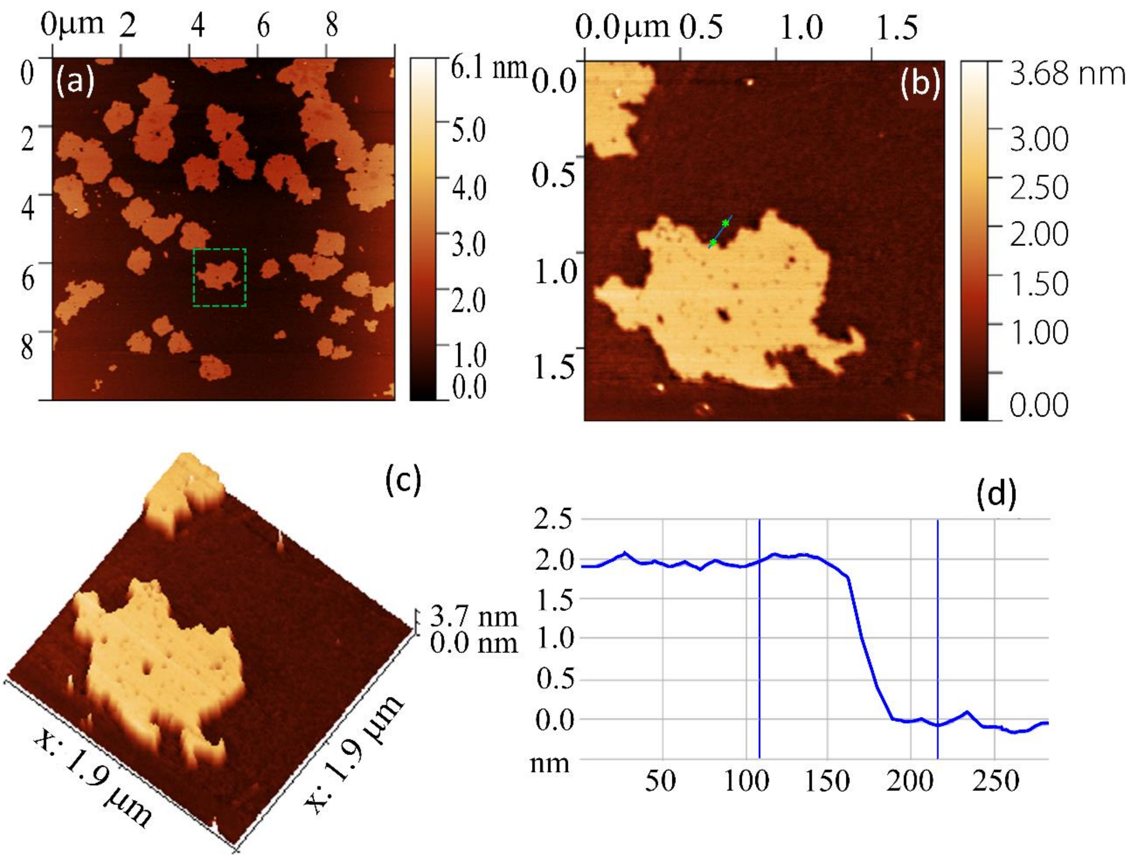

Source: the author

Since few sheets form g-C3N4, the XPS analyses can further obtention more detailed chemical composition and formal oxidation states of all sample elements. From the survey spectra in Figure 4.6a, it is seen that the g-C_3N_4 is composed mainly of C, N, and O atoms. As shown in Figure 4.6b, the high-resolution XPS spectra of C 1s can be deconvoluted in five peaks centered at 285.1, 285.8, 287.3, 288.6, and 289.5 eV. Among them, the peaks at 285.1, 285.8, and 288.6, eV can be attributed to C = C, C – N, and sp^2 C bonded to N in an aromatic ring (N=C–$(N)_2$), respectively (HUANG *et al.*, 2021). Whereas the peak at 289.5 eV is assigned to sp^2 C in the ring attached to the primary and secondary (N=C(N)–NH_x) amines (LI, K. *et al.*, 2021). The C – O and carbonyl (C = O) species seen in C 1s spectra can be attributed to the surface oxidation of g-C_3N_4 (HUANG *et al.*, 2021). The fitting of N 1s spectrum, in Figure 4.6c, showed four peaks, which corresponding to three different states of nitrogen and a π-excitation. The peak centered at 398.6 eV was assigned to sp^2 hybridized aromatic nitrogen bonded to carbon atoms in two different ways (C = N – C). Another two other states of nitrogen were observed in 399.2 and 401 eV, which correspond to tertiary nitrogen bonded to three carbon atoms ($N-(C)_3$) liking structural motif (C_6N_7) and amino functional groups ($C-NH_x$) originated from the defective condensation of tri-s-triazine structure, respectively (YANG *et al.*, 2017).

Figure 35 – XPS survey spectra (a) and high-resolution XPS spectra of C1s (b) and N1s (c) of g-C_3N_4.

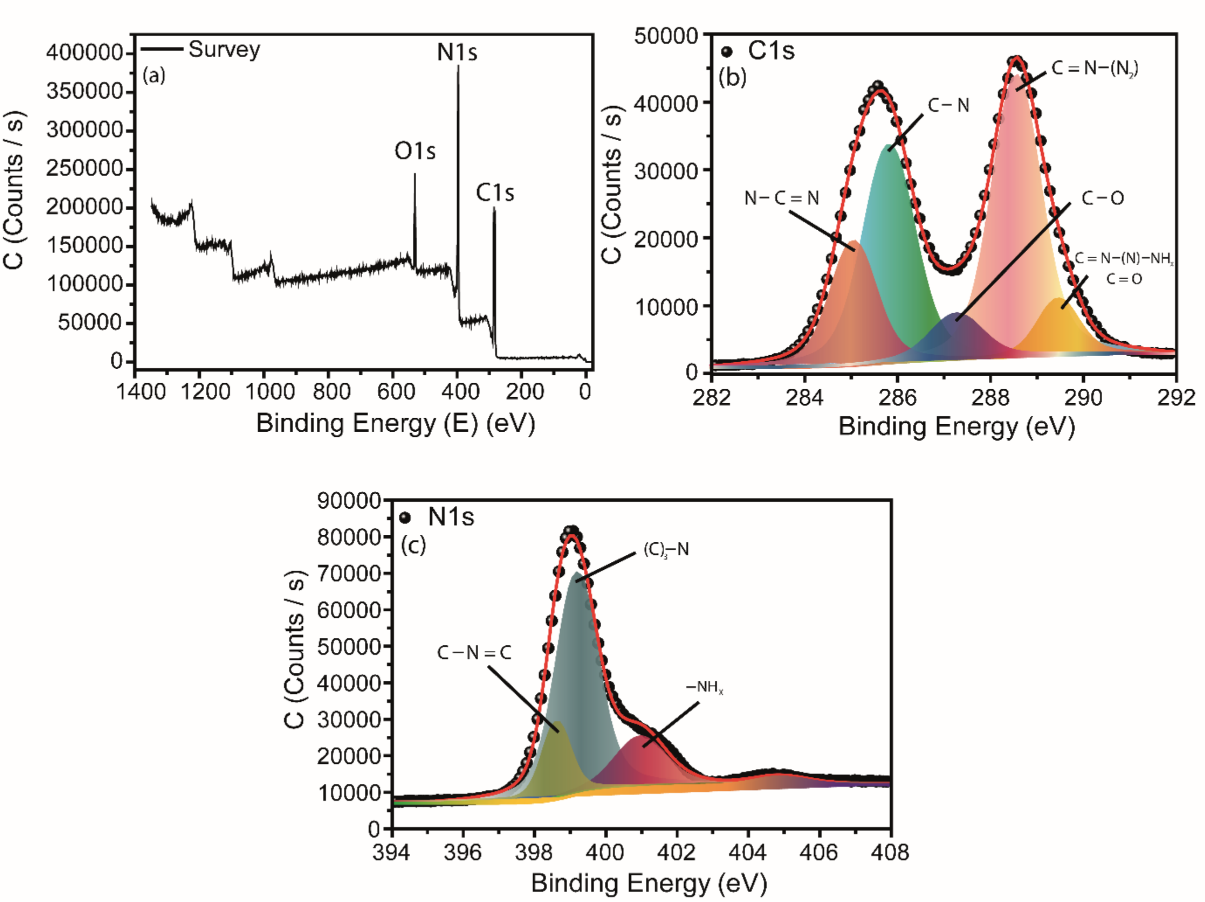

Source: the author

Indeed, the thermal polymerization of urea at 550°C by three h to a heating rate of 5 °C min^{-1} in the air provides an oxygen-doped graphite-like carbon nitride with a large lateral size length and well-compacted structure formed by stacking five or six C_3N_4 sheets, which possesses defects owing to incomplete thermal polymerization reactions of urea. Oxygen atoms seen by XPS are in accord with the decrease in the interplanar stacking distance observed from DRX. The presence of oxygen heteroatoms in the g-C_3N_4 sheet led to the stronger attraction between its layers due to the high electronegativity of these atoms, resulting in a shortened interplanar distance (SUN *et al.*, 2018). It is also important to note that in the XPS analysis has not been seen $-C \equiv N-$ bond, suggesting that the FTIR band should be assigned to C – O – C bonds.

Figure 4.7 a shows the Uv-Visible absorbance characteristic of g-C_3N_4, with stronger absorption bands in the ultraviolet region. The band at 264 nm is due π to π^* electronic transition in the 1, 3, 5-triazine aromatic systems, while the band centered at 325 nm can be assigned to n to π^* electronic transition in the conjugated heptazine rings units (CHIDHAMBARAM & RAVICHANDRAN, 2017). To extract more information from DRS spectra, the bandgap of the sample was calculated by Kubelke Munk transformation (FENG *et al.*, 2018)

$$(\alpha h v)^{\frac{1}{n}} = A(hv - E_g) \quad (1)$$

where α represents the absorption coefficient, h is the Planck constant ($4.13.10^{-15}\ eV.s$), v is the frequency, A is a characteristic constant for each semiconductor material and E_g is the bandgap of the semiconductor. The value of n is determined to be 2 as a result of the direct bandgap nature of g-C_3N_4 (DENG *et al.*, 2016). The inset in Figure 4.6 a shows the diagram obtained from the equation, where the bandgap energy was estimated as 2.87 eV. Thus, the g-C_3N_4 synthesized in this work showed a blueshift in relationship to bulk g-C_3N_4 (BI *et al.*, 2020). This blueshift may be originated by a decreased orbital conjugation degree occasioned by the formation of g-C_3N_4 nanosheets formed by thermal treatment (FAN *et al.*, 2015; IBRAHIM *et al.*, 2020). Figure 4.6 b showed the PL spectra obtained for g-C_3N_4. Notably, a broad and asymmetric PL spectrum with a maximum emission at 448 nm was observed when the sample was excited at a wavelength in the range from 280 nm to 420 nm. According to Yin and coauthors (YIN *et al.*, 2017), the independence-excitation PL behavior for g-C_3N_4 corresponds to intrinsic properties related to its semiconductor band structure. Moreover, this behavior also showed the high homogeneity of the surface and highly crystalline quality from the synthesized g-C_3N_4. Similar results have also been reported by ultrathin g-C_3N_4 (ZHANG *et al.*, 2013).

Figure 36 – (a) UV–vis diffuse reflectance spectra of g-C_3N_4.The right inset is the Kubelka–Munk transformed reflectance spectra and estimated optical bandgap. (b) PL spectra of g-C_3N_4 at different excitation wavelengths (290 – 420 nm).

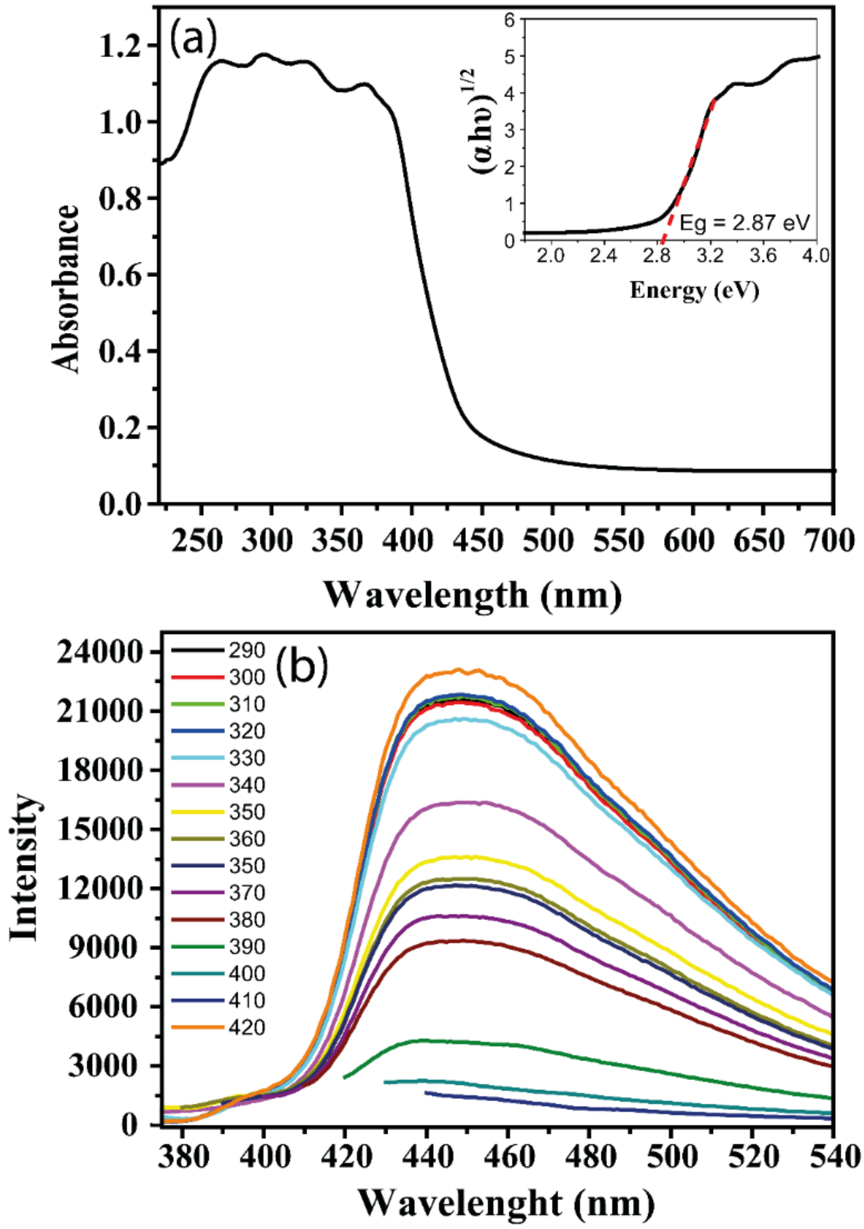

Source: the author

4.3.3. Biological application

4.3.3.1. Proliferation assay in Normal Cell Line

The proliferation assay by MTT (Figure 4.8) corroborated the safety aspect of graphitic carbon nitride (g-C_3N_4) (CHAN *et al*., 2019; PERVEEN *et al.*, 2020). The choice of FGH was made since they are among the most abundant resident cells from the oral mucosa representing a primary cell line (SOARES *et al.*, 2018). The results showed that no cytotoxic effect has been observed even in a high concentration of 100 μg/mL (Figure 4.8).

Figure 37 – MTT assay using graphitic carbon nitride in different concentrations.

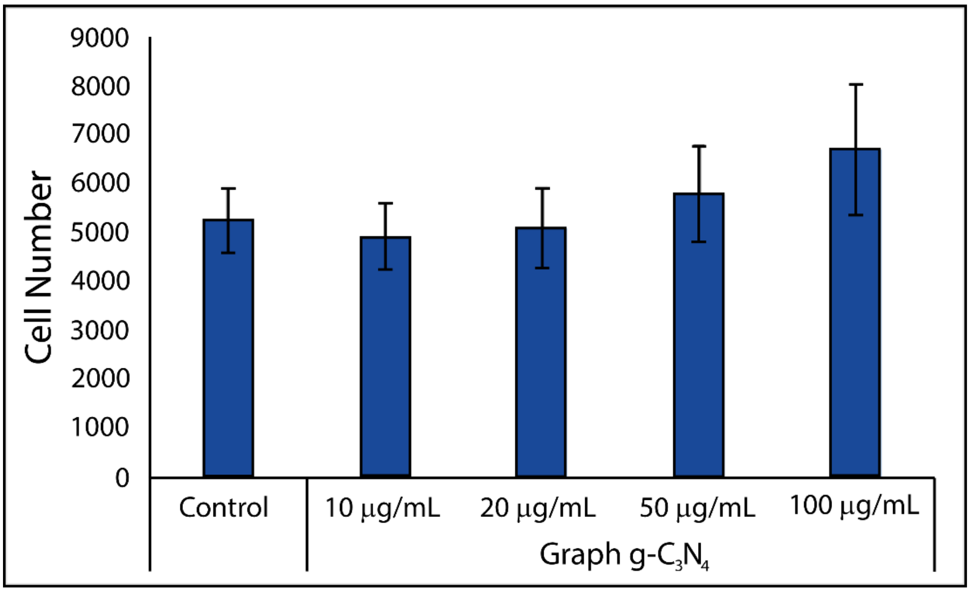

Source: the author

4.3.3.2. Proliferative assay by High Content Analysis (HCA)

The proliferative assay by HCA corroborated the results from the MTT in HFF-1 cells (Table 4.1 and Figure 4.9). The HCA analysis was performed using HFF-1 in order to make a counterpoint with the FGH cells to increase the variability of normal cells. The choice of HFF-1 has been made since this type of cell can be used to test the toxicity and effect of substances on normal cells, especially the toxicity of possible antineoplastic drugs (OLIVEIRA *et al.*, 2018). The results in HFF-1 also demonstrated a safety use aspect. Controversially, the HCA analysis showed a potent inhibitory effect of g-C_3N_4 on DU-145 cell line. It is well-know that carbon nanomaterials are responsible for augmented cell-damaging, themselves or synergistic with conventional chemotherapeutics (ERDMANN *et al.*, 2017). The accepted explanation for this effect is the accumulation into solid tumor by the EPR effect as the influence in the apoptosis (WANG *et al.*, 2011; MAHMOOD *et al.*, 2013; ARORA *et al.*, 2014; ERDMANN *et al.*, 2014; RINGEL *et al.*, 2014; MEHRA & JAIN, 2015; RAZA *et al.*, 2016; SINGH *et al.*, 2016). However, no results for g-C_3N_4 have been previously reported.

Table 7 – IC_{50} (µg/mL) according to treatment.

$g\text{-}C_3N_4$		
Cell Type	**Time (h)**	**IC_{50}**
HFF-1	24	ND
	48	ND
	72	ND
DU-145	24	7.85
	48	7.92
	72	6.54

ND – no data

Source: the author

Figure 38 – HCA analysis showing the effect of g-C_3N_4 on HFF-1 and DU-145 cell line.

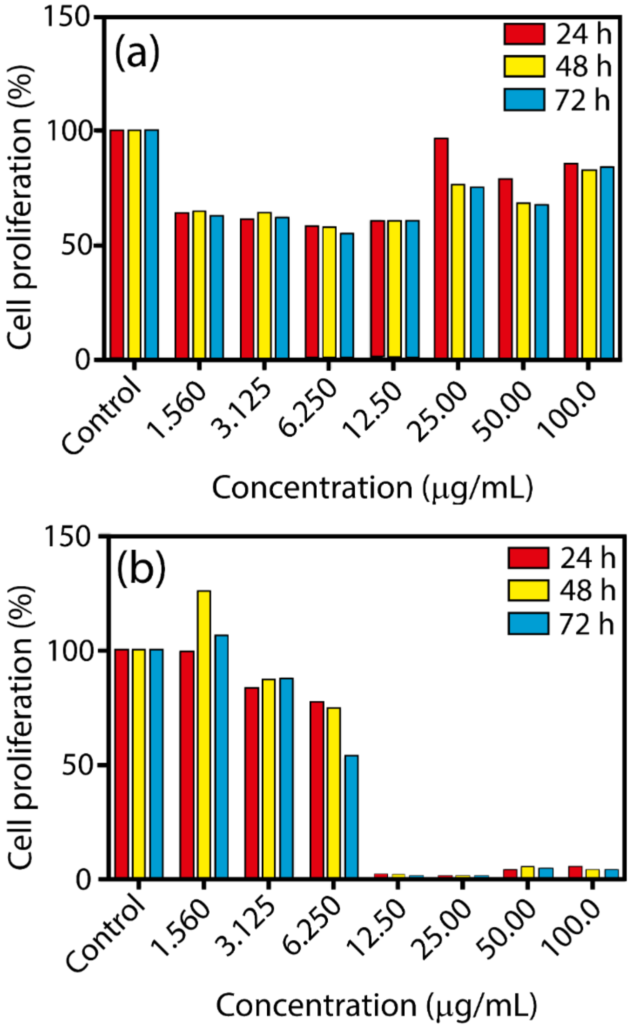

Source: the author

4.3.3.3. Proliferation assay in Cancer Cells Lines

The MTT assay in cancer cells lines is demonstrated in Figure 4.10. To the best of our knowledge, this is the first study demonstrating the cytotoxic effects of *g-C_3N_4* (solely) in cancer cells lines (MDA-MB-231, PC-3, and MV3), without any external or synergistic influence. Also is quite important to notice that although with an accentuated effect in all cancer cells lines evaluated no cytotoxic effect has been observed in normal cells lines as FGH or TFF-1. We believe that the cytotoxic effect on cancer cell lines can be explained by the same theory used to explain the cytotoxic effect of carbon nanomaterials on cancer lines, which includes: ROS generation, DNA damage, lysosomal damage, mitochondrial dysfunction, and eventual cell death via apoptosis or necrosis (YUAN *et al.*, 2019). However, the *g-C_3N_4* showed superiority since no cytotoxic effect has been observed in non-cancer cells line, differently from other carbon nanomaterials.

Figure 39 – g-C_3N_4 effects on tumor cytotoxicity. Tumor cells ($5X10^3$ cells/well) were incubated with g-C_3N_4 at different concentrations for 24, 48, and 72hs. Cytotoxicity was evaluated using an MTT assay. A. MDA-MB-231 B. PC-3 and C. MV3. Results are presented as the mean ± SD calculated from three individual experiments *$p<0.05$ related to 24h control group, #$p<0.05$ related to 48h control group, \$$p<0.05$ related to 72h control group.

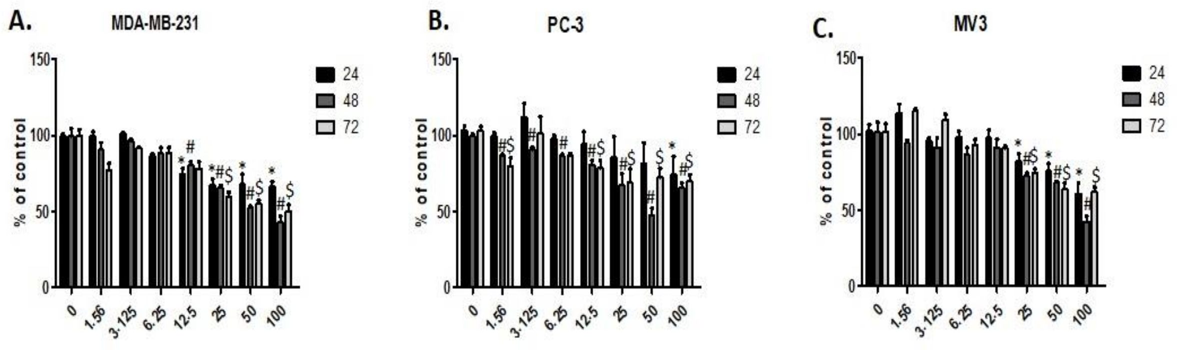

Source: the author

4.3.3.4. ROS (Reactive Oxygen Species) production assays

In order to confirm if the g-C_3N_4 could promote the ROS formation, the luminol has been performed in the four cancer cell lines using 50 µg and 100µg as described above. The results are expressed in Figure 4.11 and Figure 48 (Appendix A). The results showed that no ROS formation has been observed even in high concentrations, leading us to discard ROS as a mechanism of action responsible for cell death. Although preliminary, we believe that the mechanism of action must be via apoptosis, however, further assays should be performed to understand the mechanism.

Figure 40 – ROS assay promoted by the g-C_3N_4 in four different cancer cell lines. In A, melanoma, B, breast cancer and C prostate cancer.

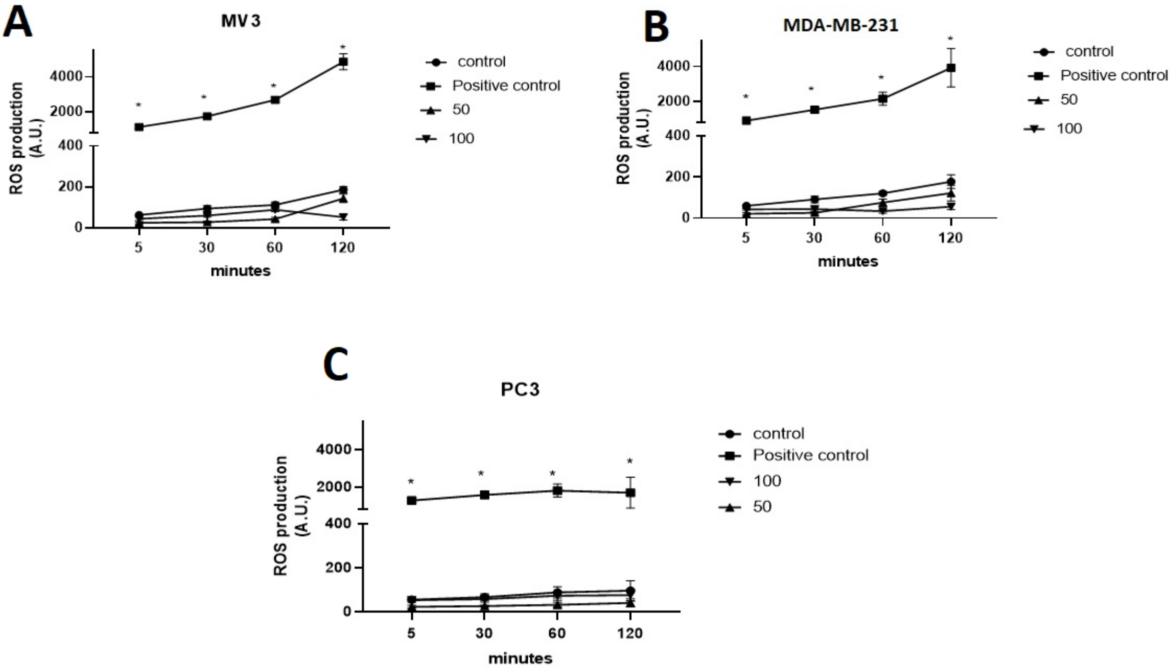

Source: the author

4.3.3.5. Radiolabeling

The radiolabeling of graphitic carbon nitride with technetium 99 metastable (99mTc) showed a high yield (Table 4.2). The use of direct radiolabeling with 99mTc was possible due to the high presence of nitrogen in the compound, which allowed the formation of nitride nucleus [99mTc≡N] $^{2+}$, forming a stable complex against hydrolysis in an aqueous medium, acting as isoelectronic forms *(COSTA et al., 2019)*.

Table 8 – Percentage of labeled g-C_3N_4 over time, after ascending chromatograms of ^{99m}Tc compared with free pertechnetate ($Na^{99m}TcO_4^-$).

Time (h)	Labeling (%) g-C_3N_4
0	99.72± 0.5%
2	99.28± 0.3%
6	95.85± 0.2%
24	100± 0.6%

Source: the author

4.3.3.6. Biodistribution – Tissue Deposition

The biodistribution at 2 and 24 hours is presented in Figure 4.12. The tissue deposition at 2 hours showed high uptake in the lungs (41.89% and 45.28% left and right, respectively). This situation could be explained considering the application route. The retro-orbital via has several blood supply routes as supraorbital vein, inferior palpebral vein, dorsal nasal vein, the superficial temporal vein, and the cava sinus, leading the nanodrug to reach the lungs directly (YARDENI et al., 2011). Nonetheless, the size has a significant influence on the biodistribution of nanoparticles. Thus, the high accumulation in lungs, especially in the first 2 hours (post-injection) may be a direct influence of size (MILLER et al., 2017; FOREST et al., 2019). In any case, the high accumulation in lungs during the initial 2 hours, may predict a potential use in several lung diseases, including as an imaging agent. For instance, due to the blue light emission from the *g-*C_3N_4*, it* can be used for lung imaging (CHAN et al., 2019). Also, due to the ability to generate ROS it can be used for therapeutic purposes, especially in localized cancer treatment (GUO et al., 2020; ZENG et al., 2020). Interestingly, after 24 hours, the *g-*C_3N_4 changed completed the biodistribution profile, and a maximum uptake was observed in the liver (71.37%). The liver accumulation is expected since nanomaterials/nanoparticles are uptakes by the mononuclear phagocytic system and preferentially accumulate in RES organs such as the liver (GARBUZENKO et al., 2014; GUSTAFSON et al., 2015; BEHZADI et al., 2017; DOS SANTOS et al., 2017).

Figure 41 – Tissue accumulation of graphitic carbon nitride at times of 2hs (blue) and 24hs (orange) in naïve animals.

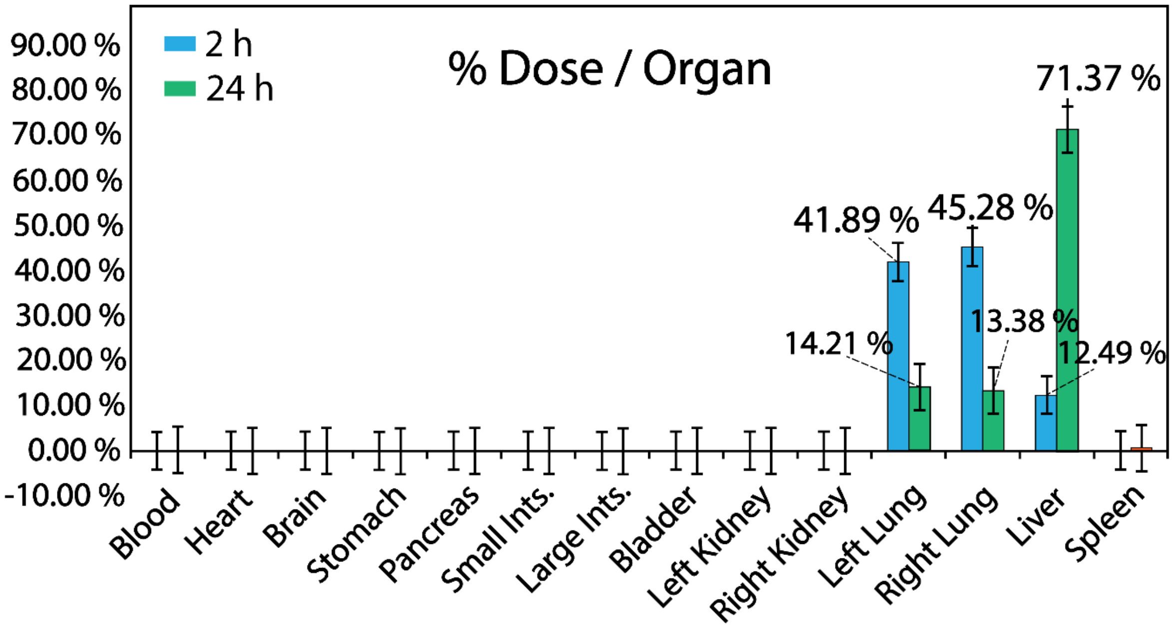

Source: the author

4.4. Conclusion

In summary, XRD, FTIR, Raman, XPS, and AFM analysis showed that 2D g-C_3N_4 sheets synthesized by the thermal method have a compacted structure formed five or six sheets stacked, which presented defects owing to incomplete thermal polymerization of urea. TEM image showed the presence of porous with irregular shape in g-C_3N_4. In addition, the hydrodynamic radius revealed the presence of large aggregates with an average size of 1000 $\pm$ 500 nm. MTT assay and Proliferative assay by HCA showed that 2D g-C_3N_4 have a tremendous inhibitory effect on cancer cell DU-145, while noncytotoxic effect in normal cells lines as FGH and TFF-1. In addition, the profile of biodistribution in the first 2 hours after injection showed that 2D g-C_3N_4 present a tendency to accumulate in lungs. However, after 24-hour g-C_3N_4 was found mainly in the liver, indicating that 2D g-C_3N_4 has excellent potential as a sustainable therapeutic agent for the treatment of prostate cancer and other types of cancer (which should be tested), and due to its profile of biodistribution, the g-C_3N_4 can also be used in the treatment of lung diseases such as covid-19, lung cancer, pneumonia, and tuberculosis as liver diseases as hepatocarcinoma.

5. CHAPTER 5 – GENERAL CONCLUSIONS

In the first study, magnetic nanocomposites of magnetite/chitosan and their derivatives modified with epichlorohydrin and glutaraldehyde were successfully synthesized through a well-established ultrafast strategy under US irradiation. Their structural, magnetic, and textural properties were studied by XRD, FTIR, TGA, XPS, TEM, VSM, and N_2 adsorption-desorption. It was observed that all modified and unmodified ChM nanocomposites presented good crystallinity with the formation of multi-core structure, high M_s ranging from 44 to 57 emu.g^{-1}, and high surface area. The results also indicated a strong interaction between chitosan and magnetite with an increase of specific surface area and pore volume after modification with glutaraldehyde and epichlorohydrin. Adsorption studies using reactive black 5 and methyl orange as adsorbates revealed a pH dependence, however with different profiles for modified and unmodified ChM nanocomposites, indicating that electrostatic interaction and molecular size have significant influence in the adsorption process. In addition, the adsorption capacity values for the ChM sample were approximately 50 and 70 mg.g^{-1} for RB5 and MO, respectively, confirming that the adsorption process is mainly affected by the dye's molecular size. Kinetic experiments showed that ChM ECH achieved equilibrium faster than ChM and ChM GL. According to isotherm models, different adsorption mechanisms were found, indicating changes in surface characteristics. Therefore, modifying ChM allows one to generate diverse functional groups on the surface, which is helpful when working in the removal of different dyes. This is particularly interesting, making these nanocomposites potentially useful in adsorption systems for textile wastewater treatment.

The second study focused on the synthesis of FeM (M = Ag, co, Cu, and Ni) nanocrystals using oleylamine reduction metal salt. Their crystalline structures and morphology were thoroughly investigated by XRD, FTIR, and Mössbauer spectroscopy, confirming the formation of bimetallic nanocrystals coated with oleylamine (FeM@OAm). Except for the FeAg sample, iron oxide was not observed on the surface of the other synthesized materials. TEM images revealed the formation of nanocrystals with narrow size distribution and different morphology. Moreover, the observed bimodal size distribution for FeAg and FeCu samples could be attributed to the difference between Cu^{2+} and Ag^{+} reduction potentials and that for Fe^{3+} ions. All the samples also exhibited a ferrimagnetic behavior with high saturation magnetization and low coercive field, assigning them as soft magnetic materials. Experiments for $H_{2(g)}$ production by electrochemical water splitting showed that all samples demonstrated electrochemical activity due to decreased glassy carbon electrode overpotential. FeCu sample presented the best HER activity, possibly due to the formation of FeCu alloys with a more Fe-rich surface. Moreover, the reaction was governed by different steps depending on the used metal: for samples using noble metals (FeAg and FeCu), the mechanism was mainly controlled by Volmer reaction; for FeNi and FeCo nanoparticles, the determining step was the Heyrovsky reaction. Besides, all the samples showed high electrochemical performance and good stability toward HER under alkaline conditions, making these materials promising candidates for $H_{2(g)}$ production by electrochemical water splitting.

The third study in this thesis was dedicated to producing graphitic-like carbon nitride for cancer treatment in different cell lines. 2D g-C_3N_4 was synthesized by thermal polymerization of urea at 550 °C and characterized by XRD, FTIR, Raman, XPS, TEM, and AFM techniques. These analyses showed a structure formed by stacks of five or six g-C_3N_4 sheets with an interplanar space of 0.319 nm and porous with irregular shape. The presence of amine groups and oxygen atoms on the surface of the sheets indicated an incomplete thermal polymerization of urea, which also influenced the optical properties as suggested by the bandgap blueshift when compared to other bulk g-C_3N_4. Biological assays indicated the remarkable performance of g-C_3N_4 for cancer treatment. MTT and proliferation assays by HCA showed that g-C_3N_4 has excellent biocompatibility with normal cells, such as FGH and TFF-1, and a significant inhibitory effect on different cancer cells, indicating its great potential as a therapeutic agent for various carcinoma treatments. ROS assays carried out to understand the g-C_3N_4 actuation on cancer cells showed a mechanism via apoptosis, since no activity was observed. In terms of biodistribution, experiments revealed that in the first two hours g-C_3N_4 could be found mainly in the lungs, therefore with potential application to treat lung diseases, such as Covid-19, lung cancer, pneumonia, and tuberculosis. However, after 24 h, the material was majority encountered in the liver, arising as a possible alternative against liver diseases such as hepatocarcinoma.

Finally, it is well known that magnetic nanoparticles also have sustainable properties for biomedical application and that 2D graphitic-like g-C_3N_4 have excellent properties for hydrogen production. Thus, this thesis also opens opportunities for future works involving composites of magnetic nanoparticles with g-C_3N_4 nanosheets to improve hydrogen production by electrochemical water splitting and to enhance cancer treatment efficiency since the insertion of magnetic nanoparticles allows the formation of a system of theranostic treatment.

SCIENTIFIC PRODUCTION DURING PH.D.

PUBLISHED ARTICLES:

1. **Freire, T.M**.; Dutra, L.M.U.; Queiroz, D.C.; Ricardo, N.M.P.S.; Barreto, K.; Denardin, J.C. ; Wurm, Frederik R. ; Sousa, C.P.; Correia, A.N.; De Lima-Neto, P ; Fechine, P.B.A. Fast Ultrasound Assisted Synthesis Of Chitosan-Based Magnetite Nanocomposites As A Modified Electrode Sensor. Carbohydrate Polymers, V. 151, P. 760-769, 2016.

2. Neto Davino, M. A.; Freire, Rafael M.; Gallo, Juan; **Freire, Tiago M**.; Queiroz, Danilo C.; Ricardo, Nágila Maria Pontes Silva.; Vasconcelos, Igor F.; Mele, Giuseppe; Carbone, Luigi; Mazzetto, Selma Elaine; Bañobre-López, Manuel; Fechine, Pierre B. A.. Rapid Sonochemical Approach Produces Functionalized Fe 3 O 4 NPs with Excellent Magnetic, Colloidal and Relaxivity Properties for MRI Application. **Journal of Physical Chemistry C**, v. 121, p. 24206-24222, 2017.

3. Souza, Camila P.; De Oliveira, Raissa C.; **Freire, Tiago M**.; Fechine, Pierre B. A.; Salvador, Michele A.; Homem-de-Mello, Paula; Morais, Simone; De Lima-Neto, Pedro; Correia, Adriana N. Chlorhexidine digluconate on chitosan-magnetic iron oxide nanoparticles modified electrode: Electroanalysis and mechanistic insights by computational simulations. **Sensors and actuators b-chemical**, v. 240, p. 417-425, 2017.

4. De Oliveira, Raissa C.; Sousa, Camila P.; **Freire, Tiago M**.; Freire, Rafael M.; Denardin, Juliano C. ; Fechine, Pierre B. A.; Becker, Helena; Morais, Simone; De Lima-Neto, Pedro; Correia, Adriana N. Chitosan-magnetite nanocomposite as a sensing platform to bendiocarb determination. **Analytical and bioanalytical chemistry**, v. 410, p. 7229-7238, 2018.

5. Cunha, Francisco A.; Cunha, Maria da C. S. O.; Da Frota, Sabrina M. ; Mallmann, Eduardo J. J.; **Freire, Tiago M.**; Costa, Luelc S.; Paula, Amauri J.; Menezes, Everardo A.; Fechine, Pierre B. A. Biogenic synthesis of multifunctional silver nanoparticles from rhodotorula glutinis and rhodotorula mucilaginosa: antifungal, catalytic and cytotoxicity activities. **World journal of microbiology & biotechnology**, v. 34, p. 127, 2018.

6. Monteiro, Rodolpho R. C.; Lima, Paula J. M.; Pinheiro, Bruna B.; **Freire, Tiago M.**; Dutra, Lillian M. U.; Fechine, Pierre B. A.; Gonçalves, Luciana R. B.; De Souza, Maria C. M.; Dos Santos, José C. S.; Fernandez-Lafuente, Roberto. Immobilization of lipase a from candida antarctica onto chitosan-coated magnetic nanoparticles. **International journal of molecular sciences**, v. 20, p. 4018, 2019.

7. Pinheiro, Bruna B.; Rios, Nathalia S.; Rodríguez Aguado, Elena; Fernandez-Lafuente, Roberto; **Freire, Tiago M.**; Fechine, Pierre B.A.; Dos Santos, José C.S.; Gonçalves, Luciana R.B. Chitosan activated with divinyl sulfone: a new heterofunctional support for enzyme immobilization. Application in the immobilization of lipase B from Candida Antarctica. **International journal of biological macromolecules**, v. 130, p. 798-809, 2019.

8. **Freire, Tiago M.**; Fechine, Lillian M. U. D.; Queiroz, Danilo C.; Freire, Rafael M.; Denardin, Juliano C.; Ricardo, Nágila M. P. S.; Rodrigues, Thaina N. B.; Gondim, Diego R.; Junior, Ivanildo J. S.; Fechine, Pierre B. A. Magnetic Porous Controlled Fe3o4-Chitosan Nanostructure: An Ecofriendly Adsorbent For Efficient Removal Of Azo Dyes. **Nanomaterials,** V. 10, P. 1194, 2020.

9. Moreira, Katerine S.; Moura Júnior, Lourembergue S.; Monteiro, Rodolpho R. C.; De Oliveira, André L. B.; Valle, Camila P.; **Freire, Tiago M.**; Fechine, Pierre B. A.; De Souza, Maria C. M.; Fernandez-Lorente, Gloria; Guisan, José M.; Dos Santos, José C. S. Optimization Of The Production Of Enzymatic Biodiesel From Residual Babassu Oil (Orbignya Sp.) Via Rsm. **Catalysts**, V. 10, P. 414, 2020.

10. Santana, Allan M.; **Freire, Tiago M.**; Da Silva, Francisco L.F.; Menezes, Fernando L. ; Ramos, Lauren L.; Cavalcante, Giovanna R.; Fechine, Lillian M.U.D.; Vieira, Laís H.S.; Ferreira, Odair P.; Freire, Rafael M.; Denardin, Juliano C.; Lopes, Gisele S.; Matos, Wladiana O.; Fechine, Pierre B.A. Organophosphorus Halloysite Nanotubes As Adsorbent For Lead Preconcentration In Wine And Grape Juice. **Applied Clay Science**, V. 200, P. 105912, 2021.

11. Do Nascimento, Carlos Pedro g. ; Moreira, Ícaro o. ; **Freire, Tiago M.** ; Fechine, Pierre B. A. ; Diógenes, Izaura C. N. ; Longhinotti, Elisane . Redox cycling of copper mediated by hydrazine: efficient catalyst systems for oxidative degradation of rhodamine B. **Journal of environmental science and health part a-toxic/hazardous substances & environmental engineering**, v. -, p. 1-12, 2021.

12. **Freire, Tiago Melo**; Sant’anna, Celso ; Yoshihara, Natalia ; Hu, Rui ; Qu, Junle ; Alencar, Luciana Magalhães Rebelo ; Oliveira Da Silva De Barros, Aline ; Helal-Neto, Edward ; Fernandes, Laila Ribeiro ; Simoes, Rafael L ; Barja-Fidalgo, Christina ; Fechine, Pierre B A ; Santos-Oliveira, Ralph. Biomedical application of graphitic carbon nitrides: tissue deposition in vivo, induction of reactive oxygen species (ROS) and cell viability in tumor cells. **Nanotechnology (Bristol. Online)**, v. 32, p. 435301, 2021.

SUBMITTED ARTICLES:

1. **T. M. Freire**; R. M. Freire; J. C. Denardin; F. G. S. Oliveira; I. F. Vasconcelos; P. de Lima-Neto; P. B. A. Fechine. Magnetic FeM (M = Ag, Co, Cu, and Ni) nanocrystals as electrocatalysts for hydrogen evolution reaction. **Journal of Alloys and Compounds.**

BOOK CHAPTER:

1. **Freire, Tiago M.**; Galvão, Wesley S.; Freire, Rafael M.; Fechine, P. B. A. Bimagnetic Core/Shell Nanoparticles: Current Status and Future Possibilities. Complex Magnetic Nanostructures. 1ed.: Springer International Publishing, 2017, v. , p. 83-119.

2. De Oliveira Sousa Neto, Vicente; **Freire, Tiago Melo**; Saraiva, Gilberto Dantas; Muniz, Celio Rodrigues; Cunha, Marcony Silva; Fechine, Pierre Basílio Almeida; Nascimento, Ronaldo Ferreira do Nascimento. Water Treatment Devices Based On Zero-Valent Metal And Metal Oxide Nanomaterials. In: Ronaldo Do Nascimento; Odair Pastor Ferreira; Amauri De Paula; Vicente Sousa Neto. (Org.). Nanomaterials Applications For Environmental Matrices. 1ed.Irvine: Elsevier, 2019, V. P. 187-225.

3. Janaína Sobreira Rocha, **Tiago Melo Freire**, Clinton Simplicio Fernandes da Silva, Jair Matheus Carvalho Chaves, Fernando Lima Menezes, Laudenor Amorim, Eduardo Viana, Pierre Basílio Almeida Fechine Rafael Melo Freire. Nanopartículas Magnéticas. 1. ed. Fortaleza: Imprensa Universitária da Universidade Federal do Ceará (UFC), 2020. v. 1. 300p.

4. Pabllo Abreu Alves, Dráulio Sales da Silva, Samuel Veloso Carneiro, **Tiago Melo Freire**, Pierre Basílio Almeida Fechine. 1. ed. Fortaleza: Imprensa Universitária da Universidade Federal do Ceará (UFC), 2020. v. 1. 300p.

REFERENCES

A. OSAWA, Rodrigo *et al.* Visible light photocatalytic degradation of amitriptyline using cobalt doped titanate nanowires: Kinetics and characterization of transformation products. **Journal of Environmental Chemical Engineering,** [s.l.], v. 8, n. 1, p. 103585, 2020. ISSN:2213-3437 DOI:https://doi.org/10.1016/j.jece.2019.103585. Available at: http://www.sciencedirect.com/science/article/pii/S2213343719307080. Access at: 2020 Feb. 01.

ABDEL MONEIM, Shimaa M. *et al.* Novel application of metal-free graphitic carbon nitride (g-C3N4) in photocatalytic reduction—Recovery of silver ions. **Journal of Environmental Chemical Engineering,** [s.l.], v. 4, n. 4, Part A, p. 4165-4172, 2016. ISSN:2213-3437 DOI:https://doi.org/10.1016/j.jece.2016.08.034. Available at: http://www.sciencedirect.com/science/article/pii/S2213343716303219. Access at: 2016 Dec. 01.

ADEGBEMIGA, Yusuf Bashir *et al.* Ni3Fe nanoparticles enclosed by B-doped carbon for efficient bifunctional performances of oxygen and hydrogen evolution reactions. **Journal of Alloys and Compounds,** [s.l.], v. 835, p. 155267, 2020. ISSN:0925-8388 DOI:https://doi.org/10.1016/j.jallcom.2020.155267. Available at: https://www.sciencedirect.com/science/article/pii/S0925838820316303. Access at: 2020 Sep. 15

ADEWUNMI, Ahmad A.; KAMAL, Muhammad Shahzad; SOLLING, Theis Ivan. Application of magnetic nanoparticles in demulsification: A review on synthesis, performance, recyclability, and challenges. **Journal of Petroleum Science and Engineering,** [s.l.], v. 196, p. 107680, 2021. ISSN:0920-4105 DOI:https://doi.org/10.1016/j.petrol.2020.107680. Available at: https://www.sciencedirect.com/science/article/pii/S0920410520307476. Access at: 2021 Jan. 01.

AGUIAR, J. E. *et al.* Correlation between PSD and adsorption of anionic dyes with different molecular weigths on activated carbon. **Colloids and Surfaces A: Physicochemical and Engineering Aspects,** [s.l.], v. 496, p. 125-131, 2016. ISSN:0927-7757 DOI:http://dx.doi.org/10.1016/j.colsurfa.2015.09.054. Available at: http://www.sciencedirect.com/science/article/pii/S0927775715302429. Access at: 2016 May 05.

AHMAD, Ayyaz *et al.* Antibacterial activity of graphene supported FeAg bimetallic nanocomposites. **Colloids and Surfaces B: Biointerfaces,** [s.l.], v. 143, p. 490-498, 2016. ISSN:0927-7765 DOI:https://doi.org/10.1016/j.colsurfb.2016.03.065. Available at: http://www.sciencedirect.com/science/article/pii/S092777651630220X. Access at: 2016 Jul. 01.

AHMED, Sameh I.; SANAD, Moustafa M. S. Maghemite-based anode materials for Li-Ion batteries: The role of intentionally incorporated vacancies and cation distribution in electrochemical energy storage. **Journal of Alloys and Compounds,** [s.l.], v. 861, p. 157962, 2021. ISSN:0925-8388 DOI:https://doi.org/10.1016/j.jallcom.2020.157962. Available at: https://www.sciencedirect.com/science/article/pii/S0925838820343267. Access at: 2021 Apr. 25.

AHSAN, Md Ariful *et al.* Biomass-derived ultrathin carbon-shell coated iron nanoparticles as high-performance tri-functional HER, ORR and Fenton-like catalysts. **Journal of Cleaner Production,** [s.l.], v. 275, p. 124141, 2020. ISSN:0959-6526 DOI:https://doi.org/10.1016/j.jclepro.2020.124141. Available at: https://www.sciencedirect.com/science/article/pii/S095965262034186X. Access at: 2020 Dec. 01.

AL-MAMUN, M. R. *et al.* Photocatalytic activity improvement and application of UV-TiO2 photocatalysis in textile wastewater treatment: A review. **Journal of Environmental Chemical Engineering,** [s.l.], v. 7, n. 5, p. 103248, 2019. ISSN:2213-3437 DOI:https://doi.org/10.1016/j.jece.2019.103248. Available at: http://www.sciencedirect.com/science/article/pii/S2213343719303719. Access at: 2019 Oct. 01.

ALMESSIERE, M. A. *et al.* Magnetic and structural characterization of Nb3+-substituted CoFe2O4 nanoparticles. **Ceramics International,** [s.l.], v. 45, n. 7, Part A, p. 8222-8232, 2019. ISSN:0272-8842 DOI:https://doi.org/10.1016/j.ceramint.2019.01.125. Available at: https://www.sciencedirect.com/science/article/pii/S0272884219301282. Access at: 2019 May 01.

ARORA, S. *et al.* Translocation and toxicity of docetaxel multi-walled carbon nanotube conjugates in mammalian breast cancer cells. **J Biomed Nanotechnol,** [s.l.], v. 10, n. 12, p. 3601-3609, 2014. ISSN:1550-7033 (Print)

1550-7033 DOI:10.1166/jbn.2014.1875 Access at: 2020 Dec. 03.

ASGARIAN, S. M.; KARGAR, Z.; MOZAFFARI, M. Investigation of cation vacancies in Zinc substituted maghemite by positron annihilation lifetime and Doppler broadening spectroscopy. **Applied Radiation and Isotopes,** [s.l.], v. 125, p. 18-22, 2017. ISSN:0969-8043 DOI:https://doi.org/10.1016/j.apradiso.2017.04.001. Available at: https://www.sciencedirect.com/science/article/pii/S0969804316309368. Access at: 2017 Sep. 01.

ASHIRI, Rouholah; AJAMI, Reza; MOGHTADA, Abdolmajid. Sonochemical Synthesis of SrTiO3 Nanocrystals at Low Temperature. **International Journal of Applied Ceramic Technology,** [s.l.], v. 12, n. S2, p. E202-E206, 2015. ISSN:1546-542X DOI:https://doi.org/10.1111/ijac.12315. Available at: https://doi.org/10.1111/ijac.12315. Access at: 2015 May 01.

ASHRAF, Muhammad *et al.* Hematite and Magnetite Nanostructures for Green and Sustainable Energy Harnessing and Environmental Pollution Control: A Review. **Chemical Research in Toxicology,** [s.l.], v. 33, n. 6, p. 1292-1311, 2020. ISSN:0893-228X

DOI:10.1021/acs.chemrestox.9b00308. Available at: https://doi.org/10.1021/acs.chemrestox.9b00308. Access at: 2020 Jun. 15.

ASLAM, Sehrish *et al.* Mixed-dimensional heterostructures of hydrophobic/hydrophilic graphene foam for tunable hydrogen evolution reaction. **Chemosphere,** [s.l.], v. 245, p. 125607, 2020. ISSN:0045-6535 DOI:https://doi.org/10.1016/j.chemosphere.2019.125607. Available at: http://www.sciencedirect.com/science/article/pii/S0045653519328474. Access at: 2020 Apr. 01.

BABIĆ-STOJIĆ, Branka *et al.* Magnetic and Structural Studies of CoFe_{2}O_{4} Nanoparticles Suspended in an Organic Liquid. **Journal of Nanomaterials,** [s.l.], v. 2013, p. 741036, 2013. ISSN:1687-4110 DOI:10.1155/2013/741036. Available at: https://doi.org/10.1155/2013/741036. Access at: 2013 Nov. 20.

BALETTO, F.; MOTTET, C.; FERRANDO, R. Growth of Three-Shell Onionlike Bimetallic Nanoparticles. **Physical Review Letters,** [s.l.], v. 90, n. 13, p. 135504, 2003. DOI:10.1103/PhysRevLett.90.135504. Available at: https://link.aps.org/doi/10.1103/PhysRevLett.90.135504. Access at: 2019 Apr. 02.

BANG, Jin Ho; SUSLICK, Kenneth S. Applications of Ultrasound to the Synthesis of Nanostructured Materials. **Advanced Materials,** [s.l.], v. 22, n. 10, p. 1039-1059, 2010. ISSN:0935-9648 DOI:https://doi.org/10.1002/adma.200904093. Available at: https://doi.org/10.1002/adma.200904093. Access at: 2015 Mar. 12.

BARBOSA, Felipe Fernandes; PERGHER, Sibele B. C.; BRAGA, Tiago Pinheiro. Synthesis of highly stable FeCo alloy encapsulated in organized carbon from ethylbenzene using H2, CH4, C2H4 generated in situ. **Journal of Alloys and Compounds,** [s.l.], v. 772, p. 625-636, 2019. ISSN:0925-8388 DOI:https://doi.org/10.1016/j.jallcom.2018.09.127. Available at: http://www.sciencedirect.com/science/article/pii/S092583881833367X. Access at: 2019 Jan. 25.

BAUMGARTNER, Jens *et al.* Nucleation and growth of magnetite from solution. **Nature materials,** [s.l.], v. 12, n. 4, p. 310-314, 2013. ISSN:1476-1122. Access at: 2015 Aug. 03.

BEHZADI, Shahed *et al.* Cellular uptake of nanoparticles: journey inside the cell. **Chemical Society reviews,** [s.l.], v. 46, n. 14, p. 4218-4244, 2017. ISSN:1460-4744 0306-0012 DOI:10.1039/c6cs00636a. Available at: https://pubmed.ncbi.nlm.nih.gov/28585944. Access at: 2020 Dec. 09.

BERMAN, Jesse D.; EBISU, Keita. Changes in U.S. air pollution during the COVID-19 pandemic. **Science of The Total Environment,** [s.l.], v. 739, p. 139864, 2020. ISSN:0048-9697 DOI:https://doi.org/10.1016/j.scitotenv.2020.139864. Available at: https://www.sciencedirect.com/science/article/pii/S0048969720333842. Access at: 2020 Oct. 15.

BERTRAM, Christoph *et al.* COVID-19-induced low power demand and market forces starkly reduce CO2 emissions. **Nature Climate Change,** [s.l.], v. 11, n. 3, p. 193-196, 2021. ISSN:1758-6798 DOI:10.1038/s41558-021-00987-x. Available at: https://doi.org/10.1038/s41558-021-00987-x. Access at: 2021 Mar. 01.

BHATIA, Subhash C.; RAVI, Natarajan. A Magnetic Study of an Fe−Chitosan Complex and Its Relevance to Other Biomolecules. **Biomacromolecules,** [s.l.], v. 1, n. 3, p. 413-417, 2000. ISSN:1525-7797 DOI:10.1021/bm0002959. Available at: https://doi.org/10.1021/bm0002959. Access at: 2015. Jul. 01.

BI, Xiaojian *et al.* Construction of g-C3N4/TiO2 nanotube arrays Z-scheme heterojunction to improve visible light catalytic activity. **Colloids and Surfaces A: Physicochemical and Engineering Aspects,** [s.l.], v. 603, p. 125193, 2020. ISSN:0927-7757 DOI:https://doi.org/10.1016/j.colsurfa.2020.125193. Available at: http://www.sciencedirect.com/science/article/pii/S092777572030786X. Access at: 2020 Oct. 20.

BIRHANU, Mulatu Kassie *et al.* Electrocatalytic reduction of carbon dioxide on gold–copper bimetallic nanoparticles: Effects of surface composition on selectivity. **Electrochimica Acta,** [s.l.], v. 356, p. 136756, 2020. ISSN:0013-4686 DOI:https://doi.org/10.1016/j.electacta.2020.136756. Available at: http://www.sciencedirect.com/science/article/pii/S001346862031149X. Access at: 2020 Oct. 01.

CABRAL, Luís *et al.* Tuning the Magnetic Properties of FeCo Thin Films through the Magnetoelastic Effect Induced by the Au Underlayer Thickness. **ACS Applied Materials & Interfaces,** [s.l.], v. 11, n. 1, p. 1529-1537, 2019. ISSN:1944-8244 DOI:10.1021/acsami.8b14736. Available at: https://doi.org/10.1021/acsami.8b14736. Access at: 2019 Jan. 09.

CAO, Chunhua *et al.* In situ preparation of magnetic Fe3O4/chitosan nanoparticles via a novel reduction–precipitation method and their application in adsorption of reactive azo dye. **Powder Technology,** [s.l.], v. 260, p. 90-97, 2014. ISSN:0032-5910 DOI:http://dx.doi.org/10.1016/j.powtec.2014.03.025. Available at: http://www.sciencedirect.com/science/article/pii/S0032591014002253. Access at: 2015 Aug. 02.

CAO, Xianyi *et al.* Engineering two-dimensional layered nanomaterials for wearable biomedical sensors and power devices. **Materials Chemistry Frontiers,** [s.l.], v. 2, n. 11, p. 1944-1986, 2018. DOI:10.1039/C8QM00356D. Available at: http://dx.doi.org/10.1039/C8QM00356D.

CASTRO, Vinícius F; DE QUEIROZ, Alvaro AA. Pontos quânticos magneto ativos: uma nova fronteira para a medicina terapêutica e diagnóstica. **Rev Bras Fís Méd,** [s.l.], v. 4, n. 3, p. 15-18, 2011.

CASULA, M. F. *et al.* Near Equiatomic FeCo Nanocrystalline Alloy Embedded in an Alumina Aerogel Matrix: Microstructural Features and Related Magnetic Properties. **The Journal of Physical Chemistry B,** [s.l.], v. 109, n. 50, p. 23888-23895, 2005. ISSN:1520-6106 DOI:10.1021/jp0546554. Available at: https://doi.org/10.1021/jp0546554. Access at: 2019 Dec. 20.

CERVELLINO, Antonio *et al.* Lattice parameters and site occupancy factors of magnetite-maghemite core-shell nanoparticles. A critical study. **Journal of Applied Crystallography,** [s.l.], v. 47, n. 5, p. 1755-1761, 2014. ISSN:1600-5767 DOI:doi:10.1107/S1600576714019840. Available at: https://doi.org/10.1107/S1600576714019840. Access at: 2014 Dec. 29.

CESTARI, Antonio R. *et al.* A novel and efficient epoxy/chitosan cement slurry for use in severe acidic environments of oil wells—Structural characterization and kinetic modeling. **Journal of Hazardous Materials,** [s.l.], v. 213-214, p. 109-116, 2012. ISSN:0304-3894 DOI:https://doi.org/10.1016/j.jhazmat.2012.01.068. Available at: http://www.sciencedirect.com/science/article/pii/S0304389412001100. Access at: 2014 Apr. 30.

CHAN, Ming-Hsien; LIU, Ru-Shi; HSIAO, Michael. Graphitic carbon nitride-based nanocomposites and their biological applications: a review. **Nanoscale,** [s.l.], v. 11, n. 32, p. 14993-15003, 2019. ISSN:2040-3364 DOI:10.1039/C9NR04568F. Available at: http://dx.doi.org/10.1039/C9NR04568F. Access at: 2020 Dec. 12.

CHAUBEY, Girija S. *et al.* Synthesis and Stabilization of FeCo Nanoparticles. **Journal of the American Chemical Society,** [s.l.], v. 129, n. 23, p. 7214-7215, 2007. ISSN:0002-7863 DOI:10.1021/ja0708969. Available at: https://doi.org/10.1021/ja0708969. Access at: 2019 Jun. 13.

CHEN, Dong *et al.* Super-adsorbent material based on functional polymer particles with a multilevel porous structure. **NPG Asia Mater,** [s.l.], v. 8, p. e301, 2016. DOI:10.1038/am.2016.117. Available at: http://dx.doi.org/10.1038/am.2016.117. Access at: 2015 Jan. 08.

CHEN, Hongmei *et al.* A facile and green microwave hydrothermal method for fabricating g-C3N4 nanosheets with improved hydrogen evolution performance. **Journal of Alloys and Compounds,** [s.l.], p. 158448, 2021. ISSN:0925-8388 DOI:https://doi.org/10.1016/j.jallcom.2020.158448. Available at: http://www.sciencedirect.com/science/article/pii/S0925838820348118. Access at: 2021 Jan. 11.

CHEN, Ku-Fan; LI, Shaolin; ZHANG, Wei-xian. Renewable hydrogen generation by bimetallic zero valent iron nanoparticles. **Chemical Engineering Journal,** [s.l.], v. 170, n. 2, p. 562-567, 2011. ISSN:1385-8947 DOI:https://doi.org/10.1016/j.cej.2010.12.019. Available at: http://www.sciencedirect.com/science/article/pii/S1385894710012234. Access at: 2020 Jan. 10.

CHEN, Liang *et al.* Adsorption mechanism of copper ions in aqueous solution by chitosan–carboxymethyl starch composites. **Journal of Applied Polymer Science,** [s.l.], v. 137, n. 18, p. 48636, 2020. ISSN:0021-8995 DOI:10.1002/app.48636. Available at: https://onlinelibrary.wiley.com/doi/abs/10.1002/app.48636. Access at: 2014 Dec 22.

CHEN, Meng *et al.* Silver Nanoparticles Capped by Oleylamine: Formation, Growth, and Self-Organization. **Langmuir,** [s.l.], v. 23, n. 10, p. 5296-5304, 2007. ISSN:0743-7463 DOI:10.1021/la700553d. Available at: https://doi.org/10.1021/la700553d. Access at: Access at: 2019 Jan. 18.

CHEN, Shuai *et al.* Self-Assembly of Perylene Imide Molecules into 1D Nanostructures: Methods, Morphologies, and Applications. **Chemical Reviews,** [s.l.], v. 115, n. 21, p. 11967-11998, 2015. ISSN:0009-2665 DOI:10.1021/acs.chemrev.5b00312. Available at: https://doi.org/10.1021/acs.chemrev.5b00312. Access at: 2020 Feb. 11.

CHEN, Y. *et al.* Two-Dimensional Nanomaterials for Cancer Nanotheranostics. **Small,** [s.l.], v. 13, n. 10, 2017. ISSN:1613-6810 DOI:10.1002/smll.201603446 Access at: 2020 Feb. 02.

CHEN, Ye *et al.* Two-Dimensional Metal Nanomaterials: Synthesis, Properties, and Applications. **Chemical Reviews,** [s.l.], v. 118, n. 13, p. 6409-6455, 2018. ISSN:0009-2665 DOI:10.1021/acs.chemrev.7b00727. Available at: https://doi.org/10.1021/acs.chemrev.7b00727. Access at: 2020 Feb. 01.

CHIDHAMBARAM, N.; RAVICHANDRAN, K. Single step transformation of urea into metal-free g-C3N4 nanoflakes for visible light photocatalytic applications. **Materials Letters,** [s.l.], v. 207, p. 44-48, 2017. ISSN:0167-577X DOI:https://doi.org/10.1016/j.matlet.2017.07.040. Available at: http://www.sciencedirect.com/science/article/pii/S0167577X17310789. Access at: 2017 Nov. 15.

CHOI, Dong Hyeok; SHIM, In-Bo; KIM, Chul Sung. Mössbauer study of antiferromagnetic CuFeO2. **Journal of Magnetism and Magnetic Materials,** [s.l.], v. 320, n. 20, p. e575-e577, 2008. ISSN:0304-8853 DOI:https://doi.org/10.1016/j.jmmm.2008.04.018. Available at: http://www.sciencedirect.com/science/article/pii/S0304885308004253. Access at: 2019 Nov. 05.

COSTA, Bianca; ILEM-ÖZDEMIR, Derya; SANTOS-OLIVEIRA, Ralph. Technetium-99m metastable radiochemistry for pharmaceutical applications: old chemistry for new products. **Journal of Coordination Chemistry,** [s.l.], v. 72, n. 11, p. 1759-1784, 2019. ISSN:0095-8972 DOI:10.1080/00958972.2019.1632838. Available at: https://doi.org/10.1080/00958972.2019.1632838. Access at: 2020 Nov. 25.

COWBURN, R. P. Property variation with shape in magnetic nanoelements. **Journal of Physics D: Applied Physics,** [s.l.], v. 33, n. 1, p. R1-R16, 1999. ISSN:0022-3727

1361-6463 DOI:10.1088/0022-3727/33/1/201. Available at: http://dx.doi.org/10.1088/0022-3727/33/1/201. Access at: 2019 Dec. 22.

CRESPO, P. *et al.* Mössbauer spectroscopy evidence of a spinodal mechanism for the thermal decomposition of f.c.c. FeCu. **Acta Materialia,** [s.l.], v. 46, n. 12, p. 4161-4166, 1998. ISSN:1359-6454 DOI:https://doi.org/10.1016/S1359-6454(98)00111-6. Available at: http://www.sciencedirect.com/science/article/pii/S1359645498001116. Access at: 2020 Feb. 02.

CUI, Jing-Jing *et al.* Facile preparation of magnetic chitosan modified with thiosemicarbazide for adsorption of copper ions from aqueous solution. **Journal of Applied Polymer Science,** [s.l.], v. 134, n. 9, p. n/a-n/a, 2017. ISSN:1097-4628 DOI:10.1002/app.44528. Available at: http://dx.doi.org/10.1002/app.44528. 2015 Feb. 15.

DEMARCHI, Carla Albertina; CAMPOS, Mayara; RODRIGUES, Clóvis Antonio. Adsorption of textile dye Reactive Red 120 by the chitosan–Fe(III)-crosslinked: Batch and fixed-bed studies. **Journal of Environmental Chemical Engineering,** [s.l.], v. 1, n. 4, p. 1350-1358, 2013. ISSN:2213-3437 DOI:http://dx.doi.org/10.1016/j.jece.2013.10.005. Available at: http://www.sciencedirect.com/science/article/pii/S2213343713001978. Access at: 2015 Feb. 12.

DENG, Yaocheng *et al.* Facile fabrication of a direct Z-scheme Ag2CrO4/g-C3N4 photocatalyst with enhanced visible light photocatalytic activity. **Journal of Molecular Catalysis A: Chemical,** [s.l.], v. 421, p. 209-221, 2016. ISSN:1381-1169 DOI:https://doi.org/10.1016/j.molcata.2016.05.024. Available at: http://www.sciencedirect.com/science/article/pii/S1381116916302060. Access at: 2019 Mar. 25. 2016/09/01/.

DENG, Yaoyao *et al.* One-dimensional nitrogen-doped carbon frameworks embedded with zinc-cobalt nanoparticles for efficient overall water splitting. **Journal of Colloid and Interface Science,** [s.l.], v. 585, p. 800-807, 2021. ISSN:0021-9797 DOI:https://doi.org/10.1016/j.jcis.2020.10.060. Available at: https://www.sciencedirect.com/science/article/pii/S0021979720314004. Access at: 2021 MAr. 01.

DONG, Guoping *et al.* A fantastic graphitic carbon nitride (g-C3N4) material: Electronic structure, photocatalytic and photoelectronic properties. **Journal of Photochemistry and Photobiology C: Photochemistry Reviews,** [s.l.], v. 20, p. 33-50, 2014. ISSN:1389-5567 DOI:https://doi.org/10.1016/j.jphotochemrev.2014.04.002. Available at: https://www.sciencedirect.com/science/article/pii/S1389556714000203. Access at: 2020 Nov. 16.

DONG, Jian *et al.* Fabrication of PEGylated graphitic carbon nitride quantum dots as traceable, pH-sensitive drug delivery systems. **New Journal of Chemistry,** [s.l.], v. 42, n. 17,

p. 14263-14270, 2018. ISSN:1144-0546 DOI:10.1039/C8NJ02542H. Available at: http://dx.doi.org/10.1039/C8NJ02542H. Access at: 2020 Feb. 02.

DOS SANTOS, Sofia Nascimento *et al.* Avoiding the mononuclear phagocyte system using human albumin for mesoporous silica nanoparticle system. **Microporous and Mesoporous Materials,** [s.l.], v. 251, p. 181-189, 2017. ISSN:1387-1811 DOI:https://doi.org/10.1016/j.micromeso.2017.06.005. Available at: http://www.sciencedirect.com/science/article/pii/S1387181117304018. Access at: 2017 Oct. 01.

DU, Xing *et al.* Control of submerged hollow fiber membrane fouling caused by fine particles in photocatalytic membrane reactors using bubbly flow: Shear stress and particle forces analysis. **Separation and Purification Technology,** [s.l.], v. 172, p. 130-139, 2017. ISSN:1383-5866 DOI:https://doi.org/10.1016/j.seppur.2016.08.011. Available at: http://www.sciencedirect.com/science/article/pii/S1383586616313399. Access at: 2020 Feb. 02.

EL-ZAWAHRY, Manal M. *et al.* Equilibrium and kinetic models on the adsorption of Reactive Black 5 from aqueous solution using Eichhornia crassipes/chitosan composite. **Carbohydrate Polymers,** [s.l.], v. 136, p. 507-515, 2016. ISSN:0144-8617 DOI:https://doi.org/10.1016/j.carbpol.2015.09.071. Available at: http://www.sciencedirect.com/science/article/pii/S0144861715009364. Access at: 2016 Jan 20.

ELWAKEEL, Khalid Z. *et al.* Comparison between the removal of Reactive Black 5 from aqueous solutions by 3-amino-1,2,4 triazole,5-thiol and melamine grafted chitosan prepared through four different routes. **Journal of Environmental Chemical Engineering,** [s.l.], v. 4, n. 1, p. 733-745, 2016. ISSN:2213-3437 DOI:http://dx.doi.org/10.1016/j.jece.2015.12.015. Available at: http://www.sciencedirect.com/science/article/pii/S2213343715301056. Access at: 2016 Mar. 01.

ERDMANN, Kati *et al.* Chemosensitizing effects of carbon-based nanomaterials in cancer cells: enhanced apoptosis and inhibition of proliferation as underlying mechanisms. **Nanotechnology,** [s.l.], v. 25, n. 40, p. 405102, 2014. ISSN:0957-4484 1361-6528 DOI:10.1088/0957-4484/25/40/405102. Available at: http://dx.doi.org/10.1088/0957-4484/25/40/405102. Access at: 2014 Sep. 16.

ERDMANN, Kati *et al.* Carbon nanomaterials sensitize prostate cancer cells to docetaxel and mitomycin C via induction of apoptosis and inhibition of proliferation. **Beilstein journal of nanotechnology,** [s.l.], v. 8, p. 1307-1317, 2017. ISSN:2190-4286 DOI:10.3762/bjnano.8.132. Available at: https://pubmed.ncbi.nlm.nih.gov/28690966

https://www.ncbi.nlm.nih.gov/pmc/articles/PMC5496539/. Access at: 2020 Nov. 02.

ESSAJAI, Rida *et al.* Shape-dependent structural and magnetic properties of Fe nanoparticles studied through simulation methods. **RSC Advances,** [s.l.], v. 9, n. 38, p. 22057-22063, 2019. DOI:10.1039/C9RA03047F. Available at: http://dx.doi.org/10.1039/C9RA03047F.

FAN, Xiangqian *et al.* Improved photocatalytic activity of g-C3N4 derived from cyanamide–urea solution. **RSC Advances,** [s.l.], v. 5, n. 11, p. 8323-8328, 2015. DOI:10.1039/C4RA16362A. Available at: http://dx.doi.org/10.1039/C4RA16362A. Access at: 2020 Feb. 02.

FENG, Chengyang *et al.* Core-shell Ag2CrO4/N-GQDs@g-C3N4 composites with anti-photocorrosion performance for enhanced full-spectrum-light photocatalytic activities. **Applied Catalysis B: Environmental,** [s.l.], v. 239, p. 525-536, 2018. ISSN:0926-3373 DOI:https://doi.org/10.1016/j.apcatb.2018.08.049. Available at: http://www.sciencedirect.com/science/article/pii/S0926337318307872. Access at: 2018 Dec. 30.

FENG, Lili *et al.* g-C3N4 Coated Upconversion Nanoparticles for 808 nm Near-Infrared Light Triggered Phototherapy and Multiple Imaging. **Chemistry of Materials,** [s.l.], v. 28, n. 21, p. 7935-7946, 2016. ISSN:0897-4756 DOI:10.1021/acs.chemmater.6b03598. Available at: https://doi.org/10.1021/acs.chemmater.6b03598. Access at: 2016 Nov. 08.

FERRANDO, Riccardo; JELLINEK, Julius; JOHNSTON, Roy L. Nanoalloys: From Theory to Applications of Alloy Clusters and Nanoparticles. **Chemical Reviews,** [s.l.], v. 108, n. 3, p. 845-910, 2008. ISSN:0009-2665 DOI:10.1021/cr040090g. Available at: https://doi.org/10.1021/cr040090g. Access at: 2019 Feb. 22.

FONTECHA-CÁMARA, María A. *et al.* Mixed iron oxides as Fenton catalysts for gallic acid removal from aqueous solutions. **Applied Catalysis B: Environmental,** [s.l.], v. 196, n. Supplement C, p. 207-215, 2016. ISSN:0926-3373 DOI:https://doi.org/10.1016/j.apcatb.2016.05.032. Available at: http://www.sciencedirect.com/science/article/pii/S0926337316303800. Access at: 2016 Nov. 05.

FOREST, Valérie *et al.* Nano to micron-sized particle detection in patients' lungs and its pathological significance. **Environmental Science: Nano,** [s.l.], v. 6, n. 5, p. 1343-1350, 2019. ISSN:2051-8153 DOI:10.1039/C8EN01301B. Available at: http://dx.doi.org/10.1039/C8EN01301B.

FREIRE, R. M. *et al.* Nanocrystal growth, magnetic and electrochemical properties of NiZn ferrite. **Journal of Alloys and Compounds,** [s.l.], v. 738, p. 206-217, 2018. ISSN:0925-8388 DOI:https://doi.org/10.1016/j.jallcom.2017.12.088. Available at: https://www.sciencedirect.com/science/article/pii/S0925838817342718. Access at: 2018 Mar. 25.

FREIRE, R. M. *et al.* Natural arrangement of AgCu bimetallic nanostructures through oleylamine reduction. **Inorganic Chemistry Frontiers,** [s.l.], v. 7, n. 24, p. 4902-4912, 2020. DOI:10.1039/D0QI00940G. Available at: http://dx.doi.org/10.1039/D0QI00940G. Access at: 2021 Feb. 02.

FREIRE, T. M. *et al.* Fast ultrasound assisted synthesis of chitosan-based magnetite nanocomposites as a modified electrode sensor. **Carbohydrate Polymers,** [s.l.], v. 151, p. 760-769, 2016. ISSN:0144-8617 DOI:https://doi.org/10.1016/j.carbpol.2016.05.095. Available at: http://www.sciencedirect.com/science/article/pii/S0144861716306397. Access at: 2016 Oct. 20.

FRENZEL, H; SCHULTES, H %J Zeitschrift für Physikalische Chemie. Luminescenz im ultraschallbeschickten Wasser. [s.l.], v. 27, n. 1, p. 421-424, 1934. ISSN:2196-7156

FREUNDLICH, Herbert. **Colloid & capillary chemistry**. ed.: Methuen & co. ltd, 1926.

GALVÃO, Wesley S. *et al.* Super-Paramagnetic Nanoparticles with Spinel Structure: A Review of Synthesis and Biomedical Applications. **Solid State Phenomena,** [s.l.], v. 241, p. 139-176, 2016. ISSN:1662-9779 DOI:10.4028/www.scientific.net/SSP.241.139. Available at: https://www.scientific.net/SSP.241.139.

GAO, Guanhua *et al.* Shape-Controlled Synthesis and Magnetic Properties of Monodisperse Fe3O4 Nanocubes. **Crystal Growth & Design,** [s.l.], v. 10, n. 7, p. 2888-2894, 2010. ISSN:1528-7483 DOI:10.1021/cg900920q. Available at: https://doi.org/10.1021/cg900920q. Access at: 2019 Sep. 07..

GAO, Mingyang *et al.* The role of adsorbed oleylamine on gold catalysts during synthesis for highly selective electrocatalytic reduction of CO2 to CO. **Chemical Communications,** [s.l.], v. 56, n. 51, p. 7021-7024, 2020. ISSN:1359-7345 DOI:10.1039/D0CC01088J. Available at: http://dx.doi.org/10.1039/D0CC01088J.

GARBUZENKO, Olga B. *et al.* Inhalation treatment of lung cancer: the influence of composition, size and shape of nanocarriers on their lung accumulation and retention. **Cancer biology & medicine,** [s.l.], v. 11, n. 1, p. 44-55, 2014. ISSN:2095-3941 DOI:10.7497/j.ISSN.2095-3941.2014.01.004. Available at: https://pubmed.ncbi.nlm.nih.gov/24738038

GAWANDE, Manoj B.; BRANCO, Paula S.; VARMA, Rajender S. Nano-magnetite (Fe3O4) as a support for recyclable catalysts in the development of sustainable methodologies. **Chemical Society reviews,** [s.l.], v. 42, n. 8, p. 3371-3393, 2013. ISSN:0306-0012 DOI:10.1039/C3CS35480F. Available at: http://dx.doi.org/10.1039/C3CS35480F.

GHOSH CHAUDHURI, Rajib; PARIA, Santanu. Core/shell nanoparticles: classes, properties, synthesis mechanisms, characterization, and applications. **Chemical reviews,** [s.l.], v. 112, n. 4, p. 2373-2433, 2011. ISSN:0009-2665

GHOSH CHAUDHURI, Rajib; PARIA, Santanu. Core/Shell Nanoparticles: Classes, Properties, Synthesis Mechanisms, Characterization, and Applications. **Chemical Reviews,** [s.l.], v. 112, n. 4, p. 2373-2433, 2012. ISSN:0009-2665 DOI:10.1021/cr100449n. Available at: https://doi.org/10.1021/cr100449n. Access at: 2020 Nov. 11.

GILIOPOULOS, Dimitrios *et al.* Polymer/Metal Organic Framework (MOF) Nanocomposites for Biomedical Applications. **Molecules,** [s.l.], v. 25, n. 1, 2020. ISSN:1420-3049 DOI:10.3390/molecules25010185

GILROY, Kyle D. *et al.* Bimetallic Nanocrystals: Syntheses, Properties, and Applications. **Chemical Reviews,** [s.l.], v. 116, n. 18, p. 10414-10472, 2016. ISSN:0009-2665 DOI:10.1021/acs.chemrev.6b00211. Available at: https://doi.org/10.1021/acs.chemrev.6b00211. Access at: 201 Sep. 28.

GRAY, Evan P. *et al.* Chemical and Colloidal Dynamics of MnO2 Nanosheets in Biological Media Relevant for Nanosafety Assessment. **Small,** [s.l.], v. 16, n. 21, p. 2000303, 2020. ISSN:1613-6810 DOI:https://doi.org/10.1002/smll.202000303. Available at: https://doi.org/10.1002/smll.202000303. Access at: 2020 May 01.

GUO, Hai *et al.* Steering exciton dissociation and charge migration in green synthetic oxygen-substituted ultrathin porous graphitic carbon nitride for boosted photocatalytic reactive oxygen species generation. **Chemical Engineering Journal,** [s.l.], v. 385, p. 123919, 2020. ISSN:1385-8947 DOI:https://doi.org/10.1016/j.cej.2019.123919. Available at: http://www.sciencedirect.com/science/article/pii/S1385894719333340. Access at: 2020 Apr. 01.

GUO, Qianyi *et al.* Engineering the electronic structure and optical properties of g-C3N4 by non-metal ion doping. **Journal of Materials Chemistry C,** [s.l.], v. 4, n. 28, p. 6839-6847, 2016. ISSN:2050-7526 DOI:10.1039/C6TC01831A. Available at: http://dx.doi.org/10.1039/C6TC01831A.

GUO, Shuangzhen *et al.* Fe3O4-CS-L: a magnetic core-shell nano adsorbent for highly efficient methyl orange adsorption. **Water Science and Technology,** [s.l.], v. 77, n. 3, p. 628-637, 2017. ISSN:0273-1223 DOI:10.2166/wst.2017.602. Available at: https://doi.org/10.2166/wst.2017.602.

GUSTAFSON, Heather Herd *et al.* Nanoparticle Uptake: The Phagocyte Problem. **Nano today,** [s.l.], v. 10, n. 4, p. 487-510, 2015. ISSN:1748-0132

1878-044X DOI:10.1016/j.nantod.2015.06.006. Available at: https://pubmed.ncbi.nlm.nih.gov/26640510

GUTHA, Yuvaraja *et al.* Magnetic-epichlorohydrin crosslinked chitosan schiff’s base (m-ECCSB) as a novel adsorbent for the removal of Cu(II) ions from aqueous environment. **International Journal of Biological Macromolecules,** [s.l.], v. 97, p. 85-98, 2017. ISSN:0141-8130 DOI:http://dx.doi.org/10.1016/j.ijbiomac.2017.01.004. Available at: http://www.sciencedirect.com/science/article/pii/S0141813016322681. Access at: 2020 Feb. 25.

HAN, Qing *et al.* Graphene/graphitic carbon nitride hybrids for catalysis. **Materials Horizons,** [s.l.], v. 4, n. 5, p. 832-850, 2017. ISSN:2051-6347 DOI:10.1039/C7MH00379J. Available at: http://dx.doi.org/10.1039/C7MH00379J.

HAN, Yingchao *et al.* Sonochemical preparation of hydroxyapatite nanoparticles stabilized by glycosaminoglycans. **Ultrasonics Sonochemistry,** [s.l.], v. 14, n. 3, p. 286-290, 2007. ISSN:1350-4177 DOI:https://doi.org/10.1016/j.ultsonch.2006.06.002. Available at: https://www.sciencedirect.com/science/article/pii/S1350417706000708. Access at: 2016 Mar. 05.

HARADA, Masafumi *et al.* Cation Distribution in Monodispersed MFe2O4 (M = Mn, Fe, Co, Ni, and Zn) Nanoparticles Investigated by X-ray Absorption Fine Structure Spectroscopy: Implications for Magnetic Data Storage, Catalysts, Sensors, and Ferrofluids. **ACS Applied Nano Materials,** [s.l.], v. 3, n. 8, p. 8389-8402, 2020. DOI:10.1021/acsanm.0c01810. Available at: https://doi.org/10.1021/acsanm.0c01810. Access at: 2020 Aug. 28.

HO, Yuh-Shan. **Absorption of heavy metals from waste streams by peat.** 1995. p. University of Birmingham, 1995.

HOANG, V. Tran *et al.* Graphene oxide/Fe 3 O 4 /chitosan nanocomposite: a recoverable and recyclable adsorbent for organic dyes removal. Application to methylene blue. **Materials Research Express,** [s.l.], v. 4, n. 3, p. 035701, 2017. ISSN:2053-1591. Available at: http://stacks.iop.org/2053-1591/4/i=3/a=035701.

HU, Cun *et al.* Nickel Phosphide Electrocatalysts for Hydrogen Evolution Reaction. [s.l.], v. 10, n. 2, p. 188, 2020. ISSN:2073-4344. Available at: https://www.mdpi.com/2073-4344/10/2/188.

HUA, Ming *et al.* Simultaneous removal of As(V) and Cr(VI) from water by macroporous anion exchanger supported nanoscale hydrous ferric oxide composite. **Chemosphere,** [s.l.], v. 171, n. Supplement C, p. 126-133, 2017. ISSN:0045-6535 DOI:https://doi.org/10.1016/j.chemosphere.2016.12.051. Available at: http://www.sciencedirect.com/science/article/pii/S0045653516317714. Access at: 2017 Mar. 05.

HUANG, Meina *et al.* Preparation and enhanced photocatalytic activity of carbon nitride/titania(001 vs 101 facets)/reduced graphene oxide (g-C3N4/TiO2/rGO) hybrids under visible light. **Applied Surface Science,** [s.l.], v. 389, p. 1084-1093, 2016. ISSN:0169-4332 DOI:https://doi.org/10.1016/j.apsusc.2016.07.180. Available at: http://www.sciencedirect.com/science/article/pii/S0169433216316427. Access at: 2016 Dec. 15.

HUANG, Shuquan *et al.* Synthesis of carbon nitride in moist environments: A defect engineering strategy toward superior photocatalytic hydrogen evolution reaction. **Journal of Energy Chemistry,** [s.l.], v. 54, p. 403-413, 2021. ISSN:2095-4956 DOI:https://doi.org/10.1016/j.jechem.2020.05.062. Available at:

https://www.sciencedirect.com/science/article/pii/S2095495620303983. Access at: 2021 Mar. 01.

HUSSAIN, Sajid *et al.* Enhanced ibuprofen removal by heterogeneous-Fenton process over Cu/ZrO2 and Fe/ZrO2 catalysts. **Journal of Environmental Chemical Engineering,** [s.l.], v. 8, n. 1, p. 103586, 2020. ISSN:2213-3437 DOI:https://doi.org/10.1016/j.jece.2019.103586. Available at: http://www.sciencedirect.com/science/article/pii/S2213343719307092. Access at: 2020 Feb. 01.

IBRAHIM, A. *et al.* Nano-structured palladium impregnate graphitic carbon nitride composite for efficient hydrogen gas sensing. **International Journal of Hydrogen Energy,** [s.l.], v. 45, n. 17, p. 10623-10636, 2020. ISSN:0360-3199 DOI:https://doi.org/10.1016/j.ijhydene.2019.04.140. Available at: http://www.sciencedirect.com/science/article/pii/S0360319919315733. Access at: 2020 Mar. 27.

ISRAEL, Liron L. *et al.* Magnetic iron oxide nanoparticles for imaging, targeting and treatment of primary and metastatic tumors of the brain. **Journal of Controlled Release,** [s.l.], v. 320, p. 45-62, 2020. ISSN:0168-3659 DOI:https://doi.org/10.1016/j.jconrel.2020.01.009. Available at: https://www.sciencedirect.com/science/article/pii/S0168365920300171. Access at: 2020 Apr. 10.

JAGIEŁŁO, Joanna *et al.* Synthesis and Characterization of Graphene Oxide and Reduced Graphene Oxide Composites with Inorganic Nanoparticles for Biomedical Applications. **Nanomaterials,** [s.l.], v. 10, n. 9, 2020. ISSN:2079-4991 DOI:10.3390/nano10091846

JANA, Jayasmita; CHUNG, Jin Suk; HUR, Seung Hyun. Carbon dot supported bimetallic nanocomposite for the hydrogen evolution reaction. **Journal of Alloys and Compounds,** [s.l.], p. 157895, 2020. ISSN:0925-8388 DOI:https://doi.org/10.1016/j.jallcom.2020.157895. Available at: http://www.sciencedirect.com/science/article/pii/S0925838820342596. Access at: 2020 Nov. 12.

JANG, Jung-tak *et al.* Critical Enhancements of MRI Contrast and Hyperthermic Effects by Dopant-Controlled Magnetic Nanoparticles. **Angewandte Chemie International Edition,** [s.l.], v. 48, n. 7, p. 1234-1238, 2009. ISSN:1433-7851 DOI:https://doi.org/10.1002/anie.200805149. Available at: https://doi.org/10.1002/anie.200805149. Access at: 2019 Feb. 02.

JI, R. *et al.* Multibubble Sonochemistry and Sonoluminescence at 100 kHz: The Missing Link between Low- and High-Frequency Ultrasound. **The Journal of Physical Chemistry B,** [s.l.], v. 122, n. 27, p. 6989-6994, 2018. ISSN:1520-6106 DOI:10.1021/acs.jpcb.8b04267. Available at: https://doi.org/10.1021/acs.jpcb.8b04267. Access at: 2018 Sep. 12.

JIANG, Jizhou *et al.* Dependence of electronic structure of g-C3N4 on the layer number of its nanosheets: A study by Raman spectroscopy coupled with first-principles calculations.

Carbon, [s.l.], v. 80, p. 213-221, 2014. ISSN:0008-6223 DOI:https://doi.org/10.1016/j.carbon.2014.08.059. Available at: http://www.sciencedirect.com/science/article/pii/S0008622314007994. Access at: 2020 Dec. 01.

JIANG, Ru *et al.* Removal of methyl orange from aqueous solutions by magnetic maghemite/chitosan nanocomposite films: Adsorption kinetics and equilibrium. **Journal of Applied Polymer Science,** [s.l.], v. 125, n. S2, p. E540-E549, 2012. ISSN:0021-8995 DOI:10.1002/app.37003. Available at: https://onlinelibrary.wiley.com/doi/abs/10.1002/app.37003.

JIANG, Wenjun *et al.* Chromium(VI) removal by maghemite nanoparticles. **Chemical Engineering Journal,** [s.l.], v. 222, n. Supplement C, p. 527-533, 2013. ISSN:1385-8947 DOI:https://doi.org/10.1016/j.cej.2013.02.049. Available at: http://www.sciencedirect.com/science/article/pii/S1385894713002155. Access at: 2015 Mar. 15.

JIANG, Zhihong; HU, Dongying. Molecular mechanism of anionic dyes adsorption on cationized rice husk cellulose from agricultural wastes. **Journal of Molecular Liquids,** [s.l.], v. 276, p. 105-114, 2019. ISSN:0167-7322 DOI:https://doi.org/10.1016/j.molliq.2018.11.153. Available at: http://www.sciencedirect.com/science/article/pii/S0167732218341242. Access at: 2019 Feb. 15.

JIN, Chen *et al.* Controllable synthesis, formation mechanism, and enhanced microwave absorption of dendritic AgFe alloy/Fe3O4 nanocomposites. **CrystEngComm,** [s.l.], v. 20, n. 14, p. 1997-2009, 2018. DOI:10.1039/C7CE02223A. Available at: http://dx.doi.org/10.1039/C7CE02223A.

JIN, Huanyu *et al.* Emerging Two-Dimensional Nanomaterials for Electrocatalysis. **Chemical Reviews,** [s.l.], v. 118, n. 13, p. 6337-6408, 2018. ISSN:0009-2665 DOI:10.1021/acs.chemrev.7b00689. Available at: https://doi.org/10.1021/acs.chemrev.7b00689. Access at: 2019 Sep. 11.

JOHNSON, C. E.; RIDOUT, M. S.; CRANSHAW, T. E. The M ssbauer Effect in Iron Alloys. **Proceedings of the Physical Society,** [s.l.], v. 81, n. 6, p. 1079-1090, 1963. ISSN:0370-1328 DOI:10.1088/0370-1328/81/6/313. Available at: http://dx.doi.org/10.1088/0370-1328/81/6/313. Access at: 2019 Jun. 06.

JÓŹWIAK, Tomasz *et al.* Effect of ionic and covalent crosslinking agents on properties of chitosan beads and sorption effectiveness of Reactive Black 5 dye. **Reactive and Functional Polymers,** [s.l.], v. 114, p. 58-74, 2017. ISSN:1381-5148 DOI:https://doi.org/10.1016/j.reactfunctpolym.2017.03.007. Available at: http://www.sciencedirect.com/science/article/pii/S1381514817300482. Access at: 2014 May 05.

JUN, Young-wook; SEO, Jung-wook; CHEON, Jinwoo. Nanoscaling Laws of Magnetic Nanoparticles and Their Applicabilities in Biomedical Sciences. **Accounts of Chemical Research,** [s.l.], v. 41, n. 2, p. 179-189, 2008. ISSN:0001-4842 DOI:10.1021/ar700121f. Available at: https://doi.org/10.1021/ar700121f. Access at: 2020 Feb 05.

KIKUCHI, Teppei *et al.* Preparation of magnetite aqueous dispersion for magnetic fluid hyperthermia. **Journal of Magnetism and Magnetic Materials,** [s.l.], v. 323, n. 10, p. 1216-1222, 2011. ISSN:0304-8853

KIM, Tae-Young; PARK, Seung-Shik; CHO, Sung-Yong. Adsorption characteristics of Reactive Black 5 onto chitosan beads cross-linked with epichlorohydrin. **Journal of Industrial and Engineering Chemistry,** [s.l.], v. 18, n. 4, p. 1458-1464, 2012. ISSN:1226-086X DOI:http://dx.doi.org/10.1016/j.jiec.2012.02.006. Available at: http://www.sciencedirect.com/science/article/pii/S1226086X12000871. Access at: 2014 Nov. 25.

KIS-CSITÁRI, J.; KÓNYA, Z.; KIRICSI, I. Sonochemical Synthesis of Inorganic Nanoparticles. *In:* Functionalized Nanoscale Materials, Devices and Systems, 2008, Dordrecht. Dordrecht: Springer Netherlands, 2008. p.369-372.

KONG, Xiangkai *et al.* Elemental two-dimensional nanosheets beyond graphene. **Chemical Society reviews,** [s.l.], v. 46, n. 8, p. 2127-2157, 2017. ISSN:0306-0012 DOI:10.1039/C6CS00937A. Available at: http://dx.doi.org/10.1039/C6CS00937A.

KUMAR, Anurag *et al.* Metal-organic hybrid: Photoreduction of CO2 using graphitic carbon nitride supported heteroleptic iridium complex under visible light irradiation. **Carbon,** [s.l.], v. 123, p. 371-379, 2017. ISSN:0008-6223 DOI:https://doi.org/10.1016/j.carbon.2017.07.080. Available at: http://www.sciencedirect.com/science/article/pii/S0008622317307625. Access at: 2017 Oct. 01.

KUMARI, Madhu; PITTMAN, Charles U.; MOHAN, Dinesh. Heavy metals [chromium (VI) and lead (II)] removal from water using mesoporous magnetite (Fe3O4) nanospheres. **Journal of Colloid and Interface Science,** [s.l.], v. 442, p. 120-132, 2015. ISSN:0021-9797 DOI:https://doi.org/10.1016/j.jcis.2014.09.012. Available at: http://www.sciencedirect.com/science/article/pii/S0021979714006614. Access at: 2015 Mar. 15.

KUMRU, Baris; ANTONIETTI, Markus. Colloidal properties of the metal-free semiconductor graphitic carbon nitride. **Advances in Colloid and Interface Science,** [s.l.], v. 283, p. 102229, 2020. ISSN:0001-8686 DOI:https://doi.org/10.1016/j.cis.2020.102229. Available at: https://www.sciencedirect.com/science/article/pii/S000186862030378X. Access at: 2020 Sep. 01.

KUNZE, Sebastian *et al.* Operando NRIXS and XAFS Investigation of Segregation Phenomena in Fe-Cu and Fe-Ag Nanoparticle Catalysts during CO2 Electroreduction.

Angewandte Chemie International Edition, [s.l.], v. 59, n. 50, p. 22667-22674, 2020. ISSN:1433-7851 DOI:https://doi.org/10.1002/anie.202010535. Available at: https://doi.org/10.1002/anie.202010535. Access at: 2020 Dec. 07.

KYZAS, George Z.; KOSTOGLOU, Margaritis; LAZARIDIS, Nikolaos K. Relating Interactions of Dye Molecules with Chitosan to Adsorption Kinetic Data. **Langmuir,** [s.l.], v. 26, n. 12, p. 9617-9626, 2010. ISSN:0743-7463 DOI:10.1021/la100206y. Available at: http://dx.doi.org/10.1021/la100206y. Access at: 2015 Jul. 15.

KYZAS, George Z. *et al.* Environmental friendly technology for the removal of pharmaceutical contaminants from wastewaters using modified chitosan adsorbents. **Chemical Engineering Journal,** [s.l.], v. 222, p. 248-258, 2013. ISSN:1385-8947 DOI:http://dx.doi.org/10.1016/j.cej.2013.02.048. Available at: http://www.sciencedirect.com/science/article/pii/S1385894713002143. Access at: 2015 Apr. 15.

LAGRERGEN, S. Zur Theorie Der Sogenannten Adsorption Gelöster Stoffe Kungliga Svenska Vetenskapsakademiens. **Handlingar,** [s.l.], v. 24, n. 4, p. 1-39, 1898.

LANGMUIR, Irving. THE ADSORPTION OF GASES ON PLANE SURFACES OF GLASS, MICA AND PLATINUM. **Journal of the American Chemical Society,** [s.l.], v. 40, n. 9, p. 1361-1403, 1918. ISSN:0002-7863 DOI:10.1021/ja02242a004. Available at: https://doi.org/10.1021/ja02242a004. Access at: 2019 Sep. 01.

LEONEL, Alice G.; MANSUR, Alexandra A. P.; MANSUR, Herman S. Advanced Functional Nanostructures based on Magnetic Iron Oxide Nanomaterials for Water Remediation: A Review. **Water Research,** [s.l.], v. 190, p. 116693, 2021. ISSN:0043-1354 DOI:https://doi.org/10.1016/j.watres.2020.116693. Available at: https://www.sciencedirect.com/science/article/pii/S0043135420312288. Access at: 2021 Feb. 15.

LESZCZYŃSKI, Błażej *et al.* The influence of oxidation process on exchange bias in egg-shaped FeO/Fe 3 O 4 core/shell nanoparticles. **Journal of Magnetism and Magnetic Materials,** [s.l.], v. 416, p. 269-274, 2016. ISSN:0304-8853

LI, Hao *et al.* Construction of a well-dispersed Ag/graphene-like g-C3N4 photocatalyst and enhanced visible light photocatalytic activity. **RSC Advances,** [s.l.], v. 7, n. 14, p. 8688-8693, 2017. DOI:10.1039/C6RA26498K. Available at: http://dx.doi.org/10.1039/C6RA26498K.

LI, Junrui *et al.* Hard-Magnet L10-CoPt Nanoparticles Advance Fuel Cell Catalysis. **Joule,** [s.l.], v. 3, n. 1, p. 124-135, 2019. ISSN:2542-4351 DOI:https://doi.org/10.1016/j.joule.2018.09.016. Available at: https://www.sciencedirect.com/science/article/pii/S2542435118304549. Access at: 2019 Jan. 16.

LI, Kexin *et al.* The synergistic photocatalytic effects of surface-modified g-C3N4 in simple and complex pollution systems based on a macro-thermodynamic model. **Environmental Science: Nano,** [s.l.], v. 8, n. 1, p. 217-232, 2021. ISSN:2051-8153 DOI:10.1039/D0EN00759E. Available at: http://dx.doi.org/10.1039/D0EN00759E.

LI, Xuemei *et al.* Single Crystalline Trigonal Selenium Nanotubes and Nanowires Synthesized by Sonochemical Process. **Crystal Growth & Design,** [s.l.], v. 5, n. 3, p. 911-916, 2005. ISSN:1528-7483 DOI:10.1021/cg049681q. Available at: http://dx.doi.org/10.1021/cg049681q. Access at: 2019 Oct. 24.

LI, Zhanfeng *et al.* Sonochemical fabrication of inorganic nanoparticles for applications in catalysis. **Ultrasonics Sonochemistry,** [s.l.], v. 71, p. 105384, 2021. ISSN:1350-4177 DOI:https://doi.org/10.1016/j.ultsonch.2020.105384. Available at: https://www.sciencedirect.com/science/article/pii/S1350417720316886. Access at: 2021 Mar. 01.

LIMA-SOUSA, Rita *et al.* Injectable in situ forming thermo-responsive graphene based hydrogels for cancer chemo-photothermal therapy and NIR light-enhanced antibacterial applications. **Materials Science and Engineering: C,** [s.l.], v. 117, p. 111294, 2020. ISSN:0928-4931 DOI:https://doi.org/10.1016/j.msec.2020.111294. Available at: http://www.sciencedirect.com/science/article/pii/S0928493120332124. Access at: 2020 Dec. 01.

LIN, Chuchu *et al.* Metal-free two-dimensional nanomaterial-mediated photothermal tumor therapy. **Smart Materials in Medicine,** [s.l.], v. 1, p. 150-167, 2020. ISSN:2590-1834 DOI:https://doi.org/10.1016/j.smaim.2020.09.001. Available at: https://www.sciencedirect.com/science/article/pii/S2590183420300156. Access at: 2020 Jan . 01.

LIN, Li-Sen *et al.* Graphitic-phase C3N4 nanosheets as efficient photosensitizers and pH-responsive drug nanocarriers for cancer imaging and therapy. **Journal of Materials Chemistry B,** [s.l.], v. 2, n. 8, p. 1031-1037, 2014. ISSN:2050-750X DOI:10.1039/C3TB21479F. Available at: http://dx.doi.org/10.1039/C3TB21479F.

LIU, Amy Y.; COHEN, Marvin L. Prediction of New Low Compressibility Solids. **Science,** [s.l.], v. 245, n. 4920, p. 841, 1989. DOI:10.1126/science.245.4920.841. Available at: http://science.sciencemag.org/content/245/4920/841.abstract.

LIU, Chaoqun *et al.* Graphitic carbon nitride nanosheets as a multifunctional nanoplatform for photochemical internalization-enhanced photodynamic therapy. **Journal of Materials Chemistry B,** [s.l.], v. 6, n. 47, p. 7908-7915, 2018. ISSN:2050-750X DOI:10.1039/C8TB02535E. Available at: http://dx.doi.org/10.1039/C8TB02535E.

LIU, Hongji *et al.* Synthesis and biomedical applications of graphitic carbon nitride quantum dots. **Journal of Materials Chemistry B,** [s.l.], v. 7, n. 36, p. 5432-5448, 2019. ISSN:2050-750X DOI:10.1039/C9TB01410A. Available at: http://dx.doi.org/10.1039/C9TB01410A.

LIU, Lingli *et al.* Facile preparation of chitosan enwrapping Fe3O4 nanoparticles and MIL-101(Cr) magnetic composites for enhanced methyl orange adsorption. **Journal of Porous Materials,** [s.l.], v. 23, n. 5, p. 1363-1372, 2016. ISSN:1573-4854 DOI:10.1007/s10934-016-0195-y. Available at: https://doi.org/10.1007/s10934-016-0195-y. Access at: 2016 Oct. 01.

LIU, Zhongmin *et al.* Synthesis of magnetic orderly mesoporous α-Fe2O3 nanocluster derived from MIL-100(Fe) for rapid and efficient arsenic(III,V) removal. **Journal of Hazardous Materials,** [s.l.], v. 343, n. Supplement C, p. 304-314, 2018. ISSN:0304-3894 DOI:https://doi.org/10.1016/j.jhazmat.2017.09.047. Available at: http://www.sciencedirect.com/science/article/pii/S0304389417307379. Access at: 2018 Feb. 05.

LÓPEZ-ORTEGA, Alberto *et al.* Applications of exchange coupled bi-magnetic hard/soft and soft/hard magnetic core/shell nanoparticles. **Physics Reports,** [s.l.], v. 553, p. 1-32, 2015. ISSN:0370-1573

LOW, Suk Khe; TAN, Mei Ching; CHIN, Nyuk Ling. Effect of ultrasound pre-treatment on adsorbent in dye adsorption compared with ultrasound simultaneous adsorption. **Ultrasonics Sonochemistry,** [s.l.], v. 48, p. 64-70, 2018. ISSN:1350-4177 DOI:https://doi.org/10.1016/j.ultsonch.2018.05.024. Available at: http://www.sciencedirect.com/science/article/pii/S1350417718300609. Access at: 2018 Nov. 01.

LU, An-Hui; SALABAS, E. L; SCHÜTH, Ferdi. Magnetic Nanoparticles: Synthesis, Protection, Functionalization, and Application. **Angewandte Chemie International Edition,** [s.l.], v. 46, n. 8, p. 1222-1244, 2007. ISSN:1433-7851 DOI:https://doi.org/10.1002/anie.200602866. Available at: https://doi.org/10.1002/anie.200602866. Access at: 2019 Nov. 27.

LU, Jiaying *et al.* Molybdenum disulfide nanosheets: From exfoliation preparation to biosensing and cancer therapy applications. **Colloids and Surfaces B: Biointerfaces,** [s.l.], v. 194, p. 111162, 2020. ISSN:0927-7765 DOI:https://doi.org/10.1016/j.colsurfb.2020.111162. Available at: http://www.sciencedirect.com/science/article/pii/S092777652030518X. Access at: 2020 Oct. 01.

MA, Zizai *et al.* Self-supported porous Ni-Fe-P composite as an efficient electrocatalyst for hydrogen evolution reaction in both acidic and alkaline medium. **Electrochimica Acta,** [s.l.], v. 219, p. 194-203, 2016. ISSN:0013-4686 DOI:https://doi.org/10.1016/j.electacta.2016.10.004. Available at: http://www.sciencedirect.com/science/article/pii/S0013468616320916. Access at: 2016 Nov. 20.

MAEDA, Kazuhiko *et al.* Photocatalytic Activities of Graphitic Carbon Nitride Powder for Water Reduction and Oxidation under Visible Light. **The Journal of Physical Chemistry C,** [s.l.], v. 113, n. 12, p. 4940-4947, 2009. ISSN:1932-7447 DOI:10.1021/jp809119m. Available at: https://doi.org/10.1021/jp809119m. Access at: 2020 Nov. 26.

MAHMOOD, M. *et al.* Carbon nanotubes enhance the internalization of drugs by cancer cells and decrease their chemoresistance to cytostatics. **Nanotechnology,** [s.l.], v. 24, n. 4, p. 045102, 2013. ISSN:0957-4484

1361-6528 DOI:10.1088/0957-4484/24/4/045102. Available at: http://dx.doi.org/10.1088/0957-4484/24/4/045102. Access at: 2019 Aug. 04.

MAJDOUB, Mohammed; ANFAR, Zakaria; AMEDLOUS, Abdallah. Emerging Chemical Functionalization of g-C3N4: Covalent/Noncovalent Modifications and Applications. **ACS Nano,** [s.l.], v. 14, n. 10, p. 12390-12469, 2020. ISSN:1936-0851 DOI:10.1021/acsnano.0c06116. Available at: https://doi.org/10.1021/acsnano.0c06116. Access at: 2020 Oct. 27.

MAJIDI, Sima *et al.* Current methods for synthesis of magnetic nanoparticles. **Artificial Cells, Nanomedicine, and Biotechnology,** [s.l.], v. 44, n. 2, p. 722-734, 2016. ISSN:2169-1401 DOI:10.3109/21691401.2014.982802. Available at: https://doi.org/10.3109/21691401.2014.982802. Access at: 2020 Feb. 02.

MANCIER, Valérie *et al.* Morphologic, magnetic, and Mössbauer spectral properties of Fe75Co25 nanoparticles prepared by ultrasound-assisted electrochemistry. **Journal of Magnetism and Magnetic Materials,** [s.l.], v. 281, n. 1, p. 27-35, 2004. ISSN:0304-8853 DOI:https://doi.org/10.1016/j.jmmm.2004.03.047. Available at: http://www.sciencedirect.com/science/article/pii/S0304885304003099. Access at: 2020 Feb. 24.

MARQUES, J. S. *et al.* Comparing homogeneous and heterogeneous routes for ionic crosslinking of chitosan membranes. **Reactive and Functional Polymers,** [s.l.], v. 103, p. 156-161, 2016. ISSN:1381-5148 DOI:http://dx.doi.org/10.1016/j.reactfunctpolym.2016.04.014. Available at: http://www.sciencedirect.com/science/article/pii/S1381514816300797. Access at: 2019 Apr.24.

MARTHA, Satyabadi; NASHIM, Amtul; PARIDA, K. M. Facile synthesis of highly active g-C3N4 for efficient hydrogen production under visible light. **Journal of Materials Chemistry A,** [s.l.], v. 1, n. 26, p. 7816-7824, 2013. ISSN:2050-7488 DOI:10.1039/C3TA10851A. Available at: http://dx.doi.org/10.1039/C3TA10851A.

MASUNGA, Ngonidzashe *et al.* Recent advances in copper ferrite nanoparticles and nanocomposites synthesis, magnetic properties and application in water treatment: Review. **Journal of Environmental Chemical Engineering,** [s.l.], v. 7, n. 3, p. 103179, 2019. ISSN:2213-3437 DOI:https://doi.org/10.1016/j.jece.2019.103179. Available at: http://www.sciencedirect.com/science/article/pii/S2213343719303021. Access at: 2019 Jun. 01.

MEHRA, Neelesh Kumar; JAIN, N. K. Cancer targeting propensity of folate conjugated surface engineered multi-walled carbon nanotubes. **Colloids and Surfaces B: Biointerfaces,** [s.l.], v. 132, p. 17-26, 2015. ISSN:0927-7765 DOI:https://doi.org/10.1016/j.colsurfb.2015.04.056. Available at: http://www.sciencedirect.com/science/article/pii/S0927776515002751. Access at: 2020 Nov. 25. 2015/08/01/.

MILLER, Mark R. *et al.* Inhaled Nanoparticles Accumulate at Sites of Vascular Disease. **ACS Nano,** [s.l.], v. 11, n. 5, p. 4542-4552, 2017. ISSN:1936-086X

1936-0851 DOI:10.1021/acsnano.6b08551. Available at: https://pubmed.ncbi.nlm.nih.gov/28443337

MIN, Ling-Li *et al.* Functionalized chitosan electrospun nanofiber for effective removal of trace arsenate from water. **Scientific Reports,** [s.l.], v. 6, p. 32480, 2016. DOI:10.1038/srep32480

http://www.nature.com/articles/srep32480#supplementary-information. Available at: http://dx.doi.org/10.1038/srep32480. Access at: 2020 Feb. 18.

MOHAMMED-IBRAHIM, Jamesh; SUN, Xiaoming. Recent progress on earth abundant electrocatalysts for hydrogen evolution reaction (HER) in alkaline medium to achieve efficient water splitting – A review. **Journal of Energy Chemistry,** [s.l.], v. 34, p. 111-160, 2019. ISSN:2095-4956 DOI:https://doi.org/10.1016/j.jechem.2018.09.016. Available at: http://www.sciencedirect.com/science/article/pii/S2095495618305370. Access at: 2019 Sep. 01.

MOHAPATRA, Jeotikanta; XING, Meiying; LIU, J. Ping. Inductive Thermal Effect of Ferrite Magnetic Nanoparticles. [s.l.], v. 12, n. 19, p. 3208, 2019. ISSN:1996-1944. Available at: https://www.mdpi.com/1996-1944/12/19/3208.

MONDAL, Bibhas *et al.* Sonochemically Synthesized Spin-Canted CuFe2O4 Nanoparticles for Heterogeneous Green Catalytic Click Chemistry. **ACS Omega,** [s.l.], v. 4, n. 9, p. 13845-13852, 2019. ISSN:2470-1343 DOI:10.1021/acsomega.9b01477. Available at: https://doi.org/10.1021/acsomega.9b01477. Access at: 2019 Aug. 27.

MONIER, M.; AYAD, D. M.; ABDEL-LATIF, D. A. Adsorption of Cu(II), Cd(II) and Ni(II) ions by cross-linked magnetic chitosan-2-aminopyridine glyoxal Schiff's base. **Colloids and Surfaces B: Biointerfaces,** [s.l.], v. 94, p. 250-258, 2012. ISSN:0927-7765 DOI:http://dx.doi.org/10.1016/j.colsurfb.2012.01.051. Available at: http://www.sciencedirect.com/science/article/pii/S0927776512000811. Access at: 2015 Jun. 23.

MOU, Yuanchun; YANG, Hu; XU, Zhenliang. Morphology, Surface Layer Evolution, and Structure–Dye Adsorption Relationship of Porous Fe3O4 MNPs Prepared by Solvothermal/Gas Generation Process. **ACS Sustainable Chemistry & Engineering,** [s.l.],

v. 5, n. 3, p. 2339-2349, 2017. DOI:10.1021/acssuschemeng.6b02670. Available at: https://doi.org/10.1021/acssuschemeng.6b02670. Access at: 2017 Mar. 06.

MOUMENI, H.; ALLEG, S.; GRENECHE, J. M. Structural properties of Fe50Co50 nanostructured powder prepared by mechanical alloying. **Journal of Alloys and Compounds,** [s.l.], v. 386, n. 1, p. 12-19, 2005. ISSN:0925-8388 DOI:https://doi.org/10.1016/j.jallcom.2004.05.017. Available at: http://www.sciencedirect.com/science/article/pii/S0925838804007054. Access at: 2019 Jan. 11.

MOURDIKOUDIS, S. *et al.* EFFECT OF AIR EXPOSURE ON STRUCTURAL AND MAGNETIC FEATURES OF FeCo NANOPARTICLES. **Modern Physics Letters B,** [s.l.], v. 21, n. 18, p. 1161-1168, 2007. DOI:10.1142/s0217984907013869. Available at: https://www.worldscientific.com/doi/abs/10.1142/S0217984907013869.

MOURDIKOUDIS, Stefanos; LIZ-MARZÁN, Luis M. Oleylamine in Nanoparticle Synthesis. **Chemistry of Materials,** [s.l.], v. 25, n. 9, p. 1465-1476, 2013. ISSN:0897-4756 DOI:10.1021/cm4000476. Available at: https://doi.org/10.1021/cm4000476. Access at: 2019 May 14.

MUNAGAPATI, Venkata Subbaiah; YARRAMUTHI, Vijaya; KIM, Dong-Su. Methyl orange removal from aqueous solution using goethite, chitosan beads and goethite impregnated with chitosan beads. **Journal of Molecular Liquids,** [s.l.], v. 240, p. 329-339, 2017. ISSN:0167-7322 DOI:https://doi.org/10.1016/j.molliq.2017.05.099. Available at: http://www.sciencedirect.com/science/article/pii/S0167732217312175. Access at: 2020 Feb. 25.

MURTHY, Arun Prasad; MADHAVAN, Jagannathan; MURUGAN, Kadarkarai. Recent advances in hydrogen evolution reaction catalysts on carbon/carbon-based supports in acid media. **Journal of Power Sources,** [s.l.], v. 398, p. 9-26, 2018. ISSN:0378-7753 DOI:https://doi.org/10.1016/j.jpowsour.2018.07.040. Available at: http://www.sciencedirect.com/science/article/pii/S0378775318307481. Access at: 2018 Sep. 15.

NABAVINIA, Mahboubeh; BELTRAN-HUARAC, Juan. Recent Progress in Iron Oxide Nanoparticles as Therapeutic Magnetic Agents for Cancer Treatment and Tissue Engineering. **ACS Applied Bio Materials,** [s.l.], v. 3, n. 12, p. 8172-8187, 2020. DOI:10.1021/acsabm.0c00947. Available at: https://doi.org/10.1021/acsabm.0c00947. Access at: 2020 Dec. 21.

NASRULLAH, Asma *et al.* High surface area mesoporous activated carbon-alginate beads for efficient removal of methylene blue. **International Journal of Biological Macromolecules,** [s.l.], v. 107, p. 1792-1799, 2018. ISSN:0141-8130 DOI:https://doi.org/10.1016/j.ijbiomac.2017.10.045. Available at: http://www.sciencedirect.com/science/article/pii/S0141813017333494. Access at: 2018 Feb. 01.

NASSAR, Mostafa Y.; ABDALLAH, Samar. Facile controllable hydrothermal route for a porous CoMn2O4 nanostructure: synthesis, characterization, and textile dye removal from aqueous media. **RSC Advances,** [s.l.], v. 6, n. 87, p. 84050-84067, 2016. DOI:10.1039/C6RA12424K. Available at: http://dx.doi.org/10.1039/C6RA12424K.

NETO, C. G. T. *et al.* Thermal Analysis of Chitosan Based Networks. **Carbohydrate Polymers,** [s.l.], v. 62, n. 2, p. 97-103, 2005. ISSN:0144-8617 DOI:http://dx.doi.org/10.1016/j.carbpol.2005.02.022. Available at: http://www.sciencedirect.com/science/article/pii/S014486170500127X. Access at: 2015 Nov. 10.

NETO, Davino M. A. *et al.* A novel amino phosphonate-coated magnetic nanoparticle as MRI contrast agent. **Applied Surface Science,** [s.l.], v. 543, p. 148824, 2021. ISSN:0169-4332 DOI:https://doi.org/10.1016/j.apsusc.2020.148824. Available at: https://www.sciencedirect.com/science/article/pii/S0169433220335832. Access at: 2021 Mar. 30.

NETO, Davino M. A. *et al.* Rapid Sonochemical Approach Produces Functionalized Fe3O4 Nanoparticles with Excellent Magnetic, Colloidal, and Relaxivity Properties for MRI Application. **The Journal of Physical Chemistry C,** [s.l.], v. 121, n. 43, p. 24206-24222, 2017. ISSN:1932-7447 DOI:10.1021/acs.jpcc.7b04941. Available at: https://doi.org/10.1021/acs.jpcc.7b04941. Access at: 2017 Nov. 02.

NIKIFOROV, V. N.; IGNATENKO, A. N.; IRKHIN, V. Yu. Size and surface effects on the magnetism of magnetite and maghemite nanoparticles. **Journal of Experimental and Theoretical Physics,** [s.l.], v. 124, n. 2, p. 304-310, 2017. ISSN:1090-6509 DOI:10.1134/s1063776117010046. Available at: https://doi.org/10.1134/S1063776117010046. Access at: 2015 Feb. 01.

NIVETHA, Ravi *et al.* Highly Porous MIL-100(Fe) for the Hydrogen Evolution Reaction (HER) in Acidic and Basic Media. **ACS Omega,** [s.l.], v. 5, n. 30, p. 18941-18949, 2020. ISSN:2470-1343 DOI:10.1021/acsomega.0c02171. Available at: https://doi.org/10.1021/acsomega.0c02171. Access at: 2020 Aug. 04.

NOVOSELOV, K. S. *et al.* Electric Field Effect in Atomically Thin Carbon Films. **Science,** [s.l.], v. 306, n. 5696, p. 666, 2004. DOI:10.1126/science.1102896. Available at: http://science.sciencemag.org/content/306/5696/666.abstract.

NUZHINA, Julia V. *et al.* Preclinical Evaluation and Clinical Translation of Magnetite-Based Nanomedicines. **Journal of Drug Delivery Science and Technology,** [s.l.], v. 54, p. 101282, 2019. ISSN:1773-2247 DOI:https://doi.org/10.1016/j.jddst.2019.101282. Available at: https://www.sciencedirect.com/science/article/pii/S1773224719309335. Access at: 2019 Dec. 01.

OLADOJA, N. A. *et al.* Preparation of magnetic, macro-reticulated cross-linked chitosan for tetracycline removal from aquatic systems. **Colloids and Surfaces B: Biointerfaces,** [s.l.], v. 117, p. 51-59, 2014. ISSN:0927-7765 DOI:http://dx.doi.org/10.1016/j.colsurfb.2014.02.006. Available at: http://www.sciencedirect.com/science/article/pii/S0927776514000733. Access at: 2019 May 01.

OLIVEIRA, Francisco G. S. *et al.* Fe–Co coatings electrodeposited from eutectic mixture of choline chloride-urea: Physical characterizations and evaluation as electrocatalysts for the hydrogen evolution reaction. **Journal of Alloys and Compounds,** [s.l.], v. 851, p. 156330, 2021. ISSN:0925-8388 DOI:https://doi.org/10.1016/j.jallcom.2020.156330. Available at: http://www.sciencedirect.com/science/article/pii/S0925838820326943. Access at: 2021 Jan. 15.

OLIVEIRA, Thomaz *et al.* Human foreskin fibroblasts: from waste bag to important biomedical applications. **Journal of Clinical Urology,** [s.l.], v. 11, n. 6, p. 385-394, 2018. ISSN:2051-4158 DOI:10.1177/2051415818761526. Available at: https://doi.org/10.1177/2051415818761526. Access at: 2018 Nov. 01.

ONG, Wee-Jun *et al.* Graphitic Carbon Nitride (g-C3N4)-Based Photocatalysts for Artificial Photosynthesis and Environmental Remediation: Are We a Step Closer To Achieving Sustainability? **Chemical Reviews,** [s.l.], v. 116, n. 12, p. 7159-7329, 2016. ISSN:0009-2665 DOI:10.1021/acs.chemrev.6b00075. Available at: https://doi.org/10.1021/acs.chemrev.6b00075. Access at: 2016 Jun. 22.

PARK, J. *et al.* Monodisperse Nanoparticles of Ni and NiO: Synthesis, Characterization, Self-Assembled Superlattices, and Catalytic Applications in the Suzuki Coupling Reaction. **Advanced Materials,** [s.l.], v. 17, n. 4, p. 429-434, 2005. ISSN:0935-9648 DOI:https://doi.org/10.1002/adma.200400611. Available at: https://doi.org/10.1002/adma.200400611. Access at: 2019 Sep. 05.

PATNAIK, Sulagna; SAHOO, Dipti Prava; PARIDA, Kulamani. Recent advances in anion doped g-C3N4 photocatalysts: A review. **Carbon,** [s.l.], v. 172, p. 682-711, 2021. ISSN:0008-6223 DOI:https://doi.org/10.1016/j.carbon.2020.10.073. Available at: http://www.sciencedirect.com/science/article/pii/S0008622320310460. Access at: 2021 Feb. 01.

PERVEEN, Mehvish *et al.* Therapeutic potential of graphitic carbon nitride as a drug delivery system for cisplatin (anticancer drug): A DFT approach. **Biophysical Chemistry,** [s.l.], v. 267, p. 106461, 2020. ISSN:0301-4622 DOI:https://doi.org/10.1016/j.bpc.2020.106461. Available at: http://www.sciencedirect.com/science/article/pii/S0301462220301691. Access at: 2020 Dec. 01.

PICCININ, Simone. The band structure and optical absorption of hematite (α-Fe2O3): a first-principles GW-BSE study. **Physical Chemistry Chemical Physics,** [s.l.], v. 21, n. 6, p. 2957-

2967, 2019. ISSN:1463-9076 DOI:10.1039/C8CP07132B. Available at: http://dx.doi.org/10.1039/C8CP07132B.

POON, Louis; WILSON, Lee D.; HEADLEY, John V. Chitosan-glutaraldehyde copolymers and their sorption properties. **Carbohydrate Polymers,** [s.l.], v. 109, p. 92-101, 2014. ISSN:0144-8617 DOI:http://doi.org/10.1016/j.carbpol.2014.02.086. Available at: http://www.sciencedirect.com/science/article/pii/S0144861714002203. Access at: 2015 Aug. 30.

PYLYPCHUK, Ie. V. *et al.* Gd-DTPA Adsorption on Chitosan/Magnetite Nanocomposites. **Nanoscale Research Letters,** [s.l.], v. 11, n. 1, p. 1-10, 2016. ISSN:1556-276X DOI:10.1186/s11671-016-1363-3. Available at: http://dx.doi.org/10.1186/s11671-016-1363-3.

QIAO, Liang *et al.* Standardizing Size- and Shape-Controlled Synthesis of Monodisperse Magnetite (Fe3O4) Nanocrystals by Identifying and Exploiting Effects of Organic Impurities. **ACS Nano,** [s.l.], v. 11, n. 6, p. 6370-6381, 2017. ISSN:1936-0851 DOI:10.1021/acsnano.7b02752. Available at: https://doi.org/10.1021/acsnano.7b02752. Access at: 2017 Jul. 27.

QU, Xiaolei; ALVAREZ, Pedro J. J.; LI, Qilin. Applications of nanotechnology in water and wastewater treatment. **Water Research,** [s.l.], v. 47, n. 12, p. 3931-3946, 2013. ISSN:0043-1354 DOI:https://doi.org/10.1016/j.watres.2012.09.058. Available at: http://www.sciencedirect.com/science/article/pii/S0043135413001772. Access at: 2019 Aug. 27.

RABINOW, Barrett E. Nanosuspensions in drug delivery. **Nature Reviews Drug Discovery,** [s.l.], v. 3, n. 9, p. 785-796, 2004. ISSN:1474-1784 DOI:10.1038/nrd1494. Available at: https://doi.org/10.1038/nrd1494. Access at: 2019 Sep. 01.

RAJA, Iruthayapandi S. *et al.* Two-Dimensional Theranostic Nanomaterials in Cancer Treatment: State of the Art and Perspectives. **Cancers,** [s.l.], v. 12, n. 6, 2020. ISSN:2072-6694 DOI:10.3390/cancers12061657

RAJAR, Kausar *et al.* One pot synthesis and characterization of Fe3O4 Nanorod-PNIPA Nanogel Composite for protein adsorption. **Materials Science and Engineering: C,** [s.l.], v. 68, p. 59-64, 2016. ISSN:0928-4931 DOI:https://doi.org/10.1016/j.msec.2016.05.095. Available at: http://www.sciencedirect.com/science/article/pii/S0928493116305288. Access at: 2016 nov. 01.

RAJEEV, Rijo *et al.* Recent advances in bimetallic based nanostructures: Synthesis and electrochemical sensing applications. **Microchemical Journal,** [s.l.], v. 163, p. 105910, 2021. ISSN:0026-265X DOI:https://doi.org/10.1016/j.microc.2020.105910. Available at: http://www.sciencedirect.com/science/article/pii/S0026265X20338522. Access at: 20221 Apr. 01.

RAJESH, Ponraj *et al.* Exchange Bias in Chemically Reduced FeCo Alloy Nanostructures. **physica status solidi (a),** [s.l.], v. 216, n. 18, p. 1900051, 2019. ISSN:1862-6300 DOI:10.1002/pssa.201900051. Available at: https://onlinelibrary.wiley.com/doi/abs/10.1002/pssa.201900051.

RAZA, Kaisar *et al.* Conjugation of Docetaxel with Multiwalled Carbon Nanotubes and Codelivery with Piperine: Implications on Pharmacokinetic Profile and Anticancer Activity. **Molecular Pharmaceutics,** [s.l.], v. 13, n. 7, p. 2423-2432, 2016. ISSN:1543-8384 DOI:10.1021/acs.molpharmaceut.6b00183. Available at: https://doi.org/10.1021/acs.molpharmaceut.6b00183. Access at: 2016 Jul. 05.

RAZMI, Fatin Amirah *et al.* Kinetics, thermodynamics, isotherm and regeneration analysis of chitosan modified pandan adsorbent. **Journal of Cleaner Production,** [s.l.], v. 231, p. 98-109, 2019. ISSN:0959-6526 DOI:https://doi.org/10.1016/j.jclepro.2019.05.228. Available at: http://www.sciencedirect.com/science/article/pii/S0959652619317627. Access at: 2019 Sep. 10.

REDDY, D. Harikishore Kumar; LEE, Seung-Mok. Application of magnetic chitosan composites for the removal of toxic metal and dyes from aqueous solutions. **Advances in Colloid and Interface Science,** [s.l.], v. 201-202, p. 68-93, 2013. ISSN:0001-8686 DOI:https://doi.org/10.1016/j.cis.2013.10.002. Available at: http://www.sciencedirect.com/science/article/pii/S0001868613001176. Access at: 2020 Feb. 02.

REDDY, L. Harivardhan *et al.* Magnetic Nanoparticles: Design and Characterization, Toxicity and Biocompatibility, Pharmaceutical and Biomedical Applications. **Chemical Reviews,** [s.l.], v. 112, n. 11, p. 5818-5878, 2012. ISSN:0009-2665 DOI:10.1021/cr300068p. Available at: https://doi.org/10.1021/cr300068p. Access at: 2020 Jul. 14.

REDLICH, O.; PETERSON, D. L. A useful adsorption isotherm. **Journal of Physical Chemistry,** [s.l.], v. 63, n. 6, p. 1024, 1959. Available at: https://www.scopus.com/inward/record.uri?eid=2-s2.0-7244241130&partnerID=40&md5=9d3c9cdb1b108f60624a845410a93693.

RINGEL, J. *et al.* Carbon nanofibers and carbon nanotubes sensitize prostate and bladder cancer cells to platinum-based chemotherapeutics. **J Biomed Nanotechnol,** [s.l.], v. 10, n. 3, p. 463-477, 2014. ISSN:1550-7033 (Print)

1550-7033 DOI:10.1166/jbn.2014.1758 Access at: 2019 Feb. 02.

RIXECKER, Georg. The difficulty of isolating grain boundary components in the Mössbauer spectra of ball-milled materials: iron and silver–iron alloys. **Solid State Communications,** [s.l.], v. 122, n. 6, p. 299-302, 2002. ISSN:0038-1098 DOI:https://doi.org/10.1016/S0038-1098(02)00161-8. Available at:

http://www.sciencedirect.com/science/article/pii/S0038109802001618. Access at: 2019 Jun. 02.

RODRÍGUEZ-PADRÓN, Daily *et al.* Improving Electrochemical Hydrogen Evolution of Ag@CN Nanocomposites by Synergistic Effects with α-Rich Proteins. **ACS Applied Materials & Interfaces,** [s.l.], v. 12, n. 2, p. 2207-2215, 2020. ISSN:1944-8244 DOI:10.1021/acsami.9b13571. Available at: https://doi.org/10.1021/acsami.9b13571. Access at: 2020 Jn. 15.

RODRÍGUEZ, V. A. Peña *et al.* Fe50Ni50 synthesized by high energy ball milling: A systematic study using X-ray diffraction, EXAFS and Mössbauer methods. **Materials Characterization,** [s.l.], v. 149, p. 249-254, 2019. ISSN:1044-5803 DOI:https://doi.org/10.1016/j.matchar.2019.01.036. Available at: http://www.sciencedirect.com/science/article/pii/S1044580318328912. Access at: 2019 Mar. 01.

ROHAIZAD, Nasuha *et al.* Two-dimensional materials in biomedical, biosensing and sensing applications. **Chemical Society reviews,** [s.l.], v. 50, n. 1, p. 619-657, 2021. ISSN:0306-0012 DOI:10.1039/D0CS00150C. Available at: http://dx.doi.org/10.1039/D0CS00150C.

RUEDA, D. R.; SECALL, T.; BAYER, R. K. Differences in the interaction of water with starch and chitosan films as revealed by infrared spectroscopy and differential scanning calorimetry. **Carbohydrate Polymers,** [s.l.], v. 40, n. 1, p. 49-56, 1999. ISSN:0144-8617 DOI:http://dx.doi.org/10.1016/S0144-8617(99)00033-8. Available at: http://www.sciencedirect.com/science/article/pii/S0144861799000338. Access at: 2015 Sep. 27.

RUSMIN, Ruhaida *et al.* Structural evolution of chitosan–palygorskite composites and removal of aqueous lead by composite beads. **Applied Surface Science,** [s.l.], v. 353, p. 363-375, 2015. ISSN:0169-4332 DOI:http://dx.doi.org/10.1016/j.apsusc.2015.06.124. Available at: http://www.sciencedirect.com/science/article/pii/S0169433215014713. Access at: 2014 Dec. 30.

SADORSKY, Perry. Wind energy for sustainable development: Driving factors and future outlook. **Journal of Cleaner Production,** [s.l.], v. 289, p. 125779, 2021. ISSN:0959-6526 DOI:https://doi.org/10.1016/j.jclepro.2020.125779. Available at: http://www.sciencedirect.com/science/article/pii/S095965262035825X. Access at: 2021 Mar. 20.

SANTHI, Kalavathy *et al.* Dendritic Ag–Fe nanocrystalline alloy synthesized by pulsed electrodeposition and its characterization. **Applied Surface Science,** [s.l.], v. 316, p. 491-496, 2014. ISSN:0169-4332 DOI:https://doi.org/10.1016/j.apsusc.2014.08.039. Available at: http://www.sciencedirect.com/science/article/pii/S0169433214017735. Access at: 2014 Oct. 15.

SARHAN, Radwan M. *et al.* Silver–Iron Hierarchical Microflowers for Highly Efficient H2O2 Nonenzymatic Amperometric Detection. **ACS Sustainable Chemistry & Engineering,** [s.l.], v. 7, n. 4, p. 4335-4342, 2019. DOI:10.1021/acssuschemeng.8b06182. Available at: https://doi.org/10.1021/acssuschemeng.8b06182. Access at: 2019 Feb. 18.

SASIDHARAN, A. *et al.* Hemocompatibility and macrophage response of pristine and functionalized graphene. **Small,** [s.l.], v. 8, n. 8, p. 1251-1263, 2012. ISSN:1613-6810 DOI:10.1002/smll.201102393 Access at: 2018 Apr. 23.

SATHYA, Ayyappan *et al.* CoxFe3–xO4 Nanocubes for Theranostic Applications: Effect of Cobalt Content and Particle Size. **Chemistry of Materials,** [s.l.], v. 28, n. 6, p. 1769-1780, 2016. ISSN:0897-4756 DOI:10.1021/acs.chemmater.5b04780. Available at: https://doi.org/10.1021/acs.chemmater.5b04780. Access at: 2016 Mar. 22.

SATO, Ryota; KANEHARA, Masayuki; TERANISHI, Toshiharu. Homoepitaxial Size Control and Large-Scale Synthesis of Highly Monodisperse Amine-Protected Palladium Nanoparticles. **Small,** [s.l.], v. 7, n. 4, p. 469-473, 2011. ISSN:1613-6810 DOI:https://doi.org/10.1002/smll.201001685. Available at: https://doi.org/10.1002/smll.201001685. Access at: 2016 Feb. 18.

SCARIA, Jaimy; NIDHEESH, P. V.; KUMAR, M. Suresh. Synthesis and applications of various bimetallic nanomaterials in water and wastewater treatment. **Journal of Environmental Management,** [s.l.], v. 259, p. 110011, 2020. ISSN:0301-4797 DOI:https://doi.org/10.1016/j.jenvman.2019.110011. Available at: https://www.sciencedirect.com/science/article/pii/S0301479719317293. Access at: 2020 Apr. 01.

SEMIÃO, Matheus Araújo; HAMINIUK, Charles Windson Isidoro; MACIEL, Giselle Maria. Residual diatomaceous earth as a potential and cost effective biosorbent of the azo textile dye Reactive Blue 160. **Journal of Environmental Chemical Engineering,** [s.l.], v. 8, n. 1, p. 103617, 2020. ISSN:2213-3437 DOI:https://doi.org/10.1016/j.jece.2019.103617. Available at: http://www.sciencedirect.com/science/article/pii/S2213343719307407. Access at: 2020 Feb. 01.

SENTHILKUMAAR, S. *et al.* Adsorption of dissolved Reactive red dye from aqueous phase onto activated carbon prepared from agricultural waste. **Bioresource Technology,** [s.l.], v. 97, n. 14, p. 1618-1625, 2006. ISSN:0960-8524 DOI:https://doi.org/10.1016/j.biortech.2005.08.001. Available at: http://www.sciencedirect.com/science/article/pii/S0960852405003810. Access at: 2015 Sep. 01 .

SHAMIM, Maria *et al.* DFT study of therapeutic potential of graphitic carbon nitride (g-C3N4) as a new drug delivery system for carboplatin to treat cancer. **Journal of Molecular Liquids,** [s.l.], v. 331, p. 115607, 2021. ISSN:0167-7322 DOI:https://doi.org/10.1016/j.molliq.2021.115607. Available at:

https://www.sciencedirect.com/science/article/pii/S0167732221003329. Access at: 2021 Jun. 01.

SHANG, Lu *et al.* Underwater superaerophobic Ni nanoparticle-decorated nickel–molybdenum nitride nanowire arrays for hydrogen evolution in neutral media. **Nano Energy,** [s.l.], v. 78, p. 105375, 2020. ISSN:2211-2855 DOI:https://doi.org/10.1016/j.nanoen.2020.105375. Available at: https://www.sciencedirect.com/science/article/pii/S2211285520309526. Access at: 2020 Dec. 01.

SHARIFI DEHSARI, Hamed; ASADI, Kamal. Impact of Stoichiometry and Size on the Magnetic Properties of Cobalt Ferrite Nanoparticles. **The Journal of Physical Chemistry C,** [s.l.], v. 122, n. 51, p. 29106-29121, 2018. ISSN:1932-7447 DOI:10.1021/acs.jpcc.8b09276. Available at: https://doi.org/10.1021/acs.jpcc.8b09276. Access at: 2018 Dec. 27.

SHARMA, Pankaj *et al.* A review on applicability of naturally available adsorbents for the removal of hazardous dyes from aqueous waste. **Environmental Monitoring and Assessment,** [s.l.], v. 183, n. 1, p. 151-195, 2011. ISSN:1573-2959 DOI:10.1007/s10661-011-1914-0. Available at: http://dx.doi.org/10.1007/s10661-011-1914-0.

SHOKROLLAHI, H. A review of the magnetic properties, synthesis methods and applications of maghemite. **Journal of Magnetism and Magnetic Materials,** [s.l.], v. 426, p. 74-81, 2017. ISSN:0304-8853 DOI:https://doi.org/10.1016/j.jmmm.2016.11.033. Available at: https://www.sciencedirect.com/science/article/pii/S0304885316313397. Access at: 2017 Mar. 15.

SINGH, Ashwani Kumar; SRIVASTAVA, O. N.; SINGH, Kedar. Shape and Size-Dependent Magnetic Properties of Fe3O4 Nanoparticles Synthesized Using Piperidine. **Nanoscale Research Letters,** [s.l.], v. 12, n. 1, p. 298, 2017. ISSN:1556-276X DOI:10.1186/s11671-017-2039-3. Available at: http://dx.doi.org/10.1186/s11671-017-2039-3.

SINGH, Rahul Pratap *et al.* Vitamin E TPGS conjugated carbon nanotubes improved efficacy of docetaxel with safety for lung cancer treatment. **Colloids and Surfaces B: Biointerfaces,** [s.l.], v. 141, p. 429-442, 2016. ISSN:0927-7765 DOI:https://doi.org/10.1016/j.colsurfb.2016.02.011. Available at: http://www.sciencedirect.com/science/article/pii/S0927776516300911. Access at: 2016 May 01.

SINGH, Ramesh P.; CHAUHAN, Akshansha. Impact of lockdown on air quality in India during COVID-19 pandemic. **Air Quality, Atmosphere & Health,** [s.l.], v. 13, n. 8, p. 921-928, 2020. ISSN:1873-9326 DOI:10.1007/s11869-020-00863-1. Available at: https://doi.org/10.1007/s11869-020-00863-1. Access at: 2020 Aug. 01.

SOARES, Aline S. L. Santoro *et al.* Comparison of primary human gingival fibroblasts from an older and a young donor on the evaluation of cytotoxicity of denture adhesives. **Journal of**

applied oral science : revista FOB, [s.l.], v. 26, p. e20160594-e20160594, 2018. ISSN:1678-7765

1678-7757 DOI:10.1590/1678-7757-2016-0594. Available at: https://pubmed.ncbi.nlm.nih.gov/29489936

SOARES, Paula P. *et al.* Iron oxide nanoparticles modified with oleic acid: Vibrational and phase determination. **Journal of Physics and Chemistry of Solids,** [s.l.], v. 99, p. 111-118, 2016. ISSN:0022-3697 DOI:http://dx.doi.org/10.1016/j.jpcs.2016.08.006. Available at: http://www.sciencedirect.com/science/article/pii/S0022369716304796. Access at: 2017 Feb. 02..

SON, Seung Uk *et al.* Designed Synthesis of Atom-Economical Pd/Ni Bimetallic Nanoparticle-Based Catalysts for Sonogashira Coupling Reactions. **Journal of the American Chemical Society,** [s.l.], v. 126, n. 16, p. 5026-5027, 2004. ISSN:0002-7863 DOI:10.1021/ja039757r. Available at: https://doi.org/10.1021/ja039757r. Access at: 2020 Mar. 28.

SONG, Gaixue *et al.* Enhanced performance of g-C3N4/TiO2 photocatalysts for degradation of organic pollutants under visible light. **Chinese Journal of Chemical Engineering,** [s.l.], v. 23, n. 8, p. 1326-1334, 2015. ISSN:1004-9541 DOI:https://doi.org/10.1016/j.cjche.2015.05.003. Available at: http://www.sciencedirect.com/science/article/pii/S1004954115001731. Access at: 2015 Aug. 01.

SPIZZO, F. *et al.* Mössbauer investigation of sputtered FexAg100−x films. **Journal of Magnetism and Magnetic Materials,** [s.l.], v. 272-276, p. 1169-1170, 2004. ISSN:0304-8853 DOI:https://doi.org/10.1016/j.jmmm.2003.12.1072. Available at: http://www.sciencedirect.com/science/article/pii/S0304885303025514. Access at: 2019 Jun. 27.

SRIKALA, D. *et al.* Effect of induced shape anisotropy on magnetic properties of ferromagnetic cobalt nanocubes. **J Nanosci Nanotechnol,** [s.l.], v. 10, n. 12, p. 8088-8094, 2010. ISSN:1533-4880 (Print)

1533-4880 DOI:10.1166/jnn.2010.3011 Access at: 2020 Dec. 02.

STEPHANIE, Ruth *et al.* Recent advances of bimetallic nanomaterials and its nanocomposites for biosensing applications. **TrAC Trends in Analytical Chemistry,** [s.l.], v. 135, p. 116159, 2021. ISSN:0165-9936 DOI:https://doi.org/10.1016/j.trac.2020.116159. Available at: https://www.sciencedirect.com/science/article/pii/S0165993620303885. Access at: 2021 Feb. 01.

SUN, Hai *et al.* Synthesis and hydrogen evolution reaction of nanosized Ag - ZnO coated MoS2. **Ceramics International,** [s.l.], 2021. ISSN:0272-8842 DOI:https://doi.org/10.1016/j.ceramint.2021.01.268. Available at:

https://www.sciencedirect.com/science/article/pii/S0272884221003060. Access at: 2021 Jan. 31.

SUN, S. Recent Advances in Chemical Synthesis, Self-Assembly, and Applications of FePt Nanoparticles. **Advanced Materials,** [s.l.], v. 18, n. 4, p. 393-403, 2006. ISSN:0935-9648 DOI:https://doi.org/10.1002/adma.200501464. Available at: https://doi.org/10.1002/adma.200501464. Access at: 2019 Apr. 17.

SUN, Shaodong *et al.* Constructing oxygen-doped g-C3N4 nanosheets with an enlarged conductive band edge for enhanced visible-light-driven hydrogen evolution. **Inorganic Chemistry Frontiers,** [s.l.], v. 5, n. 7, p. 1721-1727, 2018. DOI:10.1039/C8QI00242H. Available at: http://dx.doi.org/10.1039/C8QI00242H.

SUN, Yunkai; ZANGARI, Giovanni. Rational Compositional Control of Electrodeposited Ag–Fe films. **Inorganic Chemistry,** [s.l.], v. 59, n. 8, p. 5405-5417, 2020. ISSN:0020-1669 DOI:10.1021/acs.inorgchem.9b03600. Available at: https://doi.org/10.1021/acs.inorgchem.9b03600. Access at: 2020 Apr. 20.

SUNG, Hyuna *et al.* Global cancer statistics 2020: GLOBOCAN estimates of incidence and mortality worldwide for 36 cancers in 185 countries. **CA: A Cancer Journal for Clinicians,** [s.l.], v. n/a, n. n/a, 2021. ISSN:0007-9235 DOI:https://doi.org/10.3322/caac.21660. Available at: https://doi.org/10.3322/caac.21660. Access at: 2021 Feb 04.

SURESHKUMAR, Vaishnavi *et al.* Fabrication of chitosan–magnetite nanocomposite strip for chromium removal. **Applied Nanoscience,** [s.l.], v. 6, n. 2, p. 277-285, 2016. ISSN:2190-5517 DOI:10.1007/s13204-015-0429-3. Available at: https://doi.org/10.1007/s13204-015-0429-3. Access at: 2016 Feb. 01.

T.C, Prathna; SHARMA, Saroj Kumar; KENNEDY, Maria. Nanoparticles in household level water treatment: An overview. **Separation and Purification Technology,** [s.l.], v. 199, p. 260-270, 2018. ISSN:1383-5866 DOI:https://doi.org/10.1016/j.seppur.2018.01.061. Available at: http://www.sciencedirect.com/science/article/pii/S1383586617332525. Access at: 2018 Jun. 30.

TAMEU DJOKO, Simon Yves *et al.* Urea and green tea like precursors for the preparation of g-C3N4 based carbon nanomaterials (CNMs) composites as photocatalysts for photodegradation of pollutants under UV light irradiation. **Journal of Photochemistry and Photobiology A: Chemistry,** [s.l.], v. 398, p. 112596, 2020. ISSN:1010-6030 DOI:https://doi.org/10.1016/j.jphotochem.2020.112596. Available at: http://www.sciencedirect.com/science/article/pii/S1010603020303956. Access at: 2020 Jul. 01.

TAN, Kok Bing *et al.* Adsorption of dyes by nanomaterials: Recent developments and adsorption mechanisms. **Separation and Purification Technology,** [s.l.], v. 150, p. 229-242, 2015. ISSN:1383-5866 DOI:https://doi.org/10.1016/j.seppur.2015.07.009. Available at:

http://www.sciencedirect.com/science/article/pii/S1383586615300769. Access at: 2015 Aug. 17.

TANG, Chun *et al.* Ternary FexCo1–xP Nanowire Array as a Robust Hydrogen Evolution Reaction Electrocatalyst with Pt-like Activity: Experimental and Theoretical Insight. **Nano Letters,** [s.l.], v. 16, n. 10, p. 6617-6621, 2016. ISSN:1530-6984 DOI:10.1021/acs.nanolett.6b03332. Available at: https://doi.org/10.1021/acs.nanolett.6b03332. Access at: 2016 Ovt. 12.

TANG, Hongmei *et al.* ZIF-8-Derived Hollow Carbon for Efficient Adsorption of Antibiotics. **Nanomaterials,** [s.l.], v. 9, n. 1, p. 117, 2019. ISSN:2079-4991. Available at: https://www.mdpi.com/2079-4991/9/1/117.

TANG, Ting *et al.* Goethite promoted biodegradation of 2,4-dinitrophenol under nitrate reduction condition. **Journal of Hazardous Materials,** [s.l.], v. 343, n. Supplement C, p. 176-180, 2018. ISSN:0304-3894 DOI:https://doi.org/10.1016/j.jhazmat.2017.09.011. Available at: http://www.sciencedirect.com/science/article/pii/S0304389417306921. Access at: 2018 Feb. 05.

TEMPKIN, MI; PYZHEV, V. Kinetics of ammonia synthesis on promoted iron catalyst. **Acta Phys. Chim. USSR,** [s.l.], v. 12, n. 1, p. 327, 1940.

TETER, David M.; HEMLEY, Russell J. Low-Compressibility Carbon Nitrides. **Science,** [s.l.], v. 271, n. 5245, p. 53, 1996. DOI:10.1126/science.271.5245.53. Available at: http://science.sciencemag.org/content/271/5245/53.abstract.

THOMMES, Matthias *et al.* Physisorption of gases, with special reference to the evaluation of surface area and pore size distribution (IUPAC Technical Report). **Pure and Applied Chemistry,** [s.l.], v. 87, n. 9-10, p. 1051-1069, 2015. ISSN:1365-3075

THURSTON, John H. *et al.* Urea-derived graphitic carbon nitride (u-g-C3N4) films with highly enhanced antimicrobial and sporicidal activity. **Journal of Colloid and Interface Science,** [s.l.], v. 505, p. 910-918, 2017. ISSN:0021-9797 DOI:https://doi.org/10.1016/j.jcis.2017.06.089. Available at: http://www.sciencedirect.com/science/article/pii/S0021979717307531. Access at: 2017 Nov. 01.

TIAN, Feng *et al.* The depolymerization mechanism of chitosan by hydrogen peroxide. **Journal of Materials Science,** [s.l.], v. 38, n. 23, p. 4709-4712, 2003. ISSN:1573-4803 DOI:10.1023/a:1027466716950. Available at: http://dx.doi.org/10.1023/A:1027466716950.

TRAVLOU, Nikolina A. *et al.* Functionalization of Graphite Oxide with Magnetic Chitosan for the Preparation of a Nanocomposite Dye Adsorbent. **Langmuir,** [s.l.], v. 29, n. 5, p. 1657-1668, 2013. ISSN:0743-7463 DOI:10.1021/la304696y. Available at: https://doi.org/10.1021/la304696y. Access at: 2020 Mar. 05.

TURAL, Bilsen; TARHAN, Tuba; TURAL, Servet. REMOVAL OF REACTIVE BLACK 5 (RB5) FROM AQUEOUS SOLUTIONBY CROSS-LINKED MAGNETIC BIOSORBENT. [s.l.], 2017. Access at: 2018 Jun. 23.

UNG, David; COSSAIRT, Brandi M. Effect of Surface Ligands on CoP for the Hydrogen Evolution Reaction. **ACS Applied Energy Materials,** [s.l.], v. 2, n. 3, p. 1642-1645, 2019. DOI:10.1021/acsaem.9b00240. Available at: https://doi.org/10.1021/acsaem.9b00240. Access at: 2019 Mar. 25.

URBANOVA, Veronika *et al.* Nanocrystalline Iron Oxides, Composites, and Related Materials as a Platform for Electrochemical, Magnetic, and Chemical Biosensors. **Chemistry of Materials,** [s.l.], v. 26, n. 23, p. 6653-6673, 2014. ISSN:0897-4756 DOI:10.1021/cm500364x. Available at: https://doi.org/10.1021/cm500364x. Access at: 2014 Dec. 09.

USMAN, M. *et al.* Magnetite and Green Rust: Synthesis, Properties, and Environmental Applications of Mixed-Valent Iron Minerals. **Chemical Reviews,** [s.l.], v. 118, n. 7, p. 3251-3304, 2018. ISSN:0009-2665 DOI:10.1021/acs.chemrev.7b00224. Available at: https://doi.org/10.1021/acs.chemrev.7b00224. Access at: 2018 Apr. 11.

VARGHESE, Seba S. *et al.* Two-Dimensional Materials for Sensing: Graphene and Beyond. **Electronics,** [s.l.], v. 4, n. 3, 2015. ISSN:2079-9292 DOI:10.3390/electronics4030651

VINOSHA, P. Annie *et al.* Review on recent advances of zinc substituted cobalt ferrite nanoparticles: Synthesis characterization and diverse applications. **Ceramics International,** [s.l.], 2021. ISSN:0272-8842 DOI:https://doi.org/10.1016/j.ceramint.2020.12.289. Available at: https://www.sciencedirect.com/science/article/pii/S027288422100002X. Access at: 2021 Jan 05.

VOJOUDI, H. *et al.* Efficient device for the benign removal of organic pollutants from aqueous solutions using modified mesoporous magnetite nanostructures. **Journal of Physics and Chemistry of Solids,** [s.l.], v. 113, n. Supplement C, p. 210-219, 2018. ISSN:0022-3697 DOI:https://doi.org/10.1016/j.jpcs.2017.10.029. Available at: http://www.sciencedirect.com/science/article/pii/S0022369717306613. Access at: 2018 FEb. 01.

WALTER, Aurélie *et al.* Mastering the Shape and Composition of Dendronized Iron Oxide Nanoparticles To Tailor Magnetic Resonance Imaging and Hyperthermia. **Chemistry of Materials,** [s.l.], v. 26, n. 18, p. 5252-5264, 2014. ISSN:0897-4756 DOI:10.1021/cm5019025. Available at: https://doi.org/10.1021/cm5019025. Access at: 2014 Sep. 23.

WAN NGAH, W. S.; TEONG, L. C.; HANAFIAH, M. A. K. M. Adsorption of dyes and heavy metal ions by chitosan composites: A review. **Carbohydrate Polymers,** [s.l.], v. 83, n. 4, p. 1446-1456, 2011. ISSN:0144-8617 DOI:https://doi.org/10.1016/j.carbpol.2010.11.004.

Available at: http://www.sciencedirect.com/science/article/pii/S0144861710008908. Access at: 2020 Oct. 02.

WANG, Hui *et al.* Structural distortion in graphitic-C3N4 realizing an efficient photoreactivity. **Nanoscale,** [s.l.], v. 7, n. 12, p. 5152-5156, 2015. ISSN:2040-3364 DOI:10.1039/C4NR07645A. Available at: http://dx.doi.org/10.1039/C4NR07645A.

WANG, Jing *et al.* Non-Noble Metal-based Carbon Composites in Hydrogen Evolution Reaction: Fundamentals to Applications. **Advanced Materials,** [s.l.], v. 29, n. 14, p. 1605838, 2017. ISSN:0935-9648 DOI:https://doi.org/10.1002/adma.201605838. Available at: https://doi.org/10.1002/adma.201605838. Access at: 2017 Apr. 01.

WANG, Jiuhai; YANG, Mo. 11 - Two-Dimensional Nanomaterials in Cancer Theranostics. *In:* **Theranostic Bionanomaterials**: ed.: Elsevier, v. p.263-288, 2019.

WANG, Lei *et al.* Synergistic enhancement of cancer therapy using a combination of docetaxel and photothermal ablation induced by single-walled carbon nanotubes. **International journal of nanomedicine,** [s.l.], v. 6, p. 2641-2652, 2011. ISSN:1178-2013

1176-9114 DOI:10.2147/IJN.S24167. Available at: https://pubmed.ncbi.nlm.nih.gov/22114495

WANG, Xiansong *et al.* Hydrothermal synthesis of 3D hollow porous Fe3O4 microspheres towards catalytic removal of organic pollutants. **Nanoscale Research Letters,** [s.l.], v. 9, n. 1, p. 648, 2014. ISSN:1556-276X DOI:10.1186/1556-276x-9-648. Available at: https://doi.org/10.1186/1556-276X-9-648. Access at: 2018 Nov. 30.

WANG, Xiaoning *et al.* Robust, recoverable poly(N,N-dimethylacrylamide)-based hydrogels crosslinked by vinylated chitosan with recyclable adsorbability for acid red. **Journal of Applied Polymer Science,** [s.l.], v. 136, n. 20, p. 47473, 2019. ISSN:0021-8995 DOI:10.1002/app.47473. Available at: https://onlinelibrary.wiley.com/doi/abs/10.1002/app.47473.

WANG, Yongliang *et al.* In Situ Mineralization of Magnetite Nanoparticles in Chitosan Hydrogel. **Nanoscale Research Letters,** [s.l.], v. 4, n. 9, p. 1041, 2009. ISSN:1556-276X DOI:10.1007/s11671-009-9355-1. Available at: http://dx.doi.org/10.1007/s11671-009-9355-1.

WANG, Yu *et al.* Two-dimensional nanomaterials with engineered bandgap: Synthesis, properties, applications. **Nano today,** [s.l.], v. 37, p. 101059, 2021. ISSN:1748-0132 DOI:https://doi.org/10.1016/j.nantod.2020.101059. Available at: https://www.sciencedirect.com/science/article/pii/S1748013220302292. Access at: 2021 Apr. 01.

WANG, Zhe *et al.* Core–shell TiO2@C ultralong nanotubes with enhanced adsorption of antibiotics. **Journal of Materials Chemistry A,** [s.l.], v. 7, n. 32, p. 19081-19086, 2019. ISSN:2050-7488 DOI:10.1039/C9TA06735C. Available at: http://dx.doi.org/10.1039/C9TA06735C.

WANG, Zhenyu *et al.* Water-assisted production of honeycomb-like g-C3N4 with ultralong carrier lifetime and outstanding photocatalytic activity. **Nanoscale,** [s.l.], v. 7, n. 6, p. 2471-2479, 2015. ISSN:2040-3364 DOI:10.1039/C4NR05732E. Available at: http://dx.doi.org/10.1039/C4NR05732E.

WANG, Zhuliang *et al.* Facile synthesis of carbon-rich g-C3N4 by copolymerization of urea and tetracyanoethylene for photocatalytic degradation of Orange II. **Journal of Photochemistry and Photobiology A: Chemistry,** [s.l.], v. 358, p. 61-69, 2018. ISSN:1010-6030 DOI:https://doi.org/10.1016/j.jphotochem.2018.02.036. Available at: http://www.sciencedirect.com/science/article/pii/S101060301731777X. Access at: 2018 May 01.

WEI, Fangyan *et al.* Oxygen self-doped g-C3N4 with tunable electronic band structure for unprecedentedly enhanced photocatalytic performance. **Nanoscale,** [s.l.], v. 10, n. 9, p. 4515-4522, 2018. ISSN:2040-3364 DOI:10.1039/C7NR09660G. Available at: http://dx.doi.org/10.1039/C7NR09660G.

WILLIAMS, R. G. *et al.* Sensitivity of global warming to carbon emissions: Effects of heat and carbon uptake in a suite of earth system models. **Journal of Climate,** [s.l.], v. 30, n. 23, p. 9343-9363, 2017. DOI:10.1175/JCLI-D-16-0468.1. Available at: https://www.scopus.com/inward/record.uri?eid=2-s2.0-85033996746&doi=10.1175%2fJCLI-D-16-0468.1&partnerID=40&md5=16118d528df09efa3388b89dde88d2a7.

WONG, Y. C. *et al.* Equilibrium Studies for Acid Dye Adsorption onto Chitosan. **Langmuir,** [s.l.], v. 19, n. 19, p. 7888-7894, 2003. ISSN:0743-7463 DOI:10.1021/la030064y. Available at: http://dx.doi.org/10.1021/la030064y. Access at: 2014 Nov. 01.

WU, Feng-Chin; TSENG, Ru-Ling; JUANG, Ruey-Shin. Initial behavior of intraparticle diffusion model used in the description of adsorption kinetics. **Chemical Engineering Journal,** [s.l.], v. 153, n. 1, p. 1-8, 2009. ISSN:1385-8947 DOI:https://doi.org/10.1016/j.cej.2009.04.042. Available at: http://www.sciencedirect.com/science/article/pii/S138589470900312X. Access at: 2014 Nov. 10.

WU, Liheng *et al.* Organic Phase Syntheses of Magnetic Nanoparticles and Their Applications. **Chemical Reviews,** [s.l.], v. 116, n. 18, p. 10473-10512, 2016. ISSN:0009-2665 DOI:10.1021/acs.chemrev.5b00687. Available at: https://doi.org/10.1021/acs.chemrev.5b00687. Access at: 2016 Sep. 28.

XU, Cheng-Qun; ZHANG, Wei-De. Facile synthesis of nitrogen deficient g-C3N4 by copolymerization of urea and formamide for efficient photocatalytic hydrogen evolution.

Molecular Catalysis, [s.l.], v. 453, p. 85-92, 2018. ISSN:2468-8231 DOI:https://doi.org/10.1016/j.mcat.2018.04.029. Available at: http://www.sciencedirect.com/science/article/pii/S246882311830172X. Access at: 2018 Sep. 01.

XU, Danyang *et al.* Black Phosphorus Nanosheet with High Thermal Conversion Efficiency for Photodynamic/Photothermal/Immunotherapy. **ACS Biomaterials Science & Engineering,** [s.l.], v. 6, n. 9, p. 4940-4948, 2020. DOI:10.1021/acsbiomaterials.0c00984. Available at: https://doi.org/10.1021/acsbiomaterials.0c00984. Access at: 2020 Sep. 14 .

XU, Hui *et al.* Graphene-analogue carbon nitride: novel exfoliation synthesis and its application in photocatalysis and photoelectrochemical selective detection of trace amount of Cu2+. **Nanoscale,** [s.l.], v. 6, n. 3, p. 1406-1415, 2014. ISSN:2040-3364 DOI:10.1039/C3NR04759H. Available at: http://dx.doi.org/10.1039/C3NR04759H.

XU, Long *et al.* Chitosan in Molecularly-Imprinted Polymers: Current and Future Prospects. **International Journal of Molecular Sciences,** [s.l.], v. 16, n. 8, p. 18328, 2015. ISSN:1422-0067. Available at: http://www.mdpi.com/1422-0067/16/8/18328.

XU, Mengshu *et al.* Combination of CuS and g-C3N4 QDs on upconversion nanoparticles for targeted photothermal and photodynamic cancer therapy. **Chemical Engineering Journal,** [s.l.], v. 360, p. 866-878, 2019. ISSN:1385-8947 DOI:https://doi.org/10.1016/j.cej.2018.12.052. Available at: https://www.sciencedirect.com/science/article/pii/S1385894718325245. Access at: 2019 Mar. 15.

XU, Xing *et al.* Preparation and utilization of wheat straw bearing amine groups for the sorption of acid and reactive dyes from aqueous solutions. **Journal of Hazardous Materials,** [s.l.], v. 182, n. 1, p. 1-9, 2010. ISSN:0304-3894 DOI:https://doi.org/10.1016/j.jhazmat.2010.03.071. Available at: http://www.sciencedirect.com/science/article/pii/S0304389410003778. Access at: 2014 Dec. 21.

XU, Yuan; GAO, Shang-Peng. Band gap of C3N4 in the GW approximation. **International Journal of Hydrogen Energy,** [s.l.], v. 37, n. 15, p. 11072-11080, 2012. ISSN:0360-3199 DOI:https://doi.org/10.1016/j.ijhydene.2012.04.138. Available at: https://www.sciencedirect.com/science/article/pii/S0360319912010713. Access at: 2020 Aug. 01.

YADAV, Raghvendra Singh *et al.* Impact of Nd3+ in CoFe2O4 spinel ferrite nanoparticles on cation distribution, structural and magnetic properties. **Journal of Magnetism and Magnetic Materials,** [s.l.], v. 399, p. 109-117, 2016. ISSN:0304-8853 DOI:https://doi.org/10.1016/j.jmmm.2015.09.055. Available at: https://www.sciencedirect.com/science/article/pii/S0304885315306053. Access at: 2016 Feb. 01.

YAN, Dongmao; TANG, Bingtao; ZHANG, Shufen. Preparation and performances of sunlight-induced phase change PEG/SiO2-dye composite for solar energy conversion and storage. **Solar Energy Materials and Solar Cells,** [s.l.], v. 215, p. 110657, 2020. ISSN:0927-0248 DOI:https://doi.org/10.1016/j.solmat.2020.110657. Available at: http://www.sciencedirect.com/science/article/pii/S0927024820302592. Access at: 2020 Sep . 15.

YAN, Wei; YAN, Li; JING, Chuanyong. Impact of doped metals on urea-derived g-C3N4 for photocatalytic degradation of antibiotics: Structure, photoactivity and degradation mechanisms. **Applied Catalysis B: Environmental,** [s.l.], v. 244, p. 475-485, 2019. ISSN:0926-3373 DOI:https://doi.org/10.1016/j.apcatb.2018.11.069. Available at: http://www.sciencedirect.com/science/article/pii/S0926337318311275. Access at: 2019 May 05.

YANG, Ce; WU, Jiajia; HOU, Yanglong. Fe3O4 nanostructures: synthesis, growth mechanism, properties and applications. **Chemical Communications,** [s.l.], v. 47, n. 18, p. 5130-5141, 2011. ISSN:1359-7345 DOI:10.1039/C0CC05862A. Available at: http://dx.doi.org/10.1039/C0CC05862A.

YANG, Kai *et al.* Behavior and Toxicity of Graphene and Its Functionalized Derivatives in Biological Systems. **Small,** [s.l.], v. 9, n. 9-10, p. 1492-1503, 2013. ISSN:1613-6810 DOI:https://doi.org/10.1002/smll.201201417. Available at: https://doi.org/10.1002/smll.201201417. Access at: 2015 May 27.

YANG, Liuqing *et al.* A surface modification resultant thermally oxidized porous g-C3N4 with enhanced photocatalytic hydrogen production. **Applied Catalysis B: Environmental,** [s.l.], v. 204, p. 335-345, 2017. ISSN:0926-3373 DOI:https://doi.org/10.1016/j.apcatb.2016.11.047. Available at: https://www.sciencedirect.com/science/article/pii/S0926337316309146. Access at: 2017 May 05.

YANG, Saisai *et al.* CoP nanoparticles encapsulated in three-dimensional N-doped porous carbon for efficient hydrogen evolution reaction in a broad pH range. **Applied Surface Science,** [s.l.], v. 476, p. 749-756, 2019. ISSN:0169-4332 DOI:https://doi.org/10.1016/j.apsusc.2019.01.131. Available at: https://www.sciencedirect.com/science/article/pii/S0169433219301151. Access at: 2019 May 15.

YARDENI, Tal *et al.* Retro-orbital injections in mice. **Lab animal,** [s.l.], v. 40, n. 5, p. 155-160, 2011. ISSN:1548-4475

0093-7355 DOI:10.1038/laban0511-155. Available at: https://pubmed.ncbi.nlm.nih.gov/21508954.

YIN, Ying *et al.* One-pot evaporation–condensation strategy for green synthesis of carbon nitride quantum dots: An efficient fluorescent probe for ion detection and bioimaging. **Materials Chemistry and Physics,** [s.l.], v. 194, p. 293-301, 2017. ISSN:0254-0584

DOI:https://doi.org/10.1016/j.matchemphys.2017.03.054. Available at: http://www.sciencedirect.com/science/article/pii/S0254058417302687. Access at: 2017 Jun. 15.

YOU, Bo; SUN, Yujie. Innovative Strategies for Electrocatalytic Water Splitting. **Accounts of Chemical Research,** [s.l.], v. 51, n. 7, p. 1571-1580, 2018. ISSN:0001-4842 DOI:10.1021/acs.accounts.8b00002. Available at: https://doi.org/10.1021/acs.accounts.8b00002. Access at: 2018 Jul. 17.

YU, Jing *et al.* Metallic FePSe3 nanoparticles anchored on N-doped carbon framework for All-pH hydrogen evolution reaction. **Nano Energy,** [s.l.], v. 57, p. 222-229, 2019. ISSN:2211-2855 DOI:https://doi.org/10.1016/j.nanoen.2018.12.055. Available at: https://www.sciencedirect.com/science/article/pii/S2211285518309686. Access at: 2019 Mar. 01.

YU, Jingxue *et al.* Synthesis of high quality two-dimensional materials via chemical vapor deposition. **Chemical Science,** [s.l.], v. 6, n. 12, p. 6705-6716, 2015. ISSN:2041-6520 DOI:10.1039/C5SC01941A. Available at: http://dx.doi.org/10.1039/C5SC01941A.

YU, Yongsheng *et al.* Monodisperse MPt (M = Fe, Co, Ni, Cu, Zn) Nanoparticles Prepared from a Facile Oleylamine Reduction of Metal Salts. **Nano Letters,** [s.l.], v. 14, n. 5, p. 2778-2782, 2014. ISSN:1530-6984 DOI:10.1021/nl500776e. Available at: https://doi.org/10.1021/nl500776e. Access at: 2014 May 14.

YUAN, Xia *et al.* Cellular Toxicity and Immunological Effects of Carbon-based Nanomaterials. **Particle and Fibre Toxicology,** [s.l.], v. 16, n. 1, p. 18, 2019. ISSN:1743-8977 DOI:10.1186/s12989-019-0299-z. Available at: https://doi.org/10.1186/s12989-019-0299-z. Access at: 2019 Apr. 11.

YUSOF, Nor Saadah Mohd; ASHOKKUMAR, Muthupandian. Sonochemical Synthesis of Gold Nanoparticles by Using High Intensity Focused Ultrasound. **ChemPhysChem,** [s.l.], v. 16, n. 4, p. 775-781, 2015. ISSN:1439-4235 DOI:https://doi.org/10.1002/cphc.201402697. Available at: https://doi.org/10.1002/cphc.201402697. Access at: 2015 Mar. 16.

ZAHEER, Zoya; AL-ASFAR, Aisha; AAZAM, Elham Shafik. Adsorption of methyl red on biogenic Ag@Fe nanocomposite adsorbent: Isotherms, kinetics and mechanisms. **Journal of Molecular Liquids,** [s.l.], v. 283, p. 287-298, 2019. ISSN:0167-7322 DOI:https://doi.org/10.1016/j.molliq.2019.03.030. Available at: http://www.sciencedirect.com/science/article/pii/S016773221835801X. Access at: 2019 Jun. 01.

ZAHRA, Rubab *et al.* A review on nickel cobalt sulphide and their hybrids: Earth abundant, pH stable electro-catalyst for hydrogen evolution reaction. **International Journal of Hydrogen Energy,** [s.l.], v. 45, n. 46, p. 24518-24543, 2020. ISSN:0360-3199 DOI:https://doi.org/10.1016/j.ijhydene.2020.06.236. Available at:

http://www.sciencedirect.com/science/article/pii/S0360319920324277. Access at: 2020 Sep. 21.

ZAHRIM, A. Y. *et al.* Effective coagulation-flocculation treatment of highly polluted palm oil mill biogas plant wastewater using dual coagulants: Decolourisation, kinetics and phytotoxicity studies. **Journal of Water Process Engineering,** [s.l.], v. 16, p. 258-269, 2017. ISSN:2214-7144 DOI:https://doi.org/10.1016/j.jwpe.2017.02.005. Available at: http://www.sciencedirect.com/science/article/pii/S2214714417300272. Access at: 2020 Aug. 25.

ZENG, Xiangkang *et al.* Cooperatively modulating reactive oxygen species generation and bacteria-photocatalyst contact over graphitic carbon nitride by polyethylenimine for rapid water disinfection. **Applied Catalysis B: Environmental,** [s.l.], v. 274, p. 119095, 2020. ISSN:0926-3373 DOI:https://doi.org/10.1016/j.apcatb.2020.119095. Available at: http://www.sciencedirect.com/science/article/pii/S0926337320305105. Access at: 2020 Oct. 05.

ZHANG, Hai-Tao; WU, Gang; CHEN, Xian-Hui. Large-Scale Synthesis and Self-Assembly of Monodisperse Hexagon Cu2S Nanoplates. **Langmuir,** [s.l.], v. 21, n. 10, p. 4281-4282, 2005. ISSN:0743-7463 DOI:10.1021/la050741j. Available at: https://doi.org/10.1021/la050741j. Access at: 2016 May 01.

ZHANG, Lei *et al.* Synthesis of size-controlled monodisperse Pd nanoparticles via a non-aqueous seed-mediated growth. **Nanoscale Research Letters,** [s.l.], v. 7, n. 1, p. 312, 2012. ISSN:1556-276X DOI:10.1186/1556-276X-7-312. Available at: https://doi.org/10.1186/1556-276X-7-312. Access at: 2015 Jun. 19.

ZHANG, Ling; DOU, Yong-Hua; GU, Hong-Chen. Sterically induced shape control of magnetite nanoparticles. **Journal of Crystal Growth,** [s.l.], v. 296, n. 2, p. 221-226, 2006. ISSN:0022-0248 DOI:https://doi.org/10.1016/j.jcrysgro.2006.08.010. Available at: https://www.sciencedirect.com/science/article/pii/S0022024806007585. Access at: 2019 Nov. 01.

ZHANG, Shen *et al.* Recent advances in non-precious metal electrocatalysts for pH-universal hydrogen evolution reaction. **Green Energy & Environment,** [s.l.], 2020. ISSN:2468-0257 DOI:https://doi.org/10.1016/j.gee.2020.10.013. Available at: http://www.sciencedirect.com/science/article/pii/S2468025720301709. Access at: 2020 Oct. 14.

ZHANG, Wenxiu; CUI, Liang; LIU, Jingquan. Recent advances in cobalt-based electrocatalysts for hydrogen and oxygen evolution reactions. **Journal of Alloys and Compounds,** [s.l.], v. 821, p. 153542, 2020. ISSN:0925-8388 DOI:https://doi.org/10.1016/j.jallcom.2019.153542. Available at: https://www.sciencedirect.com/science/article/pii/S0925838819347887. Access at: 2020 Apr. 25.

ZHANG, Xiaodong *et al.* Single-Layered Graphitic-C3N4 Quantum Dots for Two-Photon Fluorescence Imaging of Cellular Nucleus. **Advanced Materials,** [s.l.], v. 26, n. 26, p. 4438-4443, 2014. ISSN:0935-9648 DOI:https://doi.org/10.1002/adma.201400111. Available at: https://doi.org/10.1002/adma.201400111. Access at: 2014 Jul. 01.

ZHANG, Xiaodong *et al.* Enhanced Photoresponsive Ultrathin Graphitic-Phase C3N4 Nanosheets for Bioimaging. **Journal of the American Chemical Society,** [s.l.], v. 135, n. 1, p. 18-21, 2013. ISSN:0002-7863 DOI:10.1021/ja308249k. Available at: https://doi.org/10.1021/ja308249k. Access at: 2015 Jan. 09.

ZHANG, Ziqi *et al.* Facile synthesis of Fe–Ni bimetallic N-doped carbon framework for efficient electrochemical hydrogen evolution reaction. **Materials Today Energy,** [s.l.], v. 16, p. 100387, 2020. ISSN:2468-6069 DOI:https://doi.org/10.1016/j.mtener.2020.100387. Available at: http://www.sciencedirect.com/science/article/pii/S246860692030006X. Access at: 2020 Jun. 01.

ZHAO, Guoqiang *et al.* Heterostructures for Electrochemical Hydrogen Evolution Reaction: A Review. **Advanced Functional Materials,** [s.l.], v. 28, n. 43, p. 1803291, 2018. ISSN:1616-301X DOI:https://doi.org/10.1002/adfm.201803291. Available at: https://doi.org/10.1002/adfm.201803291. Access at: 2018 Oct. 01.

ZHAO, Yafei *et al.* Dual-Mode Luminescent Nanopaper Based on Ultrathin g–C3N4 Nanosheets Grafted with Rare-Earth Upconversion Nanoparticles. **ACS Applied Materials & Interfaces,** [s.l.], v. 8, n. 33, p. 21555-21562, 2016. ISSN:1944-8244 DOI:10.1021/acsami.6b06254. Available at: https://doi.org/10.1021/acsami.6b06254. Access at: 2016 Aug. 24.

ZHENG, Di-Wei *et al.* Carbon-Dot-Decorated Carbon Nitride Nanoparticles for Enhanced Photodynamic Therapy against Hypoxic Tumor via Water Splitting. **ACS Nano,** [s.l.], v. 10, n. 9, p. 8715-8722, 2016. ISSN:1936-0851 DOI:10.1021/acsnano.6b04156. Available at: https://doi.org/10.1021/acsnano.6b04156. Access at: 2016 Sep. 27.

ZHOU, Limin *et al.* Adsorption of acid dyes from aqueous solutions by the ethylenediamine-modified magnetic chitosan nanoparticles. **Journal of Hazardous Materials,** [s.l.], v. 185, n. 2, p. 1045-1052, 2011. ISSN:0304-3894 DOI:http://dx.doi.org/10.1016/j.jhazmat.2010.10.012. Available at: http://www.sciencedirect.com/science/article/pii/S0304389410013002. Access at: 2015 Jan. 30.

ZHOU, Ming; LI, Can; FANG, Jiye. Noble-Metal Based Random Alloy and Intermetallic Nanocrystals: Syntheses and Applications. **Chemical Reviews,** [s.l.], v. 121, n. 2, p. 736-795, 2021. ISSN:0009-2665 DOI:10.1021/acs.chemrev.0c00436. Available at: https://doi.org/10.1021/acs.chemrev.0c00436. Access at: 2021 Jan. 27.

ZHOU, Xiaofei; SUN, Hainan; BAI, Xue. Two-Dimensional Transition Metal Dichalcogenides: Synthesis, Biomedical Applications and Biosafety Evaluation. **Frontiers in**

bioengineering and biotechnology, [s.l.], v. 8, p. 236-236, 2020. ISSN:2296-4185 DOI:10.3389/fbioe.2020.00236. Available at: https://pubmed.ncbi.nlm.nih.gov/32318550

ZHOU, Zhengkun *et al.* Adsorption of food dyes from aqueous solution by glutaraldehyde cross-linked magnetic chitosan nanoparticles. **Journal of Food Engineering,** [s.l.], v. 126, p. 133-141, 2014. ISSN:0260-8774 DOI:http://dx.doi.org/10.1016/j.jfoodeng.2013.11.014. Available at: http://www.sciencedirect.com/science/article/pii/S0260877413005906. Access at: 2014 Apr. 01.

ZHU, Bicheng *et al.* Isoelectric point and adsorption activity of porous g-C3N4. **Applied Surface Science,** [s.l.], v. 344, p. 188-195, 2015. ISSN:0169-4332 DOI:https://doi.org/10.1016/j.apsusc.2015.03.086. Available at: http://www.sciencedirect.com/science/article/pii/S0169433215006716. Access at: 2015 Sep. 30.

ZHU, Houjuan *et al.* Phototherapy with layered materials derived quantum dots. **Nanoscale,** [s.l.], v. 12, n. 1, p. 43-57, 2020. ISSN:2040-3364 DOI:10.1039/C9NR07886J. Available at: http://dx.doi.org/10.1039/C9NR07886J.

ZHU, Yue *et al.* Structural Engineering of 2D Nanomaterials for Energy Storage and Catalysis. **Advanced Materials,** [s.l.], v. 30, n. 15, p. 1706347, 2018. ISSN:0935-9648 DOI:https://doi.org/10.1002/adma.201706347. Available at: https://doi.org/10.1002/adma.201706347. Access at: 2018 Apr. 01.

ZIEGLER-BOROWSKA, Marta; CHEŁMINIAK, Dorota; KACZMAREK, Halina. Thermal stability of magnetic nanoparticles coated by blends of modified chitosan and poly(quaternary ammonium) salt. **Journal of Thermal Analysis and Calorimetry,** [s.l.], v. 119, n. 1, p. 499-506, 2015. ISSN:1588-2926 DOI:10.1007/s10973-014-4122-7. Available at: http://dx.doi.org/10.1007/s10973-014-4122-7.

ZOU, Han *et al.* Photocatalytic activity enhancement of modified g-C3N4 by ionothermal copolymerization. **Journal of Materiomics,** [s.l.], v. 1, n. 4, p. 340-347, 2015. ISSN:2352-8478 DOI:https://doi.org/10.1016/j.jmat.2015.10.004. Available at: http://www.sciencedirect.com/science/article/pii/S2352847815000775. Access at: 2015 Dec. 01.

APPENDIX A – SUPPLEMENTARY MATERIALS

Figure 42 – R_L value for (a) RB5 and (b) MO adsorption from the Langmuir isotherm.

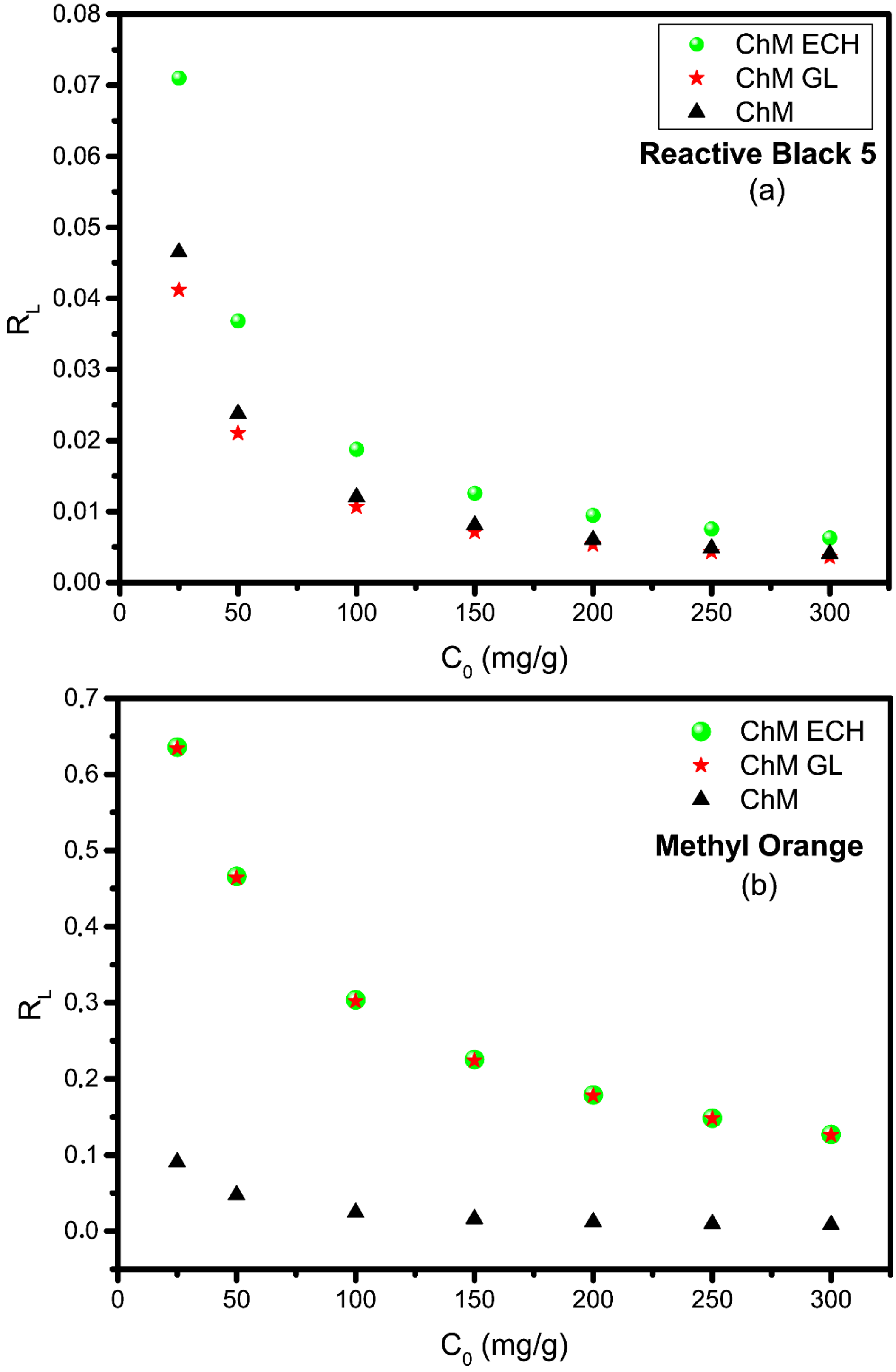

Figure 43 – Zeta potential of ChM nanocomposite at different pH levels.

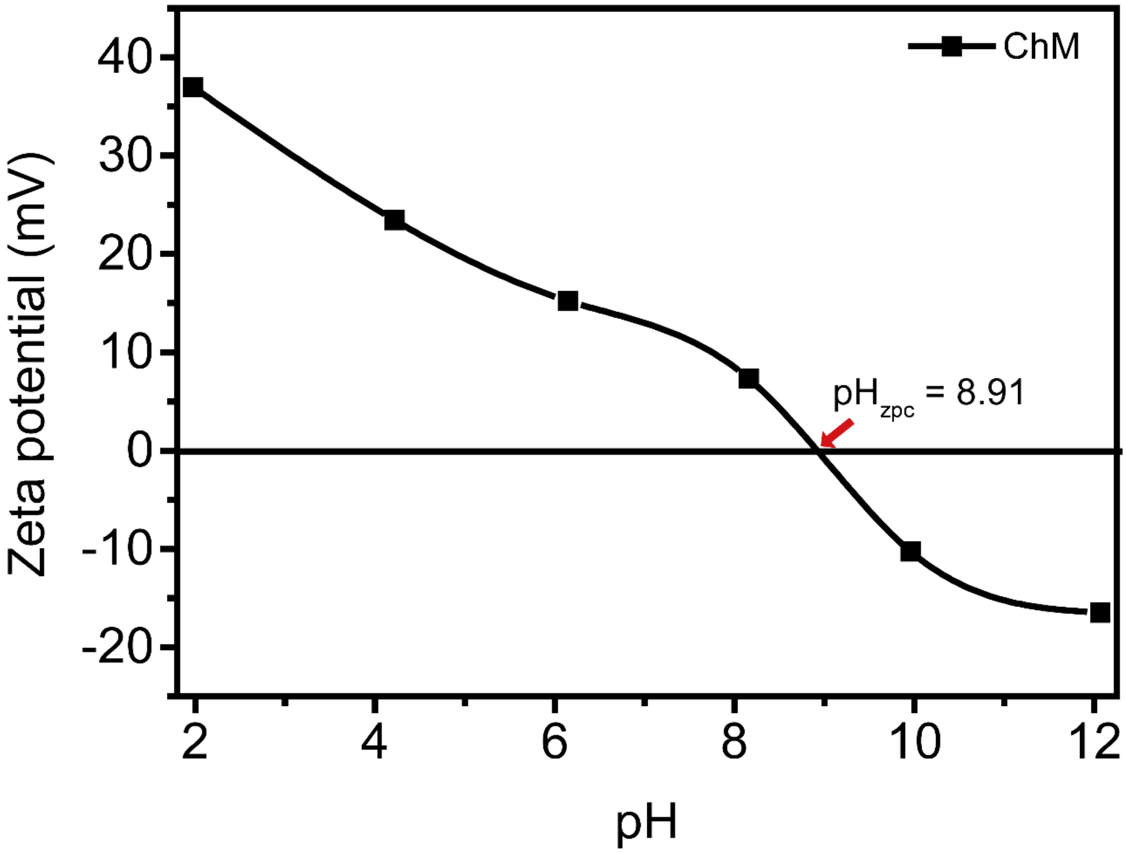

Figure 44 – Pseudo-second order plots for (a) reactive black 5 and (b) methyl orange adsorption onto nanocomposites.

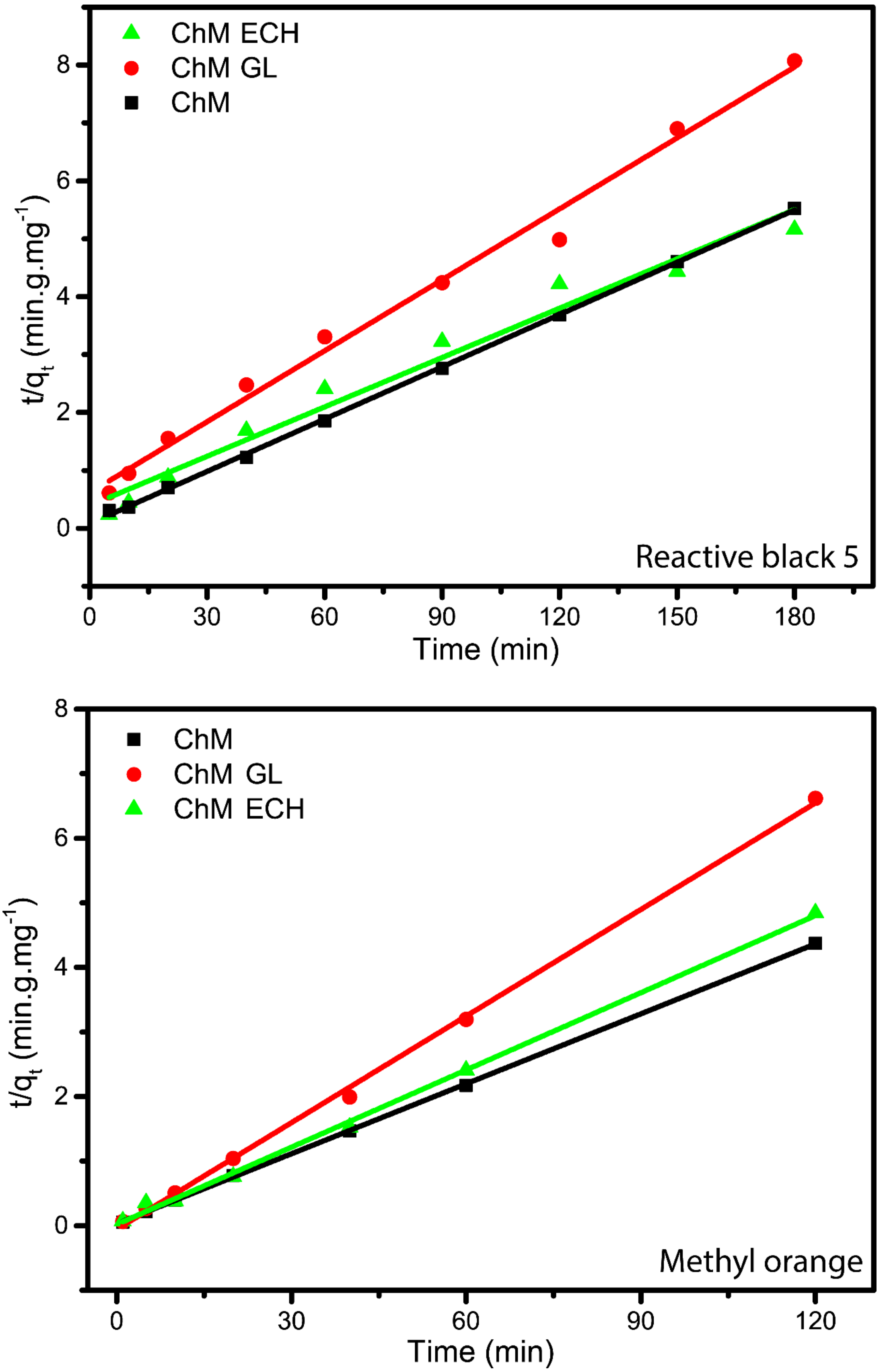

Figure 45 – (a), (b), and (c) show the intraparticle diffusion plots for sorption of MO; (d), (e), and (f) show the intraparticle diffusion plots for sorption of RB5.

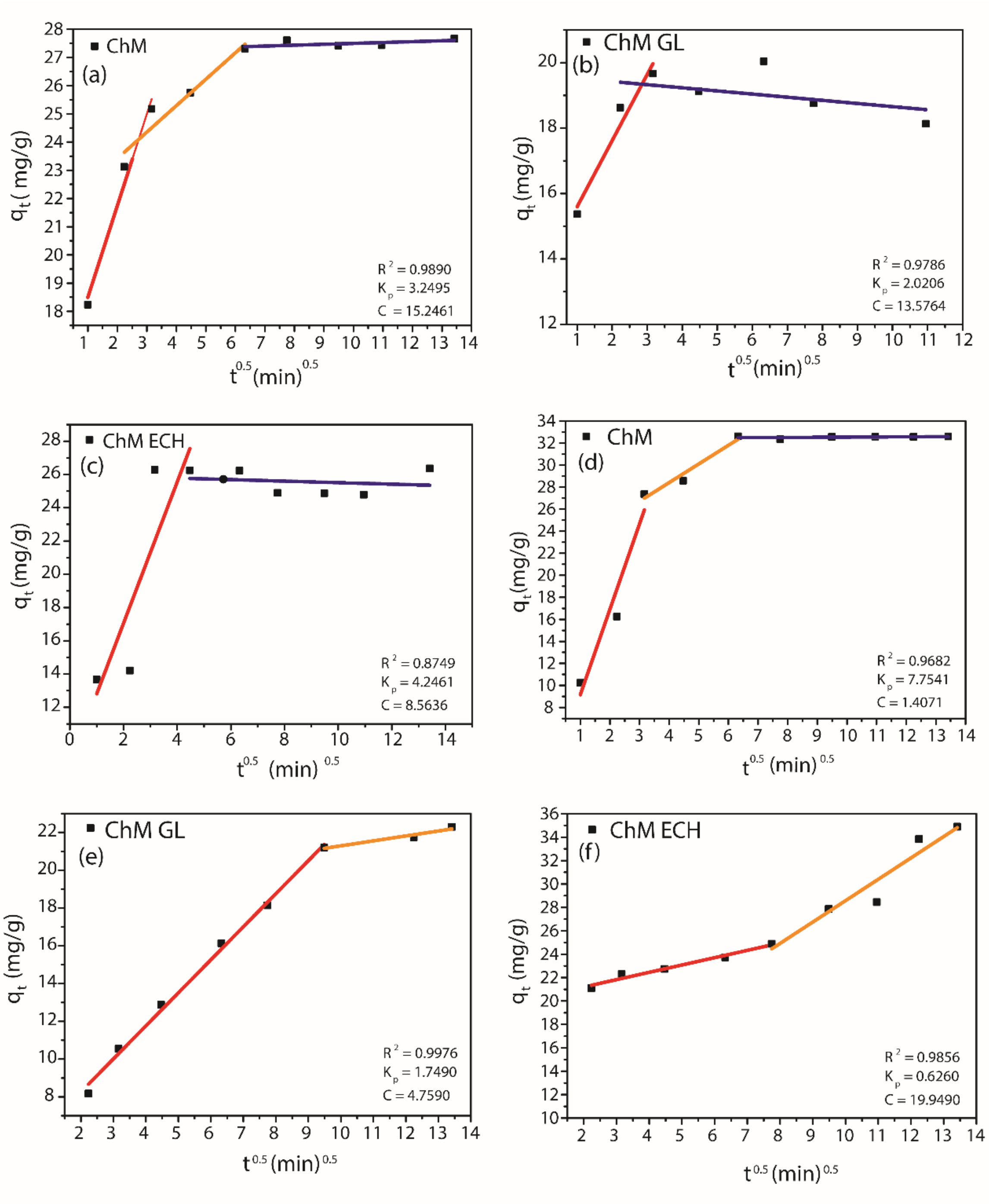

Figure 46 – Fits of applied isotherms models to the experimental data for adsorption of reactive black 5 onto (a) ChM, (b) ChM ECH and (c) ChM GL.

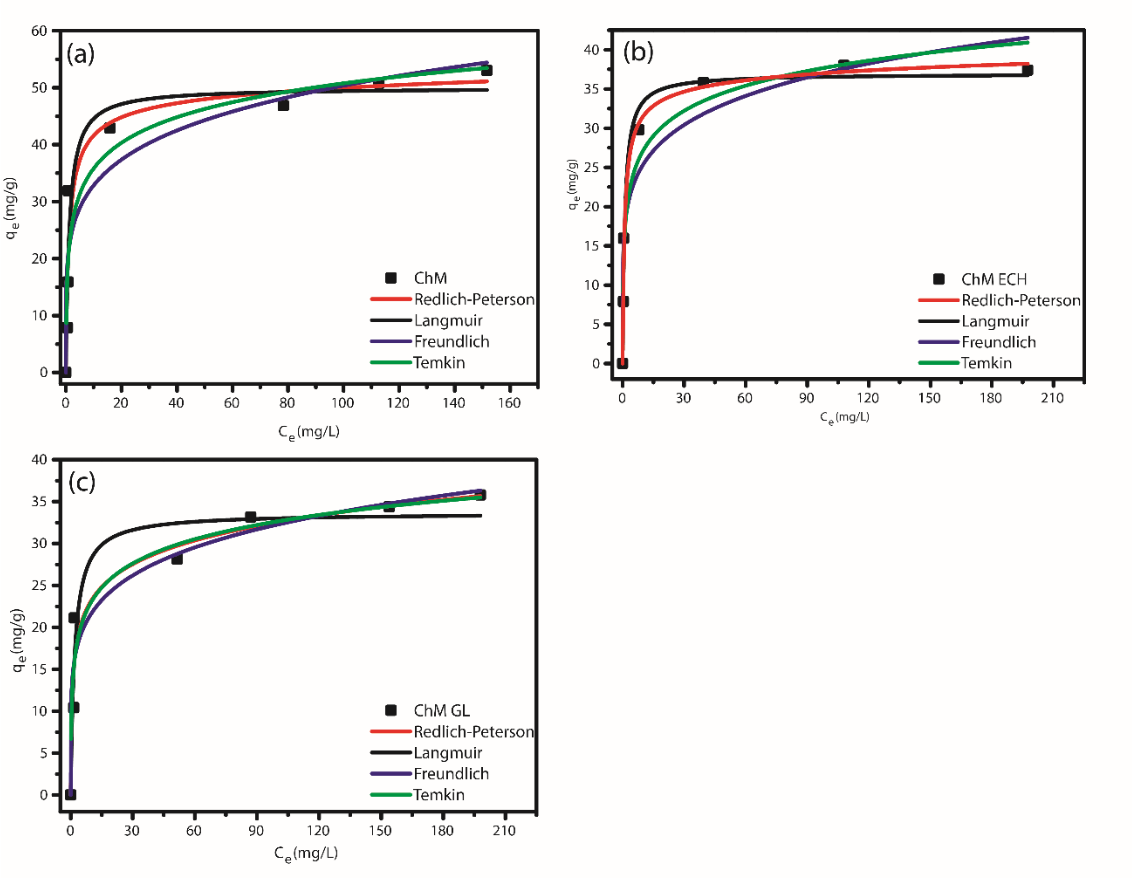

Figure 47 – Fits of applied isotherms models to the experimental data for adsorption of methyl orange onto (a) ChM, (b) ChM GL and (c) ChM ECH.

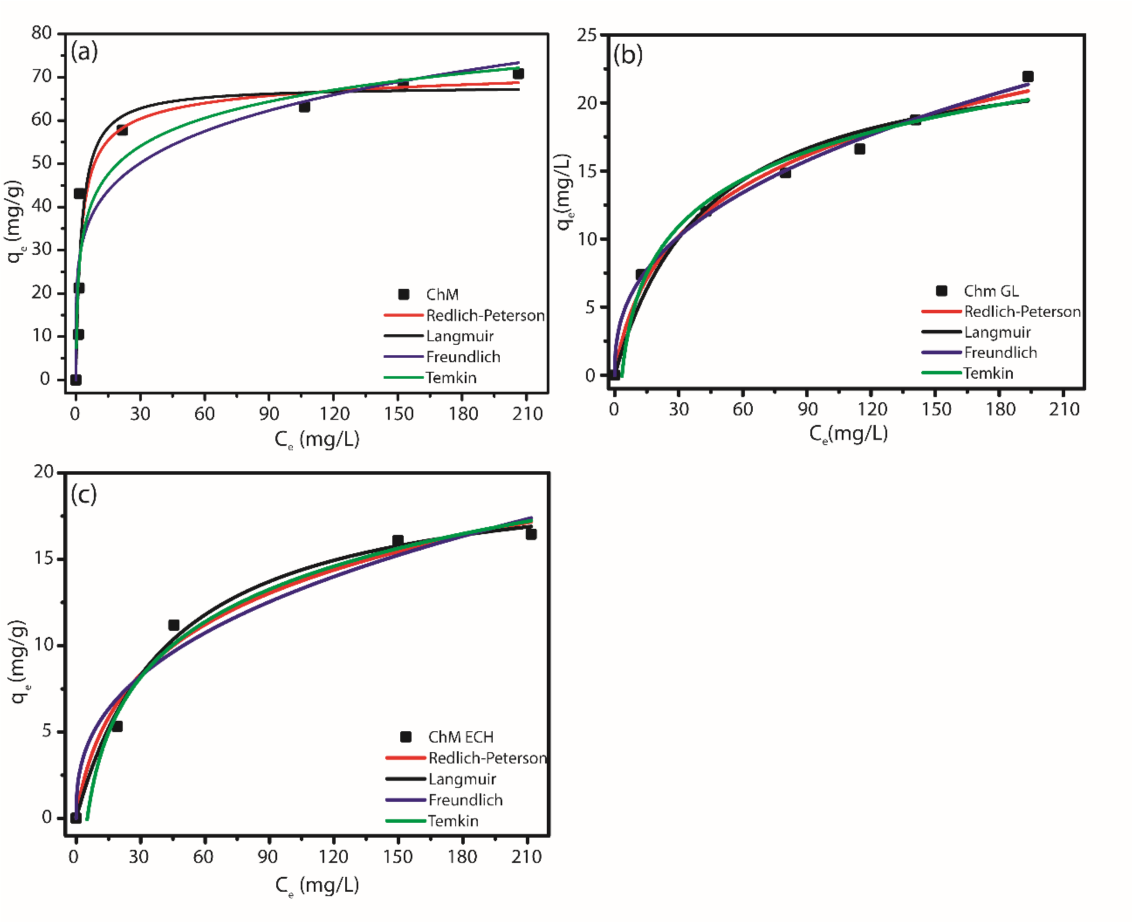

Figure 48 – ROS assay on DU-145 cell line. No ROS formation has been observed.

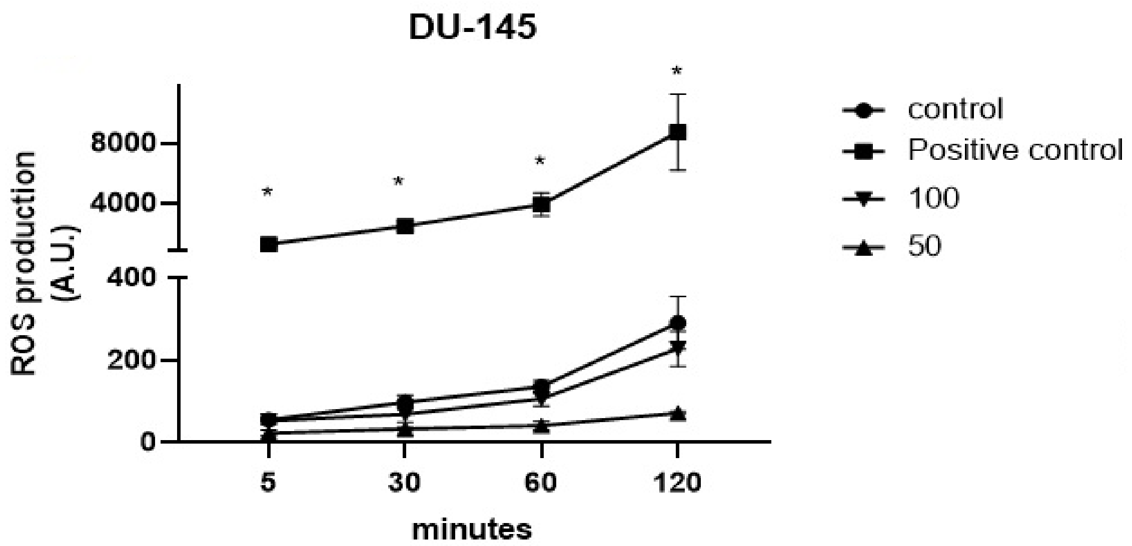

Table 9 – Comparison of the maximum adsorption capacity of ChM, ChM GL and ChM ECH to different modified chitosan adsorbents in the literature.

Adsorbent	Adsorption Capacity (mg g $^{-1}$)		Reference
	RB5	MO	
γ-Fe_2O_3/chitosan	-	29.41	(JIANG *et al.*, 2012)
Fe3O4-chitosan- L-arginine	-	338.98	(GUO *et al.*, 2017)
m-CS/Fe3O4/MIL-101	-	117	(LIU *et al.*, 2016)
chitosan/Al2O3/magnetite	-	417	
Graphene Oxide/Fe_3O_4	391	-	(TRAVLOU *et al.*, 2013)
Eichhornia crassipes/chitosan	0.606	-	(EL-ZAWAHRY *et al.*, 2016)
Magnetic chitosan - glutaraldehyde	357.10	-	(TURAL *et al.*, 2017)
Modified chitosan-pandan	169.49	-	(RAZMI *et al.*, 2019)
ChM	53.02	70.85	
ChM GL	35.77	21.93	This study
ChM ECH	37.39	16.44	